amU
Aix Marseille Université

NNT : 2024AIXM0001

THÈSE DE DOCTORAT

Soutenue à AMU — Aix-Marseille Université
le 17 décembre 2024 par

Mahawa CISSE

Optimising Fourier Filtering Wavefront Sensing for High-Contrast Imaging : Applications to Extremely Large Telescopes

Discipline
PHYSIQUE ET SCIENCES DE LA MATIERE

Spécialité
Optique, Photonique et Traitement d'Image

École doctorale
ED352 Physique et Sciences de la Matière

Laboratoire/Partenaires de recherche
ONERA - the French Aerospace Lab
Laboratoire d'Astrophysique de Marseille

Composition du jury

Maud LANGLOIS Directrice de recherche, CRAL	Rapporteure
Esteban VERA ROJAS Professeur adjoint, PUCV	Rapporteur
Rebecca JENSEN-CLEM Professeur adjointe, UCSC	Examinatrice
Marcel CARBILLET Professeur, OCA	Examinateur
Antonin BOUCHEZ Chargé de recherche, W.M.Keck Observatory	Examinateur
Magali DELEUIL Professeur, LAM	Présidente du jury
Thierry FUSCO Directeur de recherche, ONERA	Directeur de thèse
Benoit NEICHEL Chargé de Recherche, LAM	Co-directeur de thèse

ONERA
THE FRENCH AEROSPACE LAB

LAM
LABORATOIRE D'ASTROPHYSIQUE DE MARSEILLE

FOCUS
Focal Plane Array for Universe Sensing

Affidavit

I, undersigned, Mahawa CISSE, hereby declare that the work presented in this manuscript is my own work, carried out under the scientific supervision of Thierry FUSCO and Benoit Neichel, in accordance with the principles of honesty, integrity and responsibility inherent to the research mission. The research work and the writing of this manuscript have been carried out in compliance with both the french national charter for Research Integrity and the Aix-Marseille University charter on the fight against plagiarism.

This work has not been submitted previously either in this country or in another country in the same or in a similar version to any other examination body.

[Marseille] [03/09/2024]



This work is licensed under Creative Commons Attribution-NonCommercial-NoDerivatives 4.0 International Public License

Acknowledgement

D'aussi loin que je me souvienne, j'ai toujours voulu faire un doctorat. Tout au long de mes études, j'ai idéalisé le monde de la recherche. J'imaginais les chercheurs réfléchissant devant un tableau noir, résolvant des équations à la craie, expliquant aux doctorants – et donc à la prochaine génération de scientifiques – tout ce qu'ils devaient apprendre et les compétences à acquérir pour devenir les grands scientifiques de demain. Et pour être honnête, en commençant mon doctorat, j'ai assez vite déchanté... Pas de tableau noir rempli d'équations, mais un code Python/Matlab qui bug et que je passe mon temps à déboguer, des équations, oui, mais remplies de transformées de Fourier, dont une fois sur deux je ne sais plus normaliser, ce qui fait que mon code ne fonctionne pas... Vous voyez le cercle vicieux... Mais c'est grâce à vous que j'ai vu la lumière au bout du tunnel!

Et oui, je pense que l'on ne réussit jamais seul et que l'obtention de mon doctorat, je la dois en partie aux personnes que j'ai côtoyées ces dernières années.

Rentrer à Marseille pour faire mon doctorat a été une de mes meilleures décisions de ces trois dernières années, car en rentrant à la maison, j'ai pu avoir le soutien de mes parents, de mes sœurs et de mes frères, mais aussi celui de mes amis d'enfance, après trois ans dans le froid et la grisaille du plateau de Saclay.

Merci maman et papa de m'avoir soutenue tout au long de mes études. Vous avez toujours été derrière moi pour me pousser et me donner la force d'être fière de moi. Je n'oublierai pas de sitôt les discussions que nous avons eues durant ma thèse, lorsque j'avais des doutes, quand je n'étais plus motivée, et que vous m'avez aidée à y voir plus clair et à avancer avec bienveillance.

Amina, je veux te remercier de m'avoir montré la voie. Depuis le collège, je t'ai vue persévérer dans tes études jusqu'à l'obtention de ton doctorat. La première soutenance à laquelle j'ai assisté était la tienne, et j'ai été impressionnée, bien que ne comprenant pas grand-chose, par la qualité de ton travail, d'autant plus que je savais ce qui se passait en coulisses.

Comme je le disais plus haut, en rentrant à Marseille, j'ai pu renouer avec mes amis d'enfance. Anlia, je suis tellement reconnaissante que tu aies fait partie de cette aventure avec moi. Je me souviens de notre conversation téléphonique lorsque je vivais encore à Palaiseau et que je choisissais où j'allais faire mon doctorat. Tu m'as aidée à peser le pour et le contre, et ce n'est qu'un exemple parmi tant d'autres! Merci, Anlia, de m'avoir soutenue! Je suis aussi très heureuse d'avoir été présente pour la naissance de tes deux magnifiques princesses. Je vous attends, toi et ta petite famille,

à l'autre bout du monde. Je tiens aussi à te remercier, Célia, pour ton amitié depuis de très nombreuses années. Nous ne nous voyons pas très souvent, étant toutes les deux très occupées, mais notre amitié n'en a jamais pâti. On s'est vues évoluer toutes les deux. Je t'ai vue devenir maman pour la deuxième fois et je t'attends aussi à l'autre bout du monde pour plus d'aventures.

J'ai pu mener mon doctorat à son terme car j'ai été soutenue et parce que les bonnes personnes ont cru en moi et en mes capacités. Tout d'abord, je tiens à remercier Jean-François, Thierry et Benoît pour m'avoir encadrée et transmis leurs connaissances durant ces trois ans. Mais l'équipe ne s'arrête pas là... Vincent et Olivier, qui en ont rajouté une couche et sans qui cette aventure aurait été bien différente. Qui m'aidait à déboguer mes codes et à trouver mes problèmes de normalisation ? C'était vous deux. Qui répondait à mes questions bêtes (et oui, je gardais mes questionnements plus intelligents pour les chefs) ? C'était vous encore. Et plus important, vous étiez aussi présents quand j'avais besoin de me plaindre, et Dieu sait que j'aime me plaindre.

And Charlotte, thank you for your help and expertise. You were there for me on many occasions, helping me finish my first oral presentation at a conference, asking me questions to make me think about some aspects of my research that I missed, and helping me apply for postdocs. I am proud and grateful to have had the chance to work with you.

Taïssir, tu m'as aidée en temps de crise et je t'en suis très reconnaissante. Sans toi, la fin de mon doctorat aurait pu prendre une toute autre tournure ! Merci. Les derniers mois précédant la soutenance ont été rudes et intenses, et tu as su débloquer la situation et faire en sorte que tout se passe du mieux possible.

Je tiens aussi à remercier tous les membres de mon jury de thèse. J'ai longuement réfléchi à la composition de ce jury et j'en suis très fière. J'ai eu pour m'évaluer des chercheuses et chercheurs experts en leurs domaines respectifs qui ont posé un regard critique sur mes travaux. L'avant-soutenance et la soutenance elle-même n'ont pas été des plus faciles. Mais je pense que grâce à vous, membres du jury, j'en sors grandie.

Tout au long de mon parcours, j'ai été portée par de brillantes femmes scientifiques. En CPGE, avec une équipe pédagogique principalement féminine. Il y a eu aussi mon stage de fin d'études, dans l'équipe Haute Résolution Angulaire (DOTA-HRA) de l'ONERA à Châtillon, où travailler avec Aurélie n'a fait que confirmer mon désir de poursuivre une carrière dans la recherche en haute résolution angulaire. Et bien sûr, pendant mon doctorat, j'ai rencontré des chercheuses remarquables qui m'ont inspirée et donné les outils pour avancer dans ma carrière.

Audrey, Zalpha, Élodie, Lucie, Iva, Faustine, Véronique et Laurie, merci pour votre aide et votre soutien. Vous côtoyer a été une véritable source d'inspiration, qui m'a rendue plus déterminée et m'a permis de mieux comprendre ce que je voulais pour moi et pour ma carrière dans les sciences.

En choisissant le LAM pour faire mon doctorat, j'ai fait de très belles rencontres, et

sans ces personnes, encore une fois, ce doctorat aurait été différent. Merci à tous les doctorants pour les fous rires du déjeuner, les astrobeers, les repas et surtout la bonne humeur et le soutien mutuel que nous nous donnions. Quand je pense à vous, j'ai le sourire. Un grand merci à Nicolas qui m'a introduite aux jeux de rôles mais qui m'a surtout aidée sur le plan scientifique et moral pendant ces trois ans. I can say the same for Alexis. We shared offices for almost two years, and it is probably the reason why we are friends now. You were a great support during this adventure, you listened to me when I needed it, you advised me, and you were also here just to have some fun. Thank you, Lisa, I am glad I got to know you and shared crochet advice. I look forward to your defence and to seeing you somewhere around the world. La otra persona a la que quiero agradecer es a Nico. ¡Muchas gracias, Nico! Conocerte es un placer. Recuerdo cuando fuimos a la playa en verano, mientras yo escribía mi tesis, para nadar y ver la puesta de sol. Eso me permitió conocerte más y ver qué buena persona eres. También me permitió escribir esa tesis en buenas condiciones. ¡Gracias!

Je dois aussi remercier mes panthères de montagnes ou mes suptopticiennes préférées, Amani, Soizic, New, Margaux et Bérénice! Que ce soit à Marseille, à Paris ou à Milan, nos séjours ont toujours été pleins de péripéties!

Et enfin, pour conclure ces remerciements déjà très longs, je tiens à remercier mes salseras et salseros préférés! Parmi vous, il y a Nico, Lorette, Pauline, Victoria, Jorge, Manon, Diego, Lorenzo, Marine, Julie, Angela et Marta.

Nico, nous nous connaissons bien avant la salsa, bien avant le Mexique et ton activisme. Je suis tellement fière de te compter parmi mes amis. Ces trois dernières années ont été tellement riches en émotions pour toi que les décrire prendrait un livre entier, sans parler du mois d'octobre 2024... J'espère avoir été là pour toi quand tu en avais besoin, je sais que malgré ta vie mouvementée, tu as été là pour moi! Nos conversations interminables jusqu'à 4 ou 5 heures du matin, où nous nous racontions nos vies et où nous nous donnions des clés pour nous sortir de certaines situations, m'ont été d'un grand soutien! Merci encore.

Et Lorette, 10 ans d'amitié! Nous sommes rentrées à Marseille toutes les deux en 2021, nous nous sommes soutenues quand ça n'allait pas, tu as toujours été de bon conseil et à l'écoute quand j'en avais besoin. J'espère te revoir bientôt rayonnante à l'autre bout du monde .

Et mes salseras et salseros, sachez que vous étiez ma petite bouffée d'air frais à chaque fois que je vous voyais!



List of communications

Publication in journal as first author : Submitted

1. **CISSE, Mahawa**, FAUVARQUE, Olivier, CHAMBOULEYRON, Vincent, LEVRAUD, Nicolas, BOND, Charlotte Z., NEICHEL, Benoit, SAUVAGE, Jean-François and FUSCO, Thierry. *How to describe Fourier filtering wavefront sensors non-linearity with interaction matrices*. Journal of Astronomical Telescopes, Instruments, and Systems, 2024

Publication in journal : in the authors list

1. CHAMBOULEYRON, Vincent, FAUVARQUE, Olivier,PLANTET, Cédric, SAUVAGE, Jean-François, LEVRAUD, Nicolas, **CISSE, Mahawa**, NEICHEL, Benoit and FUSCO, Thierry. *Modeling noise propagation in Fourier-filtering wavefront sensing, fundamental limits, and quantitative comparison*. A&A 670, A153, 2023
2. LEVRAUD, Nicolas, CHAMBOULEYRON, Vincent, SAUVAGE, Jean-François, NEICHEL, Benoit, **CISSE, Mahawa**, FAUVARQUE, Olivier, AGAPITO, Guido, PLANTET, Cédric, CHEFFOT, Anne-Laure, PINNA, Enrico, ESPOSITO, Simone and FUSCO, Thierry. *A strategy for sensing the petal mode in the presence of AO residual turbulence with the pyramid wavefront sensor*. A&A 682, A84, 2024
3. BONNEFOIS, Aurélie Montmerle, VELLUET, Marie-Thérése, **CISSÉ, Mahawa**, et al. Feasibility demonstration of AO pre-compensation for GEO feeder links in a relevant environment. Optics Express, 2022, vol. 30, no 26, p. 47179-47198.

Conference proceedings :

1. **CISSE, Mahawa**, CHAMBOULEYRON, Vincent, FAUVARQUE, Olivier, BOND, Charlotte Z., LEVRAUD, Nicolas, SAUVAGE, Jean-François, NEICHEL, Benoit, FUSCO, Thierry. *The phase-shifted Zernike wave-front sensor. Description of the non-linear behaviour of Fourier filtering wavefront sensor using matrix formalism : the specific matrix*. In : Adaptive Optics Systems VIII. SPIE, 2024
2. **CISSE, Mahawa**, MUSLIMOV, Eduard, HERITIER, Cedric Taissir, CHAMBOULEYRON, Vincent, FETICK, Romain, LEVRAUD, Nicolas, SAUVAGE, Jean-François, NEICHEL, Benoit, FUSCO, Thierry. *PAPYRUS : Second stage adaptive optics with a vector Zernike wavefront sensor*. In : Adaptive Optics for Extremely Large Telescopes 7th Edition. 2023.

3. **CISSE, Mahawa**, CHAMBOULEYRON, Vincent, FAUVARQUE, Olivier, BOND, Charlotte Z., LEVRAUD, Nicolas, SAUVAGE, Jean-François, NEICHEL, Benoit, FUSCO, Thierry. *The phase-shifted Zernike wave-front sensor.* In : Adaptive Optics Systems VIII. SPIE, 2022. p. 258-265.

Conference proceedings : In the authors list

1. LEVRAUD, Nicolas, **CISSE, Mahawa**, CHAMBOULEYRON, Vincent, et al. *Properties of petal mode and its measurement in an adaptive optic closed loop.* In : Adaptive Optics Systems IX. SPIE, 2024. p. 130972E.
2. MOTTE, Mathieu et al. *High-performance AO systems : impact of the chromatic pupil shift in the case of RISTRETTO.* In : Adaptive Optics Systems IX. SPIE, 2024. p.30976A, https ://doi.org/10.1117/12.3018993
3. NEICHEL, Benoit et al. *Cassiopée : toward technological development for XAO on ELT.* In : Adaptive Optics Systems IX. SPIE, 2024. P130971G, https ://doi.org/10.1117/12.3019601
4. CHAMBOULEYRON, Vincent, **CISSÉ, Mahawa**, SALAMA, Maïssa, et al. *Reconstruction methods for the phase-shifted Zernike wavefront sensor.* In : Adaptive Optics Systems IX. SPIE, 2024. p. 349-361.
5. STRIFFLING, Arnaud, FÉTICK, Romain JL, CHAMBOULEYRON, Vincent, SAUVAGE, Jean-François, HERITIER, Cédric Taissir, **CISSE, Mahawa**, LEROUX, François, NEICHEL, Benoit, FUSCO, Thierry, JOUVE Pierre, Idir Boudjema/ *Reconstruction methods for the phase-shifted Zernike wavefront sensor.* In : Adaptive Optics Systems IX. SPIE, 2024. p. 349-361.
6. FÉTICK, Romain JL, FUSCO, Thierry, STRIFFLING, Arnaud, **CISSÉ, Mahawa**, et al. *PAPYRUS : from an adaptive optics system to an instrumental platform.* In : Adaptive Optics Systems IX. SPIE, 2024. p. 275-282.
7. FÉTICK et al. *PAPYRUS : one year of on-sky operations* In : Adaptive Optics for Extremely Large Telescopes 7th Edition, ONERA, Jun 2023, Avignon, France. ⟨10.13009/AO4ELT7-2023-014⟩⟩
8. SAUVAGE, Jean-François et al. *HARMONI at ELT : impact of low wind effect on SCAO mode performance* : Proceedings Volume 12185, Adaptive Optics Systems VIII ; 1218519 (2022) https ://doi.org/10.1117/12.2627698
9. LEVRAUD, Nicolas,CHAMBOULEYRON, Vincent, FAUVARQUE, Olivier, **CISSÉ, Mahawa**, et al. *First light for PAPYRUS, the pyramid based adaptive optics system at LAM/OHP* In : Adaptive Optics Systems IX. SPIE, 2022.
10. CHAMBOULEYRON et al. *First light for PAPYRUS, the pyramid based adaptive optics system at LAM/OHP* In : Adaptive Optics Systems IX. SPIE, 2022.

Résumé

Mots clés : Optique Adaptative, Analyseurs à filtrage de Fourier, Analyseur Zernike, Analyseur pyramide

Depuis 1995, des milliers d'exoplanètes ont été identifiées à l'aide de diverses techniques parmi lesquelles l'imagerie à haut contraste (ou imagerie directe) qui contribue à la détection et à la charactérisation spectrale de ces planètes. Pour fonctionner de manière optimale, ce type d'instrument doit recevoir un front d'onde corrigé de toutes aberrations. Ils intègrent donc des systèmes d'optique adaptative (OA), composés d'un miroir déformable, d'un analyseur de surface d'onde (ASO) et d'un calculateur temps réel, pour mesurer et compenser en temps réel toutes les perturbations de phase induites par la turbulence atmosphérique, le télescope et l'instrument lui même.

L'avènement des télescopes géants (de 24 à 39m de diamètre) présente de nouveaux défis pour les systèmes d'OA en matière de correction du front d'onde permettant la détection d'Exo-Terre (exoplanète similaire à la Terre). Les miroirs primaires de la prochaine génération de télescopes géants seront segmentés afin d'atteindre la taille souhaitée. Les problèmes liés à la segmentation du miroir primaire (en particulier, liés à l'ombre porté des supports du miroir secondaire) nécessite la mise en œuvre de stratégies de mesure et de correction de phase innovantes pour gérer à la fois la fragmentation de la pupille et la turbulence atmosphérique. Les approches classiques pour l'analyse de surface d'onde (Shack-Hartmann, Pyramide modulée) sont optimisées pour mesurer la turbulence atmosphérique mais sont insensibles au piston différentiel généré par les pupilles fractionnées. Inversement, certains autres analyseurs comme les pyramides non-modulées ou le masque de Zernike sont plus sensibles à la fragmentation de la pupille mais moins efficaces pour mesurer la turbulence atmosphérique du fait de leur domaine de linéarité tres réduit.

Cette thèse de doctorat porte sur les ASO de nouvelle génération qui feront partie intégrante des systèmes d'OA des télescopes géants segmentés. Ces analyseurs appartiennent à la famille des ASO à filtrage de Fourier dont le masque de Zernike et l'analyseur pyramide non-modulée en sont des exemples. Le principal objectif de mon doctorat était de développer une compréhension approfondie de la réponse non-linéaire de ces analyseurs et de son impact sur l'estimation du front d'onde. J'ai alors, proposé deux solutions permettant de diminuer les effets non-linéaires : une modification de l'ASO et une modification du reconstructeur utilisé pour l'estimation du front d'onde. Les solutions proposées devraient améliorer la correction fournie par le système d'OA.

Abstract

Keywords: Adaptive Optics, Fourier filtering Wavefront Sensor, Zernike Wavefront Sensor, Pyramid Wavefront Sensor

Since 1995, thousands of exoplanets have been identified using various techniques including high-contrast imaging (or direct imaging) which contributes to the detection and spectral characterisation of these planets. To function optimally, this type of instrument must receive a wavefront corrected for all aberrations. They therefore integrate adaptive optics (AO) systems, composed of a deformable mirror, a wavefront sensor (WFS) and a real-time computer (RTC), to measure and compensate in real time all phase perturbations induced by atmospheric turbulence, the telescope and the instrument itself.

The advent of giant telescopes (from 24 to 39m in diameter) presents new challenges for AO systems in terms of wavefront correction allowing the detection of Exo-Earth (exoplanet similar to Earth). The primary mirrors of the next generation of giant telescopes will be segmented to reach the desired size. The problems related to the segmentation of the primary mirror (in particular, related to the shadow cast by the secondary mirror supports) require the implementation of innovative measurement and phase correction strategies to manage both pupil fragmentation and atmospheric turbulence. Classical approaches for wave surface analysis (Shack-Hartmann, Modulated Pyramid) are optimised to measure atmospheric turbulence but are insensitive to the differential piston generated by fragmented pupils. Conversely, some other sensors such as unmodulated pyramids or Zernike masks are more sensitive to pupil fragmentation but less effective in measuring atmospheric turbulence due to their very reduced linearity domain.

This PhD thesis focuses on new generation of WFSs that will be an integral part of the AO systems of giant segmented telescopes. These sensors belong to the Fourier filtering WFS family of which the Zernike mask and the unmodulated pyramid are examples. The main objective of my PhD was to develop a thorough understanding of the nonlinear response of these sensors and its impact on wavefront estimation. I then proposed two solutions to reduce the nonlinear effects: a modification of the WFS itself and a modification of the reconstructor used for wavefront estimation. The proposed solutions should improve the correction provided by the AO system.

Résumé étendu

Mots clés : Optique Adaptative, Analyseurs à filtrage de Fourier, Analyseur Zernike, Analyseur pyramide

L'un des principaux objectifs de l'astronomie moderne est de parvenir à une compréhension complète de la formation de la vie sur Terre. Cette quête comprend : la découverte de nouveaux mondes, la réponse à la question "Sommes-nous seuls dans l'univers ?", mais aussi l'étude des systèmes planètaires. De cette « curiosité » découlent d'énormes défis technologiques.

En 1995 a été découverte la première exoplanète en orbite autour d'une étoile semblable au Soleil, 51 Pegasi b (Mayor & Queloz 1995). À ce jour, plus de 7000 exoplanètes ont été découvertes à l'aide de différentes techniques. L'étape suivante consiste naturellement à trouver une planète capable d'abriter la vie.

L'imagerie directe ou imagerie à haut contraste (voir Fig.1) permet de faire l'image d'exoplanètes en éliminant la lumière de son étoile hôte. Cette aproche donne accès au spectre de la planète et l'analyse du spectre permet d'identifier d'éventuels biomarqueurs dans leur atmosphère, ce qui est crucial dans notre recherche de la vie extraterrestre. Pour faire de l'imagerie à haut contraste deux éléments sont indispensables : le coronographe - instrument permettant d'éliminer la lumière de l'étoile de l'image et de rendre visible la planète - et de grands télescopes.

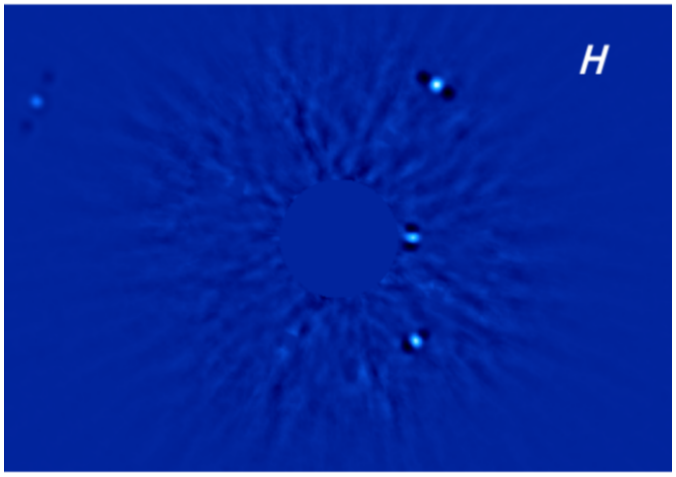

FIGURE 1 – Système planétaire HR8799, *Credits : Vigan et al. (2016)*

Un télescope est un instrument optique utilisé pour capturer des images de scènes astronomiques, avec pour principal objectif de collecter un maximum de photons. L'information provenant d'une scène astronomique provient de la lumière qu'elle émet ou réfléchit, ainsi, pour recueillir le plus d'informations possible, un télescope doit être grand. Le pouvoir de collecte d'un télescope dépend du diamètre de son miroir primaire, et augmente comme le carré de son diamètre, D^2. Ainsi, plus un miroir est grand, plus il collecte de photons, ce qui entraîne une augmentation de la sensibilité ou, en d'autres termes, augmente le nombre d'objets observables. Le second objectif d'un télescope est d'augmenter la résolution angulaire qui se définit comme étant la capacité de l'instrument à distinguer des objets proches, et à retranscrire avec précision le contenu fréquentiel de la scène. Comme le pouvoir de collecte de l'instrument, la résolution dépend du diamètre du miroir primaire et de la longueur d'onde d'observation suivant la relation : $\theta = \lambda / D$ qui définit la limite de diffraction du télescope. Une définition plus détaillée de la résolution est donnée dans le chapitre 1.

La prochaine génération de télescopes terrestres -Giant Segmented Telescopes (GST)- aura des miroirs primaires de plus de 20 m de diamètre. Parmi ces futurs télescopes figurent l'European Extremely Large Telescope (ELT) (Gilmozzi & Spyromilio 2007; Cavarroc et al. 2006), en construction, ses homologues américains : le Thirty Meter Telescope (TMT), (Nelson & Sanders 2008) et le Giant Magellan Telescope (GMT), (Gunnels et al. 2004; Fanson et al. 2018). L'ELT aura une optique primaire de 39 m de diamètre composée de 798 segments hexagonaux (voir Fig.2). Son design optique comprend cinq miroirs, opérant dans le domaine optique/infrarouge proche, avec un champ de vue de 10 minutes d'arc.

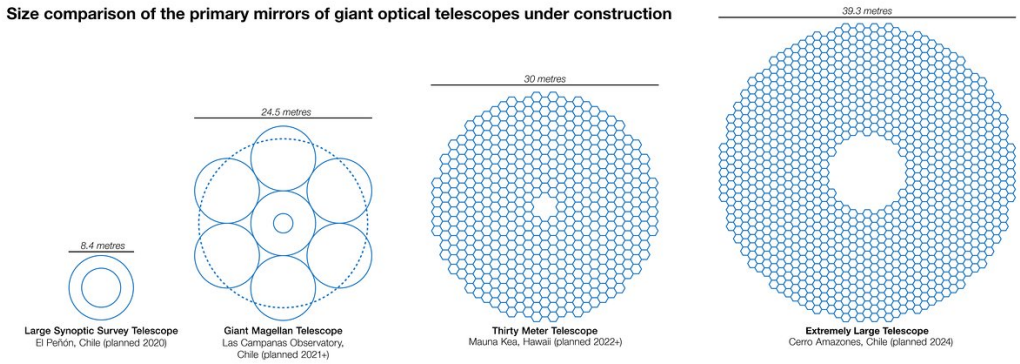

FIGURE 2 – Miroirs primaires de différents télescopes. *Crédits : ESO*

De part sa taille, l'ELT recueillera 20 fois plus de lumière qu'une seule unité du Very Large Telescope (VLT). L'ELT permettra l'étude de planètes similaires à la Terre (Exo-Terre). Néanmoins, la difficulté réside dans la proximité de ce type de planètes avec leur étoile hôte ainsi que dans la différence de luminosité, en effet, le contraste

entre la planète et l'étoile peut être aussi grand que 10^{10}.

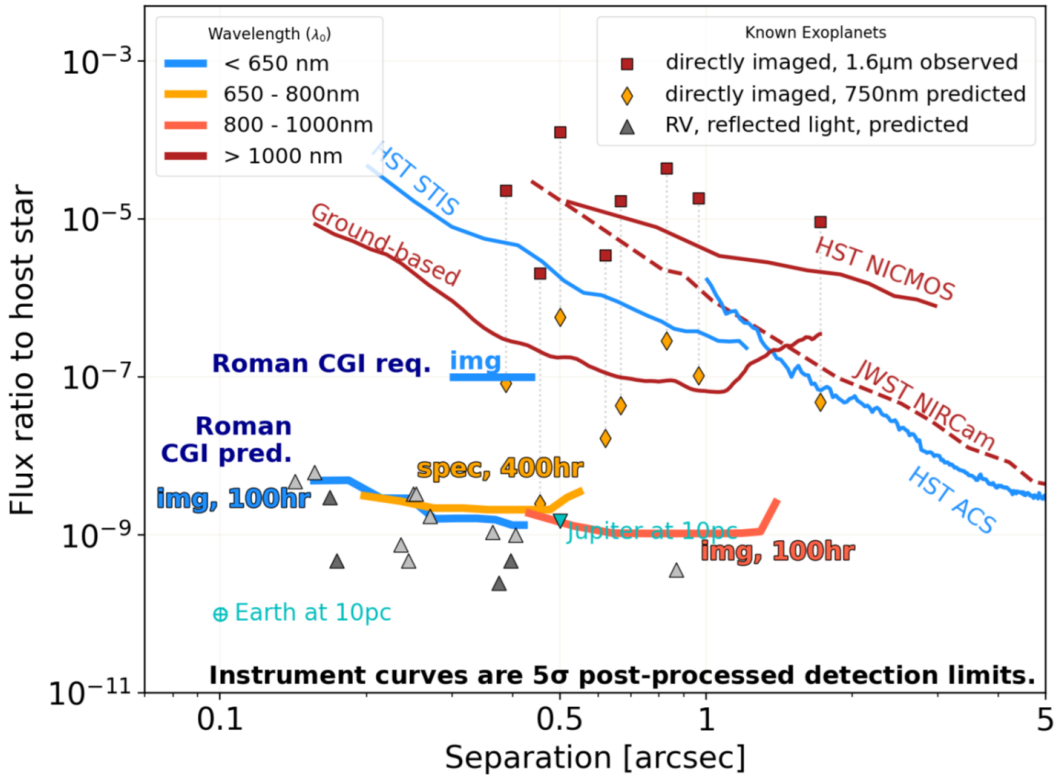

FIGURE 3 – Limite de détection d'actuels et futurs instruments. *Crédits :* https://github.com/nasavbailey/DI-flux-ratio-plot

Les Exo-Terres sont situées à une séparation angulaire < 0.1" alors que les planètes de type Jupiter (planètes actuellement imagées) sont à une séparation angulaire > 0.5" (voir Fig.3). L'objectif est donc de faire l'image de telles planètes dans notre "environnement proche", c'est-à-dire, autour de jeunes étoiles situées à une dizaines de parsecs. Avec une séparation angulaire de l'ordre de grandeur de la résolution du télescope, $\theta = \lambda/D$, typiquement 12 mas @500nm, il devrait être possible de faire une telle image avec un télescope comme le VLT dans le domaine visible. Cependant, pour les télescopes terrestres, la difficulté provient de la qualité de l'image brute. En effet, nous avons défini précédemment θ comme la limite de diffraction théorique d'un télescope parfait. Pourtant, les images d'un télescope ne sont pas, dans la plupart des cas, limitées par la diffraction car elles souffrent de la présence d'aberrations. Les aberrations optiques sont responsables de la modification du front d'onde du champ électromagnétique (EM) incident, elles dégradent la qualité de l'image et donc la résolution du télescope. Ces aberrations ont plusieurs sources, elles peuvent être causées par l'instrument lui-même, soit le télescope, ou elles peuvent être induites par la turbulence atmosphérique. Une autre difficulté provient des limites de l'instrument

à haut contraste : les systèmes actuels parviennent à atteindre des contrasts de l'ordre de 10^6 ce qui est suffisant pour des planètes massives loin de leurs étoiles mais reste très loin du contraste nécessaire à l'imagerie d'une Exo-Terre.

Nous nous intéressons ici aux aberrations induites par l'atmosphère et par le télescope. Après un long voyage dans l'Univers, le champ EM se propagera à travers l'atmosphère sur quelques centaines de kilomètres avant d'atteindre l'instrument. L'impact de la turbulence atmosphérique est détaillé au chapitre 1. Les fluctuations de l'indice de réfraction de l'air dans l'atmosphère induisent des aberrations de phase dans le champ EM, ce qui dégrade la qualité de l'image (voir Fig.4).

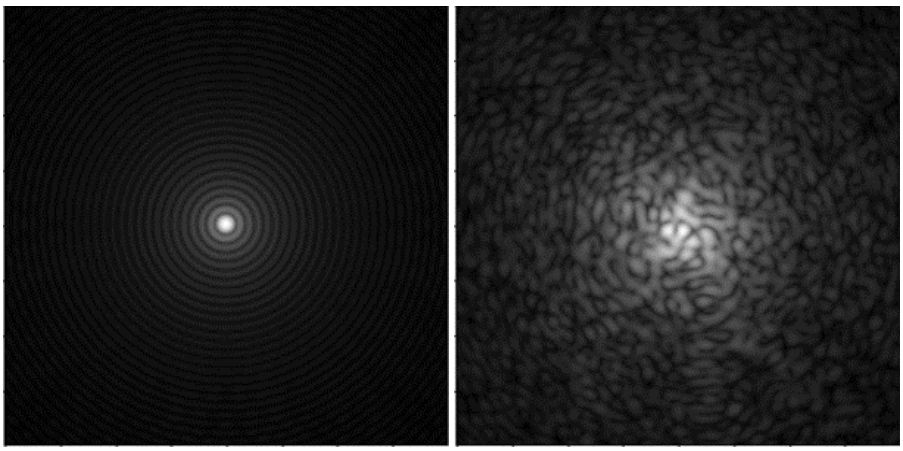

(a) Propagation sans aberration

(b) Propagation en présence d'aberrations

FIGURE 4 – Image d'une étoile à travers un télescope en l'absence et en présence d'aberrations.

L'optique adaptative (OA) (plus de détails au chapitre 1) a été pensée par Babcock (1953) et développée pour atténuer les effets de la turbulence atmosphérique et retrouver la résolution du télescope (voir Fig.5). Le système d'AO est composé :

— d'un miroir déformable (Deformable Mirror (DM) en anglais) : composant d'optique actif qui modifie son état de surface pour corriger la phase de l'onde incidente.

— d'un analyseur de surface d'onde (WaveFront Sensor (WFS) en anglais) : composant qui mesure les déformation du front d'onde à partir du signal de la caméra.

— d'un calculateur temps réel (Real-Time Computer (RTC) en anglais) : composant qui envoie les commandes appropriées au DM pour qu'il prenne la forme souhaitée dans le but de corriger les aberrations mesurées par l'ASO.

En configuration boucle fermée, le système fonctionne de la façon suivante : la lumière émise par le point source ou étoile est réfléchit par le DM, une portion de la lumière est envoyé à l'instrument scientifique (imageur haut constraste par exemple), le reste de la lumière est envoyé au WFS pour mesurer les défauts de phase. Enfin, le RTC calcule les commandes à envoyer au DM pour compenser les aberrations. Ce processus est itératif et fonctionne à une fréquence de l'ordre de la centaine de Hertz voire kiloHertz (Roddier 1999). Plus de détails sur l'OA sont données au chapitre 1.

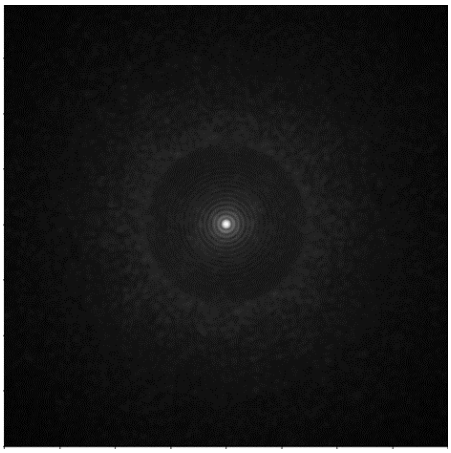

FIGURE 5 – Simulation d'une image après correction par OA. À comparer à l'image sans correction Fig.4(b)

Les aberrations induites par le télescope sont d'une autre nature. Pour les GST, l'aberration que nous considérons est l'aberration dite de fragmentation de la pupille ou piston différentiel. La fragmentation de l'ELT est induite par les structures métalliques (bras) qui maintiennent le miroir secondaire (M2). En raison de la taille des miroirs, les bras doivent être épais pour supporter le poids de M2, si bien que l'ombre des bras projetée sur le miroir primaire (M1) coupe la pupille en 6 fragments, brisant ainsi la continuité du front d'onde à travers la pupille. Dans ce cas, le système d'OA est parfaitement capable de corriger la turbulence atmosphérique sur chacun des fragments mais ne peut corriger la turbulence située sous les bras du télescope, ce qui crée un piston différentiel entre les différents fragments de la pupille (Schwartz et al. 2018; Bertrou-Cantou 2021; Levraud 2023) (voir Fig.9). Plus de détails sur la fragmentation de la pupille et son impact sur la qualité d'imagerie au chapitre 1, section 1.3 et chapitre 2.

Le défi pour l'astronomie au sol dans le domaine de l'imagerie directe des exo-Terres est donc de fournir au système à haut contraste un front d'onde aussi plan que possible, en particulier près de l'étoile hôte, et donc le domaine des basses/moyennes fréquences spatiales. La qualité du front d'onde dépend principalement des mesure faites par le WFS. Dans le contexte des GST, les systèmes d'OA classiques utilisés pour corriger la turbulence atmosphérique doivent être repensés afin d'atteindre le niveau de correction nécessaire à la détection de ces planètes. En effet, en plus de corriger la turbulence atmosphérique, des stratégies doivent être mises en œuvre pour

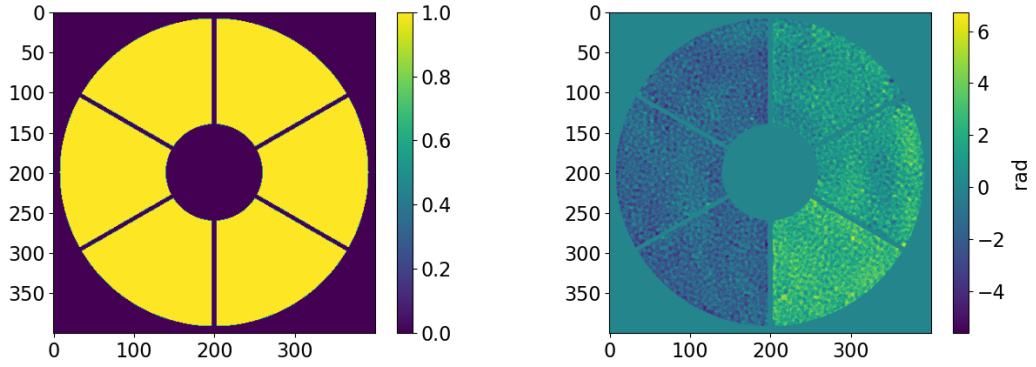

(a) Pupille de l'ELT

(b) Écran de phase résiduelle

FIGURE 6 – Simulation d'une boucle d'OA pour l'ELT. Gauche : pupille ELT utilisée pour les simulations. Droite : écran de phase résiduelle d'amplitude 1.9 rad RMS.

corriger le piston différentiel. Les WFS classiques ne peuvent pas mesurer les deux ; le Shack-Hartmann (SH) est parfait pour mesurer la turbulence atmosphérique mais est insensible aux défauts de fragmentation, et inversement pour la pyramide (Pyramid WaveFront Sensor (PWFS) (en anglais)) non-modulée (cf chapitre 1). Cependant, en ajoutant un étage de modulation, la pyramide peut contrôler la turbulence atmosphérique mais perd sa sensibilité au piston différentiel (Bertrou-Cantou et al. 2020; Levraud 2023). Un autre WFS prometteur pour de telles mesures est le masque de Zernike (Zernike WaveFront Sensor (ZWFS) (en anglais)) (Dohlen et al. 2006; N'Diaye et al. 2013) mais son utilisation en temps réel est rendu difficile par sa réponse non linéaire.

Ce manuscrit de thèse se concentre sur l'étude de l'analyseur pyramidal ainsi que du masque de Zernike, tous deux font partie d'une famille d'analyseur nommée les analyseurs à filtrage de Fourier (Fourier Filtering WaveFront Sensor (FF-WFS) (en anglais)). Ces analyseurs seront au cœur des systèmes d'OA de la prochaine génération de télescopes de part leur haute sensibilité : capacité à fournir une mesure précise de la phase en régime de faible flux. L'objectif est de développer une compréhension approfondie de la réponse non-linéaire de ces WFS et de son impact sur l'estimation du front d'onde.

Nous nous concentrerons dans un premier temps sur la modification du WFS dans le but d'augmenter la dynamique de mesures. Ces travaux seront menés à travers l'exemple du ZWFS (voir chapitre 2), ou nous étudierons alors un nouveau masque de Zernike, le Phase-Shifted Zernike WaveFront Sensor (PS-ZWFS) (Doelman et al. 2019). Ce nouveau WFS, plus dynamique que le Zernike améliore d'un facteur trois l'estimation du piston différentiel (voir Fig.7).

Nous utiliserons aussi ce WFS dans des systèmes d'OA à multi-étage. En effet, la

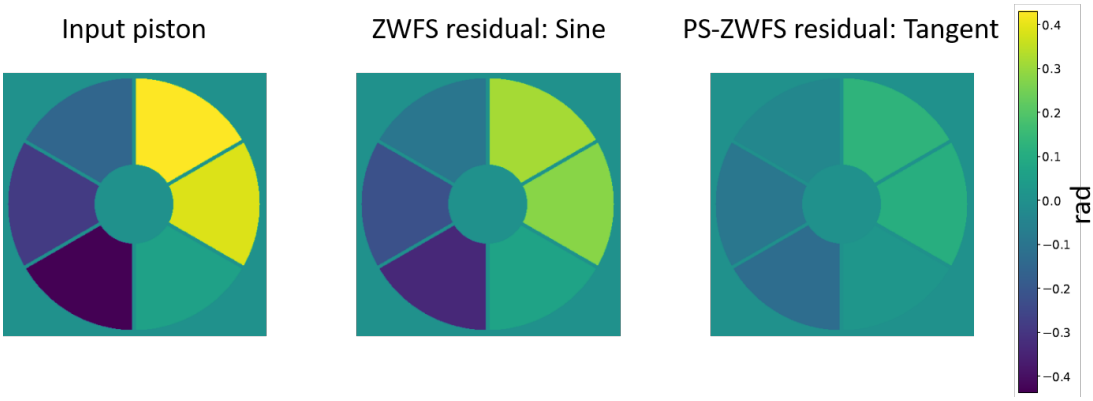

FIGURE 7 – Estimation d'un piston différentiel en boucle ouverte en présence de résidus d'OA d'amplitude 1rad RMS (124 nm RMS). Piston différentiel initial, 0.32rad RMS (0.13λ PV), ZWFS erreur = 0.24rad RMS, PS-ZWFS erreur = 0.1 rad RMS.

communauté de l'OA opte désormais pour des systèmes d'OA à plusieurs étages afin d'améliorer le niveau de correction dans le visible ou l'infrarouge proche, au plus près de l'étoile. Un système d'OA à trois étages est envisagé pour le GMT avec GMagAO-X (Haffert et al. 2022). En ce qui concerne les systèmes d'OA actuels, une mise-à-jour du système d'OA de Spectro-Polarimetric High-contrast Exoplanet Research (SPHERE) est également prévue pour augmenter le contraste au plus près de l'étoile et détecter des planètes situées entre 3 et 10 au ; SAXO+ (Vidal et al. 2022; Mazoyer et al. 2024) vise à réduire l'erreur temporelle de la première boucle d'OA avec un deuxième étage plus rapide et à corriger les aberrations quasi-statiques. SAXO+, est un démonstrateur technologique pour Planetary Camera and Spectrograph (PCS) futur instrument de l'ELT (Kasper et al. 2021). C'est donc dans ce contexte d'OA multi-étage que nous testerons notre PS-ZWFS, avec sa grande dynamique, il permettra d'améliorer le niveau de correction et donc de dimuner le niveau d'aberrations au plus près de l'étoile (voir Fig.8). Une mise en pratique expérimentale en collaboration avec le Jet Propulsion Laboratory (JPL) est prévu sur le banc PAPYRUS situé à l'Observatoire de Haute-Provence. Le but de cette manipulation est de reproduire un système d'OA multi-étage de type SAXO+ utilisant un PS-ZWFS comme second analyseur. Des travaux sur la caractérisation du PS-ZWFS fournit par JPL et le design optique du second étage de correction sont en cours.

L'autre stratégie abordée dans ce manuscrit, pour limiter l'impact des phénomènes non-linéaires sur l'estimation de front d'onde, est la modification du reconstructeur des FF-WFS avec l'exemple de la pyramide. L'objectif est de faire fonctionner une pyramide sans modulation pour contrôler à la fois la turbulence et les défauts de fragmentation. Cette méthode se base sur une approche linéaire à paramètres variables. Nous complétons le formalisme des gains optiques (OG) introduit par Korkiakoski et al. (2008), Fauvarque (2017), Deo (2019) et Chambouleyron (2021), développé pour la pyramide modulée, et l'adaptons à la pyramide non modulée. Cette nouvelle approche permet la construction d'une matrice de gain dense qui non seulement intègre les

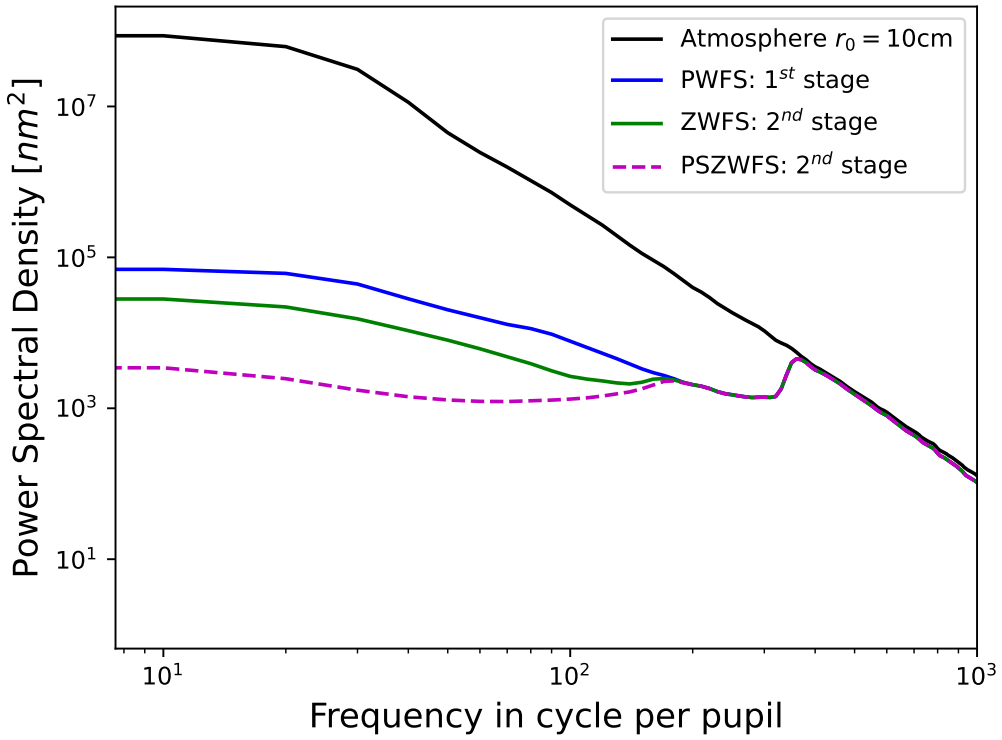

FIGURE 8 – Densité spectrale de puissance (PSD) obtenue après les différents étages de correction (chapitre 2). PSD après le premier étage de correction en bleu, après le second en vert pour le masque de Zernike et en magenta pour le PS-ZWFS.

gain modaux mais aussi les termes de couplage responsables de la confusion modale. En tenant compte de ces effets de couplage, le reconstructeur permet une mesure plus précise du front d'onde. Plus de détails au chapitre 3.
Le reconstructeur combine un suivi trame-à-trame des OG en utilisant une caméra plan focal, comme introduit par Chambouleyron et al. (2021b), et une approche statistique pour tenir compte des termes hors diagonaux. Cette combinaison permet un ajustement dynamique du reconstructeur dans la boucle OA, garantissant une estimation au plus proche de la phase absolue à chaque itération. A travers l'exemple d'une pyramide non-modulée, nous démontrons la faisabilité de cette méthode, montrant qu'il est possible de fermer la boucle sans modulation dans des conditions de fortes turbulences. Cette avancée significative pourrait permettre l'utilisation de pyramides non-modulées pour contrôler à la fois la turbulence atmosphérique et les aberrations spécifiques aux GST, telles que le piston différentiel. Le contrôl de la turbulence sans modulation représente une étape majeure (voir Fig.9), pouvant améliorer les performances des systèmes d'OA des télescopes de nouvelle génération.

Naturellement, pour poursuivre ce travail, une validation expérimentale serait essentielle pour confirmer les prédictions des simulations. Les plateformes expérimentales

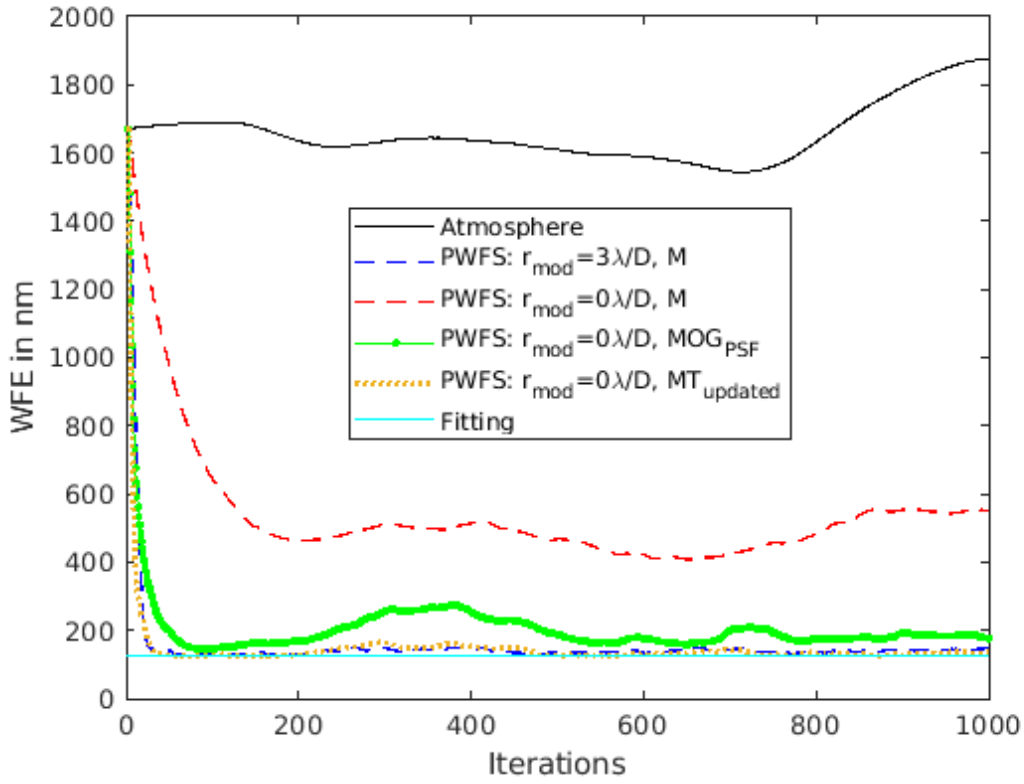

FIGURE 9 – Boucle fermée d'une pyramide avec et sans modulation, r_0 = 6.9cm, vent moyen de $v = 6.7m.s^{-1}$, gain intégrateur de 0.4 (chapitre 3). Comparaison entre l'approche classique modulé $r_{mod} = 3\lambda/D$ en bleue et différent reconstructeur pour la pyramide non-modulée : matrice d'interaction en rouge, compensation modal des gains en vert et compensation complète des gains en jaune. L'erreur de fitting est en cyan.

existantes du LAM offrent des environnements idéaux pour de telles études. La première étape consiste à terminer la caractérisation du PS-ZWFS et du DM avant de l'implémenter sur le banc PAPYRUS. En intégrant la correction de deuxième étage avec le PS-ZWFS fonctionnant à une fréquence de trame plus élevée que le premier étage, nous pouvons valider expérimentalement un système de correction à deux étages et comparer les différentes stratégies de contrôle. De plus, l'introduction d'un DM segmenté dans le plan pupille pourrait être intéressante pour évaluer les performances de la mesure des pistons différentiels en présence de résidus OA.
Il serait aussi très intéressant de tester le nouveau reconstructeur sur le banc PAPYRUS afin de démontrer sur ciel la possibilité de fermer une boucle sans modulation.
Enfin, le banc LOOPS, équipé de modulateurs spatiaux de lumière (SLM), à la fois en plan pupille et en plan focal, peut simuler un pupille de type ELT et diverses configurations de FF-WFS, y compris le ZWFS, le PS-ZWFS et la pyramide non-modulée et pourrait aussi être utilisé pour une validation expérimentale des concepts abordés

durant cette thèse.
Ces bancs optiques fournissent des plateformes complètes pour comparer ces ASO dans le contexte de la mesure du piston différentiel, la quantification de l'impact du bruit sur leurs performances et les différentes méthodes de reconstruction du front d'onde.

Table des matières

List of communications 6

Résumé 8

Abstract 9

Résumé étendu 10

Table des figures 22

Liste des tableaux 29

Liste des acronymes 30

INTRODUCTION 33

1 TOOLS AND TECHNIQUES 47
- 1.1 Imaging through the atmosphere . . . 48
  - 1.1.1 Image formation . . . 48
  - 1.1.2 Atmospheric Turbulence . . . 57
- 1.2 Adaptive Optics (AO) . . . 64
  - 1.2.1 Deformable mirror (DM) . . . 66
  - 1.2.2 Wavefront Sensor . . . 67
  - 1.2.3 Reconstruction and control of the wavefront in an Adaptive Optics system . . . 81
  - 1.2.4 Adaptive optics error budget . . . 85
- 1.3 Adaptive Optics with Giant Segmented Telescopes . . . 88
  - 1.3.1 Adaptive Optics and Pupil Fragmentation . . . 88
  - 1.3.2 Modal basis to describe phase discontinuity aberrations . . . 90
- 1.4 Interest of Fourier filtering wavefront sensors . . . 91
  - 1.4.1 Sensitivity of FF-WFS . . . 92
  - 1.4.2 Dynamic of FF-WFS . . . 92
  - 1.4.3 Optical gains approach . . . 96
- 1.5 Summary . . . 100

2 MODIFICATION OF THE ZERNIKE-TYPE SENSOR FOR HIGH-CONTRAST APPLICATIONS 101
- 2.1 Phase-Shifted Zernike : Boosting the dynamic of Zernike-type WFS . . . 102
  - 2.1.1 Pedagogical description of the Phase-Shifted ZWFS . . . 103

2.1.2 Signal processing for the Phase-Shifted Zernike 103
2.1.3 Sensitivity and dynamic of the PS-ZWFS 105
2.2 Applications to multi-stage AO systems 118
2.2.1 Measurement of differential piston using the PS-ZWFS 118
2.2.2 Cascaded-AO system for AO residuals control 125
2.2.3 Choice of the second stage WFS 128
2.2.4 Second stage in the VIS 129
2.2.5 Second stage in the NIR 132
2.2.6 Summary 133
2.3 Designing a second stage AO correction using the vector Zernike on the PAPYRUS testbed 135
2.3.1 Different technologies to manufacture the Phase-Shifted ZWFS 135
2.3.2 PAPYRUS, the Fourier filtering AO bench 137
2.3.3 Second stage wavefront sensing in the Near Infrared 139
2.4 Conclusion 143

3 MODELISATION OF THE NON-LINEARITIES OF FOURIER FILTERING WAVEFRONT SENSORS : EXAMPLE WITH THE PYRAMID 144
3.1 Non-linear behaviour of Fourier-type sensors 146
3.1.1 1-Dimension analogy 146
3.2 Towards the specific matrix 148
3.2.1 Modelling/reconstruction error outside the linear regime 149
3.2.2 1-dimension analysis 150
3.2.3 Equation of propagation towards the specific matrix 151
3.2.4 First results with the specific matrix 156
3.3 Toward a practical implementation of the specific matrix 164
3.3.1 Adaptation of the optical gains formalism 164
3.3.2 Implementation in closed-loop for the non-modulated pyramid 171
3.4 Summary 174

CONCLUSION 175

PERSPECTIVES 178

Table des figures

1 Système planétaire HR8799, *Credits :Vigan et al. (2016)* 10
2 Miroirs primaires de différents télescopes. *Crédits : ESO* 11
3 Limite de détection d'actuels et futurs instruments. *Crédits :* `https://github.com/nasavbailey/DI-flux-ratio-plot` 12
4 Image d'une étoile à travers un télescope en l'absence et en présence d'aberrations. 13
5 Simulation d'une image après correction par OA. À comparer à l'image sans correction Fig.4(b) 14
6 Simulation d'une boucle d'OA pour l'ELT. Gauche : pupille ELT utilisée pour les simulations. Droite : écran de phase résiduelle d'amplitude 1.9 rad RMS. 15
7 Estimation d'un piston différentiel en boucle ouverte en présence de résidus d'OA d'amplitude 1rad RMS (124 nm RMS). Piston différentiel initial, 0.32rad RMS (0.13λ PV), ZWFS erreur = 0.24rad RMS, PS-ZWFS erreur = 0.1 rad RMS. 16
8 Densité spectrale de puissance (PSD) obtenue après les différents étages de correction (chapitre 2). PSD après le premier étage de correction en bleu, après le second en vert pour le masque de Zernike et en magenta pour le PS-ZWFS. 17
9 Boucle fermée d'une pyramide avec et sans modulation, r_0 = 6.9cm, vent moyen de $v = 6.7 m.s^{-1}$, gain intégrateur de 0.4 (chapitre 3). Comparaison entre l'approche classique modulé $r_{mod} = 3\lambda/D$ en bleue et différent reconstructeur pour la pyramide non-modulée : matrice d'interaction en rouge, compensation modal des gains en vert et compensation complète des gains en jaune. L'erreur de fitting est en cyan. 18

1 Milky-way blazes at European Southern Observatory (ESO) in Paranal, Chile. *Credits : ESO* 34
2 Artistic view of an extra-solar planet. *Credits :* `https://iau.org/` . . . 36
3 Different telescope configurations. Form left to right : Newtond's configuration, Cassegrain's configuration and Nasmyth's configuration. . . . 38
4 Atmospheric transmission with the wavelength. *Credits : NASA, STScI* . 39
5 ELT in construction. *Credits : ESO* 40
6 Schematic of ELT design. *Credits : ESO* 41
7 Schematic of a simple coronagraph instrument composed of an apodizer, a focal plane mask and a Lyot stop. 42

8 Example of a coronagraph image obtained with the VLT/SPHERE instrument after post-processing. *Credits :* Chauvin et al. (2017). 42
9 HARMONI, SCAO simulation. Left : ELT pupil used for simulation. Right : residual phase screen of amplitude 1.9 rad RMS. Differential piston is visible in the AO residuals. 44
10 Image of a star in the perfect case without aberrations on the left and with atmospheric aberrations on the right. 44

1.1 Impact of the pupil (Top) on the PSF shape (Bottom). The PSFs are displayed in logarithm scale to highlight the effects of the diffraction. . 49
1.2 Normalised PSF cut for a full circular aperture without (solid black line) and with a central obstruction(dashed red line) 50
1.3 Normalised MTF cut for a full circular aperture without central obstruction. The cut-off frequency of the system is $\nu = D/\lambda$. 51
1.4 Phase and PSF in logarithm scale of the common aberrations : Tip, Defocus and Astigmatism. The red vertical lines stands for the reference positions. 53
1.5 First Zernike polynomials : credits `https://en.wikipedia.org/wiki/Zernike_polynomials` 55
1.6 Incoming sine wavefront and its associated PSF in the focal plane. The PSF is plotted in logarithmic scale. 56
1.7 Normalised MTF cut for a full circular aperture. The incoming wavefront is a sine wave of period 3 cycle. (a) Phase amplitude is 0.73 rad RMS (cf Fig.1.6). (b) Phase amplitude is 0.85 rad RMS. 57
1.8 Normalised MTF cut for a full circular aperture. The different wavefront have an amplitude of π rad RMS. The associated phase and PSF are plotted in Fig.1.4. 57
1.9 Taylor hypothesis : frozen flow, turbulent wavefronts are frozen and translate across the pupil at wind speed V 59
1.10 Anisoplanatism : pointing in different directions. 60
1.11 Impact of turbulence on the PSF shape. The PSFs are displayed in logarithm scale to highlight the effect of the turbulence. Left : perfect PSF (Airy pattern), middle : short exposure PSF with turbulence and right : long exposure PSF with turbulence for $\frac{D}{r_0} = 10$. 62
1.12 Normalised MTF cut for a system without aberrations (black line) and with aberrations (red line). The observation conditions are such as $\frac{D}{r_0} = 10$. 63
1.13 Schematic of a Single-Conjugated Adaptive Optics (SCAO). 66
1.14 Illustrative representation of the WFS's response ΔI to the incoming phase ϕ. The linear range is represented by the green verticals lines and the horizontal arrow, the sensitivity by the slope of the curve. 69
1.15 Schematic of the Shack-Hartmann. 69
1.16 Schematic of the Fourier Filtering concept. 71
1.17 PWFS schematic, *Credits : (Crass 2014)* 72

1.18 Non-modulated PWFS illustration of the saturation. From left to right increasing amplitude of a tip/tilt aberration. 74
1.19 Modulated PWFS illustration of the saturation. From left to right increasing amplitude of a tip/tilt aberration. 75
1.20 1-Dimension representation of the WFS's response to the incoming phase. Orange curve non-modulated PWFS and blue curve modulated PWFS. The linear response is represented by the orange and cyan verticals lines and the horizontal arrows respectively for the non-modulated and the modulated PWFS, and the sensitivity by the slope of the curves. 76
1.21 Impact of the modulation on the spatial frequency of an incoming wave, illustration with a 2-sided prism. Left : spatial frequency ν inside the modulation radius. Right : spatial frequency ν outside the modulation radius 76
1.22 Schematic of the ZWFS 77
1.23 Different terms of the ZWFS equations obtained for a Zernike mask of $1.06\lambda/D$. (a) Reference intensity and (b) Intensity obtained without the ZWFS in the focal plane (Pupil image). 79
1.24 Intensity as a function of the phase 80
1.25 Schematic of an interaction matrix. 83
1.26 Left : AO feed-back loop. Right : chronogram of an AO system with two frames delay 85
1.27 LWE on the ELT pupil, optical path difference up to $2\mu m$. *Credits :Martins et al. (2022)* 90
1.28 ELT petal basis used for the simulations $\{P_i\}$. 91
1.29 Projection on the petal basis of the residual screen in Fig.9. 91
1.30 FF-WFS sensitivities : Zernike WFS, Pyramid WFS and modulated Pyramid WFS. 93
1.31 Reconstruction curves of the first five Zernike modes using a ZWFS and an interaction matrix as a reconstructor. 94
1.32 Impact of the non-linear response on the phase estimation using a ZWFS and an interaction matrix as a reconstructor. 95
1.33 Reconstruction curves of Z_5 without phase residual (red curve) and in presence of phase residual (dashed-blue curve) using the modulated PWFS ($r_{mod} = 2\lambda/D$) and an interaction matrix as a reconstructor. . . . 96
1.34 Reconstruction curves of Z_5 in presence of phase residual after OG compensation dotted-green curve using a modulated PWFS. Same simulation as in Fig.1.33. 98
1.35 WFE comparison between the interaction matrix and the push-pull matrix around the phase to be measured using a non-modulated PWFS. 98

2.1 Schematic optical set-up of the Phase Shifted ZWFS using two different Zernike masks. This "toy model" is used for clarity. The section 2.3.1 details the different methods to manufacture PS-ZWFS. 103

2.2 Intensity as a function of the input phase of a single pixel for the Z_+ (classical ZWFS) and Z_-. The red and the green vertical lines represent the bijective regime of respectively the ZWFS and PS-ZWFS. 106

2.3 Comparison of PS-ZWFS, ZWFS and PWFS sensitivities. Left : RON sensitivities. Right : Photon noise sensitivities. 107

2.4 Dynamic study for the different KL modes from left to right KL_4, KL_{36} and KL_{136}. Top : KL mode of amplitude 1 rad RMS. Bottom : Linearity curves for the different modes of varying amplitude. The blue curve is the linearity curve obtained with iMat, the red one with the analytical linear model, the green one with the $arcsine$ reconstructor and the dotted-magenta curve with the $atan2$ reconstructor. The blue and magenta vertical lines represent the dynamic range of the ZWFS using the interaction matrix and the PS-ZWFS. 109

2.5 PSF in logarithm scale of the KL modes : KL_4, KL_{36}, and KL_{136}, obtained for in input wavefront of amplitude 0.7 rad RMS. 110

2.6 WFE obtained for the different KL modes listed in Fig.2.4 with the different reconstructors : iMat, Linear and $arcsine$ for the ZWFS and $atan2$ for the PS-ZWFS. 111

2.7 Input modes of amplitude 0.7 rad RMS. Projection of the estimated phase with the different reconstructors : iMat, Linear and $arcsine$ for the ZWFS and $atan2$ for the PS-ZWFS. 112

2.8 Input mode KL_{36} of amplitude 0.7 rad RMS residual wavefront with the different reconstructors : iMat, Linear and $arcsine$ for the ZWFS and $atan2$ for the PS-ZWFS. The respective WFE are 0.35rad RMS (iMat), 0.35 rad RMS (Linear), 0.39 rad RMS ($arcsine$) and 0.11 rad ($atan2$) . 113

2.9 Caption 114

2.10 Average WFE as a function of the turbulent screen amplitude. The different reconstructors are : iMat, Linear and $arcsine$ for the ZWFS and $atan2$ for the PS-ZWFS. (b) Zoom on the range [0;0.5] rad RMS. 115

2.11 Input phase of amplitude 0.7 rad RMS and residual wavefront with the different reconstructors : iMat, Linear and $arcsine$ for the ZWFS and $atan2$ for the PS-ZWFS. The respective WFE are 0.17rad RMS (iMat), 0.20 rad RMS (Linear), 0.24 rad RMS ($arcsine$) and 0.11 rad ($atan2$) . 116

2.12 Iterative approach *Credits : Chambouleyron et al. (2024)* 117

2.13 (a) Amplitude of the residual phase screens of the ELT AO-loop simulations. The black dot correspond to the total amplitude of the phase screen. The green stars correspond to the amplitude of the atmospheric residual (differential piston removed) and the red crosses to the amplitude of the differential piston for each screens. (b) SR in H-band and K-band for each phase screen of the ELT AO-loop simulations. 119

2.14 Turbulence phase screen with and without differential piston. Impact of the differential piston on the PSF at different time of the simulation. Top : Phase screen at 4, 7.6 and 4.2 seconds. Bottom : PSFs displayed in logarithm scale to highlight the differential piston effect. Their respective differential piston amplitude are [0.78; 0.63; 0.04] rad RMS @λ_H. 120
2.15 ELT phase screen with varying differential piston. The amplitude of the residual is equal to 0.93 rad RMS @λ_{wfs} which corresponds to 118 nm RMS, so $SR_H = 81\%$. 121
2.16 Linearity curve of a petal mode with and without phase residual. The phase residual amplitude is 0.93 rad RMS @λ_{wfs} (so $SR_H = 81\%$). We compare the $arcsine$ and the $atan2$ reconstructors respectively for the ZWFS and the PS-ZWFS. 122
2.17 (a) AO loop of 20 iterations on the differential piston at 7.4s. (b) Coefficient of the residual piston at the end of the AO loop. 123
2.18 (a) Petalometer loop : Differential piston WFE versus the screen numbers. Each differential piston is estimated in two step measurement. (b) SR in H-band per phase screens. 124
2.19 (a) Petalometer in H-band. (b) SR in H-band 124
2.20 Architecture of a cascade AO system. *Credits : Cerpa-Urra et al. (2022)* . 126
2.21 WFE versus star magnitude in medium seeing condition for the different stages : 1st stage PWFS and 2nd stage PS-ZWFS. 130
2.22 Power Spectrum Density (PSD) obtained for the different stages blue curve for the PWFS, green curve for the ZWFS and dashed-magenta curve for the PS-ZWFS. 1st and 2nd stage in I-band magnitude 7, split 50/50, science @750nm. Top : PSD obtained for a r_0 of 15cm@500nm. Bottom : PSD obtained for a r_0 of 10cm@500nm. 131
2.23 Power Spectrum Density (PSD) obtained for the different stages blue curve for the PWFS, green curve for the ZWFS and dashed-magenta curve for the PS-ZWFS. 1st stage in I-band magnitude 7, 2nd stage in J-band, magnitude 7, science @750nm, r_0 = 15cm @500nm. Top : PSD obtained for a r_0 of 15cm. Bottom : PSD obtained for a r_0 of 10cm. . . . 134
2.24 Layout of the PS-ZWFS made of liquid crystals *Credits : Doelman et al. (2019)*. 136
2.25 Metasurface substrate of a PS-ZWFS *Credits : Wallace et al. (2023)*. Note that this mask is the one we received at LAM to be installed on PAPYRUS. 137
2.26 PAPYRUS 138
2.27 PAPYRUS bench, *Credits : Fetick et al. (2023)* 139
2.28 PAPYRUS PSF, *Credits : Fetick et al. (2023)* 139
2.29 Optical design of the second stage WFS 141
2.30 Zemax : Optical design of the second stage WFS. *Credits : Eduard Muslimov optical designer at the University of Oxford* 141
2.31 Alignment of the second stage WFS 142

3.1 1D analogy with f(x) 147

3.2 Rainbow WFS 154
3.3 Intensity as a function of the phase for the different configurations : classical ZWFS with $\theta = \pi/2$ in red, $\theta = \pi/4$ in blue, $\theta = \pi/8$ in dashed-green and $\theta = 3\pi/8$ in dotted-magenta. 155
3.4 Intensity as a function of the phase for the different configuration : classical ZWFS with $\theta = \pi/2$ and $p = 1.06\lambda_1/D$ in red, $\theta = \pi/4$ and $p = 0.27\lambda_2/D$ in blue, $\theta = \pi/8$ and $p = 0.53\lambda_3/D$ in dashed-green and $\theta = 3\pi/8$ and $p = 0.80\lambda_4/D$ in dotted-magenta. 156
3.5 Top : input phase and corresponding E2E intensity. Middle : intensity cuts obtained with the interaction matrix $\mathbf{M}$ in dashed red and with the push-pull matrix around the phase $\mathbf{M}(0,\delta\phi)$ in dashed blue. Bottom : intensity cuts obtained with the average matrix $\mathbf{M}_{av}$ in dashed yellow and with the different approximation of the specific matrix $\mathbf{M}_n$ with $n \in \{1;5;20\}$. 159
3.6 Intensity cut obtained with E2E simulation and two different specific matrices $\mathbf{M}(\delta\phi,0)$ and $\mathbf{M}(\delta\phi",0)$ to demonstrate the specificity of the reconstructor. 160
3.7 Specificity of the specific matrix in a strong turbulence regime, example of phase unwrapping 161
3.8 Phase coefficients using different reconstructors in the linear regime . 162
3.9 Left : Optical gains. Right : Projected coefficients after gain compensation 163
3.10 Projected coefficients after full compensation, reconstructors $\left(\mathbf{MT}(0,\delta\phi)\right)^\dagger$ and $\left(\mathbf{MT}(\delta\phi,0)\right)^\dagger$. 163
3.11 Average OG obtained for 20 residual phase screens. The equivalent Strehl ratio is 55% in the H band. The OG are obtained from the different matrices $\mathbf{OG}(0,\delta\phi)$, $\mathbf{OG}(\delta\phi,0)$ and $\mathbf{OG}_{av}$ and the focal plane camera $\mathbf{OG}_{PSF}$. The first 500 modes are shown for clarity. The shaded area represents the standard deviation. 166
3.12 Schematic of the statistical approach to obtain the coupling terms . . . 166
3.13 Left : full average gain matrix obtained for a phase set whose Strehl ratio is equal to 42% in H band. Right : line 30 of gain matrices describing the coupling between the modes. The lines are normalised by the OG value. T_1 and T_2 are the average gain matrices obtained for a set of phases whose equivalent Strehl ratio is respectively 85% and 42% in H band. . 167
3.14 WFE for residual phase screens, the equivalent Strehl ratio in the H band is within the range SR $\in$ [30;99]%. The shaded area represents the standard deviation. 168
3.15 WFE for residual phase screens, the reconstructor $\mathbf{MT}_{bis}$ corresponds to the updated reconstructor using equation 3.22 but with a unique dense gain matrix for the whole range. The equivalent Strehl ratio in the H band is within the range SR $\in$ [30;99]%. The shaded area represents the standard deviation. 170

3.16 Closed-loop r_0 = 6.9cm and average wind speed of $v = 6.7 m.s^{-1}$, loop gain=0.4. Comparison between the classical modulated PWFS $r_{mod} = 3\lambda/D$ blue dashed curve and the different reconstructor using the non-modulated PWFS. The classical interaction matrix in red dashed curve, modal gain compensation in green curve and the full gain compensation in yellow dotted curve. The fitting error is plotted in cyan. 173

Liste des tableaux

1.1 The first six Zernike polynomials 54

2.1 Dynamic range in rad RMS (maximum absolute value) and in rad PV (maximum absolute value) of the ZWFS and the PS-ZWFS for different spatial frequency KL modes. 108
2.2 Simulation parameters of the ELT AO loop 119
2.3 Parameters of the two-stages AO system 127
2.4 Scenario 1 : Parameters of the two-stages AO system 129
2.5 Scenario 2 : parameters of the two-stages AO system 132
2.6 Second stage optimised integrator gain depending on the magnitude of the star in J-band. First stage I-band magnitude fixed at 7. The loop gain of the first stage was fixed to 0.4. 133

3.1 Mathematical notation 146
3.2 Simulation parameters 157
3.3 WFE in radian RMS using different reconstructors. The reference phase equals zero. The incident phase is shown in Fig. 3.5, its RMS norm is 1.51 rad RMS. 158
3.4 Phase regime summary for different reconstructors considering a 10% deviation from the fitting error. 169
3.5 Closed-loop parameters 172
3.6 Statistical study of close-loop for three different r_0 made for 20 different atmosphere screens for each r_0. The average wind speed is $6.7 m.s^{-1}$ considering the 3 atmospheric layers. The close-loop WFE and the standard deviation are specified in nm RMS. The average WFE is computed for the last 800 iterations. 172

Liste des acronymes

ANDES
ArmazoNes high Dispersion Echelle Spectrograph. 43, 89

AO
Adaptive Optics. 40, 44, 47, 64

DM
Deformable Mirror. 13, 43, 65, 89

ELT
European Extremely Large Telescope. 11, 37, 39

EM
Electromagnetic Field. 43, 48

ESO
European Southern Observatory. 22, 34

FF-WFS
Fourier Filtering WaveFront Sensor. 15, 46, 47, 56, 67, 68, 70

GLAO
Ground Layer Adaptive Optics. 65

GMT
Giant Magellan Telescope. 11, 39

GST
Giant Segmented Telescopes. 11, 39, 47, 88, 118

HARMONI
High Angular Resolution - Monolithic - Optical and Near-infrared -Integral field spectrograph. 40

HWO
Habitable World Observatory. 38, 102

IFS
Integral Field Spectrograph. 40

LPV
Linear Parameter Varying. 97, 144, 145

LTAO
Laser Tomographic Adaptive Optics. 65

LWE
Low-Wind Effect. 89

MCAO
Multi-Conjugated Adaptive Optics. 65

METIS
Mid-Infrared EELT Imager and Spectrograph. 41

MICADO
Multi-AO Imaging Camera for Deep Observations. 40

MTF
Modulation Transfer Function. 50

NCPA
Non-Common Path Aberrations. 88, 125, 135

OG
Optical gains. 94, 96, 146

OOMAO
Object-Oriented Matlab Adaptive Optics toolbox. 153

OTF
Optical Transfer Function. 50

PAPYRUS
Provence Adaptive optics PYramid Run System. 137

PCS
Planetary Camera and Spectrograph. 16, 125

PSD
Power Spectral Density. 58

PSF
Point Spread Function. 49

PS-ZWFS
Phase-Shifted Zernike WaveFront Sensor. 15, 101–103

PWFS
Pyramid WaveFront Sensor. 15, 72

RMS
Root Mean Square. 54

RTC
Real-Time Computer. 13, 65

SCAO
Single-Conjugated Adaptive Optics. 23, 65, 66

SH
Shack-Hartmann. 15, 67, 68

SNR
Signal to Noise Ratio. 68

SPHERE
Spectro-Polarimetric High-contrast Exoplanet Research. 16, 46

SR
Strehl ratio. 63

TMT
Thirty Meter Telescope. 11, 39

VLT
Very Large Telescope. 11, 38

WFE
WaveFront Error. 62

WFS
WaveFront Sensor. 13, 47, 56, 65

XAO
eXtrem Adaptive Optics. 43, 68, 86, 145

ZWFS
Zernike WaveFront Sensor. 15, 77

INTRODUCTION

The Big Bang occurred approximately 13.8 billion years ago. The radiation of the universe at that time was tremendously intense due to extreme high pressures and temperatures. About 10,000 years later, as the universe began to cool, it became dense and opaque. About 380,000 years after the Big Bang, the temperature continued to drop, allowing stable hydrogen atoms and hydrogen molecules to form. The residual light from this era, known as the Cosmic Microwave Background, is detectable today. Following this period, hydrogen atoms and molecules started to gather due to the gravitational attraction, forming increasingly large gas clouds. As these clouds grew, the internal temperature and pressure created conditions suitable for nuclear fusion, marking the birth of the first stars. This period is known as the reionisation of the universe. Stars, influenced by each other's gravitational fields, began to form star clusters. Then galaxies, a collections of stars, gas, dust, and dark matter moving in coordinated motion, formed. Among these galaxies is our own, the Milky Way. The luminous strip of the Milky Way visible in the night sky has fascinated human civilisations throughout history (see Fig.1).

From this fascination for the inaccessible night sky emerged a science : cosmology, named after the Greek word "kosmos" meaning universe. The earliest traces of cosmology date back to the Sumerians, between 5000 and 7000 years Before Christ. Star charts were conceived to study the motion of the Sun, the Moon, and planets. This heritage was handed down to the Babylonian, Greek, and Roman civilisations. Around the same period of time, in what is now southern England, other civilisations were also deeply interested in astronomy. Archaeologists now believe that Stonehenge may have served as a gigantic sundial to celebrate the seasons and mark the winter and summer solstices. The Ancient Egyptian calendar started with the appearance of the brightest star in the sky and consisted of 12 months of 30 days each, with 5 additional days added to have 365 days in total to describe a whole year. Egyptian astronomers also recognised the need to add an extra day to the calendar every four years by calculating the positions of the stars. Around 2000 years BC, in what is now China, the Xia, Shang, and Zhou dynasties kept meticulous records of astronomical events, including eclipses and "guest star" events-descriptions of stars that appeared in the night sky for days or months, which were actually supernovae. These ancient civilisations used advanced instruments like the armillary sphere and celestial globe for their astronomical studies.

About 300 years BC, the mathematician Aristarchus of Samos, from island of Samos, questioned the geocentric hypothesis. He was one of the few scientists who disagreed with this hypothesis, which was supported by prominent figures like Plato and Aristotle. Hundreds of years later on another continent in Asia, Aryabhata, an



FIGURE 1 – Milky-way blazes at European Southern Observatory (ESO) in Paranal, Chile. *Credits : ESO*

Indian mathematician and astronomer wrote a treatise (Aryabhatiya), in which he explained the origin of eclipses and provided measurements of the Earth's diameter. He also subscribed to the heliocentric hypothesis. In Middle East, astronomy was also flourishing. In the early 9th century, Al-Khawarizmi, a mathematician from what is now Uzbekistan, built upon and refined the work of his predecessors, both Greek and Indian, on calculating the positions of stars. He made significant contributions to the development of algebra and astronomical tables, influencing later Islamic and European scholars. A few centuries later, in the early 11th century, Al-Biruni, another mathematician, astronomer, and physicist from what is now Uzbekistan, calculated the Earth's diameter with remarkable precision. He was also favourable towards the heliocentric hypothesis.

In this part of the world, a rigorous method for astronomy was born, based on observation, data analysis, scientific interpretation, and repeatability. This scientific tradition culminated in the 13th century with the establishment of the Maragha Observatory in Persia (modern-day Iran). This observatory was one of the most advanced of its time, and much of the observational data collected there were later used by European astronomers, such as Copernicus, to validate the heliocentric hypothesis.

A step forward in time takes us to the 17th century to see Galileo's improvements in instrumentation. His refracting telescope with a magnification of 20 changed the field of astronomy. He observed Jupiter's moons for the first time, and used his observations

to understand that the various planets in the solar system revolved around the Sun rather than the Earth. A few years later, Newton replaced the lenses of the refracting telescope with mirrors, inventing the reflecting telescope. Less than a century later, William Herschel, a musician and astronomer, used his homemade telescope to discover Uranus, another planet in our solar system. When mentioning William, we cannot forget Caroline Herschel. The two siblings worked together. Caroline was known not only for her work as a mirror polisher and telescope maker, but also as an astronomer whose observations led to the identification of several new nebulae and comets.

In the 19th century, the French physicist Léon Foucault developed an innovative optical setup known as the "Foucault knife-edge test" to evaluate the quality of mirror surfaces. By using this technique, Foucault was able to precisely measure the surface quality of mirrors, allowing for the correction of any imperfections during the manufacturing process. This method was particularly significant in the context of improving the polishing process of telescope mirrors. The precision and effectiveness of Foucault's knife-edge test led to significant advancements in the field of optics and astronomy. This method remains in use today, particularly among amateur astronomers who rely on it to ensure the quality of their telescope mirrors. He also contributed to the use of silver-coated mirrors to improve the reflectivity of telescopes and built an 80 cm diameter telescope that can still seen at the Observatoire de Marseille.

These non-exhaustive paragraphs on part of the history of astronomy show the importance of this science in all civilisations and the tremendous breakthroughs that have been made throughout history. Astronomy is a good example of collective science. Astronomers lived at different times, in different countries or on different continents, but they relied on the work of others to validate or reject hypotheses and advance discoveries that were made possible thanks to sophisticated instruments. I would like now to narrow the field of astronomy to the study of planetary systems.

It is widely accepted that our solar system formed from a rotating nebula of gas and dust. Most of this material collapsed under gravity to form the Sun at the centre, while the remaining gas and dust settled into a surrounding disk. Within this disk, Jupiter captured a significant portion of the leftover gas, becoming the largest planet. The remaining material then coalesced to form the other planets, moons, asteroids, and comets, completing the solar system. Therefore, if our planetary system could develop in this way, it is likely that other planetary systems could exist as well (see Fig.2).

In search for other worlds

One of the important goals of astronomy today is to achieve an understanding of the conditions necessary for life to evolve. This quest includes not only finding new worlds and answering the question, "Are we alone in the universe?" but also understanding the origin of life on Earth and planet formation. Observing exoplanets planets will help us understand our own existence. From this "instinctive need" comes tremendous technological challenges.



FIGURE 2 – Artistic view of an extra-solar planet. *Credits :* https://iau.org/

In 1995, the first exoplanet, a planet orbiting a star other than the Sun, 51 Pegasi b (Mayor & Queloz 1995), was discovered orbiting around a Sun-like star, marking the identification of a planet outside our solar system. Since 1995, more than 7,000 exoplanets have been discovered using different techniques (see https://exoplanet.eu/home/). The next step is naturally to find planets capable of sustaining life.

Among the different existing techniques to find exoplanets we identify two main ones : indirect methods and direct imaging techniques. Indirect methods consist of several different approaches such as : **radial velocity**, which measures periodic shifts in the light spectrum of a star. These shifts occur due to movement of both objects (star + planet) around their barycenter, causing the star to move toward and away from Earth, which changes the observed wavelengths through the Doppler effect. By analysing these spectral changes, astronomers can infer the presence, mass, and orbital properties of the exoplanet (Cochran & Hatzes 1996; Khan et al. 2017) ; **transit**, which can be understood as a stellar eclipse (Wright & Gaudi 2012) ; or **gravitational microlensing**, which allows the detection of non massive low mass objects using the principle of gravitational lensing (Bennett 2008). This is not an exhaustive list of indirect methods ; there are other techniques available. As a matter of fact, indirect methods have enabled the detection of the majority of extrasolar planets. These techniques provide information about the planet's mass, orbital parameters, and part of the planet's spectrum.

Another approach to study exoplanets consists of the study of the circumstellar

environment. The main problem is that the star is too bright, a million to a few billion times brighter than the reflected or emitted light from planets that might orbit around it, hence, it is difficult to image their surroundings.

Direct imaging techniques allow us the removal of the star light to image the planet. Furthermore, in some cases, the planet can be imaged during its whole orbit, providing access to the planet's spectrum. Analysing the spectrum can help identify biomarkers in the planet's atmosphere, which is crucial in our search for life. This technique requires large telescopes and high-contrast instrumentation.

In this introduction, we will explore the need for building large telescopes to enable direct imaging of Earth-like planets. First, we will introduce the European Extremely Large Telescope (ELT), the largest telescope ever constructed on Earth, which will be the first telescope capable of imaging Earth-like planets. Finally, we will examine the challenges faced by ground-based astronomy to achieve high angular resolution and discuss the techniques employed to enhance image quality.

The generation of giant telescopes - example of the Extremely Large Telescope

Telescope

A telescope is an optical instrument used to capture images of astronomical scenes, with the primary goal of collecting as many photons as possible. A simple design of large telescopes consists of two mirrors facing each other. One of the first telescopes was suggested by Isaac Newton in 1671 and was composed of a spherical primary mirror and a secondary flat mirror that redirects the light off-axis to an eyepiece - see Fig.3 (first case). A few years later, Laurent Cassegrain suggested another configuration, more compact, composed of a parabolic mirror and a hyperbolic mirror - see Fig.3 (second case). A distinctive feature is that a central hole (central obstruction) is made in the primary optic to let the light pass through. However, nowadays this configuration limits the number of instrument that can be placed at the focus of the telescope. That is why telescopes usually use the Nasmyth configuration (similar to Newton's configuration), as it allows for more instruments to be used since they can be placed on a separate platform, see Fig.3(third case).

The information from an astronomical scene comes from the photons it emits or reflects. So, to gather as much information as possible, a telescope needs to be large. The collecting power of a telescope depends on the diameter of its primary mirror; it varies with the square of the diameter D^2. Thus, a larger primary mirror collects more photons, which leads an increase in sensitivity, or in other words, a larger number of observable objects. Collecting as much light as possible is the first step to observe the details of an astronomical scene. The second step is increasing the angular resolution, which is the instrument's ability to distinguish close objects and

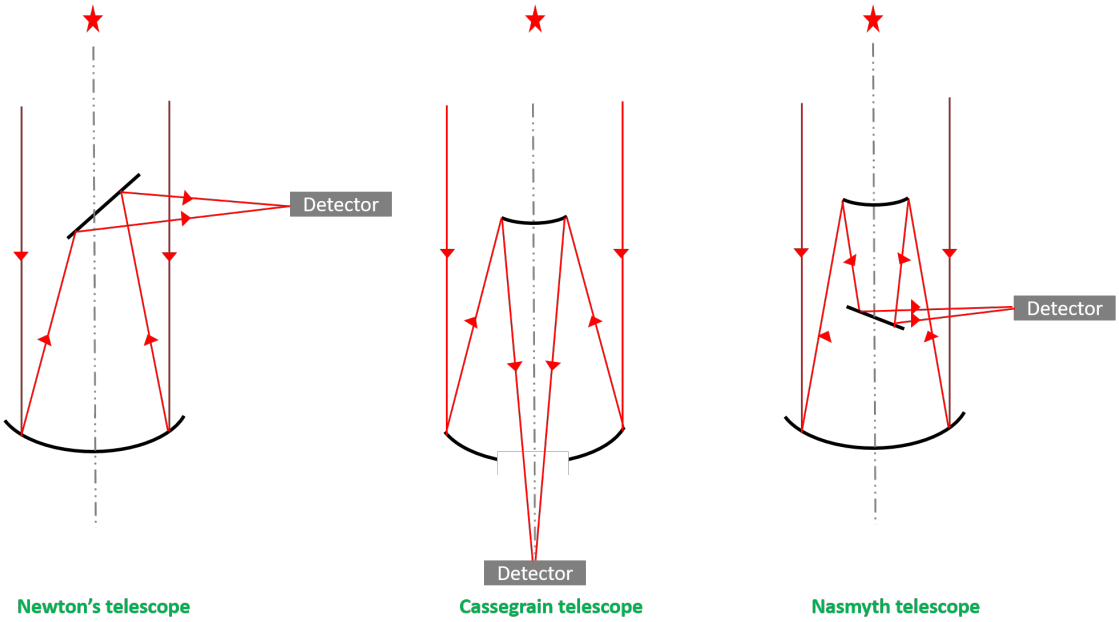

FIGURE 3 – Different telescope configurations. Form left to right : Newtond's configuration, Cassegrain's configuration and Nasmyth's configuration.

accurately represent the frequency content of the scene. A more detailed definition of the resolution is given in the next chapter1, in section 1.1. Similar to the collecting power of the instrument, resolution depends on the diameter of the primary mirror and the observing wavelength, following the relation : $\theta = \lambda / D$. Thus, a larger telescope results in a smaller angle θ, revealing more details in the image.

To achieve the goals of modern astronomy, we need large telescopes. However, the largest monolithic mirror (constructed from a single piece) one can manufacture has a diameter of 8m, as seen with the Very Large Telescope (VLT) (Quattri et al. 1988; Wirenstrand 1995). To build larger primary mirrors, the only solution is to use segmented optics. For instance, the Keck telescopes have a diameter of 10m, each consisting of 36 hexagonal segments (Medwadowski 1989; Matthews et al. 1996). The next generation of ground-based facilities will also feature segmented designs.

For space-based telescopes, the constraints are similar, with the main limitation being the satellite payload, which restricts the optics diameter. The Hubble Space Telescope, for example, was a 2m class telescope. The space community is also adopting segmented primary optics to launch larger telescopes in a more compact form. The James Webb Space Telescope (JWST) is an example of such a structure : a 6m class segmented telescope (Sabelhaus & Decker 2004). JWST is the precursor to future space missions under the Habitable World Observatory (HWO) project, which will include several 10m class telescopes dedicated to the search of Earth-like planets (Leboulleux 2023).

The future of astronomy will feature both ground and space-based observatories as

the two methods complement each other as the choice is driven by the science cases. Indeed, the ground-based community has more options and more degrees of freedom to build large facilities, but they are affected by atmospheric turbulence, which impacts the image quality and also limits the accessible part of the electromagnetic spectrum. As for space astronomy, the space-based community works with telescopes of limited mass/volume and does not have the possibility to upgrade or modify the instruments, yet they are not impacted by the atmosphere (see Fig.4).

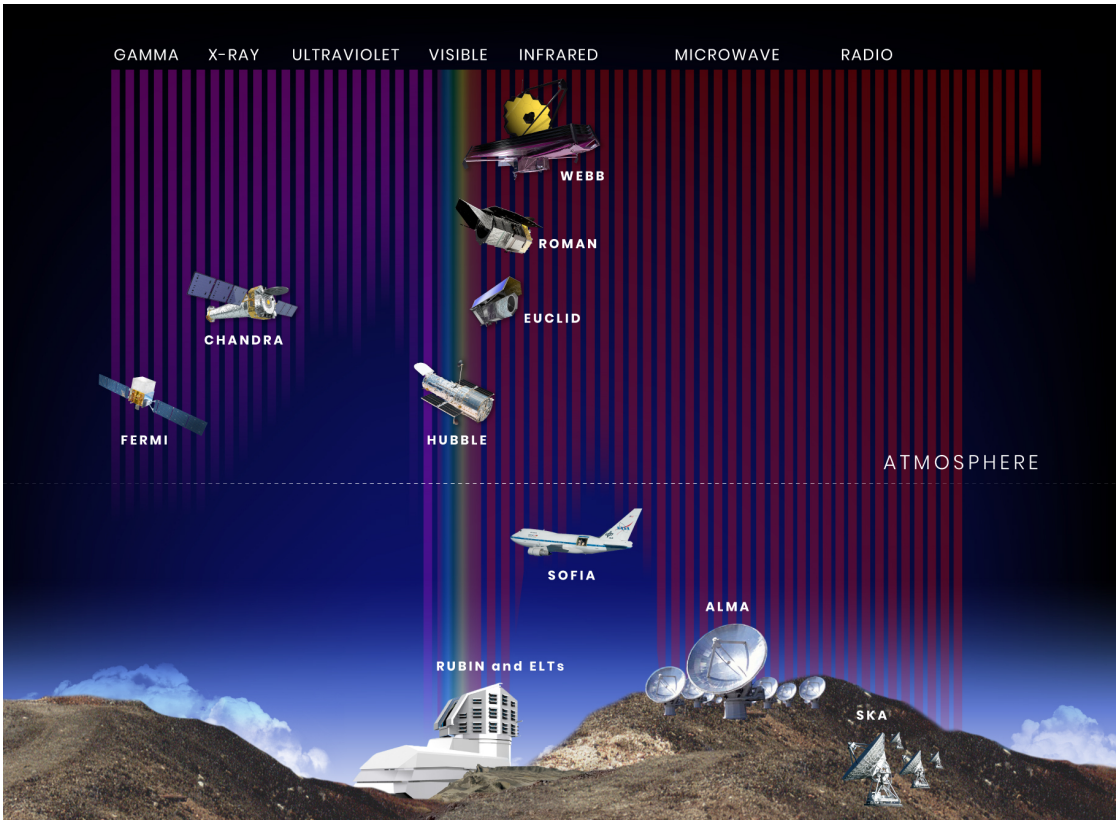

FIGURE 4 – Atmospheric transmission with the wavelength. *Credits : NASA, STScI*

High angular resolution with giant telescopes

This PhD focuses on ground-based observations in the context of the Giant Segmented Telescopes (GST). The next generation of ground-based telescopes will have primary mirrors larger than 20m in diameter. Among these colossal future telescopes are the European Extremely Large Telescope (ELT), (Gilmozzi & Spyromilio 2007; Cavarroc et al. 2006), currently under construction, (see Fig.5) and its US counterparts the Thirty Meter Telescope (TMT), (Nelson & Sanders 2008; Sanders 2013) and the Giant Magellan Telescope (GMT) (Gunnels et al. 2004; Fanson et al. 2018). The ELT will have a primary optic of 39m in diameter composed of 798 hexagonal segments. Its optical design includes five mirrors, operating in the optical/near-infrared range, with

a field of view of 10 arcminutes. With this size, the ELT will gather 20 times more light than a single unit of the VLT.



FIGURE 5 – ELT in construction. *Credits : ESO*

Thanks to its size, the ELT has the potential to study Earth-like planets. The challenge in imaging these kind of exoplanets is twofold : first, their proximity to their host star, which makes direct detection difficult, and then the contrast between the planet and the star, which can be smaller than 10^{-8} for an Earth-like planet orbiting around a Sun-like star. However, ELT's large size will facilitate such detection. With instruments such as :

— Multi-AO Imaging Camera for Deep Observations (MICADO), (Davies et al. 2016), with multiple Adaptive Optics (AO) modes and a coronagraphic mode, providing high contrast at small angular separation from the host star. It would allow direct imaging and characterisation of exoplanets in the near-infrared (NIR).

— High Angular Resolution - Monolithic - Optical and Near-infrared -Integral field spectrograph (HARMONI), (Schnetler et al. 2022), with its Integral Field Spectrograph (IFS) will provide spectrometric capabilities to the ELT. With several AO

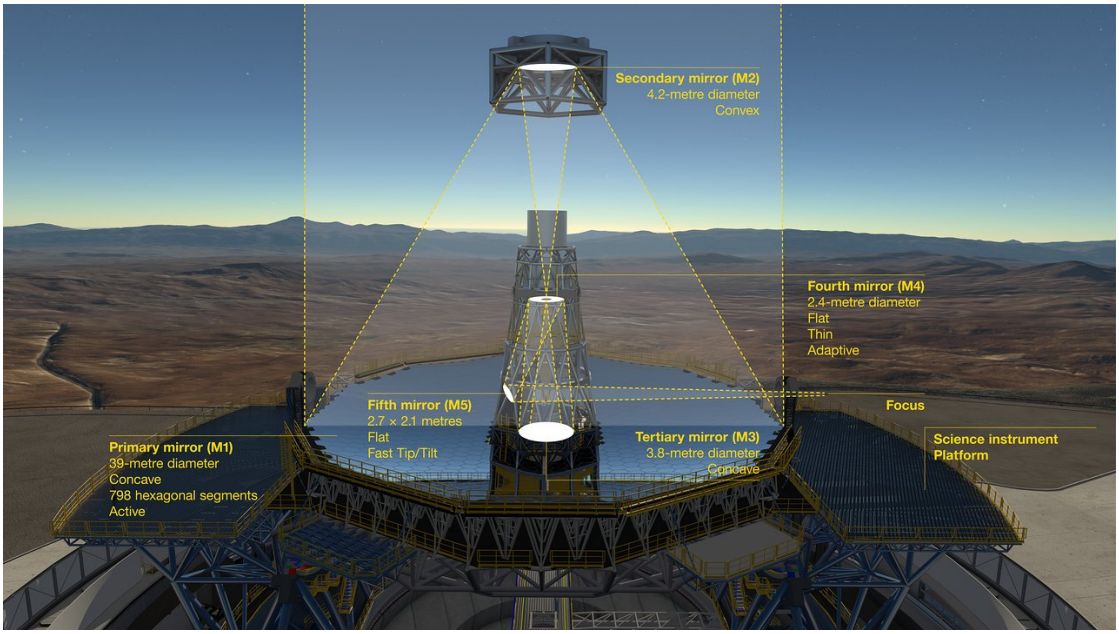

FIGURE 6 – Schematic of ELT design. *Credits : ESO*

modes, including a high-contrast module (Hours et al. 2022) providing a contrast of 10^{-6} at 0.1" in the NIR.

— Mid-Infrared EELT Imager and Spectrograph (METIS),(Brandl et al. 2014), dedicated to direct imaging of Earth-like planets in thermal infrared, L-band.

Search for Earth-like planets outside the solar system

This section explores the field of direct imaging techniques for exoplanet detection. This technique, also called high-contrast imaging, completes the catalogue of exoplanets by either discovering new planets or adding new information about known planets such as their temperature, pressure, or the composition of their atmospheres.

High-contrast imaging requires the use of a coronagraph, an optical component used to block the central star light and transmit the flux from the objects surrounding the host star. The name of this component comes from its original use - the study of the solar corona (Lyot 1932). Its use was adapted in high-contrast imaging to enable the study of circumstellar disks, (Wang & Vaughan 1988; Malbet 1996; Ruane et al. 2018; Jovanovic et al. 2018). Most coronagraphs have in the optical path three main components (see Fig.7) :

1. an apodizer : shapes the incident star light so it focuses on the focal plane mask and reduces diffraction effects.
2. a focal plane mask : blocks the incident star light. It can be replaced by a transparent optical component that ejects the star light from the pupil (Roddier & Roddier 1997; Mawet et al. 2005)
3. a Lyot stop : blocks the residual light diffracted by the focal plane mask.

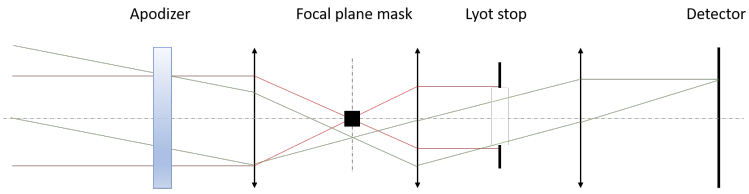

FIGURE 7 – Schematic of a simple coronagraph instrument composed of an apodizer, a focal plane mask and a Lyot stop.

The coronagraph relies on the fact that the exoplanet is off-axis and so the light from the planet will not be blocked by the focal plane mask or the Lyot stop. Hence, on the detector after the Lyot stop, ideally, only the planet is visible. In practice, residual starlight remains in the image due to the diffraction effects from the telescope and the focal plane mask but also from adaptive optics phase residuals - for ground-based observations - but can be removed in post-processing (see Fig.8). The metric to assess the performance of a coronagraph and the accessibility of planets with this technique is its ability to reduce the starlight, i.e., the contrast. The contrast is defined as the ratio between the flux from the planet and the one from the star. The smaller the contrast, the more effective the coronagraph is in blocking the star light.

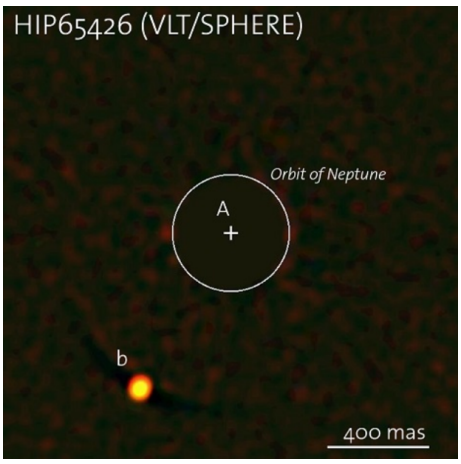

FIGURE 8 – Example of a coronagraph image obtained with the VLT/SPHERE instrument after post-processing. *Credits :* Chauvin et al. (2017).

One difficulty for imaging Earth-like planets relies on the fact that they are "too close", when considering the diffraction limit of current telescopes, from their host star. These planets are located within an angular separation < 0.1" whereas Jupiter-like planets (planets currently imaged) are at an angular separation > 0.5". The main objective is to image such planets (angular separation < 0.1") in our "close" environment, around young stars at distance of tens parsecs.

With an angular separation of the order of magnitude of $\theta = \lambda/D$, typically 12 mas @ 500nm, it should be possible to image such planets with telescopes such as the VLT working in visible wavelengths. This possibility led to the RISTRETTO project,

(Blind et al. 2022), which aims to image Prox Cen b located at 35 mas from its host star, corresponding to two times the diffraction limit in the visible (VIS). As reaching the diffraction limit in the visible is challenging (see chapter 1), RISTRETTO will be equipped with an eXtrem Adaptive Optics (XAO) system to obtain a high quality wavefront in this spectral band.

The other challenge in imaging an Earth-like planet is the contrast provided by the coronagraph. Indeed, imaging an Earth-like planet is extremely challenging as these planets are ten of billions of times dimmer than their host star in the VIS or NIR. This means that the coronagraph instrument has to reduce the flux of the star by a factor of 10^{10}. The current achievable contrast for ground-based facilities is 10^{-6} with the SPHERE instrument on the VLT,(Fusco et al. 2006; Beuzit et al. 2008, 2019) and GPI on the Gemini telescope (Graham et al. 2007; Macintosh et al. 2008, 2014) after post-processing.

Impact of atmospheric turbulence on ground-based observations

Reaching a contrast smaller than 10^{-8} in the VIS or NIR is the main challenge for high-contrast imaging. Research is ongoing to improve coronagraph instruments, and new post processing techniques can be used to increase the contrast, such as Angular Differential Imaging (Marois et al. 2006), and including a maximum likelihood estimation to discriminate the speckle from possible planets (Mugnier et al. 2009; Cantalloube et al. 2015). However, for ground-based facilities, another difficulty comes from the quality of the raw image as images from the telescope are not, diffraction limited as they suffer from the presence of aberrations. Optical aberrations are responsible for modifying the wavefront of the incoming Electromagnetic Field (EM), degrading the image quality, and hence decreasing the resolution of the telescope. These aberrations have several sources, such as those coming from the telescope itself, or those induced by the propagation of the light in turbulent media, in the atmosphere for ground-based facilities.

Instrument-induced aberrations can be caused by misalignment of the telescope mirror, misalignment of the scientific instrument, errors in the co-phasing of the telescope segments, or fragmentation/differential piston errors. In the case of the ELT, the fragmentation is induced by the spider-arms holding the secondary mirror (M2). Because of the size of the mirrors, the spider needs to be thick to support the weight of M2. The shadow of the spiders on M1 cuts the pupil in 6 fragments breaking with the wavefront continuity across the pupil (see Fig.9) and disturbing the wavefront correction (see chapter1, section1.3). For the ELT, none of the first light instruments will have a dedicated sensor to measure and control differential piston. Nonetheless, it will be the case for the second generation of instruments such as ArmazoNes high Dispersion Echelle Spectrograph (ANDES), (Marconi et al. 2022). The strategy for the first light instruments is to mitigate the effect of the differential piston by constraining the Deformable Mirror (DM) actuators (Schwartz et al. 2018).

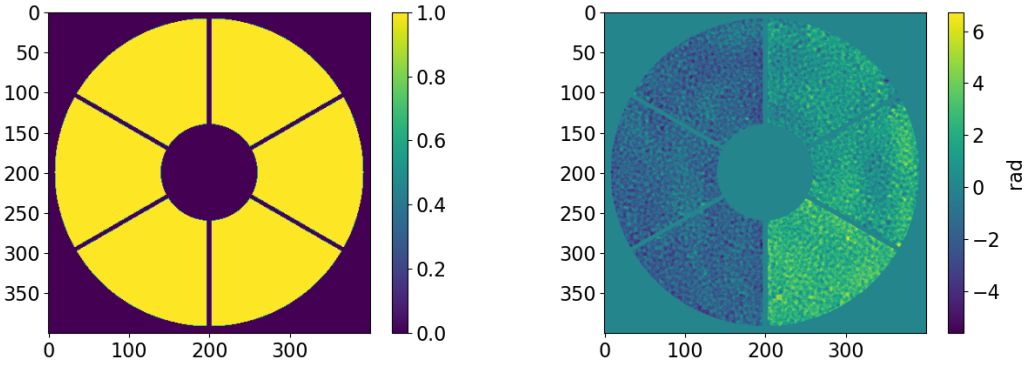

(a) ELT pupil (b) Phase screen

FIGURE 9 – HARMONI, SCAO simulation. Left : ELT pupil used for simulation. Right : residual phase screen of amplitude 1.9 rad RMS. Differential piston is visible in the AO residuals.

The other source of aberrations is the presence of the atmosphere. The impact of atmospheric turbulence is detailed in chapter 1, section 1.1. After a long journey in the universe, for the last hundreds of kilometres, the EM field will propagate through the turbulent atmosphere. The fluctuations of the refractive index in the atmosphere will induce additional phase aberrations in the EM field, which will degrade the image quality, hence reducing the resolution of the instrument (see Fig.10). Adaptive Optics (AO) (more details in chapter 1 section 1.2) was proposed by (Babcock 1953) and developed to mitigate the atmospheric effects and retrieve the resolution of the telescope.

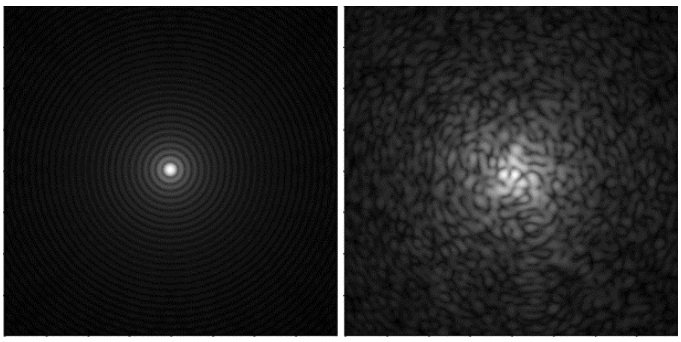

(a) Perfect case (b) With aberrations

FIGURE 10 – Image of a star in the perfect case without aberrations on the left and with atmospheric aberrations on the right.

With the advent of GST, the challenge for ground-based facilities for the direct

detection of Earth-like planets is therefore to provide high-contrast systems with an aberration-free wavefront, particularly at small angular separation from the host star, hence at low and medium spatial frequencies. A full study of the impact of turbulence on the image, together with a full description of the AO system, is given in the next chapter1.

Problematic of the thesis

The astronomical community is about to add a new brick to an age-old quest : "How are planets formed and what is the origin of life? To answer these questions, which have puzzled humankind for thousands of years, the community is ready to push ahead with the development of extraordinary facilities such as the ELT, the GMT, and the future HWO. However, for ground-based facilities one of the main limitations is the mitigation of external aberrations that deteriorate the image quality. AO is used to reduced in real-time the level of aberrations, resulting in a wavefront that is almost diffraction-limited, which is necessary for high-contrast imaging.

Former and current AO systems, have shown incredible results, such as direct imaging of the first exoplanet using VLT/NACO (Chauvin et al. 2004), and the discovery of the first circumstellar disk around β Pic B in (Smith & Terrile 1984). The combination of AO and high-contrast imaging allowed the imaging of fainter exoplanets such as the system HR8799 with Spectro-Polarimetric High-contrast Exoplanet Research (SPHERE) on the VLT (Fusco et al. 2006), NIRC2 on Keck and NIRI in Gemini (Hodapp et al. 2003; Marois et al. 2008; Currie et al. 2012). With the advent of GST, the classical AO systems used to correct for the atmospheric turbulence need to be rethought in order to reach the level of correction needed to detect an Earth-like planet. Additionally to correct for atmospheric turbulence, strategies to correct pupil fragmentation need to be implemented in the correction stage. It appears that classical WFS cannot measure both; the Shack-Hartmann WFS is well-suited to measure the atmosphere but insensitive to pupil fragmentation. The non-modulated pyramid, on the other hand, has demonstrated sensitivity to differential piston but cannot correct for the turbulence.

This PhD manuscript focuses on the study of the next generation of WFS, specifically those selected to be part of the AO systems of the GST. These sensors belong to the family of Fourier Filtering WaveFront Sensor (FF-WFS), with the Zernike mask and pyramid sensors being the most prominent examples. Due to their specific characteristics, these sensors are the leading candidates for achieving diffraction-limited wavefronts for the GST. In the first chapter 1 of this thesis, we will establish the fundamental concepts of optical propagation, adaptive optics, and wavefront sensing that are relevant to this research. Following this, a detailed account of the work carried out during this PhD will be presented. The research conducted on FF-WFS is divided into two chapters. The primary focus of my PhD was to develop a comprehensive understanding of the non-linear response of these sensors and how it affects wavefront estimation. To address the challenges posed by these non-linear effects, I proposed two main solutions : (i) a modification of the phase mask (chapter2), and (ii) an alteration of the reconstructor used for wavefront estimation (chapter3).

1 TOOLS AND TECHNIQUES

This chapter explores the basics of optical propagation through a ground-based telescope and the impact of turbulence on the image quality. We give an overview on Adaptive Optics (AO) systems which aim at reducing the impact of the atmospheric turbulence on observations. A section is dedicated to WaveFront Sensor (WFS) - systems that aim at measuring the optical perturbation. The final section explores Fourier Filtering WaveFront Sensor (FF-WFS), the WFS of the future Giant Segmented Telescopes (GST). The equations and the information of this chapter come from the literature, the references are listed in the text.

Contents

1.1 Imaging through the atmosphere . . . 48
1.1.1 Image formation . . . 48
1.1.2 Atmospheric Turbulence . . . 57
1.2 Adaptive Optics (AO) . . . 64
1.2.1 Deformable mirror (DM) . . . 66
1.2.2 Wavefront Sensor . . . 67
1.2.3 Reconstruction and control of the wavefront in an Adaptive Optics system . . . 81
1.2.4 Adaptive optics error budget . . . 85
1.3 Adaptive Optics with Giant Segmented Telescopes . . . 88
1.3.1 Adaptive Optics and Pupil Fragmentation . . . 88
1.3.2 Modal basis to describe phase discontinuity aberrations . . . 90
1.4 Interest of Fourier filtering wavefront sensors . . . 91
1.4.1 Sensitivity of FF-WFS . . . 92
1.4.2 Dynamic of FF-WFS . . . 92
1.4.3 Optical gains approach . . . 96
1.5 Summary . . . 100

1.1 Imaging through the atmosphere

This section describes the formalisms used in litterature for describing the image formation through an optical system and the different sources of perturbations or phenomena that can impact the image quality of an imaging system.

1.1.1 Image formation

In this manuscript we consider the case of an optical system observing a point source. This case is useful for two reasons. On one side, a point source is the mostly used case for characterising an optical system. Second, it fits well to the science case supporting this thesis which is the observation of planets around stars.

1.1.1.1 Point Spread Function

We therefore consider a point source object, positioned at a significant distance such as it can be considered as being at infinity. The incoming field, $\psi_0(\mathbf{r})$ is considered to be monochromatic of wavelength λ. Furthermore, given its infinite distance, the wavefront coming from the point source is perceived as flat. Under these hypothesis, the Electromagnetic Field (EM) field incoming, i.e., the EM field at the entrance plane of a telescope, ψ_0 emitted by the point source is given by the following expression :

$$\psi_0(\mathbf{r}) = A(\mathbf{r})e^{i\phi(\mathbf{r})}, \tag{1.1}$$

where $\mathbf{r}$ is the position vector in the plane of the telescope $\mathbf{r} = (x, y)$, A($\mathbf{r}$) is the amplitude of the EM field and $\phi(\mathbf{r})$ the phase of the EM field in radian defined as $\phi(\mathbf{r}) = \frac{2\pi\delta(\mathbf{r})}{\lambda}$ with δ the optical path difference. Without any perturbation the phase of the incoming wavefront is null $\phi(\mathbf{r}) = 0$ and its amplitude equal to 1 $A(\mathbf{r}) = 1$.
The EM field ψ_{in} at the entrance of the telescope can be expressed as follows

$$\psi_{in}(\mathbf{r}) = \mathbb{I}_p(\mathbf{r})\psi_0(\mathbf{r}), \tag{1.2}$$

where $\mathbb{I}_p(\mathbf{r})$ is the pupil function defined as a binary mask expressed as follows

$$\mathbb{I}_p(\mathbf{r}) = \begin{cases} 1 & \text{if } \mathbf{r} \text{ in the pupil ,} \\ 0 & \text{outside of the pupil.} \end{cases} \tag{1.3}$$

The EM field in the focal plane of the telescope, by omitting the distension factor induced by the focal length of the instrument and the wavelength $\frac{1}{(f\lambda)^2}$, is the Fourier transform of the EM field in the entrance pupil

$$\psi_{out} = \mathscr{F}\left(\psi_{in}\right), \tag{1.4}$$

where $\mathscr{F}$ stands for the Fourier transform function.

The intensity on the detector in the focal plane is modelled by the square modulus of ψ_{out}

$$I_d = \left|\psi_{out}\right|^2. \tag{1.5}$$

For a point source at infinity, the intensity pattern on the focal plane of the system is called the Point Spread Function (PSF) or the impulse response of the system I_d = PSF. The PSF only depends on the entrance pupil geometry and on the aberrations of the incoming field carried by ϕ. The PSF is normalised to 1. In the case of a full circular aperture and in presence of a flat wavefront, *e.g.* $\phi(\mathbf{r})$=0, the PSF is an Airy disk and its analytical expression is given by the first order Bessel function J_1 :

$$Airy(\rho) = \frac{\pi D^2}{4\lambda^2}\left|\frac{2J_1(\pi D\rho/\lambda)}{\pi D\rho/\lambda}\right|^2. \tag{1.6}$$

When considering a different pupil, the shape of the PSF is modified and its analytical expression can be complex to obtain. It can however be computed numerically using Fourier transform tools. As an example, the impact of the pupil shape on the PSF is provided in Fig.1.1 where PSF corresponding to a full circular pupil with and without central obstruction and in the presence of spiders are compared [1]. In addition,

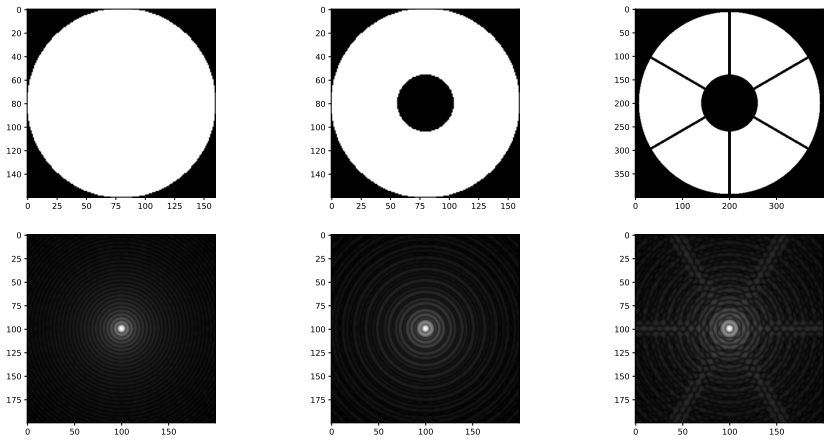

FIGURE 1.1 – Impact of the pupil (Top) on the PSF shape (Bottom). The PSFs are displayed in logarithm scale to highlight the effects of the diffraction.

Fig.1.2 provides a 1D cut of the PSF for a uniform circular pupil with and without a central obstruction. This plot shows that the relative intensity between the core and the first Airy ring is different.

1. Mechanical structures that support a secondary mirror for instance

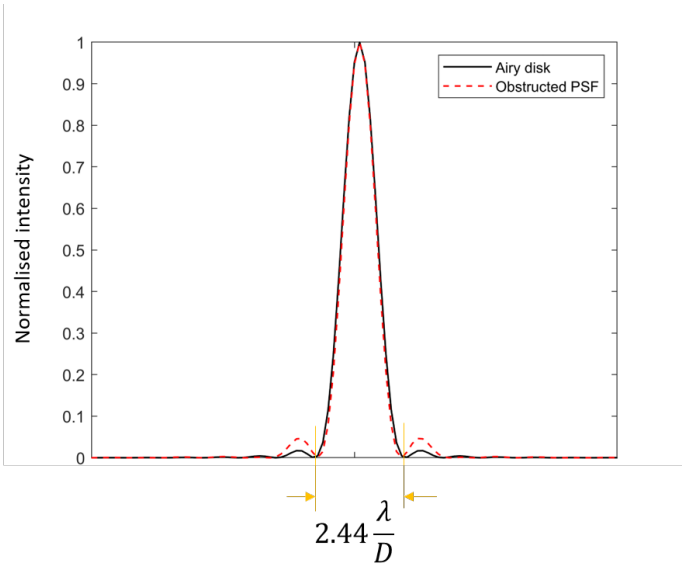

FIGURE 1.2 – Normalised PSF cut for a full circular aperture without (solid black line) and with a central obstruction(dashed red line)

1.1.1.2 Optical Transfer Function

Related to the PSF, we introduce the notion of the Optical Transfer Function (OTF) that is defined as the Fourier transform of the PSF

$$OTF(\nu) = \mathscr{F}(PSF). \tag{1.7}$$

If we develop the expression we can note that the OTF corresponds to the auto-correlation of the entrance pupil

$$\begin{aligned} OTF(\nu) &= \mathscr{F}\left(\left|\mathscr{F}(\mathbb{I}_p)\right|^2\right) \\ &= \mathbb{I}_p \otimes \mathbb{I}_p, \end{aligned} \tag{1.8}$$

where $\otimes$ is the correlation operator.

The OTF is expressed in the frequency domain and indicates how each spatial frequency is transmitted through the optical system. Since the OTF is a complex quantity, it is often useful to consider the Modulation Transfer Function (MTF) that is defined as the modulus of the OTF

$$MTF = |OTF|. \tag{1.9}$$

An example of an MTF corresponding to a telescope with a circular pupil and no phase aberration is provided in Fig. 1.3. The MTF exhibits a cutoff frequency that depends

on both the observing wavelength and the diameter of the telescope, denoted as

$$\nu_c = D/\lambda. \tag{1.10}$$

As such, the OTF and the MTF indicate that an optical system behaves like a low-pass filter where all the spatial frequencies exceeding ν_c are blocked.

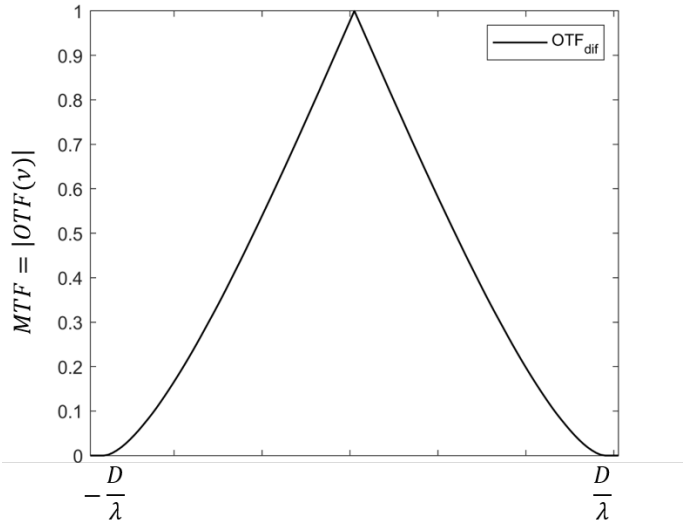

FIGURE 1.3 – Normalised MTF cut for a full circular aperture without central obstruction. The cut-off frequency of the system is $\nu = D/\lambda$.

1.1.1.3 Resolution of a Telescope

We can define the resolution of a telescope through the example of the image of two point sources. Indeed the resolution can be defined as the ability of the optical system to resolve two very close objects with sufficient contrast, and the capability to transcribe the frequency content of a scene.
Two definitions of the angular resolution are therefore introduced :

— The first one stems from the typical shape of the telescope's impulse response. Indeed, the PSF is not a singular point but rather a (modified) Airy pattern. One criterion widely used is the Rayleigh criterion, which states that two point sources are separated when the peak of each PSF coincidates with the first dark ring of the other, (Rayleigh 1880). Thus, the minimum angular separation between the sources is equal to θ_c given by

$$\theta_c = 1.22\lambda/D. \tag{1.11}$$

— The second one comes from the cutoff frequency of the MTF. The maximum spatial frequency transfered by an optical system being D/λ, one can define a

minimum angular separation to distinguish two point sources denoted as

$$\theta_c = \lambda / D, \tag{1.12}$$

where θ_c defines the Sparrow criterion, (Sparrow 1916).

1.1.1.4 Optical aberrations and modal decomposition

An optical aberration is a change in the phase of the electromagnetic field due to the propagation of light through an optical element (lens, mirror, etc.) or a turbulent medium (atmosphere, liquids, biological medium, etc.). This deviation from the perfect case (flat wavefront or zero phase) has a direct impact on image quality, and consequently on the angular resolution of the system.

The most common optical aberrations that can be encountered in our everyday life are (see Fig.1.4) :

— A **Tip/Tilt** consists in the inclination of the incoming beam with respect to the optical axis. In this case, if no other optical aberrations are present, the PSF remains the same on the focal plane but is not anymore centred on axis : the Tip/Tilt aberration induces a displacement of the PSF.

— A **defocus** corresponds to a displacement of the focus point on the optical axis and results in a blurring of the PSF. This aberration is common in photography when the objective is not set properly and the detector is misplaced with respect to the focus point of the light.

— An **astigmatism** corresponds to a different curvature radius of an optical element in two directions and results in the blurring of the image in a given direction. This aberration is typically present in the cornea of the human eye and can be compensated using optical glasses.

To characterise the optical aberrations and compare different optical systems formally, the phase is usually decomposed as a linear combination on a basis of optical aberrations

$$\phi = \sum_{k=0}^{+\infty} a_k B_k, \tag{1.13}$$

where B_k is a vector of the basis B and a_k the corresponding coefficient of the decomposition. The vectors B_k of the basis B are often refereed as "modes" associated to the modal coefficients a_k.

Different basis can be employed depending on the application. Two are presented in the following sections : the Zernike basis and the Fourier basis (pure spatial frequencies basis).

1.1.1.5 Zernike Modal basis

The most common basis to describe optical aberrations is the Zernike polynomials' basis, (Zernike 1934). The Zernike basis is an orthonormal basis for phase aberrations

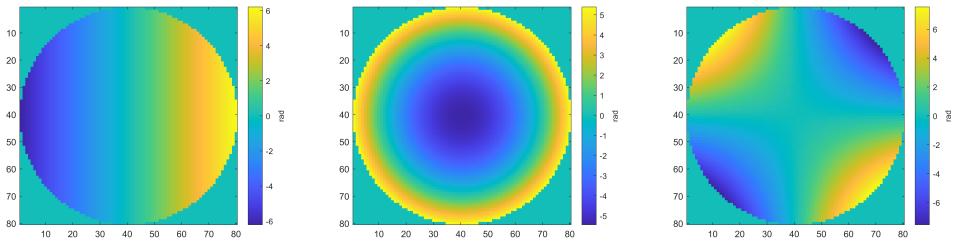

(a) Tip (b) Defocus (c) Astigamism

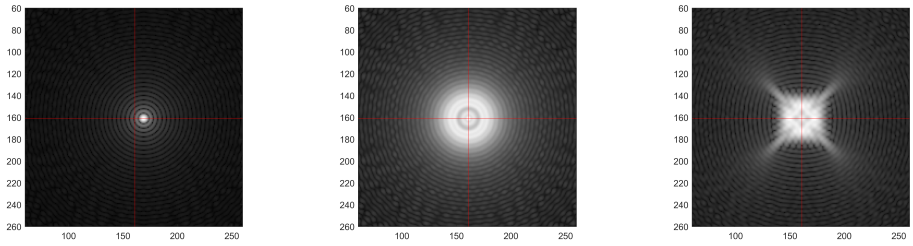

(d) PSF Tip (e) PSF Defocus (f) PSF Astigmatism

FIGURE 1.4 – Phase and PSF in logarithm scale of the common aberrations : Tip, Defocus and Astigmatism. The red vertical lines stands for the reference positions.

defined on a full circular aperture.

The Zernike polynomials are organised according to the radial degree n and the azimutal degree m with $m < n$ and m with the same parity of n. Therefore, the analytical expression of the Zernike polynomials uses the polar coordinates $\boldsymbol{\rho} = (\rho, \theta)$. The radial part of the polynomials is expressed as follows

$$R_n^m(\rho) = \sum_{k=0}^{\frac{n-m}{2}} \frac{(-1)^k (n-k)!}{k!(\frac{n+m}{2}-k)!(\frac{n-m}{2}-k)!} \rho^{n-2k}, \tag{1.14}$$

where ρ is the radial distance $0 \leq \rho \leq 1$.

The azimutal degree of the polynomial defined the final expression of the Zernike polynomials

$$Z_n^m(\rho,\theta) = \sqrt{n+1} \begin{cases} \sqrt{2} cos(m\theta) R_n^m(\rho) & \text{if m even} \\ \sqrt{2} sin(m\theta) R_n^m(\rho) & \text{if m odd} \\ 1 & \text{if m=0,} \end{cases} \tag{1.15}$$

where $0 \leq \theta \leq 2\pi$.

The polynomials are orthonormal

$$\begin{aligned} \langle Z_n^m | Z_{n'}^{m'} \rangle &= \frac{1}{\pi} \int_0^{2\pi} d\theta \int_0^1 d\rho Z_n^m(\rho,\theta) Z_{n'}^{m'}(\rho,\theta) \\ \langle Z_n^m | Z_{n'}^{m'} \rangle &= \delta_{n,n'} \delta_{m,m'} \end{aligned} \tag{1.16}$$

with this scalar product, the Root Mean Square (RMS) norm is define as

$$||x|| = \sqrt{\langle x|x \rangle}.$$

The first 16 polynomials are plotted in Fig.1.5.

n	m	Expression	Name	Notation
0	0	1	Piston	Z_0^0
1	-1	$2\rho cos(\theta)$	Tip	Z_1^{-1}
1	1	$2\rho sin(\theta)$	Tilt	Z_1^{-1}
2	-2	$\sqrt{6}\rho^2 sin(2\theta)$	Oblique astigmatism	Z_2^{-2}
2	0	$\sqrt{3}(2\rho^2 - 1)$	Defocus	Z_2^0
2	2	$\sqrt{6}\rho^2 cos(2\theta)$	Vertical astigmatism	Z_2^2

TABLEAU 1.1 – The first six Zernike polynomials

The decomposition of the phase on the Zernike basis is expressed as follows

$$\phi(\mathbf{r}) = \sum_{n=0}^{+\infty} \left(\sum_{m=-n,step=2}^{n} a_n^m Z_n^m(\mathbf{r}) \right). \tag{1.17}$$

The Zernike basis is an orthonormal basis so the phase variance can be expressed as

$$\sigma_\phi^2 = \sum_{n=0}^{+\infty} \left(\sum_{m=-n,step=2}^{n} (a_n^m)^2 \right). \tag{1.18}$$

The Zernike polynomial basis is widely used in optics because of its accurate representation of low-order aberrations, which are common in optical systems. However, it has several limitations. Firstly, its orthogonality is limited to circular apertures. In addition, higher-order Zernike polynomials concentrate their energy near the pupil edge, and the basis lacks a clear organisation based on spatial frequency. Finally, the Zernike coefficients are not statistically independent of atmospheric turbulence (its impact is studied in section 1.1.2), so other modal bases have been proposed to solve these problems (see next section as an example) .

1.1.1.6 Karhunen-Loève basis

In the previous section, we introduced the Zernike basis to describe the optical aberrations of a system or those induced by atmospheric turbulence. However, this

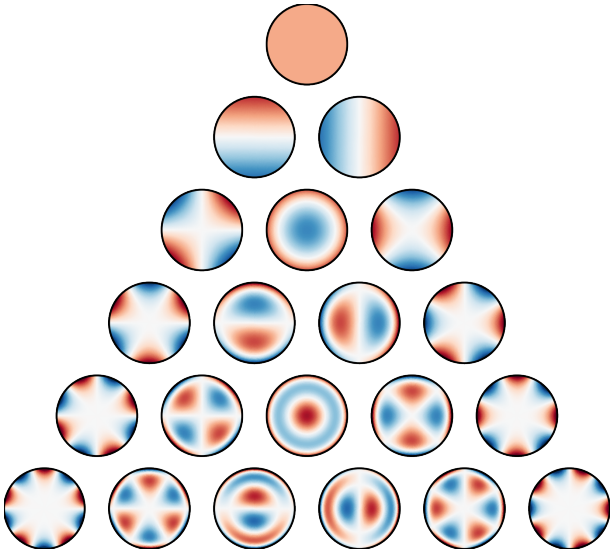

FIGURE 1.5 – First Zernike polynomials : credits https://en.wikipedia.org/wiki/Zernike_polynomials

basis has certain limitations that can be addressed by using alternative modal bases. The Karhunen-Loève (KL) basis offers an alternative to the Zernike polynomial basis as it does not have the disadvantages of the Zernike polynomials. The KL basis is obtained from the eigenmodes of the spatial covariance matrix of the turbulent phase in the telescope pupil

$$\mathrm{Cov}(\mathbf{r},\mathbf{r'})) = \langle \mathbb{I}_p(\mathbf{r})\phi(\mathbf{r})\mathbb{I}_p(\mathbf{r'})\phi(\mathbf{r'})\rangle_\tau. \tag{1.19}$$

By construction, the KL coefficients are statistically independents regarding the atmospheric turbulence and sorted in terms of turbulent energy. The modes are orthogonal for the considered pupil and the energy is not concentrated at the edges of the pupil, (Dai 1995). The main drawback is that, there is no analytical expression for the KL functions.

1.1.1.7 Fourier basis

The Fourier basis describes the pure spatial frequency content of the wavefront. Therefore, the phase can be decomposed into its Fourier series $\{sin(2\pi n\mathbf{r}/\lambda), cos(2\pi n\mathbf{r}/\lambda)\}_n$. To be considered as pure spatial frequency, the support on which the modes are defined should be infinite which is not the case when a pupil is applied. As such, the denomination "Fourier" basis used here is a generalisation of a pure sine wave defined on a finite support defined by the pupil. As an example, a sine wave at the entrance pupil (with a small amplitude) creates a PSF with two secondary spots in the direction of the sine wave and reduces the amplitude of the PSF core compared to the diffraction limited case. The frequency of the sine wave has a direct impact on the distance between the core and the spot of the PSF, the larger the period the larger the distance.

The PSF obtained for a sine wave at the entrance pupil of amplitude 0.73 rad RMS and 3 cycles in the pupil is provided in Fig.1.6

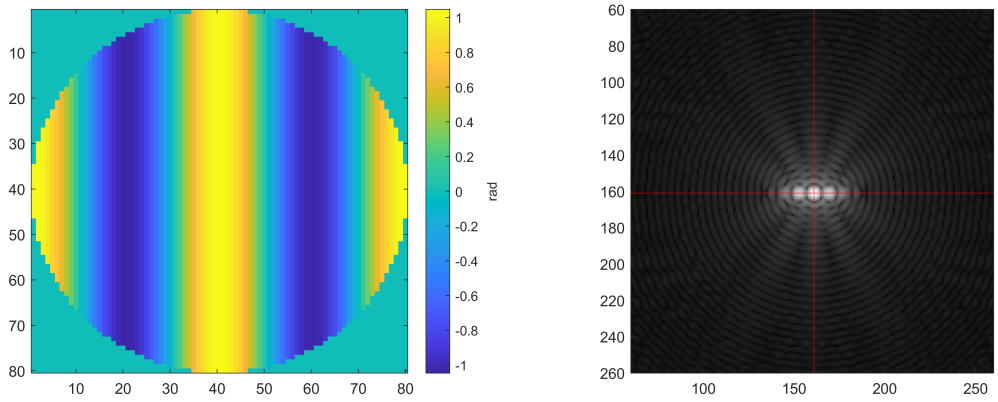

(a) Phase : 3 cycles in the pupil, amplitude 0.73rad RMS

(b) Associated PSF in logarithm scale

FIGURE 1.6 – Incoming sine wavefront and its associated PSF in the focal plane. The PSF is plotted in logarithmic scale.

This modal basis is not often used to describe optical aberrations but is practical to study the behaviour of a WaveFront Sensor (WFS) (see section 1.2.2) across all the spatial frequencies. In particular, this basis will be used in the section 1.4 to compare the sensitivity of the Fourier Filtering WaveFront Sensor (FF-WFS).

Impact of optical aberrations on the OTF

As shown in Fig.1.6 and Fig.1.4, optical aberrations have a direct impact on the PSF shape and therefore on the cutoff frequency of the system. For instance, when the incoming wavefront is a pure sine wave, the amplitude of the sine wave will change the amplitude of the secondary lobes, hence resulting in local minima in the OTF - see Fig.1.7. The higher the amplitude of the sine wave, the deeper the dips in the OTF, preventing the system form probing these spatial frequencies. For Zernike modes, their impact on the resolution of the instrument depends on the considered modes. For instance, the tip and tilt do not have an impact on the resolution as they only move the PSF on the focal plane - see Fig.1.8(a). Yet, defocus and the astigmatism, modify the shape of the PSF but not its position of the focal plane, hence reduce the resolution of the system - see Fig.1.8(b,c).

These different representations correspond to a single aberration and the situation becomes more problematic when multiple aberration are summed up as multiple areas of the spatial frequency domain are affected. This situation is encountered when propagating light through the atmosphere that is described in the next section.

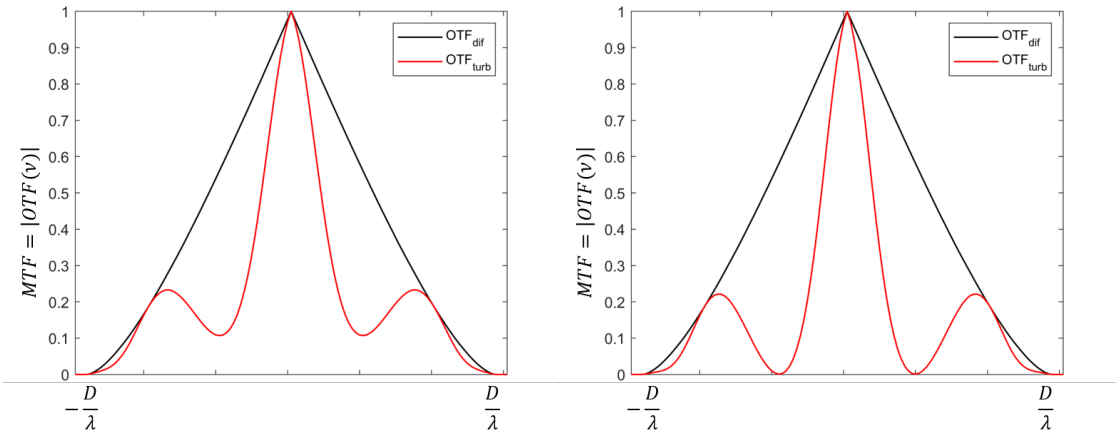

(a) MTF for incoming phase of 0.73 rad RMS (b) MTF for incoming phase of 0.85rad RMS

FIGURE 1.7 – Normalised MTF cut for a full circular aperture. The incoming wavefront is a sine wave of period 3 cycle. (a) Phase amplitude is 0.73 rad RMS (cf Fig.1.6). (b) Phase amplitude is 0.85 rad RMS.

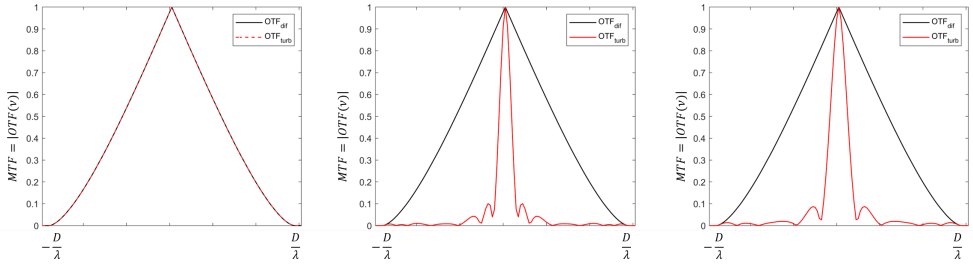

(a) MTF Tip (b) MTF Defocus (c) MTF Astigmatism

FIGURE 1.8 – Normalised MTF cut for a full circular aperture. The different wavefront have an amplitude of π rad RMS. The associated phase and PSF are plotted in Fig.1.4.

1.1.2 Atmospheric Turbulence

The previous section introduced the theory of image formation in the case of an ideal optical system, and presented optical aberrations and their impact on instrument resolution. Another source of aberrations is the medium in which the electromagnetic field propagates. For ground-based observations, the medium is the atmosphere. Although photons travel light-years through the interstellar medium without phase disruption, they eventually encounter the turbulent atmosphere in the last few moments of their journey, which extends over only a few tens of kilometres.

Composed of multiple air masses of varying chemical composition, temperature and humidity, the atmosphere undergoes convective processes leading to turbulent phenomena. The mixing of these masses induces local fluctuations in temperature and

humidity, causing fluctuations in the refractive index, denoted n, of the air. Fluctuations in refractive index give rise to fluctuating aberrations in the incoming wavefront. To a first approximation, these aberrations can be represented by layers of turbulence that are thin in relation to the propagation path between them.

The statistics of refractive index fluctuations are given by the Kolmogorov-Obukhov law (Kolmogorov 1941). They are characterised by their structure function D_n, the average over time of the refractive index under the isotropic hypothesis

$$D_n(\boldsymbol{\rho}) = \langle |n(\mathbf{r}) - n(\mathbf{r}+\boldsymbol{\rho})|^2 \rangle = C_n^2 \boldsymbol{\rho}^{2/3}, \tag{1.20}$$

where $\boldsymbol{\rho}$ is the position vector of a point in the considered atmospheric layer and C_n^2 is the index structure constant.

The structure function D_n describes the strength of the turbulence in each layer. It measures the statistical correlation at a given altitude between the refractive index at a given point $\boldsymbol{\rho}$ and its near neighbours. The turbulence profile is directly linked to the evolution of the C_n^2 with the altitude.

The fluctuations of the refractive index can be described by the Kolmogorov spectrum (Kolmogorov 1941), given by the Power Spectral Density (PSD) of the structure function D_n

$$W_n(\mathbf{f}) = 0.033(2\pi)^{-2/3} C_n^2 f^{-11/3}, \tag{1.21}$$

where $\mathbf{f}$ is the spatial frequency vector. The PSD exhibits an asymptotic law in $f^{-11/3}$ characteristic of the turbulence. The Kolmogorov spectrum will diverge for the low spatial frequencies. The Von-Karman spectrum (Von Karman 1948; Consortini et al. 1973; Chassat 1992), corrected it using L_0 the outer-scale, the characteristic sizes of the vortices

$$W_n(\mathbf{f}) = 0.033(2\pi)^{-2/3} C_n^2 \left[f^2 + \frac{1}{L_0^2} \right]^{-11/6}. \tag{1.22}$$

1.1.2.1 Fried parameter

The strength of the turbulence is given by the Fried parameter r_0 (Fried 1966)

$$r_0(\lambda) = \left[0.423 \left(\frac{2\pi}{\lambda} \right)^2 \frac{1}{cos(\gamma)} \int_0^{h_{max}} C_n^2(h) \mathrm{d}h \right]^{-3/5}, \tag{1.23}$$

where γ is the zenith angle and where $C_n^2(h)$ corresponds to the contribution of the atmospheric layer at the altitude h. In practice, the Fried parameter is an integrated value that represents the typical area over which the wave-front is small enough so that the signal can be considered as coherent (*e.g.* with a phase variance $< 1\ rad^2$). Typically, the layers close to the ground have a larger contribution hence a higher value of $C_n^2(h)$.

It is important to notice that the Fried parameter is chromatic in $\lambda^{6/5}$ following this relation

$$r_0(\lambda_2) = r_0(\lambda_1)\left(\frac{\lambda_2}{\lambda_1}\right)^{6/5}. \tag{1.24}$$

From the definition of r_0, one can derive another atmospheric parameter called seeing and defined as

$$s \simeq \lambda / r_0 \ @500\text{nm}. \tag{1.25}$$

The seeing represents nothing but the typical FWHM of a long exposure image of a point sources observed by a telescope in presence of turbulence when the telescope diameter is significantly larger than r_0.

1.1.2.2 Temporal coherence

Fried's parameter r_0 is one of the key parameters for describing and quantifying the spatial effects of turbulence. r_0 is a statistical parameter defined under the assumption of a long (from a convergence point of view) and stationary process. This section addresses the temporal aspect and aims at defining the characteristics time of the turbulent phase evolution. Let's assume, first of all, that all turbulent vortices are affected by the mean wind speed in the direction of flow, with no change in their properties, i.e. they translate unchanged with a speed $V(h)$. This assumption is commonly used in AO and it is called the Frozen Flow hypothesis or the Taylor hypothesis (Taylor 1933). The variance of the phase difference between two time instances separated by time τ can be obtained from the phase structure function D_ϕ, (Fried 1990)

$$\sigma^2_{\Delta\phi}(\tau) = D_\phi(\boldsymbol{\rho} = \bar{v}\tau) = 6.88\left(\frac{\bar{v}\tau}{r_0}\right)^{5/3}, \tag{1.26}$$

where $\bar{v}$ is the weighted average wind speed by the strength of each turbulent layer

$$\bar{v} = \left[\frac{\int_0^\infty v^{5/3}(h)C_n^2(h)dh}{\int_0^\infty C_n^2(h)dh}\right]^{\frac{3}{5}}. \tag{1.27}$$

From this expression, one can express the temporal evolution τ_0 of the phase, i.e., the characteristic time for which the variance is equal to $1rad^2$:

$$\tau_0 = 0.314\frac{r_0}{\bar{v}} \tag{1.28}$$



FIGURE 1.9 – Taylor hypothesis : frozen flow, turbulent wavefronts are frozen and translate across the pupil at wind speed V

1.1.2.3 Isoplanatic angle

The isoplanatic angle is the angular counterpart of the time characteristic of turbulence. Because of its altitude distribution (between the ground and typically 20 to 30km height), the wavefront also evolves in the field of view. The volume of turbulence changes depending on the pointing direction, in this manner, the variance of the phase difference at two given directions separated by θ (Fried 1982) is given by

$$\sigma^2_{aniso}(\theta) = D_\phi(\rho = \theta z) = 6.88\left(\frac{\theta z}{r_0}\right)^{5/3}. \tag{1.29}$$

The isoplanetic angle is the characteristic angle for which the variance is equal to $1rad^2$:

$$\theta_0 = \left[2.91\left(\frac{2\pi}{\lambda}\right)^2 \int_0^{h_max} h^{5/3} C_n^2 \mathrm{d}h\right]^{-3/5}. \tag{1.30}$$

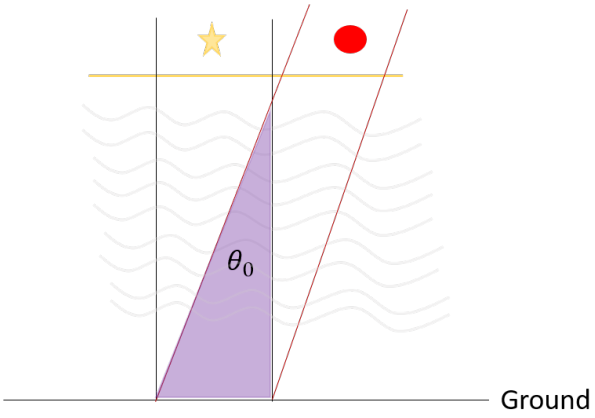

FIGURE 1.10 – Anisoplanatism : pointing in different directions.

The dependency of θ_0 on $h^{5/3}$ means its value depends on the higher layers of the atmosphere.

The anisoplanatism is a source of error in AO that we will not consider in this PhD manuscript as we are considering the on-axis mode of the AO (SCAO). Furthermore, the angular separation between the host star and the planet is negligible compare to the isoplanatic angle θ_0.

1.1.2.4 Impact of the turbulence on the EM field

The phase aberrations have a large impact on the image quality. The phase shift induced by a point at a given position $\mathbf{r}$ of a layer of altitude h is given by

$$\phi(\mathbf{r}, h) = \frac{2\pi}{\lambda} \int_h^{h+\delta h} (n(\mathbf{r}, z) - 1)\mathrm{d}z. \tag{1.31}$$

From this equation and by using the structure function of the refractive index (equation 1.20) one can express the structure function of the phase following Kolmogorov statistics, (Fried 1966)

$$\begin{aligned} D_\phi(\boldsymbol{\rho}) &= \langle |\phi(\mathbf{r}) - \phi(\mathbf{r}+\boldsymbol{\rho})|^2 \rangle \\ &= 6.88 \left(\frac{\boldsymbol{\rho}}{r_0} \right)^{5/3}, \end{aligned} \tag{1.32}$$

where D_ϕ gives information on the strength of the turbulence within an air column. The Kolmogorov PSD of the phase is therefore, (Kolmogorov 1941)

$$W_\phi(\mathbf{f}) = 0.023 r_0^{-5/3} f^{-11/3}. \tag{1.33}$$

The Kolmogorov PSD of the phase will diverge for low spatial frequencies. The Von-Karman PSD of the phase corrected with the outer scale prevents this divergence (Von Karman 1948)

$$W_\phi(\mathbf{f}) = 0.023 r_0^{-5/3} \left[f^2 + \frac{1}{L_0^2} \right]^{-11/6}. \tag{1.34}$$

This expression shows that the outer-scale L_0 mainly affects the contribution of the low spatial frequencies and its impact for higher frequencies can be neglected.

1.1.2.5 Impact of the atmospheric turbulence on the PSF

The Fried parameter stands out as the most critical factor, as the quality of the resulting image depends on its value at the imaging wavelength. This parameter exhibits chromatic behaviour, being directly proportional to $\lambda^{6/5}$ as indicated by equation 1.24. Consequently, the turbulence has a bigger impact on visible light (VIS) compared to near-infrared (NIR). The parameter r_0, known as the atmospheric coherence length, characterises the spatial coherence of atmospheric turbulence. Effectively, the atmosphere behaves as if the telescope aperture was limited to r_0 in diameter. In the absence of turbulence correction, the telescope's performance is constrained by observation conditions, hence by r_0.

The quantity $\frac{D}{r_0}$ can be used as a proxy for the observing conditions : If $\frac{D}{r_0} \longrightarrow 0$, it corresponds to a turbulence-free scenario, resulting in a diffraction limited PSF. As $\frac{D}{r_0}$ increases, the effect on the PSF becomes noticeable :

— $\frac{D}{r_0} < 3$ typically, the dominant effect is located in the Tip-Tilt modes, the flux remains concentrated in a single airy pattern and thus the main effect is a PSF jitter;

— $\frac{D}{r_0} > 3$ the PSF splits into a several speckles patterns (each with the same characteristic size of λ/D)

As an example, the case for $\frac{D}{r_0} = 10$ is provided in Fig.1.11. This figure shows the impact on the PSF for a short exposure (*e.g* for an integration time smaller than the coherence

time of the atmosphere) and a long exposure case (respectively for an integration time larger than the coherence time of the atmosphere). Focusing on the short exposure PSF, we can notice that the typical speckle pattern size is of the order of magnitude of λ/D. We can interpret these speckles as the result of the summation of fringes from small interferometers between each pair of surface elements of the pupil on which the phase is locally constant, but of random value. These short exposure speckles pattern averages out in the long-exposure image leading to a large PSF with a Full Width Half Maximum (FWHM) roughly equal to λ/r_0.

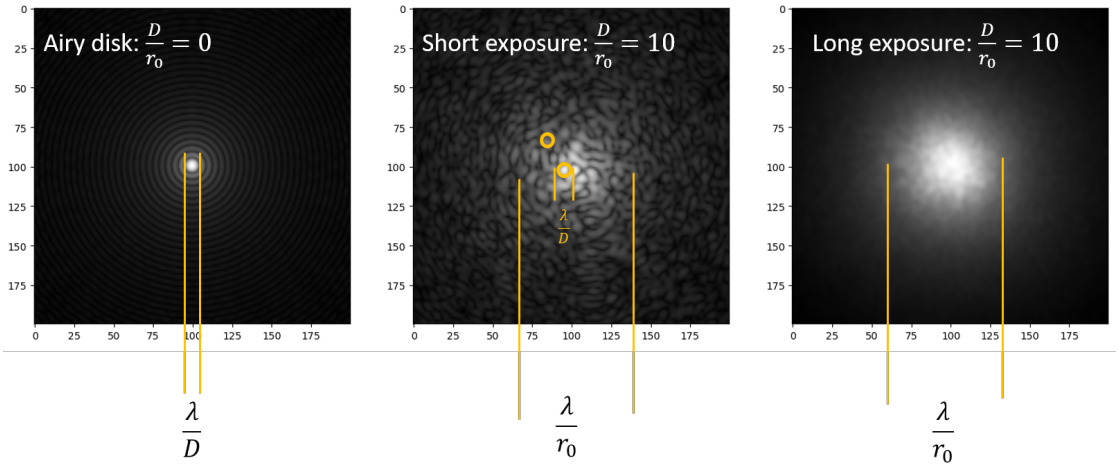

FIGURE 1.11 – Impact of turbulence on the PSF shape. The PSFs are displayed in logarithm scale to highlight the effect of the turbulence. Left : perfect PSF (Airy pattern), middle : short exposure PSF with turbulence and right : long exposure PSF with turbulence for $\frac{D}{r_0} = 10$.

In presence of turbulence, the OTF (the Fourier transform of the PSF cf equation 1.7) is now expressed as follows

$$OTF(\nu)_{turb} = OTF(\nu).e^{-\frac{1}{2}D_\phi(\nu)}. \tag{1.35}$$

The corresponding MTF for a turbulent and diffraction-limited case are provided in Fig.1.12 and show the reduced cutoff frequency of the system in presence of turbulence : from ν_c given by equation 1.10 to $\nu = r_0/\lambda < \nu_c$ (see Fig.1.12). It reduces significantly the probing frequency of the instrument and its angular resolution $\theta \approx \lambda/r_0$ (cf equation 1.12).

1.1.2.6 Performance criteria of an optical system

The amplitude of the aberrations degrades the image quality. The WaveFront Error (WFE) given in rad is a chromatic quantity that gives the RMS amplitude of the wavefront. It is chromatic since the phase is chromatic. Therefore, for a given wavefront,

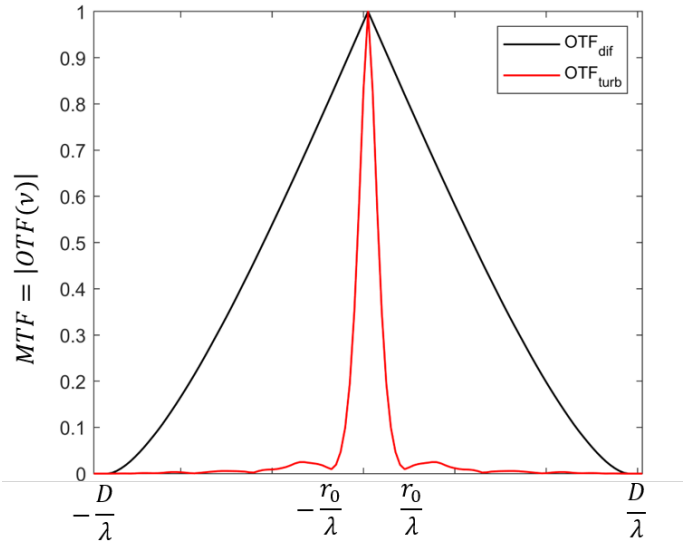

FIGURE 1.12 – Normalised MTF cut for a system without aberrations (black line) and with aberrations (red line). The observation conditions are such as $\frac{D}{r_0} = 10$.

the WFE will be larger in the visible than in the infrared. The WFE is computed as follows

$$\text{WFE} = \sqrt{\frac{1}{N_{pix}} \sum_{i=0}^{N_{pix}} \left(\sum_{j=0}^{N_{pix}} \left| \phi_{i,j} - \bar{\phi} \right|^2 \right)}, \tag{1.36}$$

where N_{pix} is the number of pixels in the phase screen and $\bar{\phi}$ the average of the wavefront.

From the Kolmogorov spectrum of the turbulence, one can compute the variance of the atmospheric phase as a function of the diameter and the Fried parameter r_0, (Fried 1966)

$$\langle \sigma_\phi^2 \rangle_\tau = 1.03 \left(\frac{D}{r_0} \right)^{5/3}, \tag{1.37}$$

where $\langle \sigma_\phi^2 \rangle_\tau$ is in rad^2.

The variance of the phase provides insights into the amplitude of turbulence. However, it alone does not offer information on how well an optical system performs in the presence of these aberrations. The Strehl ratio (SR), (Strehl 1895), defined in equation1.38, serves as a criterion to measure the effect of the aberrations on the image quality.

$$SR = \frac{I(\mathbf{r} = 0)}{I_{diff}(\mathbf{r} = 0)}, \tag{1.38}$$

where $I(\mathbf{r}=0)$ is the intensity of the aberrated incoming wavefront in the focal plane (so $I(\mathbf{r}=0) = PSF$) and $I_{diff}(\mathbf{r}=0)$ is the intensity obtained for a flat wavefront in the focal plane at the reference position, so the diffraction limited PSF ($I_{diff}(\mathbf{r}=0) = PSF_{diff}$) [2].

The SR can also be expressed as the ratio between the integral of the OTF of the aberrated system and that of a perfect system

$$SR = \frac{\int_{\mathbb{R}^2} OTF_{ab}(\nu)\mathrm{d}\nu}{\int_{\mathbb{R}^2} OTF(\nu)\mathrm{d}\nu}. \tag{1.39}$$

In the small phase regime, $\sigma_\phi^2 < 1$, the SR can also be approximated using the Maréchal formula, (Mahajan 1983)

$$SR = e^{-\sigma_\phi^2}. \tag{1.40}$$

According to Maréchal criteria, in presence of phase aberrations smaller than $\lambda/14$, the wavefront is considered as diffraction limited.

1.2 Adaptive Optics (AO)

The previous section showed the dramatic impact of atmospheric turbulence on the performance and the resolution of optical instruments. To tackle this problematic and increase the effective resolution of ground-based telescopes, the concept of Adaptive Optics (AO) has been introduced by Horace Babcock in 1953 (Babcock 1953). This technology consists of controlling in real time active optical elements to compensate for the optical aberrations created by the rapid fluctuations of the atmospheric refractive index (See 1.1). However, the technology at the time was not sufficiently advanced to actually build such systems. It was not until the 1970s that AO found practical application, primarily in defence contexts. Subsequent advancements in detector and DM technologies paved the way for AO in astronomy by the late 1980s. Notably, the COME-ON project in 1989 marked a significant milestone, featuring the first AO system capable of correcting lower-order atmospheric turbulence for astronomy,(Rousset et al. 1990). Initially deployed at the Observatoire de Haute-Provence (OHP), this technology later found its way to the VLT, ushering in a new era of ground based high-resolution astronomical observations to enable astronomers to overcome the limitations imposed by Earth's turbulent atmosphere, thereby enhancing the resolution of astronomical observations.

An AO system is composed of three main components :

2. Note that the diffraction-limited PSF is not an Airy pattern but the PSF obtained without aberrations for the considered pupil.

— The Deformable Mirror (DM) (see section1.2.1) : the component that modifies its shape to compensate for optical aberrations.

— The WaveFront Sensor (WFS) (see section1.2.2) : the component that measures a signal related to the incoming wavefront.

— The Real-Time Computer (RTC) (see section1.2.3) : the component to compute the DM commands from the measurement of the WFS.

Different flavours of AO systems exist depending on the scientific applications. Among them we count :

1. Single-Conjugated Adaptive Optics (SCAO) : (Davies & Kasper 2012) using one DM and one WFS to correct distortions at a single location in the atmosphere. The DM is conjugated to the telescope's pupil. It is ideal for point sources, such as observing planets, stars, and small galaxies.
2. Ground Layer Adaptive Optics (GLAO) : (Ragazzoni 2000; Tokovinin et al. 2005) corrects turbulence close to the ground, improving image quality over a wider field of view (≈5–10 arcminutes.). It uses multiple guide stars and a DM conjugated to the ground layer to correct low-altitude turbulence. It is used for wide-field surveys, observing star clusters, and large nebulae.
3. Laser Tomographic Adaptive Optics (LTAO) : (Gilles & Ellerbroek 2006; Neichel et al. 2010) uses multiple laser guide stars to build a 3D model of atmospheric turbulence, enabling high-resolution imaging for a moderate field of view (few arcsecond). It uses multiple laser guide stars to sample atmospheric turbulence at various altitudes, multiple DM and WFS to reconstruct atmospheric profiles. It aims at observing faint, extended objects, like distant galaxies or nebulae.
4. Multi-Conjugated Adaptive Optics (MCAO) : (Rigaut et al. 2000) uses multiple DM and WFS to provide a wide-field correction. The DMs are conjugated to different atmospheric layers. It aims at observing over large fields, like monitoring globular clusters or studying stellar populations. It provides a uniform correction over a large field of view (around 1 arcminutes).

In this thesis we will focus on the simplest AO system, the on axis AO mode, the Single-Conjugated Adaptive Optics (SCAO). In an AO closed-loop configuration (see Fig.1.13) , the WFS is located downstream the DM. The process unfolds as follows : light emitted from a point source encounters the DM. The incoming beam is split in two : a portion of the light is directed towards the scientific instrument, while another portion is sent to the WFS. In general, the WFS and the scientific camera receive different parts of the spectrum (for example, VIS for the WFS and NIR for the scientific camera). The WFS detects and measures signals from the incoming wavefront. Subsequently, the RTC reconstructs the wavefront based on the WFS measurements and calculates the appropriate commands for the DM to correct for the incoming wavefront. This iterative process operates within a feedback loop, typically running at frequencies ranging from a few hundreds Hz to a few kHz, (Roddier 1999).

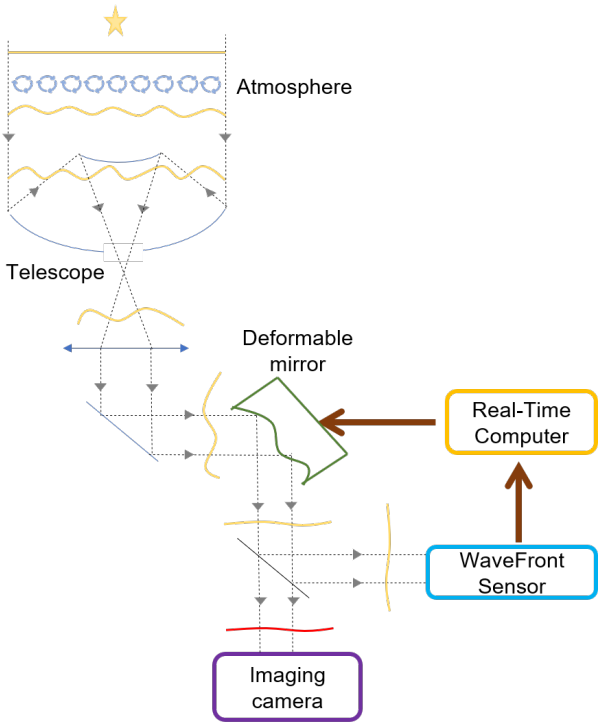

FIGURE 1.13 – Schematic of a Single-Conjugated Adaptive Optics (SCAO).

1.2.1 Deformable mirror (DM)

The DM is an active optical component capable of introducing controlled phase distortions to a light beam to compensate for the aberrations of the optical system. The DM consists of a flexible reflective surface supported by piezoelectric, magnetic, or electrostatic actuators (Roddier 1999; Madec 2012). By applying voltages to these actuators, the mirror's shape can be dynamically adjusted, altering the optical path difference and compensating for the system's aberrations. Commonly, the DM is located in the main optical path of the system and its reflective coating is usually chosen to provide good optical performance for the different wavelengths considered so that both the imaging path and the WFS path can benefit from its correction.

The DM is usually characterised by its set of influence functions that correspond to the DM surface resulting from the actuation of each individual actuator. The influence functions correspond to a modal basis (commonly refereed as zonal modal basis) that captures all the degrees of freedom of the DM. As such, the phase applied to the DM can be decomposed as a linear combination of actuator coefficients using the same equation as 1.13

$$\phi^{cor} = Nu, \tag{1.41}$$

where N is the influence matrix that characterises the influence functions f_i and u the voltage command vector. For a modal control of the phase, each column of N is the decomposition of f_i on the modal basis (Roddier 1999).

The key characteristics of a DM are its actuator density, its stroke - the maximum movement amplitude per actuator - and its temporal response. The actuator density will define the maximal spatial frequency that can be corrected (or in other words, the number of corrected modes). We call pitch the separation between actuators d_{act}. The spatial region, in the focal plane, where the AO correction is effective is limited. Considering a DM whose actuators are placed in a Cartesian grid (square grid) with $n_a \times n_a$ actuator, the corrected area in the focal plane is a square zone of edge $n_a \times \lambda/D$.

The mechanical stroke of a DM depends on the expected level of turbulence detected by the AO system. Since turbulence strength remains unpredictable, both the AO system and the DM are typically engineered to handle worst-case scenarios. The typical stoke needed to correct for atmospheric turbulence is in the order of magnitude of a few μm. However, a considerable portion of atmospheric turbulence energy is concentrated in low-order modes (see Kolmogorov spectrum of the atmospheric turbulence in the previous section), and especially in Tip/Tilt modes. Addressing atmospheric Tip/Tilt using the DM would require a substantial stroke, potentially impeding its ability to effectively compensate for higher-order modes. Hence, it is common to use a dedicated mirror specifically designed for Tip/Tilt correction, thereby allowing the DM to prioritise higher-order mode correction (cf SPHERE instrument (Fusco et al. 2006; Beuzit et al. 2008)). This is typically used in order to facilitate Tip/Tilt offsets between the science and AO.

1.2.2 Wavefront Sensor

The WFS is an optical device that aims to measure the wavefront. In the VIS and in the NIR, there is no detector/technology capable of directly measuring the phase of the EM field because the temporal frequencies are too high. It is therefore necessary to encode the phase information of the incoming EM field into intensity information on the detector that can be processed rapidly. Different WFS concepts have been proposed to provide the indirect measurement of the wave-front and new concepts are regularly introduced by the community to benefit from new technological progresses.

The choice of the WFS concept usually results from a trade-off to minimize the AO residual error (see section 1.2.4). In this section, we first introduce the notion of sensitivity and dynamic of a WFS as the most common metrics to characterise and compare different WFS concepts. Then, in a second time, we present the most common concepts of WFS, the Shack-Hartmann (SH) and the Fourier Filtering WaveFront Sensor (FF-WFS) that are currently the baseline to equip the future SCAO systems of the next generation of telescopes.

1.2.2.1 Sensitivity and Dynamic of a WFS

This section aims at providing a first global definition of the two main metrics used to characterise a WFS. The specificity of the different WFS concepts requires to complement these general definition and will be detailed in the dedicated sections

(see section 1.4.1). In this section we assume that a WFS intensity is a function of the input phase that follows the curve presented in Figure 1.14. This figure is used for illustration purpose only to define the different metrics introduced in the section and does not correspond to a real WFS system.

Sensitivity : The sensitivity describes the robustness of the phase reconstruction in the presence of noise. In eXtrem Adaptive Optics (XAO), it is important to use extremely sensitive WFS as they will provide a better estimation of the wavefront in the low flux regime, increasing the sky coverage (targeting fainter guide stars) and/or the speeds of the AO loop. Indeed, XAO systems operate at very high speed (> 1kHz), with a reduced the number of photons per frame, thus reducing the Signal to Noise Ratio (SNR). The different sources of noise are :

— **Photon noise :** Comes from the quantum nature of light. It follows a Poisson distribution of mean $E(N) = \alpha\Delta t$ and a standard deviation of $\sigma(N) = \sqrt{\alpha\Delta t}$, where Δt is the integration time per pixel and α is proportional to the flux of the source. In the case of photon noise, the SNR is proportional to $\sqrt{N}$, with N the number of photons. To increase the SNR one has to collect more photons, by increasing the size of the telescope or increasing the integration time of the detector.

— **Read-Out-Noise :** is a uniform noise generated by the electronic circuit which converts the stored charge of each pixel into an analogue voltage to be quantified by A/D conversion. This noise depends on the characteristics of the detector and its electronics. It is expressed in electron RMS per pixel and per frame ($e^-/pix/frame$). For the best cameras (EMCCD in the visible and APD in the IR), RON can be lower than $1e^-/pix/frame$.

In Fig.1.14, an example of the WFS's response to the incoming wavefront is provided. The sensitivity can be defined as the level of intensity variations, with a change in phase, in other words, it is the slope of the dashed curve represented in violet. The higher the slope, the more a small phase change will induce a large intensity variation in the detector plane.

Linearity : The linearity or dynamical range describes the phase regime where the relationship between the intensity and the incoming phase is linear. In fig.1.14, the linear regime is delimited by the vertical green lines. Outside this phase range, the intensities are no longer linear with the wavefront. The system is no longer bijective (one intensity for one and only one phase amplitude), might be saturating, which will lead to phase estimation errors when using linear phase reconstruction algorithms.

To choose the WFS of an AO system, the sensitivity and the linear range of the sensor are the main important characteristics one has to take into account. It will be driven by the scientific case. In the next paragraphs, we will introduced the Shack-Hartmann (SH), the historical WFS in AO and the new generation of WFS, more sensitives than the SH : Fourier Filtering WaveFront Sensor (FF-WFS).

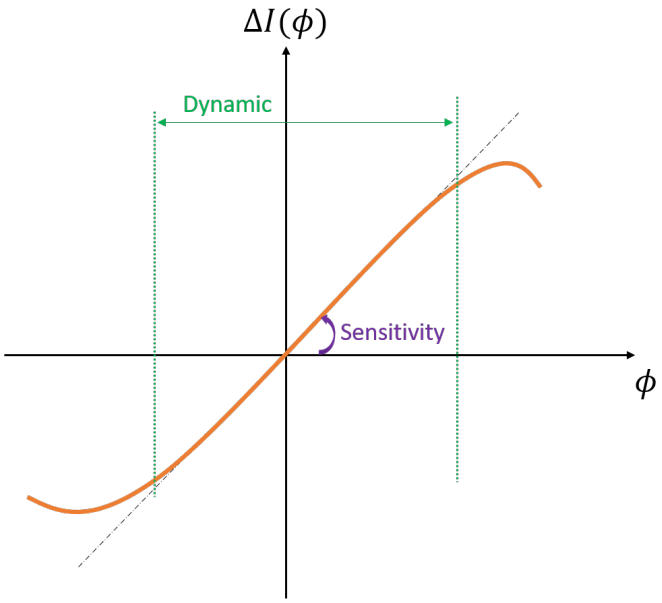

FIGURE 1.14 – Illustrative representation of the WFS's response ΔI to the incoming phase ϕ. The linear range is represented by the green verticals lines and the horizontal arrow, the sensitivity by the slope of the curve.

1.2.2.2 Shack-Hartman WFS

The Shack-Hartman (SH), (Shack 1971) is the most commonly used WFS in AO. It is composed of a micro-lens array positioned at the pupil plane, where each micro-lens defines a sub-aperture. Subsequently, a detector is employed to capture the PSF of each micro-lens.

Processing of the SH signals : By measuring the displacement of the PSF's centre of gravity, the local slope of the wavefront as perceived by the micro-lens can be determined. This measurement is proportional to the local slopes of the phase and thus, by using an integration process (cf equation1.42) it can give access to the phase itself.

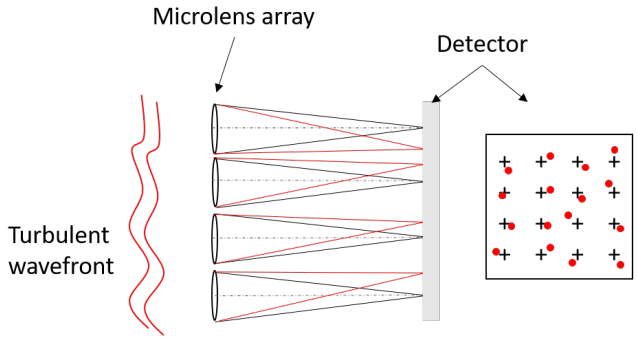

FIGURE 1.15 – Schematic of the Shack-Hartmann.

$$\alpha_x = \frac{d_x}{Gf} = \frac{\lambda}{2\pi f S_{subap}} \int_{subap} \frac{\partial \phi}{\partial x} \mathrm{d}x\mathrm{d}y, \tag{1.42}$$

$$\alpha_y = \frac{d_y}{Gf} = \frac{\lambda}{2\pi f S_{subap}} \int_{subap} \frac{\partial \phi}{\partial y} \mathrm{d}x\mathrm{d}y, \tag{1.43}$$

where S_{subap} the surface of the sub-aperture, f the focal length of the micro-lens, G the angular magnification and (d_x, d_y) the centre of gravity the image. The choice of the focal lens of the micro-lenses enable the adjustment of the dynamic and the sensitivity of the SHWFS.

The centre of gravity of the images is given by

$$d_x = \frac{\sum_{i,j} I(,i,j) x_{i,j}}{\sum_{i,j} I(i,j)}, \tag{1.44}$$

$$d_y = \frac{\sum_{i,j} I(,i,j) y_{i,j}}{\sum_{i,j} I(i,j)}, \tag{1.45}$$

where $I(i,j)$ is the intensity value of the pixel of coordinates $(x_{i,j}, y_{i,j})$. Other centroiding algorithms exist that are more robust to noise such as the thresholded centre of gravity or the weighted centre of gravity where respectively, the pixel intensities under a given threshold are not considered in the measurement. The choice of the centroiding algorithm also has an impact on the linearity and the sensitivity (defined in more detailed in section1.4) of the SH, (Nicolle et al. 2004; Nicolle 2006; Thomas et al. 2006; Basden et al. 2012).

Despite the success of the SH, this WFS exhibits a few limitations. The sub-division of the pupil plane into sub-aperture used by the SH brings a lot of constraints. Indeed, to probe more spatial frequencies, the SH requires more micro-lenses, which will limit the SNR per sub-aperture. This also leads to a smaller displacement of centres of gravity (smaller sensitivity). This limits the SNR, thus limiting the guide star magnitude of the AO system.

1.2.2.3 Fourier Filtering WFS

The concept of Fourier Filtering WaveFront Sensor (FF-WFS) constitutes an alternative to the SH as it allows to compress the information on fewer pixels. The concept of Fourier filtering consists in adding a mask in the intermediate focal plane to apply a filtering of the EM field and to re-image the pupil plane on a detector (Goodman 2005). A schematic of a FFWFS is provided in Fig.1.16. These type of WFS do not rely on the displacement of the centre of gravity as the sensing is happening on the pupil plane, hence increasing the sensitivity of the WFS.

To understand the concept of FFWFS, let's start again from the propagation equations from section 1.1 to obtain the following expressions. The EM field arriving in the

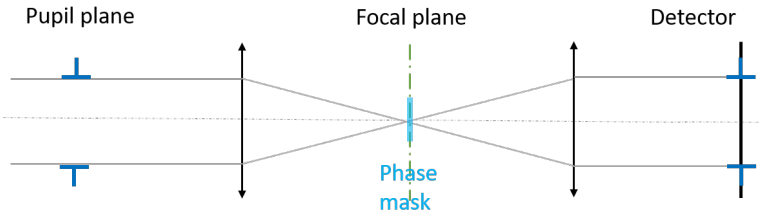

FIGURE 1.16 – Schematic of the Fourier Filtering concept.

focal plane where the mask is located is the Fourier transform of the incoming EM field

$$\psi_- = \mathscr{F}(\psi_{in}). \tag{1.46}$$

We call t the mask transmission function. t can be a complex function and its module is inferior to one $|t| \leq 1$ (*e.g.* no energy created). The EM field after the mask is

$$\psi_+ = \mathscr{F}(\psi_{in}) \times t. \tag{1.47}$$

Then the EM field on the detector is the Fourier transform of ψ_+

$$\begin{aligned} \psi_{det} &= \mathscr{F}(\psi_+) \\ &= \psi_{in} * \mathscr{F}(t), \end{aligned} \tag{1.48}$$

where $*$ stands for the convolution product.

As a summary :

$$\psi_{in} \longrightarrow \psi_+ = \mathscr{F}(\psi_{in}) \times t \longrightarrow \psi_{det} = \psi_{in} * \mathscr{F}(t)$$

The intensity on the last pupil plane, i.e., on the detector is

$$I = |\psi_{det}|^2 = |\psi_{in} * \mathscr{F}(t)|^2, \tag{1.49}$$

where the EM field on the detector ψ_{det}, is the input EM field ψ_{in} filtered by the mask t on the focal plane. Adding a mask in the focal plane enables it to act directly on the frequency information of the input field.

Equation 1.49 is the fundamental equation when considering FF-WFS. The expression of the intensity on the detector will differ only from the expression of the transmission function t. A complete analysis of FF-WFS has been done by Fauvarque (2017). The next sections present two of the most common example of FFWFS, the Pyramid WFS and the Zernike WFS.

1.2.2.4 Pyramid WFS

The Pyramid WaveFront Sensor (PWFS) is a FF-WFS that involves placing a 4-sided glass pyramid in the focal plane to perform the filtering of the EM field. It was introduced in 1996 by (Ragazzoni 1996) as a solution to achieve high performances in terms of correction and sensitivity and was implemented on sky in the Adaptive Optics for the Telescopio Nazionale Galileo module in 2003, (Ghedina et al. 2003).

The various on-sky demonstrations of the PWFS at the Large Binocular Telescope (Tozzi et al. 2008), at Subaru telescope (Guyon et al. 2011) and at Keck (Bond et al. 2018), to name only a few, led most of the first light instruments of the ELT to use a PWFS for the SCAO module : HARMONI (Fusco et al. 2010; Schnetler et al. 2022), METIS (Bertram et al. 2018, 2023) or MICADO (Davies et al. 2016; Clénet et al. 2019).

Processing of the PWFS signals : The PWFS is a Fourier-type WFS whose principle was derived from the Foucault-knife edge experiment (Ragazzoni 1996). The schematic of the PWFS is shown in Fig1.17. The pyramid is a transparent glass pyramid located in the focal plane (see Fig1.16).

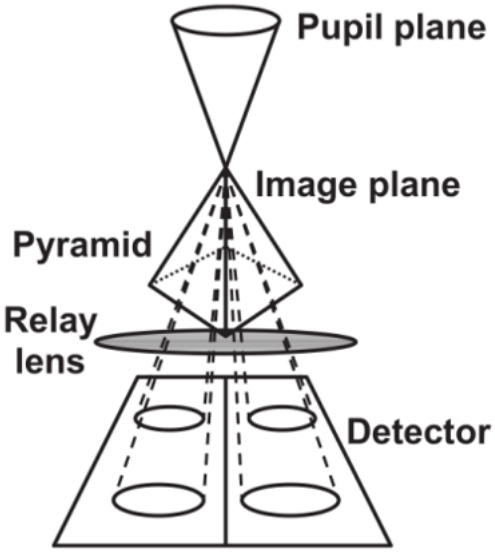

FIGURE 1.17 – PWFS schematic, *Credits : (Crass 2014)*

The equation of propagation are the same as the one derived in the previous section for FF-WFS. The intensity on the detector can be expressed as equation 1.49. The pyramid transmission function can be expressed as follows

$$t(x,y) = \exp\left(\frac{2i\pi}{\lambda}\alpha(|x|+|y|)\right), \tag{1.50}$$

where the angle of the faces, α controls the separation of the images on the detector

and (x, y) the spatial coordinates.

Different techniques can be used for the post-processing of the PWFS signals. The initial approach suggested by (Ragazzoni 1996) was a quad-cell approach to compute the slopes

$$S_x(x,y) = \frac{I_1(x,y) - I_2(x,y) + I_4(x,y) - I_3(x,y)}{I_{tot}(x,y)}, \tag{1.51}$$

$$S_y(x,y) = \frac{I_1(x,y) - I_4(x,y) + I_2(x,y) - I_3(x,y)}{I_{tot}(x,y)}, \tag{1.52}$$

where $I_{tot} = I_1(x,y) + I_2(x,y) + I_4(x,y) + I_3(x,y)$.

An alternative to the slopes approach is to use the reduced intensities for post-processing that is based directly on the intensity pattern on the detector. The advantage of this approach is that it provides the same mathematical formalism for all the FF-WFS without taking into account any combination of intensity pattern of the mask, (Fauvarque 2017), especially when changing the number of faces of the pyramid for instance, (Deo et al. 2018; Chambouleyron 2021). The reduced intensity is by definition

$$\begin{aligned} \Delta I(\delta\phi, \phi_r) &= I(\phi) - I(\phi_r) \\ &= I(\delta\phi + \phi_r) - I(\phi_r), \end{aligned} \tag{1.53}$$

where $\phi = \phi_r + \delta\phi$ is the incoming phase, ϕ_r is the reference wavefront and $\delta\phi$ is the phase to be measured.

Considering a PWFS with a modulation stage (explanation in the next paragraph) and using equation 1.49 the intensity can also be expressed following the notation in Fauvarque et al. (2016, 2019)

$$I(\phi_r + \delta\phi)|_{\vec{\mathbf{R}}} = \int_{\mathbb{R}^4} \mathbb{I}_P|_{\vec{\mathbf{r}}'} \mathbb{I}_P|_{\vec{\mathbf{r}}} e^{\imath(\phi_r|_{\vec{\mathbf{r}}'} - \phi_r|_{\vec{\mathbf{r}}})} \mathscr{F}(t)|_{\vec{\mathbf{R}}-\vec{\mathbf{r}}'} \bar{\mathscr{F}}(t)|_{\vec{\mathbf{R}}-\vec{\mathbf{r}}} \mathscr{F}(w)|_{\vec{\mathbf{r}}'-\vec{\mathbf{r}}} \, e^{\imath(\delta\phi|_{\vec{\mathbf{r}}'} - \delta\phi|_{\vec{\mathbf{r}}})} \, \mathrm{d}^2\vec{\mathbf{r}}'\mathrm{d}^2\vec{\mathbf{r}}, \tag{1.54}$$

where $\bar{x}$ stands for the conjugation of x and w is the modulation weight function. For energy conservation, $\int w(\alpha)\mathrm{d}^2\vec{\boldsymbol{\alpha}} = 1$. $\vec{\mathbf{r}}'$, $\vec{\mathbf{r}}$ and $\vec{\mathbf{R}}$ are the 2D spatial variables, respectively in the entrance pupil plane and on the detector plane.

which leads to

$$\Delta I(\delta\phi, \phi_r)|_{\vec{\mathbf{R}}} = \int_{\mathbb{R}^4} \mathbb{I}_P|_{\vec{\mathbf{r}}'} \mathbb{I}_P|_{\vec{\mathbf{r}}} e^{\imath(\phi_r|_{\vec{\mathbf{r}}'} - \phi_r|_{\vec{\mathbf{r}}})} \mathscr{F}(t)|_{\vec{\mathbf{R}}-\vec{\mathbf{r}}'} \bar{\mathscr{F}}(t)|_{\vec{\mathbf{R}}-\vec{\mathbf{r}}} \mathscr{F}(w)|_{\vec{\mathbf{r}}'-\vec{\mathbf{r}}} \left(e^{\imath(\delta\phi|_{\vec{\mathbf{r}}'} - \delta\phi|_{\vec{\mathbf{r}}})} - 1 \right) \, \mathrm{d}^2\vec{\mathbf{r}}'\mathrm{d}^2\vec{\mathbf{r}}. \tag{1.55}$$

The need of coupling the PWFS with TT modulation : The PWFS is often used with a modulation step in the pupil plane to move the PSF to different positions in the focal plane. The modulation increases the range of phase amplitudes the WFS can measure. Indeed, the PWFS can measure aberrations when the distribution of the intensity signal changes from one sub-pupils to the other. The amount of light collected by one sub-pupil is given by the amount of light that reaches the glass prism related face. In this manner, if we consider a the situation without any aberration of the optical path, all the faces of the PWFS receive the same amount of light because the PSF is centred on top of the PWFS. If now we consider a tip/tilt aberration, the PSF will move in one direction, which will lead to a one sub-pupil I_i having more light than the others. If we increase the amplitude of this aberration, the PSF will be only on one face on the prism $I_{j\neq i} = 0$. If we keep increasing the amplitude of this aberrations, the PSF will still be on the same face of the pyramid leading to the same situation as before, no light reached the other face $I_{j\neq i} = 0$. This example is illustrated in Fig1.18, when looking at the detector image, the third and the fourth image are the same : the WFS is saturating. The saturation of the signal, illustrated in Fig1.18, prevents the use of the PWFS to measure large phase amplitude. In particular it is not usable on sky with the classical inversion technique described the in following section 1.2.3.1.

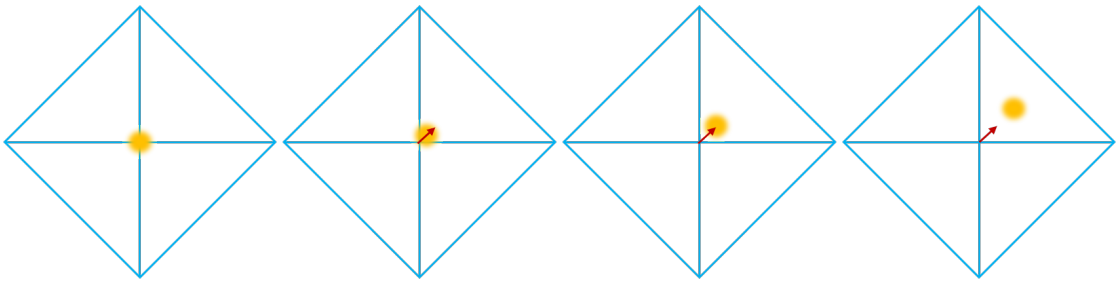

FIGURE 1.18 – Non-modulated PWFS illustration of the saturation. From left to right increasing amplitude of a tip/tilt aberration.

To overcome this difficulty, Ragazzoni (1996) suggested to add the spatial oscillation of the prism in the focal plane. The prism is oscillating in a circular or square pattern which allows to artificially delay the saturation of the WFS. Another way to obtained exactly the same result consists in using a circular modulation in the pupil plane,(Esposito & Riccardi 2001) so the PSF moves in a circle on top of the PWFS. For the PSF to describe a circle, a known tip/tilt aberration is introduced in the pupil plane, this way the PSF is sent in each direction. The detector integration time is synchronised with the modulation so that one frame corresponds to a PSF describing an entire modulation circle. This modulation is inextricably linked with the use of the PWFS.

We now consider a modulated PWFS whose modulation angular radius is θ, the slopes computation can be linked with the wavefront gradient and the modulation radius by (Vérinaud 2004)

$$S_x(x,y) \sim \frac{\lambda}{\pi^2\theta}\frac{\partial\phi}{\partial x}. \tag{1.56}$$

This modulation step allows to delay the saturation regime consequently increasing the range of phase amplitude the WFS can measure. Indeed, following the same argument as for the non-modulated PWFS, if we consider a tip/tilt aberration, a bigger phase amplitude is required to put the entire modulated PSF on one face of the prism, see Fig1.19, the third and the forth image on the detector are no longer the same.

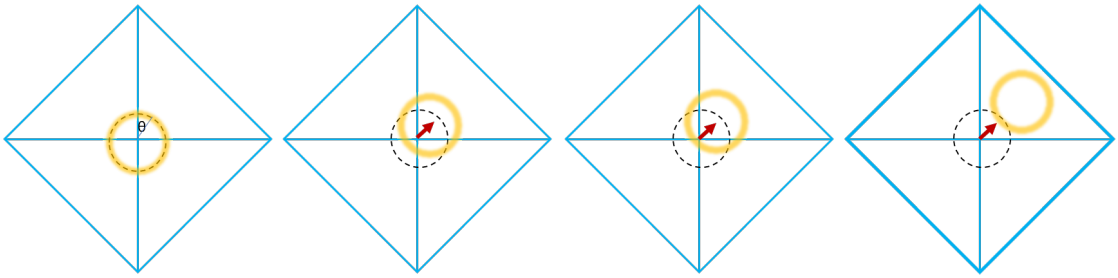

FIGURE 1.19 – Modulated PWFS illustration of the saturation. From left to right increasing amplitude of a tip/tilt aberration.

The modulation of the pyramid makes possible its use for on-sky operation under different seeing conditions. Yet, this modulation stage reduces the sensitivity of the PWFS. Indeed, following the same example, the same tip/tilt variation will not produce the same intensity variation with or without modulation. This is illustrated in Fig.1.20. In the case of the modulated PWFS, the signal is linear with the phase over a larger range, but the slope is smaller in comparison to the case without modulation (blue curve).

Furthermore, all the spatial frequencies are not affected the same way by the modulation. Let's consider a 2-sided prism for clarity. This will explain the behaviour of the 4-sided prism along one direction. The incoming wavefront is a pure sine wave of frequency ν, the WFS is sensitive to this spatial frequency only if the replica of the PSF are divided in the two faces of the prism. Now, let's add a modulation step. Two cases have to be considered, the case where the spatial frequency of the wave is within the modulation circle and the case where it is outside. In the first case, the signal variation will occur in the modulated image because it depends on the time each replica spend on each face. Now in the other case, where the spatial frequency is higher than the modulation circle, each replica will describe a circle on its own face hence the signal won't be modified. Despite the modulation the spatial frequency remains poorly measured since the WFS signal will be the same whatever its amplitude (Chambouleyron 2021).

1.2.2.5 Zernike WFS

The principle was introduced by Fritz Zernike for phase contrast in microscopy in 1934 and was awarded by the Nobel price in 1953 (Zernike 1934). It consists in creating interference between a reference beam and the incoming wavefront. In AO there is no direct reference beam because all the light coming from the point source suffers from the propagation in the atmosphere. To overcome this lack of reference

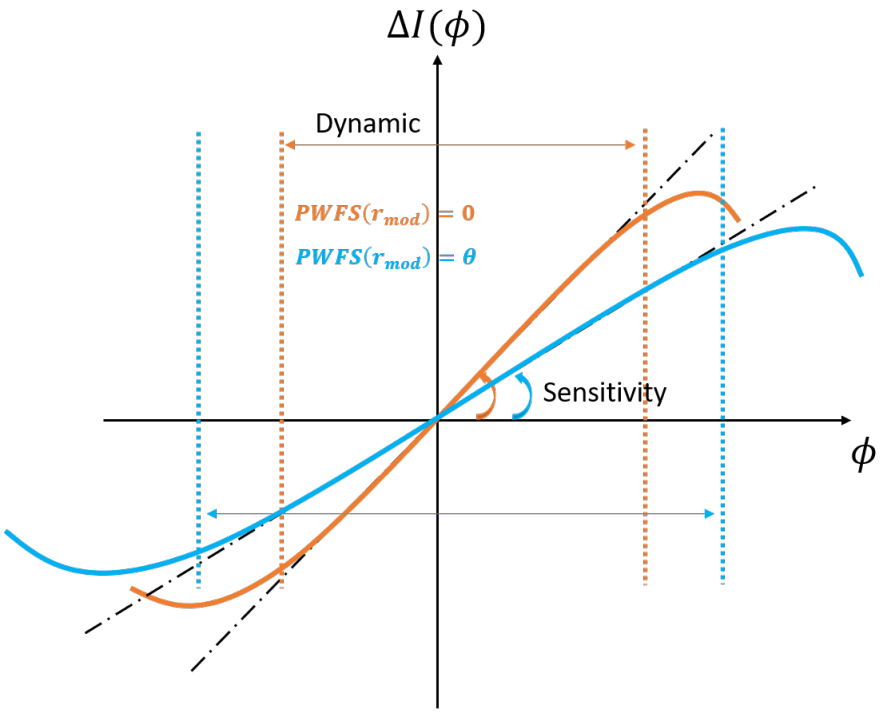

FIGURE 1.20 – 1-Dimension representation of the WFS's response to the incoming phase. Orange curve non-modulated PWFS and blue curve modulated PWFS. The linear response is represented by the orange and cyan verticals lines and the horizontal arrows respectively for the non-modulated and the modulated PWFS, and the sensitivity by the slope of the curves.

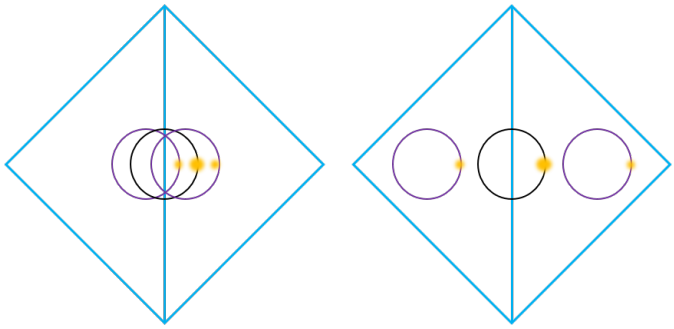

FIGURE 1.21 – Impact of the modulation on the spatial frequency of an incoming wave, illustration with a 2-sided prism. Left : spatial frequency ν inside the modulation radius. Right : spatial frequency ν outside the modulation radius

beam, a transparent dot creating a phase shift of $\pi/2$ is placed in the focal plane. In this manner, the reference beam is the diffracted light coming from the PSF core, hence, it has been spatially filtered out from upstream aberrations. Then this beam will interfere with the light coming from the external part of the PSF that contains the phase information of the incoming wavefront. The $\pi/2$ shift ensures constructive inter-

ferences that will encode the phase signal. This phase mask combined with a detector directly located in the following pupil plane is the Zernike WaveFront Sensor (ZWFS). The study of the phase mask is at the heart of this manuscript as part of my work aimed at increasing the dynamic range of Zernike-type WFS - more details in chapter2.

The intensity on the detector is the result of the interference between two EM fields : the reference beam u_1 and the measurement u_2. u_1 and u_2 can also be interpreted as respectively the low-frequency and the high-frequency component of the EM field.

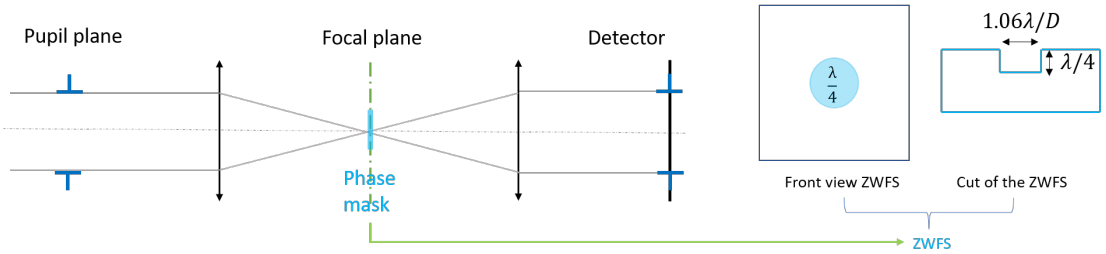

FIGURE 1.22 – Schematic of the ZWFS

Processing of the ZWFS signals : *The equations presented in this section are coming from Steeves et al. (2020) whose results are based on the work done by Dohlen et al. (2006) and N'Diaye et al. (2013).*

The ZWFS is a phase mask in the focal plane which consists of a dimple whose size is of the order of the diameter of the PSF, i.e $1.06\lambda/D$, introducing a phase-shift of $\pi/2$, (N'Diaye et al. 2013). To introduce a phase shift of $\pi/2$, the mask has a depth of $\lambda/4$ (cf Fig.1.22). This way, the phase mask filters out the aberrated signal of the EM field creating the reference beam. The result is an interference between u_2, the high spatial frequency of the EM field not affected by the phase mask, and u_1, the low spatial frequency affected by the phase mask.

We rewrite the equation of the propagation in the case of a ZWFS

$$u(\mathbf{r}) = \mathbb{I}_p(\mathbf{r})\, A_0 e^{i\phi(\mathbf{r})}, \tag{1.57}$$

where $u(\mathbf{r})$ is the EM field in the pupil plane, A_0 is the average amplitude of the EM field, $\mathbb{I}_p$ the pupil transmission function and ϕ the phase to be measured.

The EM field propagates towards the focal plane where the ZWFS is located. The EM field before the mask is the Fourier transform of the field in the pupil plane as in equation 1.46.

The ZWFS transmission function is the well-known hat function

$$M(\mathbf{r}) = \begin{cases} 1 & \text{if } |\mathbf{r}| < \frac{a}{2} \\ 0 & \text{otherwise.} \end{cases} \tag{1.58}$$

The total expression of the phase mask is therefore

$$t = 1 - (1 - e^{i\theta})M, \tag{1.59}$$

where θ is the phase-shift of the phase mask.

The EM field after the phase mask is the Fourier transform of the incoming EM field multiply by the phase mask (cf equation 1.47)

$$u_+(\epsilon) = \mathscr{F}(u_-)(\epsilon)(1 - M) + \mathscr{F}(u_-)(\epsilon)Me^{i\theta}. \tag{1.60}$$

The EM field on the detector is the Fourier transform of the EM field in the previous focal plane (cf equation 1.48)

$$\begin{aligned} u_{det}(\mathbf{r}) &= \mathscr{F}(u_+) \\ &= A_0 P(\mathbf{r}) e^{i\phi(\mathbf{r})} - A_0 b(\mathbf{r}) e^{i\beta(\mathbf{r})} + A_0 b(\mathbf{r}) e^{i\beta(\mathbf{r})} e^{i\theta}, \end{aligned} \tag{1.61}$$

where $b(\mathbf{r})$ and $\beta(\mathbf{r})$ are the amplitude and the phase of the low spatial frequency of the EM field. We can name $u_2(\mathbf{r}) = A_0 \mathbb{I}_p(\mathbf{r}) e^{i\phi(\mathbf{r})} - A_0 b(\mathbf{r}) e^{i\beta(\mathbf{r})}$ the high spatial frequency EM field and $u_1(\mathbf{r}) = A_0 b(\mathbf{r}) e^{i\beta(\mathbf{r})} e^{i\theta}$ the low spatial frequency EM field.

The intensity on the detector is the modulus square of the EM field on the detector (cf equation 1.49)

$$\begin{aligned} I(\mathbf{r}) &= |u_1(\mathbf{r}) + u_2(\mathbf{r})|^2 \\ &= A_0^2 \left(\mathbb{I}_p^2 + 4b^2 sin^2(\theta/2) + 4\mathbb{I}_p b sin\left(\phi - \beta - \frac{\theta}{2}\right) sin(\theta/2) \right). \end{aligned} \tag{1.62}$$

By naming $I_p = A_0^2 \mathbb{I}_p^2$ and $I_b = A_0^2 b^2$ we get

$$I(\mathbf{r}) = I_p + 4I_b sin^2(\theta/2) + 4\sqrt{I_p I_b} sin\left(\phi - \beta - \frac{\theta}{2}\right) sin(\theta/2). \tag{1.63}$$

Note that the Zernike-type WFS used in the whole manuscript is simulated as a 2-Dimension vector, the size of the dimple is linked to the size of the PSF's core size so it depends on the Shannon sampling. As a reminder, at Shannon sampling, the PSF core fits within square of 2 pixels side, so the associated ZWFS with a dimple size of λ/D will also fits within a square of 2 pixels side. For instance, the simulation of the Zernike mask in this manuscript where done using a sampling factor of 4 so for dimple size of λ/D, the mask fits within a square of 8 pixels diameter.

The variables β and I_b come from the part of the EM that has been spatially filtered by the phase mask. β and I_b correspond respectively to the wavefront and the intensity of the "reference" EM field, i.e., the portion of the EM field that pass through the ZWFS. $\beta = 0$ in first approximation and I_b is the intensity we get on the detector if instead of

having a phase mask in the focal plane we put an amplitude mask of the same size as the ZWFS. I_p is the intensity measurement of the pupil without the phase mask. In simulation, we can easily get these three terms (cf Fig.1.23). I_p is equal to the pupil itself.

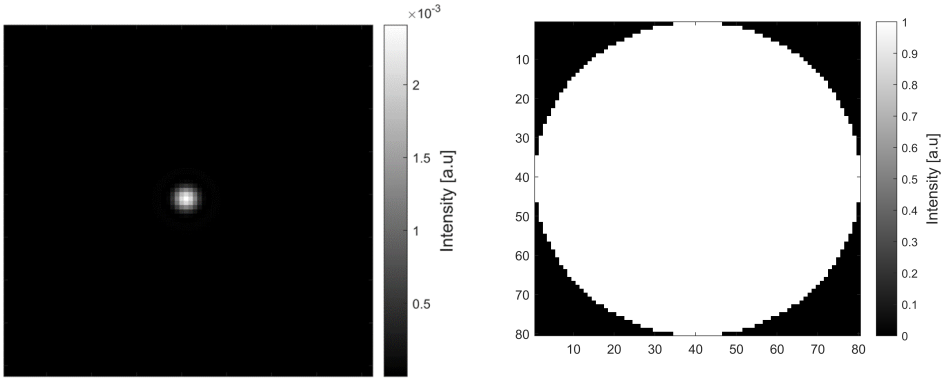

(a) I_b (b) I_p

FIGURE 1.23 – Different terms of the ZWFS equations obtained for a Zernike mask of $1.06\lambda/D$. (a) Reference intensity and (b) Intensity obtained without the ZWFS in the focal plane (Pupil image).

The reduced intensity is obtained by subtracting the reference intensity I_{ref}. We give the expression of the reference intensity considering a flat reference wavefront $\phi_r = 0$

$$I_{ref} = I(\phi(\mathbf{r}) = 0) = I_p + 4I_b sin^2(\theta/2) - 4\sqrt{I_p I_b} sin\left(+\beta + \frac{\theta}{2}\right) sin(\theta/2). \tag{1.64}$$

Hence, the reduced intensity is

$$\begin{aligned} \Delta I(\phi(\mathbf{r})) &= I(\phi(\mathbf{r})) - I_{ref} \\ &= 4\sqrt{I_p I_b} sin(\theta/2)[sin(\phi - \beta - \theta/2) + sin(\beta + \theta/2)]. \end{aligned} \tag{1.65}$$

With a classical Zernike mask $\theta = \pi/2$ and by making the following hypotheses : (i) the phase of the reference beam is null $\beta = 0$, (ii) $b = 1/2$ with a phase mask of diameter $1.06\lambda/D$, (N'Diaye et al. 2013), the expression of the intensity becomes

$$I(\mathbf{r}) = A_0^2 \mathbb{I}_p^2 + \frac{1}{2} A_0^2 + \sqrt{2} A_0^2 \mathbb{I}_p sin\left(\phi - \frac{\pi}{4}\right). \tag{1.66}$$

In this context, the reference intensity becomes (cf equation 1.64)

$$I_{ref}(\mathbf{r}) = \frac{1}{2} A_0^2, \tag{1.67}$$

since $\mathbb{I}_p = \mathbb{I}_p^2$ as $\mathbb{I}_p$ is the pupil transmission function.

It is interesting to study the evolution of the intensity with the wavefront. The expression given in 1.66 predicts a sine evolution of the wavefront not centred at zero due to the phase shift of $\pi/4$ in the sine. To plot the intensity as a function of the wavefront, we use the small phase approximation and a perfect PSF. We will only modify the phase of one pixel in the pupil plane, this way the PSF shape will not change. Figure 1.24 validates the sine response of the intensity with the wavefront. It also shows that the response of the ZWFS is not symmetric and the bijective regime of the phase mask is very limited. The asymmetric response and the limited bijective regime of the ZWFS will have an impact on the linear range of the phase mask. A method to increase the linear range of Zernike type sensors will be discuss in chapter 2, section 2.1.

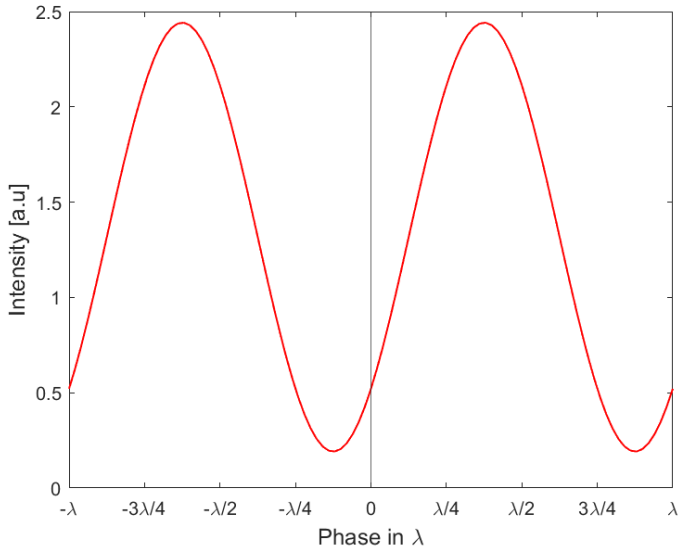

FIGURE 1.24 – Intensity as a function of the phase

From the expression of the intensity (equation 1.63) one can also exhibit a linear reconstructor that will provide a proper phase estimation in the small phase regime

$$\phi = \frac{1}{cos\left(\beta+\frac{\theta}{2}\right)}\left(sin\left(\beta+\frac{\theta}{2}\right)+\frac{I(x)-I_p-4I_b sin^2(\theta/2)}{4\sqrt{I_p I_b}sin(\theta/2)}\right), \tag{1.68}$$

$$\phi = \frac{1}{cos\left(\beta+\frac{\pi}{4}\right)}\left(sin\left(\beta+\frac{\pi}{4}\right)+\frac{I(x)-I_p-2I_b}{2\sqrt{2I_p I_b}}\right), \text{ if } \theta=\pi/2. \tag{1.69}$$

Also from equation 1.63 and Fig.1.24, one can build a non-linear reconstructor using the $arcsine$ function

$$sin\left(\phi-\beta-\frac{\theta}{2}\right) = \frac{I(\mathbf{r})-I_p-4I_b sin^2(\theta/2)}{4\sqrt{I_p I_b}sin(\theta/2)}, \tag{1.70}$$

$$\phi-\beta = \frac{\theta}{2}+arcsin\left(\frac{I(\mathbf{r})-I_p-4I_b sin^2(\theta/2)}{4\sqrt{I_p I_b}sin(\theta/2)}\right). \tag{1.71}$$

For the classical ZWFS with $\theta=\pi/2$, the non-linear reconstructor can be written

$$\phi-\beta=\frac{\pi}{4}+arcsin\left(\frac{I(\mathbf{r})-I_p-2I_b}{2\sqrt{2I_p I_b}}\right). \tag{1.72}$$

By taking $\beta=0$, which means that the phase of the reference EM field is equal to zero, this reconstructor will provide an accurate phase estimation in the range $\phi\in\left[\frac{-\pi}{4};\frac{3\pi}{4}\right]$ Peak-To-Valley (PV).

1.2.2.6 Conclusion on WFS :

This sub-section introduced several WFS concepts used in AO. The WFS is the key element of the AO system as it measures the aberrations that need to be corrected. In this section we introduced first concept of sensitivity and dynamic of a WFS that drive the choice of a WFS. We then introduced the SH : WFS widely used in AO for its simplicity and robustness. Finally, we introduced the FF-WFS as another method to measure the wavefront. In that case, the measurement is done thanks to an optical element located in the focal plane to encode the phase of the incoming EM field into intensity on the detector. This sensing method is very versatile and has recently being fully mathematically formalised in Fauvarque (2017).

From the expression of the intensity on the detector, one can directly notice that the intensities are not linear with the wavefront (see equations 1.55 and 1.63). FF-WFS and especially the PWFS and the ZWFS are intrinsically non-linear with the wavefront. This inherent non-linear behaviour is the main challenge one has to face when using these sensors, in particular when using the classical control method that will be introduced in the following section 1.2.3.1.

1.2.3 Reconstruction and control of the wavefront in an Adaptive Optics system

The last block of the AO system is the RTC that links the DM and the WFS. The control of the AO loop has to take into consideration both the spatial wavefront reconstruction and the temporal aspect to maximise the performances of the AO system.

1.2.3.1 Spatial wavefront reconstruction

The measurement chain can be described as follows : the incident phase enters the WFS optical system. The EM field propagates through the optical system before being detected by the 2D sensor. During the detection process, noise (read noise, photon noise, etc.) may be added to the signal; the sum "signal plus noise", which is now a digital quantity, passes through a numerical operator, the reconstructor **R**, which inverts it and provides an estimation of the phase. The reconstructor **R** is assumed to be linear in order to met the real time constraints of an AO system. Mathematically, this process can be formulated as follows

$$\begin{aligned} s &= \mathbf{h}(\phi) + \text{Noise}, && (1.73)\\ \hat{\phi} &= \mathbf{R}[\mathbf{h}(\phi) + \text{Noise}], && (1.74) \end{aligned}$$

where s is the WFS signal and $\mathbf{h}$ is a function of ϕ the phase and $\hat{\phi}$ the estimated phase.

Assuming a linear operator, the error of estimation will be

$$\begin{aligned} \epsilon &= \hat{\phi} - \phi \\ &= \mathbf{R}[\text{Noise}] + (\mathbf{R}[\mathbf{h}(\phi)] - \mathbf{Identity}[\phi]). \end{aligned} \quad (1.75)$$

If the function h is invertible then

$$\mathbf{R} = \mathbf{h}^{-1} \longrightarrow \mathbf{Rh} = \mathbf{Identity}. \quad (1.76)$$

In that case, the only source of error is the noise propagation through the reconstructor. The noise propagation has been extensively studied in the literature (Guyon 2005; Rigaut & Gendron 1992) and is related to the WFS sensitivity, which must be maximised (Chambouleyron et al. 2021a; Fauvarque et al. 2015).

Interaction matrix : Most of the AO systems calibrate the system DM/WFS to be as close as possible to the real optical system, so to describe the path of the incoming wavefront. The main purpose of the AO control loop is to convert the measurements from the WFS into the deformations to be applied to the DM. These conversions have to be carried out very quickly (typically milliseconds rate), and most of the time we are in closed loop configuration, where the WFS is located downstream of the DM and therefore only measures the phase residuals uncorrected at the previous iteration. The calibration process supposes a linear relation between the wavefront on the DM and the signal on the WFS detector. It is done as follow : the actuators of the DM are activated sequentially to collect their response through the WFS. These responses are combined into a matrix called the "interaction matrix" which constitutes the calibration of the DM/WFS system. Under this linear hypothesis, the function $\mathbf{h}$ becomes the interaction matrix $\mathbf{M}$. Three cases can be consider :

1. The matrix $\mathbf{M}$ is perfectly invertible $\mathbf{R} = \mathbf{M}^{-1}$, the only source of error is the noise

$\epsilon = \mathbf{M}^{-1}$Noise.

2. The matrix $\mathbf{M}$ is not invertible. In that case the reconstructor will be the pseudo-inverse of the matrix $\mathbf{M}$: $\mathbf{R} = \mathbf{M}^{\dagger} = (\mathbf{M}^t\mathbf{M})^{-1}\mathbf{M}^t$, where not all the modes are corrected.
3. The matrix $\mathbf{M}$ only describes the input/output relationship in a specific phase regime.

In practice, the linear hypothesis is valid, especially when using a SH sensor, as defined in the previous section1.2.2, and allows us to use a Matrix-Vector Multiplication (MVM) formalism to link the WFS measurements to the DM commands.

To address this direct problem (cf equation1.73) it becomes essential to compute the interaction matrix $\mathbf{M}$ which makes the connection between the DM and the WFS. Constructing an interaction matrix requires the selection of a basis, which could either be the basis of the DM actuators, called a zonal control of the DM, or a modal basis such as the Zernike modes, leading to modal control of the DM, (Roddier 1999). In either scenario, the interaction matrix $\mathbf{M}$ describes how each mode of the chosen basis is seen by the WFS, as illustrated in Figure 1.25.

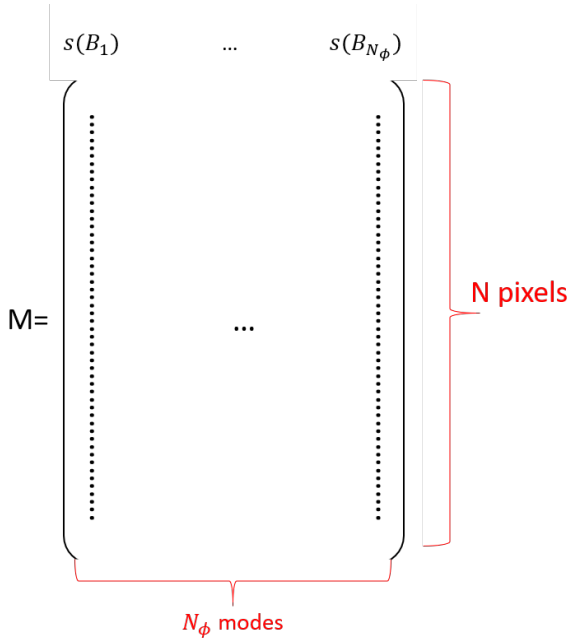

FIGURE 1.25 – Schematic of an interaction matrix.

The WFS measurements s are directly linked to the decomposition of the wavefront on the chosen basis by the following relation (the noise has been removed from the equation for simplicity)

$$s = \mathbf{Ma}, \tag{1.77}$$

where **a** is the vector of the decomposition of the phase ϕ on the basis $\{B_i\}$, cf equation 1.13. The number of controlled modes N_ϕ is defined by the number of actuators on the DM. The phase ϕ can be decomposed in the following way

$$\phi = \sum_{i=1}^{N_\phi} a_i B_i + \sum_{i=1+N_\phi}^{+\infty} a_i B_i \tag{1.78}$$

$$\phi = \phi_{//} + \phi_\perp, \tag{1.79}$$

where the first term of the equation represent the controlled modes and the second term, the uncontrolled modes by the system.

Inverting equation 1.77 give us the estimation of phase mode to be applied on the DM given the WFS measurements In the case of a simple inversion process the phase reconstructor is nothing but the pseudo-inverse of the interaction matrix **M** as reminded below

$$\mathbf{R} = \mathbf{M}^\dagger = \left(\mathbf{M}^t\mathbf{M}\right)^{-1}\mathbf{M}^t, \tag{1.80}$$

where † correspond to the pseudo-inverse of a matrix.

One method to invert this matrix is to use the Singular Values Decomposition (SVD) of that matrix using the Moore Penrose algorithm (Moore 1920; Penrose 1955).

Linearisation of FF-WFS intensity : From the expression of the intensity for FF-WFS, we notice that the intensities are not linear with the wavefront (see equations 1.55 and 1.63). Yet, in the small phase regime, the expression of the intensities can be simplified to extract a linear dependency of the signal with the wavefront allowing to use the interaction matrix formalism.

Going back to the expression of the intensity of FF-WFS equation 1.55. In the linear approximation or in the small phase regime, $\delta\phi \longrightarrow 0$ and using the Kernel formalism, (Fauvarque et al. 2017)

$$\mathbf{K}(0,\phi_r)|_{\vec{\mathbf{R}},\vec{\mathbf{r}}} = 2\mathbf{Im}\left[\bar{\mathscr{F}}(t)|_{\vec{\mathbf{R}}-\vec{\mathbf{r}}}\int_{\mathbb{R}^2}\mathbb{I}_P|_{\vec{\mathbf{r}}'}\,\mathscr{F}(t)|_{\vec{\mathbf{R}}-\vec{\mathbf{r}}'}\mathscr{F}(w)|_{\vec{\mathbf{r}}'-\vec{\mathbf{r}}}e^{\imath(\phi_r|_{\vec{\mathbf{r}}'}-\phi_r|_{\vec{\mathbf{r}}})}\right]\mathrm{d}^2\vec{\mathbf{r}}'. \tag{1.81}$$

The linear intensity can be written

$$\Delta I(\delta\phi,\phi_r)|_{\vec{\mathbf{R}}} = \int_{\mathbb{R}^2}(\mathbb{I}_P|_{\vec{\mathbf{r}}}\delta\phi|_{\vec{\mathbf{r}}})\,\mathbf{K}(0,\phi_r)|_{\vec{\mathbf{R}},\vec{\mathbf{r}}}\mathrm{d}\vec{\mathbf{r}}. \tag{1.82}$$

An interaction matrix can be understood as the response of the kernel regarding a given phase basis B_i, thus each column of the matrix can be expressed as

$$\mathbf{M}_i|_{\vec{\mathbf{R}}} = \int_{\mathbb{R}^2} (\mathbb{I}_P|_{\vec{\mathbf{r}}} B_i|_{\vec{\mathbf{r}}})\, \mathbf{K}|_{\vec{\mathbf{R}},\vec{\mathbf{r}}} \mathrm{d}\vec{\mathbf{r}}. \tag{1.83}$$

1.2.3.2 Temporal wavefront reconstruction

The interaction matrix and its pseudo-inverse, the command matrix control the spatial reconstruction of the wavefront. To address the temporal aspect, it is necessary to focus on the control of the loop. As explained in the introduction of the section, the DM located upstream of the WFS, gives a feed-back after the correction. However, there is a cumulative delay between the WFS measurement and the moment when the commands are applied to the DM. The evolution of the turbulence in this small period induces errors in the correction leading the phase residuals $\phi_{res} = \phi - \hat{\phi} \neq 0$.

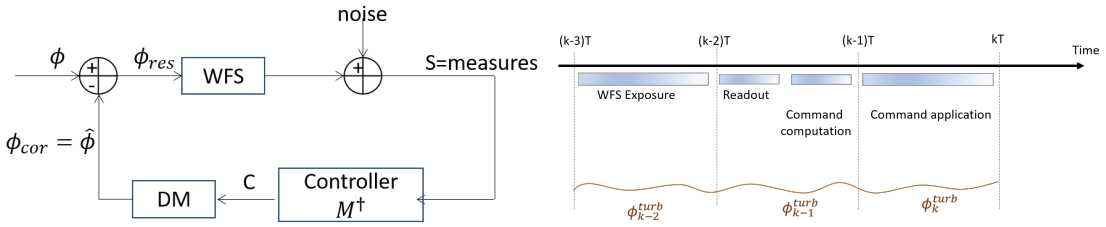

(a) AO feed-back loop (b) Chronogram of an AO loop

FIGURE 1.26 – Left : AO feed-back loop. Right : chronogram of an AO system with two frames delay

The delay of the loop is illustrated in Fig.1.26. At least one frame delay is needed to read the WFS detector and another one to calculate the command to be applied. There is typically two frames delay between the WFS measurement and the application of the correction. This delay has an impact on the performance of the AO system. It can be mitigated using appropriate control law. The most simple and the most common law used in AO is the integrator

$$\mathbf{C}_k = \mathbf{C}_{k-1} - g\mathbf{R}\mathbf{a}_k, \tag{1.84}$$

where g is the loop gain, $\mathbf{R}$ the command matrix, $\mathbf{a}_k$ the decomposition of the residual phase and C_k the DM command corresponding to the phase residual at the moment k. The value of the loop gain is optimised to ensure performances and the stability of the AO loop. It varies between 0.2 and 0.5. Smarter but more complex laws have been developed such as the Linear Quadratic Gaussian (Sivo 2013) for instance. However,in this thesis, we are only considering an integrator law for the AO loop.

1.2.4 Adaptive optics error budget

The previous sections presented the three main components of the AO system : the DM, the WFS and the RTC. All these components will have an impact on the

performance of the AO system. The AO error budget defines the quality of the corrected wavefront and is defined by the variance of the phase residuals. Depending on the applications, this error budget has to be minimised. It is the case of state-of-the-art AO system such as SPHERE on the VLT, this AO system is considered as an eXtrem Adaptive Optics (XAO) system as it provides the science instrument a highly corrected wavefront (Fusco et al. 2006, 2015; Beuzit et al. 2019).

The error budget depends on several independent factors, so the total phase variance is the quadratic sum of each factor. This is called the AO error budget and is given by equation1.85. The important terms of error that we will consider here in this PhD manuscript are the temporal error and the reconstruction error

$$\sigma^2_\phi = \sigma^2_{fit} + \sigma^2_{tempo} + \sigma^2_{WFS} + \sigma^2_{aniso} + \sigma^2_{chromatic} + \sigma^2_{scint} + \sigma^2_{cal} + \sigma^2_{NCPA}, \tag{1.85}$$

where σ^2_i is in rad^2. Each factor is directly link to the three main component forming the AO system.

The fitting error, σ^2_{fit}, is directly link to the finite number of actuators under the DM surface. As mentioned in equation 1.78, the high order of the turbulence will not be corrected by the DM inducing error in the phase correction. The expression of the fitting error depends on the strength of the turbulence expressed by the Fried parameter r_0 and the pitch, d_{act} average distance between the actuator. For a square grid of actuator it is expressed as follow (Roddier 1999)

$$\sigma^2_{fit} = \alpha \left(\frac{d_{act}}{r_0} \right)^{5/3}, \tag{1.86}$$

where the α coefficient depends on the shape of the DM's influence function (IF) (or, in other words, on the DM's modal base). In the case of pure sinusoids (Fourier modes), this value is equal to 0.23. For more classical IF forms, it will vary between this lower limit and up to 0.3. It is mainly linked to the IF coupling factor (i.e. the action of an IF on its nearest neighbors).

The temporal error, σ^2_{tempo}, is linked to the delay of the AO loop (cf Fig.1.26) and the latency. This error depends on the performances of the RTC and the control law. The faster the computation, the smaller is the temporal error. A very first approximation of its value is given by equation 1.26. However, the faster the loop, the less photons for the WFS camera. Hence the importance of working with very high sensitive WFS (see section1.2.2.1) to ensure the performances of the WFS in low flux regime for XAO systems.

The WFS measurement errors σ^2_{WFS}, can be decomposed on several contribution such as aliasing and noise errors

— The **aliasing** is induced by the high order of the turbulence that are not seen

by the WFS nor controlled by the DM. This is due to folding of the high order modes of the spectrum on the lower order modes and will induce error in their measurement / estimation process by the WFS.

— The **noise** is the error induced by all possible sources of noise at the WFS detection level (the detector itself). The three most important are photon noise, background noise and readout noise. Photon and background noise (induced by the observed target and the properties of the instrumental environment) represent a fundamental limit for any detection process and will determine the final performance of a given WFS concept. Readout noise is linked to the camera's readout properties and represents a technological challenge. The propagation of these different noises in the phase estimation error ($\boldsymbol{\sigma}^2_{WFS}$) will ultimately depend on several critical system choices (WFS concepts and algorithm, type of reconstructors, AO loop schemes ...).

The anisoplanatism error, $\boldsymbol{\sigma}^2_{aniso}$, is given by equation 1.29. Anisoplanatism is related to the evolution of the turbulent phase in the field of view. For a "classic" AO system using only one measuring direction and one DM in the pupil (Single Conjugate AO [SCAO]), when correcting for turbulence, the correction zone around the guide star is delimited by the isoplanatic angle θ_0 defined in equation 1.30. Outside this zone, OA correction is no longer effective. For high-contrast applications, this error is negligible, as the OA loop is closed on the star itself and the planet is well within θ_0.

The chromatic errors, $\sigma^2_{chromatic}$, are due to wavelength differences between the scientific path and the detection path. It is due to the wavelength dependence of the refractive index of the atmosphere. This effect induces differential refraction, i.e. a shift in the beam for two different wavelengths, which can be considered as anisoplanatic degradation. For further details, see Fusco et al. (2006) (and references included).

The scintillation and diffraction errors, σ^2_{scint}, are due to the modification of the phase and amplitude by the Fresnel effects induced by the propagation between two separated turbulent layers. These effects depend on the turbulence profile (C_n^2) and on the wavelength. They affect both the focal plane images and the WFS accuracy. They are usually negligible in astronomical observations (Fusco et al. (2006)) but they could become a problem in case of low elevation observation (lower than typically 50°) and strong turbulence cases).

The AO calibration error, $\boldsymbol{\sigma}^2_{cal}$, quantifies the accuracy of models, laboratory characterisations or calibration measurements of any component of the AO loop. Ultimately, all these models and measurements will provide a description of the complete AO loop, often simplified into a single reconstruction matrix that allows the WFS measurement to be passed to the DM form. Any error in this global description (mismatch, non-linearity, drift, etc.) will propagate through the system and induce either a bias or an additional RMS error on the final performance of the AO loop. A typical example

is the mismatch between the calibrated matrix (using an internal calibration source) and the actual on-sky matrices. It has been demonstrated (particularly in the case of Pyramid WFS) that poor calibrations can lead to significant errors in the AO loop (up to loop divergences), see Heritier (2019).

The Non-Common Path Aberrations (NCPA), $\boldsymbol{\sigma}^2_{NCPA}$, are caused by the different between the optical path of the sensing branch and the one of the scientific instrument. The WFS corrects the aberrations in the common path and in the sensing path but cannot correct for the one in the instrument. Thus, some uncorrected aberrations remains in the science branch (Blanc et al. 2003; Sauvage et al. 2007; Dohlen et al. 2018; Clénet et al. 2019). As a matter of fact, this source of error is the main limitation of the contrast of current instrument (Mazoyer et al. 2024).

1.3 Adaptive Optics with Giant Segmented Telescopes

As explained in the introduction to this manuscript, the telescope itself can be a source of aberrations that need to be managed by the AO system. This is particularly the case with Giant Segmented Telescopes (GST) telescopes, as their primary mirror will be segmented in several ways :

— **physically**, by all the segments that make up the primary mirror, which will need to be co-positioned (or co-phased).

— **optically**, due to the shadow of the secondary mirror supports (spiders) which will cut the pupil into different zones.

In the case of the ELT and for the purposes of our studies, we will only consider the fragmentation induced by the arms of the spider holding the secondary mirror (M2), and not the segmentation induced by the 798 segments that make up the pupil. We will assume that these segments are perfectly co-phased and that the pupil is equivalent to a monolithic 39m pupil. Because of the size of the mirrors, the spider must be thick enough to support M2's weight (25 to 50 cm). The shadow of the spiders on M1 cuts the pupil into 6 fragments, breaking the continuity of the wavefront across the pupil (see Fig.1.1).

1.3.1 Adaptive Optics and Pupil Fragmentation

The lack of continuity of the wavefront is visible when simulating the AO loop. The main issue is the assumption behind the wavefront estimation made by the AO system. The AO system assumes a continuous wavefront across the pupil. However, due to the fragmentation of the pupil, the information underneath the spider is not accessible, thus the AO system cannot provide an accurate wavefront estimation of the hidden part of the pupil. Yet, the AO system is perfectly capable of measuring the

visible part of the wavefront on each fragment, leading to differential pistons between the fragments as seen in Fig.9. This problematic characteristic of the GST have been intensively studied the past few years in order to find a solution to mitigate the impact of the phase discontinuity on the image quality and reach the full potential of the GST. For the ELT, none of the first light instruments will have a dedicated sensors to measure and control differential pistons. Nonetheless, it will be the case for the second generation of instruments such as ArmazoNes high Dispersion Echelle Spectrograph (ANDES) (Marconi et al. 2022). The strategy for the first light instruments is to mitigate the effect of the differential pistons by constraining the Deformable Mirror (DM) actuators. Schwartz et al. (2018) introduced the minioning of the DM actuator to ensure the continuity of the wavefront on both side of the spider allowing to reduced the differential pistons.

Engler et al. (2022) proposes a solution based on a unique WFS pyramid that exploits the difference in terms of characteristic time between turbulent and the differential pistons. By modifying, the characteristics of the pyramid sensor (stopping modulation every tenth frame during observation to measure pupil fragmentation), it demonstrates the ability to measure both turbulence and petal modes. The main limitation of the method is currently technological (ability to change modulation structure from one frame to the next).

Following N. Schwartz works, Bertrou-Cantou et al. (2020) presents a continuous basis that has the advantage of reducing the residual differential pistons follow with a dedicated WFS used to reduce even more the remaining petal. Bertrou-Cantou et al. (2020) compares then the use of a non-modulated PWFS or a ZWFS as a petalometer (WFS dedicated to the measurement of petal modes) but concludes that at visible wavelength, the use of neither of the two WFS helps increasing the AO performances in strong seeing conditions.

More recently, Levraud et al. (2024a) presents a two path system composed of a modulated PWFS dedicated to the control of atmosphere turbulence and a petalometer using a non-modulated PWFS with a spatial filter at visible wavelength. And in Levraud et al. (2024b), he presents the use of a spatially filtered modulated PWFS as a petalometer. In comparison with his previous work on the non-modulated PWFS, a small modulation radius allows the petalometer to be more robust in strong seeing condition. For the GMT, the natural guide star WFS will use holography to interfere individual segments of the aperture (HDFS) and use in a broad wavelength range it allows to lift the λ ambiguity when measuring the differential pistons (Haffert et al. 2022; Quirós-Pacheco et al. 2022).

Another source of aberration is the Low-Wind Effect (LWE),(Sauvage et al. 2015; Milli et al. 2018), it comes from local optical aberrations induced by the difference of temperature between the air and the telescope mechanical structures (see Fig.1.27). These aberrations have a very different spatial and temporal characteristics compared to the atmospheric ones, and standard AO systems are not able to properly measure, hence correct, for these effects : the image contrast and the corresponding planet detectability is lost. The ELT, with it colossal mechanical structure will induce signi-

ficantly more of these aberrations, it is expected that in the worst-case scenario, the LWE could be on the order of $1-2\mu m$ Martins et al. (2022), and the future AO systems must anticipate ways to cope with it in order to achieve the best planet detection possible.

For the next generation of telescopes, pupil fragmentation and the LWE will cause a decrease in performance if not corrected. Only phase sensors such as Zernike-type WFS or non-modulated PWFS (presented in section 1.2.2.4) can be used to measure and control these aberrations. However, the main limitation of these sensors is their small dynamic range, which depends on the observation conditions. Therefore, it is important to develop strategies to enable their measurement if these events occur during observation (see chapter 2).

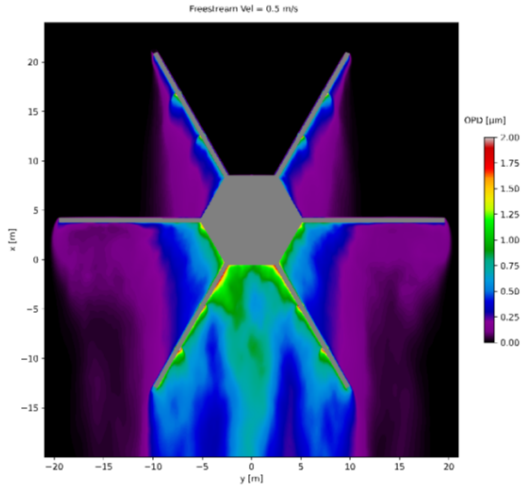

FIGURE 1.27 – LWE on the ELT pupil, optical path difference up to $2\mu m$. *Credits :Martins et al. (2022)*

1.3.2 Modal basis to describe phase discontinuity aberrations

From the fragmented pupil of the ELT one can build a petal mode basis composed of each fragment (see Fig.1.28). The petal mode basis is orthogonal, however, the petal modes are not orthogonal to the Zernike modes.

The differential pistons of each ELT residual screen is obtained by projecting the screen on the petal basis (see Fig.1.29). The same basis can be used for LWE. Nonetheless, the petal mode are not orthogonal to the standard basis such as the Zernike polynomials, therefore to control other modes, the complete basis has to be orthogonalised (Bertrou-Cantou et al. 2020).

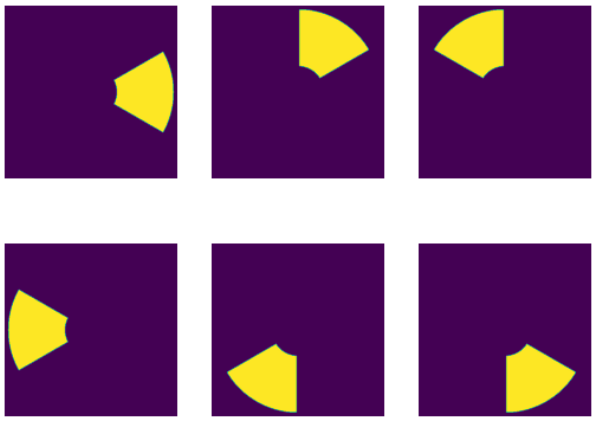

FIGURE 1.28 – ELT petal basis used for the simulations $\{P_i\}$.

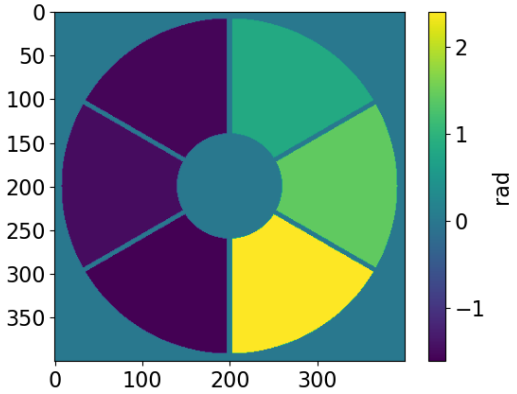

FIGURE 1.29 – Projection on the petal basis of the residual screen in Fig.9.

1.4 Interest of Fourier filtering wavefront sensors

FF-WFS will be the WFS of the next generation of ground-based telescopes as they are essential to reach the extreme level of wavefront correction. Indeed, when the atmospheric conditions are evolving faster than the AO correction rate, significant residuals from uncorrected star light pollute the images in the region where exoplanets could be discovered, Cantalloube et al. (2020). The exoplanet detectability (or contrast) is reduced by factors 2 to 10. To tackle this issue, the AO corrections must be applied at a faster rate, typically 2 to 3 times faster than the 1.2 kHz which is the current standard for both SPHERE and GPI. But running faster means that less photons are available for the wavefront sensing, and calls for ultra-sensitive WFSs see section 1.2.2.4.

1.4.1 Sensitivity of FF-WFS

The sensitivity of a WFS was defined in section 1.2.2.1 and describes the robustness to noise propagation of a WFS. Different methods has been developed to propose a uniform mathematical formalism the sensitivity of FF-WFS (Guyon 2005; Chambouleyron et al. 2023). The sensitivities with respect to the RON and the photon noise, s_{RON} and s_{ph} of a FF-WFS (cf section 1.2.2.1) can be expressed as respectively the ratio between 2-norm of the intensity and the 2-norm of the input wavefront and the ratio between the 2-norm of the intensity and the square root of the reference intensity (cf equations 1.87) (Chambouleyron et al. 2023). These models were derived assuming a small phase regime to ensure a linear relation between the intensities pattern and the wavefront. The higher this criteria, the less the reconstruction is affected by the noise propagation. However is has been demonstrated that $s_i \leq 2$, which gives theoretical upper limit for the any FF-WFS sensitivity.

Figure 1.30 represents the sensitivity curves of FF-WFS using a Fourier modal basis (see 1.1.1.4). Pure spatial frequencies (Fourier modes) are sent to the WFS and the incoming flux is used to properly normalise the intensities (this ensures that the sensitivity plots can be used to compare WFSs in a fair manner). The first thing one can notice is the poor sensibility of FF-WFS to low spatial frequencies, which means that the presence of noise will worsen the estimation of these low-order modes. It is important to notice that the modulation affects the spatial frequencies contained in the modulation ring (see section 1.2.2.4).

Furthermore, the most sensitive WFS among the considered FF-WFS is the ZWFS when considering the RON. It is interesting to note that the photon noise sensitivity of the ZWFS can be improved by increasing the size of the dimple as it is shown in (Chambouleyron et al. 2021a). This particular sensor will be further studied in the following chapter 2.

$$s_{RON}(\phi_i) = \frac{\|\Delta I(\phi_i)\|_2}{\|\phi_i\|_2}, \tag{1.87}$$

$$s_{ph}(\phi_i) = \left\| \frac{\Delta I(\phi_i)}{\|\phi_i\|_2 \sqrt{I_{ref}}} \right\|_2, \tag{1.88}$$

1.4.2 Dynamic of FF-WFS

The dynamic range of a WFS is the phase regime in which the reconstruction provides an accurate phase estimate. Unlike sensitivity, there is no clear definition or measure of the dynamic range of a WFS. It can be either the bijective regime (or capture range) of a WFS, or the regime in which the estimated phase is directly and linearly proportional to the input wavefront. However, we can see, by expanding the equation, that FF-WFSs are inherently non-linear WFSs, which means that when using a calibration approach, the relationship used to describe the input/output relation-

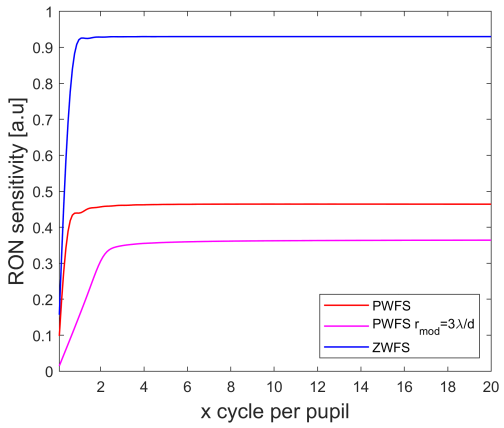

(a) RON sensitivity

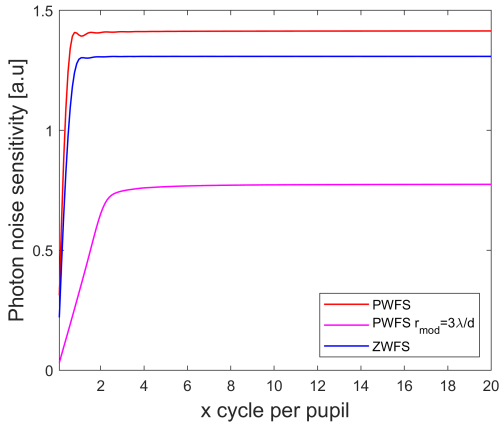

(b) Photon noise sensitivity

FIGURE 1.30 – FF-WFS sensitivities : Zernike WFS, Pyramid WFS and modulated Pyramid WFS.

ship is only true in a specific regime (usually the regime of small phase around the reference phase). Outside this phase regime, the interaction matrix will no longer provide a proper estimation of the phase, inducing error in the phase reconstruction. These errors are induced by the non-linear behaviour of the WFS (saturation of the intensity pattern for instance as explained in section 1.2.2.4 for the pyramid).

One solution to have a better understanding of the dynamic range of a WFS is to plot the reconstruction curve of one phase mode ϕ_i. For that purpose, we use, as an example, a ZWFS with a dimple size of $1.06\lambda/D$. The reconstruction is done using an interaction matrix. The calibration is done using a Zernike modal basis with a procedure described in section 1.2.3.1). Noise-free simulations are considere here as the goal is to asses the linear regime in the perfect case. Fig.1.31 represents the amplitude of the reconstructed mode with respect to the input amplitude using the defined ZWFS. These curves show the limited linear range of the ZWFS, thus the limit

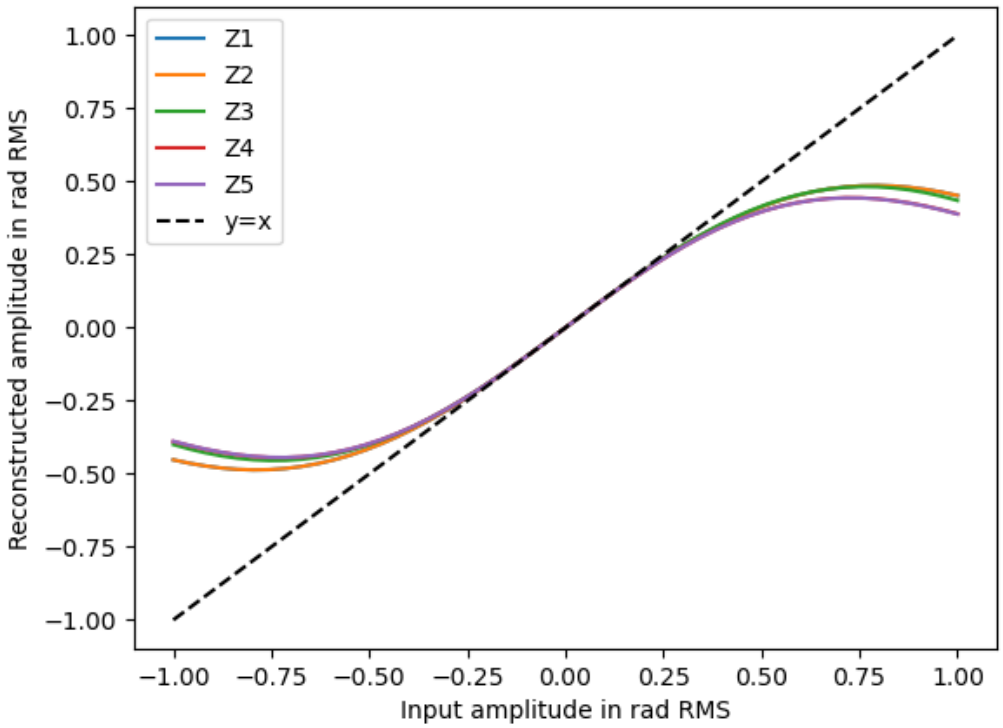

FIGURE 1.31 – Reconstruction curves of the first five Zernike modes using a ZWFS and an interaction matrix as a reconstructor.

of the matrix formalism when estimating the wavefront. I define the dynamic range of the WFS as the domain were the relative error between the input coefficient and the output coefficient is smaller than 10%. With this definition, the interaction matrix is not suitable to estimate wavefront amplitude larger than 0.3 rad RMS. To understand the limitation of the formalism, we need to have a look at the estimated wavefront.

1.4.2.1 Impact of the non-linear response of the ZWFS in the phase reconstruction

Let's delve into the non-linear behaviour of the ZWFS and its impact on phase estimation. Figure 1.32 shows the coefficients of the input phase and the estimated coefficients. Several issues can be identified in this estimation. The first issue is the underestimation of the input coefficient. Outside the linear regime (input phase of amplitude 0.5 rad RMS) of the WFS, the reconstructor will underestimate the wavefront at first order, this is what we call an Optical gains (OG) issue as shown in the Fig.1.32(c). The second issue is modal confusion, which is evident in this plot by the presence of modes that are absent in the input phase but appear in the reconstructed phase. Outside the linear regime of the WFS, the reconstructor will systematically introduce

mode confusion or cross-talk as shown on Fig.1.32(c). The underestimation of the input mode and the reconstruction of new phase modes are two non-linear effects that compromise the phase reconstruction, hence limit the amplitude range where the reconstructors provide an accurate estimation of the wavefront. These effects are interconnected and cannot be separated, so any efforts to minimise their impact must consider them together.

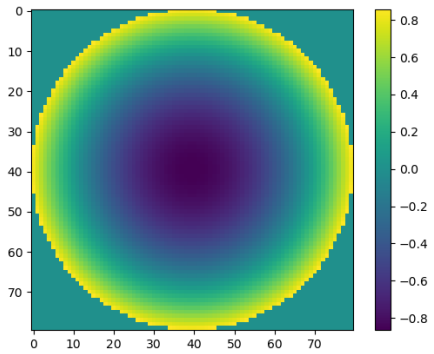

(a) Input phase $\delta\phi$, 0.5rad RMS

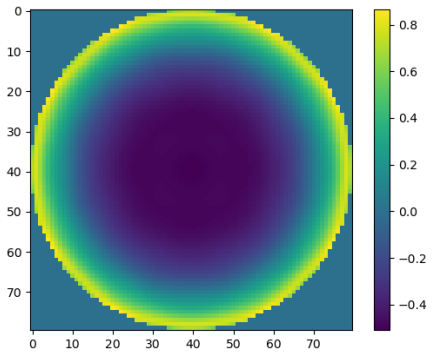

(b) Estimated phase $\widehat{\delta\phi}$, WFE 0.12 rad RMS

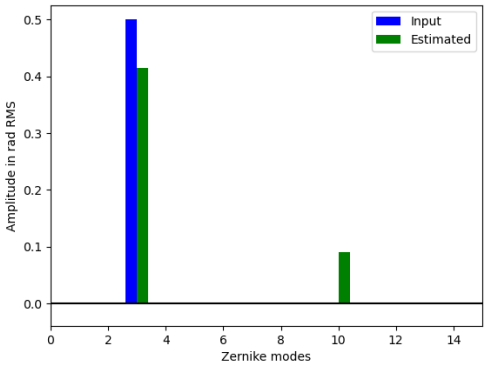

(c) Projection on the Zernike polynomials

FIGURE 1.32 – Impact of the non-linear response on the phase estimation using a ZWFS and an interaction matrix as a reconstructor.

Another scenario where we experience a loss of sensitivity when trying to estimate a wavefront is in the presence of phase residuals. In this case, we are using a modulated PWFS ($r_{mod} = 2\lambda/D$) and assess its performance in measuring a specific Zernike mode, both in the absence and presence of phase residuals (see Fig.1.33). The calibration is done using the Zernike basis. The red curve shows the estimation of Z_k in the absence of AO residuals, while the dashed blue curve represents the estimation of the same mode in the presence of AO residuals. In this scenario, the estimation suffers from a 30% underestimation of the incoming wavefront due to the presence of AO residuals.

This is another limitation of the calibration approach, which is constrained to the phase regime around the reference wavefront, and prove the non-linear response of the FF-WFS - here the pyramid.

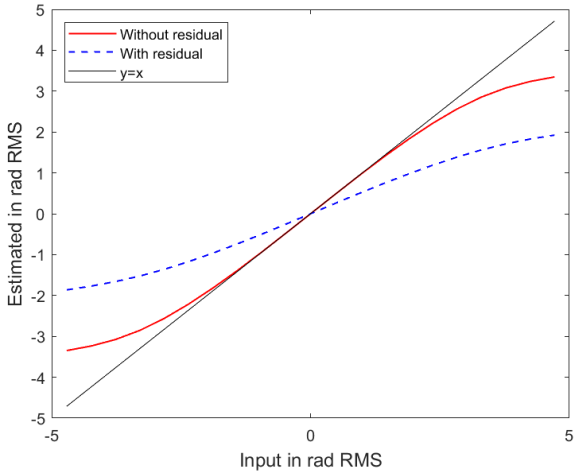

FIGURE 1.33 – Reconstruction curves of Z_5 without phase residual (red curve) and in presence of phase residual (dashed-blue curve) using the modulated PWFS ($r_{mod} = 2\lambda/D$) and an interaction matrix as a reconstructor.

These two simple examples using the ZWFS and the PWFS demonstrate the inherent non-linear behaviour of FF-WFS, which manifests as an underestimation of the wavefront (OG) and the appearance of extra terms in the phase estimation (modal confusion or cross-talk) (demonstrated for the PWFS in Cisse et al. (2024)). To overcome these effects, we can increase the dynamic range of a sensor through two main strategies : (i) modifying the WFS optical setup (chapter 2) or (ii) modifying the phase estimator (chapter 3).

1.4.3 Optical gains approach

As mentioned in the introduction of this section and in the development of the equation of propagation, FF-WFS such as the PWFS or the ZWFS suffers from inherent non-linear behaviour when the amplitude of the wavefront increases. To a first order, this non-linear behaviour, can be seen as a change of the sensitivity/behaviour of the sensor with high amplitude phase or with different operating condition. It is a direct consequence of the calibrating approach describe in section1.2.3.1. The interaction matrix is only representative of the system around the calibrated regime, usually around small (or even flat) wavefronts, meaning that the command matrix will give an accurate measurements of the wavefronts only in that regime. Outside this regime the command matrix is no longer adequate.

This loss of sensitivity induced by the presence of AO residuals has been studied intensively and has led to the Optical gains (OG) formalism for modulated PWFS (Korkiakoski et al. 2008; Deo et al. 2019; Chambouleyron et al. 2020; Bertrou-Cantou et al.

2022; Agapito et al. 2023). The gain formalism considers the nonlinear behavior of PWFS as a first-order nonlinear problem. It considers that the linearity of the FF-WFS varies from mode to mode, hence the modal gain compensation. The mathematical formalism used for the gain is that developed by Fauvarque (2017) and Chambouleyron (2021). The mathematical development was based on the idea that, to perfectly describe the observation conditions, the interaction matrix must be calculated in the operating regime, i.e. in the regime in which it will be used. In this way, another push-pull matrix can be defined : $\mathbf{M}(0, \phi_r + \delta\phi)$, a push-pull matrix computed around the phase to be measured $\delta\phi$. This matrix is assumed to be the linear link between the WFS signal and the wavefront according to the following equation

$$\Delta I(\delta\phi) = \mathbf{M}(0, \phi_r + \delta\phi)\mathbf{a}(\delta\phi), \tag{1.89}$$

where $\mathbf{a}(\delta\phi)$ is the decomposition of $\delta\phi$ on the chosen control basis.

This Linear Parameter Varying (LPV) approach involves adapting the linear relationship to describe non-linear behaviour, while maintaining a linear formalism. The matrix that defines the linear relationship between signal and phase depends on the measured phase $\delta\phi$, which complicates the calculation of this reconstructor when the unknown is actually $\delta\phi$. However, rather than using this matrix directly, the aim is to better understand the differences between calibration and on sky regimes. With this in mind, the quantity of interest becomes the projection of this matrix onto the $\mathbf{M}^\dagger$ reconstructor

$$\mathbf{T}(0, \phi_r + \delta\phi) = \mathbf{M}^\dagger\mathbf{M}(0, \phi_r + \delta\phi), \tag{1.90}$$

$$\mathbf{OG}(0, \phi_r + \delta\phi) = \mathbf{diag}(\mathbf{T}(0, \phi_r + \delta\phi)), \tag{1.91}$$

where $\mathbf{T}(0, \phi_r + \delta\phi)$ is a square matrix $N_\phi \times N_\phi$ which describes the differences between the two regimes. The OG are the diagonal terms of the matrix $\mathbf{T}$, which is a vector of size $(1 \times N_\phi)$. Once calculated, the OG are used to update the reconstruction matrix with the modal gain at each iteration of the close-loop to improve the phase estimation. The new reconstructor becomes

$$\mathbf{R} = \Big(\mathbf{MOG}(0, \phi_r + \delta\phi)\Big)^\dagger. \tag{1.92}$$

Following this approach (cf equation1.90) and to illustrate the OG compensation, we plotted in Fig.1.34 an example of OG compensation with a modulated PWFS, $r_{mod} = 2\lambda/D$. The OG vector provides information on the loss of sensitivity per modes allowing the compensation in operation. It can also be obtained thanks to a focal plane camera,(Chambouleyron et al. 2021b). This method is identical to changing the system's operating point. By updating the reconstructor with the OG frame by frame, the system no longer works around the reference wavefront, but around a new wavefront characteristic of the AO loop's performance. Furthermore, this gain compensation does not take into account the modal confusion that occurs when the WFS operates outside its linear regime, (Cisse et al. 2024).

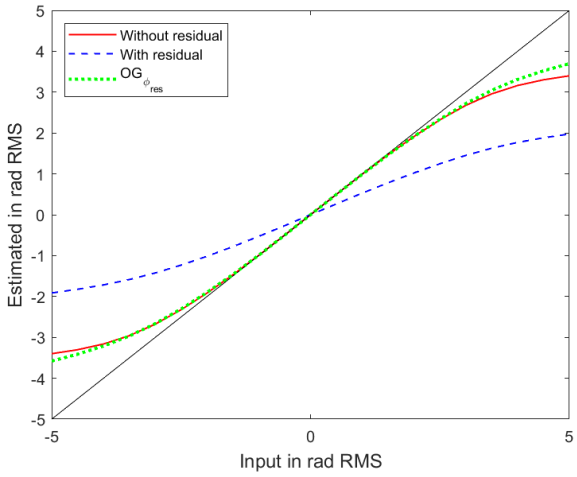

FIGURE 1.34 – Reconstruction curves of Z_5 in presence of phase residual after OG compensation dotted-green curve using a modulated PWFS. Same simulation as in Fig.1.33.

Instead of its approximation through the OG formalism, one can think that a more accurate reconstructor would be the matrix computed around the phase to be measured, to take all the non-linear responses into account. This approach is only possible in simulation where the phase to be estimated and reconstructed is "known". We plotted in Fig.1.35 the average WFE as a function of the amplitude of the wavefront.

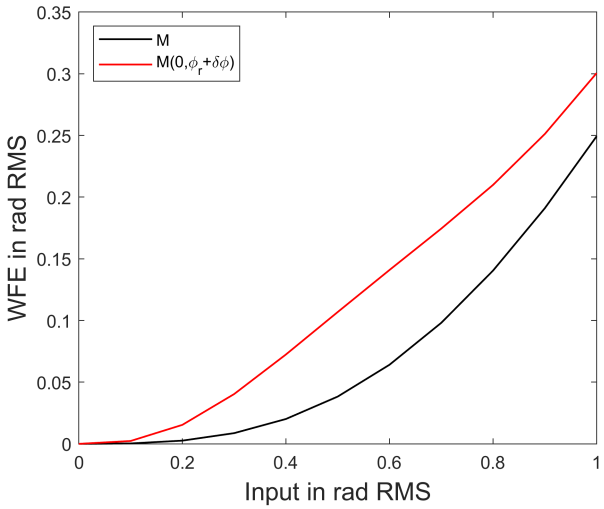

FIGURE 1.35 – WFE comparison between the interaction matrix and the push-pull matrix around the phase to be measured using a non-modulated PWFS.

The study, using a non-modulated PWFS, was made on 100 phase screens per amplitude, following the Kolmogorow power-law (section 1.1.2) and each phase is projected on 300 Zernike modes. The screen are normalised and their amplitudes is scaled from

0 to 1 rad RMS. This figure shows that instead of providing the perfect phase estimation or at least, decreasing the WFE in comparison with the use of the interaction matrix $\mathbf{M}$, the matrix $\mathbf{M}(0, \phi_r + \delta\phi)$ tends to increase the WFE. It does not provide an accurate phase measurement. This is the first contradiction we are facing : the OG approximation is providing part of the solution to overcome the non-linear behaviour of the FF-WFS but when trying to push further the formalism by using considering the full matrix instead of its diagonal approximation, it does not work. Indeed, as we will show latter, this matrix is not the proper matrix to describe the relation between the signal and the wavefront.

This figure highlights a key issue addressed in the thesis : using the matrix $\mathbf{M}(0, \phi_r + \delta\phi)$ does not lead to improved phase estimation or a reduction in WFS as one might expect. Instead, it actually increases the WFE. This presents a major inconsistency in the previous formalism and is at the origin of the developments proposed in the next chapters. In fact, I will show that $\mathbf{M}(0, \phi_r + \delta\phi)$ is not the appropriate matrix to capture the relationship between wavefront signal and phase changes. And while the OG formalism developed for modulated PWFS has resolved part of the nonlinear behavior of FF-WFS, namely the underestimation of the wavefront, it does not resolve the modal confusion that prevents accurate wavefront estimation when using these sensors outside their linear regimes. More general approaches need to be developed to achieve this. One way of improving phase estimation is to use a non-linear phase reconstruction algorithm. However, to continue using the matrix formalism, which has the advantage of limiting the number of mathematical operations (MVM only), we need to find the matrix that best describes the response of the WFS outside its linear regime. This study is based on the OG formalism described above and forms the core of chapter 3.

1.5 Summary

In this chapter, we explored the optical propagation equations essential for understanding how light propagates in turbulent media such as the atmosphere. We introduced AO as a crucial tool for mitigating the effects of atmospheric turbulence on image quality. We have shown that wavefront sensors (WFS) are at the heart of any AO systems. Among the WFSs reviewed, Fourier-type WFSs stand out as next-generation sensors for giant telescopes to come. Thanks to their high sensitivity, these sensors can accurately estimate the wavefront in low-flux regimes, improving both AO loop speed and sky coverage, essential features for extreme AO systems.

However, the final section of this chapter addressed the challenge of the limited dynamic range of these sensors and the keystone of my research activities. Although FF-WFS provide accurate phase estimation, this accuracy is generally confined to small phase regimes. Therefore, the main objective of this PhD manuscript is to develop strategies that extend the dynamic range of these sensors without sacrificing their high sensitivities. The first part examines the characterisation of a modified, more linear Zernike mask (chapter 2), while the second part builds on Olivier Fauvarque's extensive work on the propagation equation to address non-linearities in FF-WFS with a new perspective (chapter 3).

2 MODIFICATION OF THE ZERNIKE-TYPE SENSOR FOR HIGH-CONTRAST APPLICATIONS

This chapter is dedicated to the study and characterisation of Zernike-type WFSs. I start by introducing the concept of Phase-Shifted Zernike WaveFront Sensor (PS-ZWFS), a Zernike-type WFS composed of two Zernike masks. My approach is driven by the need to extend the dynamic range of these kind of sensors in order to extend their field of applications. By combining the information of two ZWFS I add diversity in the phase estimation process, hence increasing the dynamic range of Zernike-type WFS.

Contents

2.1 Phase-Shifted Zernike : Boosting the dynamic of Zernike-type WFS . . . 102
2.1.1 Pedagogical description of the Phase-Shifted ZWFS 103
2.1.2 Signal processing for the Phase-Shifted Zernike 103
2.1.3 Sensitivity and dynamic of the PS-ZWFS 105
2.2 Applications to multi-stage AO systems 118
2.2.1 Measurement of differential piston using the PS-ZWFS 118
2.2.2 Cascaded-AO system for AO residuals control 125
2.2.3 Choice of the second stage WFS 128
2.2.4 Second stage in the VIS 129
2.2.5 Second stage in the NIR 132
2.2.6 Summary 133
2.3 Designing a second stage AO correction using the vector Zernike on the PAPYRUS testbed 135
2.3.1 Different technologies to manufacture the Phase-Shifted ZWFS 135
2.3.2 PAPYRUS, the Fourier filtering AO bench 137
2.3.3 Second stage wavefront sensing in the Near Infrared 139
2.4 Conclusion 143

The ground-based astronomical community, working toward High-Contrast imaging of exoplanet, shows a growing interest for Zernike-type WFS (Dohlen et al. 2006; N'Diaye et al. 2013; Mennesson et al. 2020; Salama et al. 2024b). The advantage of using these sensors comes first from their exceptional characteristics in terms of sensitivity. Indeed, for high-contrast applications, the sensitivity of the WFS determines (almost 1 :1) the final exoplanet detection capability (see the introduction). In other words, by optimising the sensitivity of a WFS, one can expect a reduction in AO residuals, and therefore a gain in the detectability of planets. The second motivation for using Zernike-type WFSs comes from the nature of the signal that can be directly linked to the wavefront. For instance, Zernike-type sensors are phase sensors which make them sensitive to phase discontinuities. Discontinuity phase aberrations is a major issue that arise on segmented telescopes such as the one of the Keck telescopes, the one of the future ELT and the one of the GMT. To illustrate this, the case of the Keck II telescope is interesting as it has been demonstrated that misalignment between the segments is a primary contributor to the contrast limits Jensen-Clem et al. (2021); Ragland et al. (2022), that could be measured and controlled thanks to Zernike-type WFS van Kooten et al. (2022); Salama et al. (2024a,b). This is a full scale demonstration of the potential of these sensors for phasing segmented telescopes, and a promising result for the future ELTs, that will likely suffer from similar effects. Finally, Zernike-type WFS are also gaining interest for space missions, as for instance the CGI instrument of the Nancy Roman Space telescope which is equipped with such a sensor dedicated to the measurement of low-order aberrations Shi et al. (2016); Mennesson et al. (2020); Riggs et al. (2021). ZWFS are also strongly considered for Habitable World Observatory (HWO) (Ruane et al. (2020)), as their ability to measure down to the picometer level in temperature-stabilised environments has been experimentally demonstrated Steeves et al. (2020).

In this chapter, and after having introduced the Phase-Shifted Zernike WaveFront Sensor (PS-ZWFS), I will characterise its performance in terms of sensitivity and dynamics, and compare it with the classical Zernike WFS. I will then explore the capabilities of these WFS to measure fragmentation errors and their abilities to improve the AO correction in a multi-stage scenario. Finally I will present the ongoing experiment dedicated to the implementation of a Zernike-type WFS for PAPYURS at the Observatoire de Haute-Provence.

2.1 Phase-Shifted Zernike : Boosting the dynamic of Zernike-type WFS

As describe in the previous chapter 1, the ZWFS is a very sensitive WFS with a very small dynamic range. Not only the dynamic range of the ZWFS is limited but also, its bijective regime is relatively small making difficult the use of this sensor. To lift the degeneracy in the wavefront measurement and increase the dynamic range of the ZWFS a modification of the phase mask can be made, so called Phase-Shifted

Zernike WaveFront Sensor (PS-ZWFS). In the following sections, the characterisation and comparison of both sensors will enable us to define a phase amplitude regime where the use of the PS-ZWFS is beneficial compared to the ZWFS, making it an asset to the AO system.

2.1.1 Pedagogical description of the Phase-Shifted ZWFS

The Phase-Shifted Zernike WaveFront Sensor (PS-ZWFS) is a Zernike-type WFS, which consists in using jointly two Zernike masks in the focal plane, with each ZWFS imposing a different phase shift. Following N'Diaye et al. (2013), we know that the optimal phase-shift in terms of sensitivity for a single ZWFS is $\pi/2$. In addition, Chambouleyron et al. (2024) demonstrated that to optimise the diversity introduced by the intensity patterns of two ZWFS, a phase-shift difference of π must be introduced. Therefore, two Zernike masks, noted Z_+ and Z_-, with respective phase shifts of $\pm\pi/2$ will be considered in the following sections.

To understand the optical path of the light, we consider a version of the PS-ZWFS composed of two separated Zernike masks. This "toy model" of the PS-ZWFS, presented in Fig.2.1, is used for clarity, and in section 2.3.1, we will present the different technologies used to manufacture this phase mask in a more sophisticated manner. After the pupil plane, a beamsplitter (50/50) is installed to separate the incoming beam. The two collimated beams are focused by a lens onto the focal plane, forming two focal points where the Zernike masks are placed. A lens then re-images the pupil plane onto a detector, creating two images of the pupil on the same detector, each modulated by its respective focal plane mask. The next section describes how the two intensities maps are combined to extract the phase information.

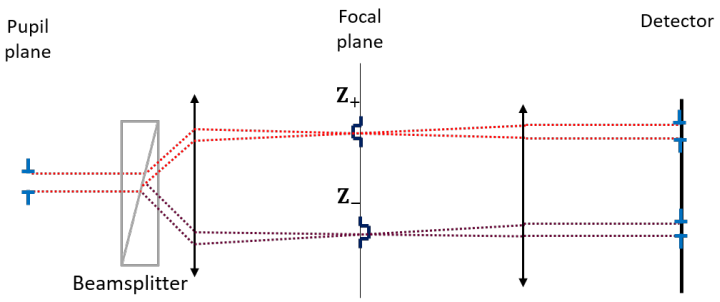

FIGURE 2.1 – Schematic optical set-up of the Phase Shifted ZWFS using two different Zernike masks. This "toy model" is used for clarity. The section 2.3.1 details the different methods to manufacture PS-ZWFS.

2.1.2 Signal processing for the Phase-Shifted Zernike

We write the intensity equations for a PS-ZWFS composed of two ZWFS of diameter $1.06\lambda/D$ and respective phase shift of $\pm\pi/2$. The intensity corresponding to the phase

mask Z_+ is given by equation 1.66. Starting from equation 1.63, with $\beta = 0$, $b = 1/2$ and $\theta = -\pi/2$ (cf chapter 1), the intensity corresponding to the phase mask Z_- is expressed as follow

$$I_-(\phi(\mathbf{r})) = A_0^2\mathbb{I}_p^2 + \frac{1}{2}A_0^2 - \sqrt{2}A_0^2\mathbb{I}_p sin\left(\phi + \frac{\pi}{4}\right). \tag{2.1}$$

Note that the implementation of the PS-ZWFS was proposed by Doelman et al. (2019) to retrieve the amplitude and the phase of the incoming EM field. However, as the main focus of this chapter is to study phase measurement dynamical range of the PS-ZWFS, in the following we will assume that the field amplitude A_0 is constant and the EM field amplitude in both branches is the same. Doing so, we end up with the following set of equations for the PS-ZWFS

$$\begin{aligned} I_+(\phi) &= \mathbb{I}_p^2 + \frac{1}{2} + \sqrt{2}\mathbb{I}_p sin\left(\phi - \frac{\pi}{4}\right), \text{ for } Z_+, \\ I_-(\phi) &= \mathbb{I}_p^2 + \frac{1}{2} - \sqrt{2}\mathbb{I}_p sin\left(\phi + \frac{\pi}{4}\right), \text{ for } Z_-. \end{aligned} \tag{2.2}$$

By using the trigonometry formula $sin(c+d)$, the intensities can also be written

$$\begin{aligned} I_+(\phi) &= \mathbb{I}_p^2 + \frac{1}{2} + \mathbb{I}_p\left(sin(\phi) - cos(\phi)\right), \text{ for } Z_+, \\ I_-(\phi) &= \mathbb{I}_p^2 + \frac{1}{2} - \mathbb{I}_p\left(sin(\phi) + cos(\phi)\right), \text{ for } Z_-. \end{aligned} \tag{2.3}$$

And by doing linear combination of the equation I_+ and I_-, one can have access to the $sine$ and the $cosine$ of the phase

$$\begin{aligned} sin(\phi) &= \frac{I_+(\phi) - I_-(\phi)}{2\mathbb{I}_p}, \\ cos(\phi) &= \frac{2\mathbb{I}_p^2 + 1 - \left(I_+(\phi) + I_-(\phi)\right)}{2\mathbb{I}_p}. \end{aligned} \tag{2.4}$$

By making use of the $atan2$ function, the estimated phase is given by

$$\phi = atan2\Big(sin(\phi), cos(\phi)\Big). \tag{2.5}$$

We preferred the use of the function $atan2$ to invert the relation within the range $[-\pi;\pi]$ (PV amplitude), since this function takes into account the sign of the $cosine$ and the $sine$ to measure the expected angle in the range $[-\pi;\pi]$. At the contrary, the use of the function $atan\left(\frac{sin(X)}{cos(X)}\right)$ whose bijective regime is the same as the $sine$ function $\left[\frac{-\pi}{2};\frac{\pi}{2}\right]$, and does not lift the sign ambiguity. Therefore, the use of the $atan2$ reconstructor allows to double the theoretical dynamic range of ZWFS from π to 2π.

An illustration of this explanation is provided in Fig. 2.2, which replicates the plot from Fig. 1.24, where we presented the evolution of the intensity as a function of the

phase of a given pixel in the pupil plane for a single ZWFS. In Fig. 2.2, we also include the response of the phase mask Z_{-}.

The sine response, characteristic of the ZWFS, results in the same intensity value twice within the phase range $\left[\frac{-5\lambda}{8};\frac{3\lambda}{8}\right]$ (as an example, the phases $-5\lambda/8$ and $3\lambda/8$ have the same intensity values), effectively reducing the usable phase reconstruction range of the ZWFS to $\left[\frac{-\lambda}{8};\frac{3\lambda}{8}\right]$. The introduction of a second Zernike mask, Z_{-}, lifts this phase degeneracy by producing a shifted sine wave response. This static shift provides intensity diversity, granting access to both the $sine$ and the $cosine$ components of the wavefront (see equations 2.4), thereby enabling a full, unambiguous phase reconstruction over the range $\left[\frac{-\lambda}{2};\frac{\lambda}{2}\right]$.

This technique can be understood through an analogy to the well-established phase-shifting interferometry (PSI) method, which is widely used in optical metrology for precise wavefront and surface measurements (Schwider (1990)). In PSI, a known phase shift is applied to a reference beam in a series of steps, and the interference pattern between the reference beam and the test beam is recorded at each step. By introducing multiple phase shifts, PSI obtains a set of intensity measurements that can be combined to uniquely determine the optical wavefront. In the context of wavefront sensing, PSI applies phase diversity by introducing controlled phase shifts, which allows the reconstruction of the full complex electric field. This is akin to the process described in Malacara (2007) and Schwider (1990), where PSI is used to lift phase ambiguities and improve measurement accuracy.

Note that, as demonstrated by Haffert (2024), this phase-shifting approach can also be directly applicable to the classical ZWFS. By using known phase probes, the $atan2$ function can be employed for phase reconstruction. This increases the dynamic range by a factor two using a single ZWFS. The PSI technique applied to the ZWFS proposed by Haffert (2024) has one major limitation : the use of dynamic phase probes. To optimise the phase estimation accuracy with this technique, one has first to perfectly know the phase probe introduced and second, to modify the shape of the DM during the estimation process. With this limitation, the real time implementation of this approach can be challenging. In comparison, the static phase shift imposed by the two ZWFS enables to have the same dynamic range without the real time constraints of the PSI.

2.1.3 Sensitivity and dynamic of the PS-ZWFS

In this section, I characterise the PS-ZWFS in terms of sensitivity and dynamic range using the same approach described in section 1.4 of the previous chapter. This allows us to demonstrate the advantages of this modified version of the Zernike mask and its potential use in a closed-loop system to measure and control phase aberrations.

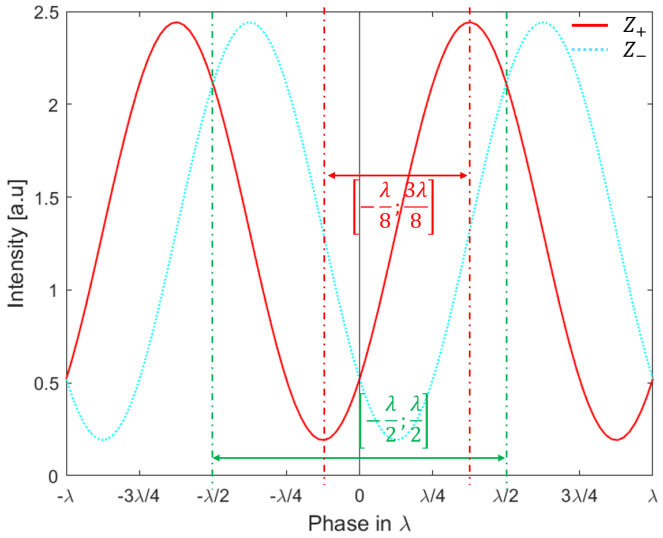

FIGURE 2.2 – Intensity as a function of the input phase of a single pixel for the Z_+ (classical ZWFS) and Z_-. The red and the green vertical lines represent the bijective regime of respectively the ZWFS and PS-ZWFS.

2.1.3.1 Sensitivity of the PS-ZWFS

As a reminder, the sensitivity curves are plotted using the equations 1.87 extracted from Chambouleyron (2021). In the small phase regime of Zernike-type WFS, the linear dependency of the signal with the wavefront is contained in the pupil (cf equation 8.17 of Fauvarque (2017)). The pixels outside the pupil on the detector image also contain phase information as their values will change depending on the amplitude of the incoming wavefront. However, the information they contain is not linear with the wavefront, and disregarded here. Yet, it is important to emphasise that even if only the pixels within the pupil are kept, the overall flux (inside and outside the pupil) is used to normalise the intensities. This ensures that the sensitivity plots are properly normalised, and can be used to compare WFSs in a fair manner.

As an illustration, it has been demonstrated in Chambouleyron et al. (2021a), that the classical ZWFS with a dimple size of $1.06\lambda/D$ is not optimal in terms of sensitivity, as almost half of the photons are ejected from the pupil support on the detector image. In other words, it means that only half of the photons contribute to the wavefront estimation (the linear information is contained in the pupil support). To improve the sensitivity a simple solution was to increase the size of the dimple, as a larger dimple will collect more photons in the pupil support. This resulted in a direct gain of sensitivity, demonstrating how the overall flux is properly taken into account in our sensitivity computation.

Note that in the following, and for seek of demonstration, I decided to stick to Zernike-type WFS of dimple size of $1.06\lambda/D$ and of phase-shift of $\pm\pi/2$. One could easily scale the results for different dimple sizes, following the results of Chambouleyron

et al. (2021a).

Back to the sensitivity estimation of the phase-shifted WFS, Fig 2.3 shows the results for the RON (left) and for the photon-noise (right). As the PS-ZWFS consists of two ZWFSs that produce two images on the detector, the RON sensitivity is directly reduced by a factor $\sqrt{2}$ compared to the classical ZWFS. However, the phase-shifted Zernike WFS remains more sensitive than the PWFS when only considering the RON (see red vs. green). As for the photon noise, the total flux remains unchanged, so the sensitivity is the same as that of the ZWFS, slightly below the PWFS one. As a reminder, the sensitivity curves were obtained for a Zernike-type sensor with dimple size of $1.06\lambda/D$ to stick with the classical ZWFS. To improve the photon noise sensitivity one has to increase the size of the dimple as demonstrated in Chambouleyron et al. (2021a).

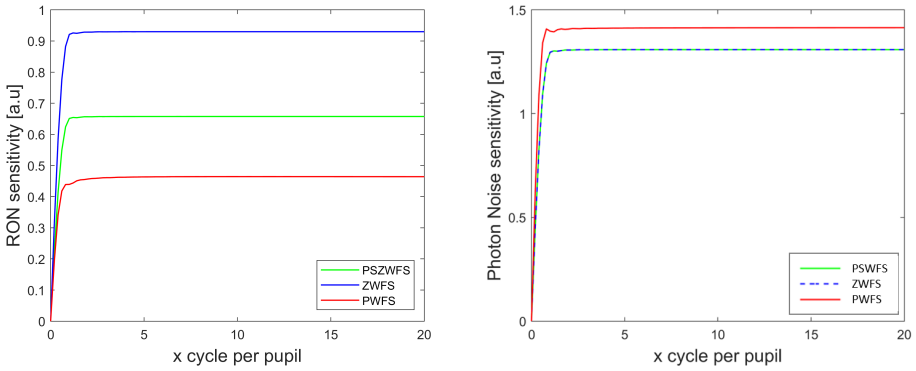

(a) RON sensitivity (b) Photon noise sensitivity

FIGURE 2.3 – Comparison of PS-ZWFS, ZWFS and PWFS sensitivities. Left : RON sensitivities. Right : Photon noise sensitivities.

As mentioned in the previous chapter, in section 1.4, the RON of state-of-the-art visible cameras is negligible, with technologies offering near-noiseless performance (RON $\ll 1e^{-1}/pix/frame$). With such advanced detectors, the fundamental noise limit in wavefront sensing is set by photon noise. In this photon-limited regime, the PS-ZWFS offers a significant advantage over the classical ZWFS. While both sensors have the same photon noise sensitivity, the PS-ZWFS benefits from a double dynamic range due to the phase diversity introduced by the two pupil images on the detector. The PS-ZWFS, by providing access to both the $sine$ and $cosine$ of the wavefront via phase diversity, not only increases the dynamic range, hence increases the estimation accuracy in low-SNR conditions. This larger dynamic range allows the PS-ZWFS to operate effectively in more challenging scenarios, such as under high wavefront aberrations or at low SNR regime, where the classical ZWFS might suffer from saturation or phase-wrapping issues. In these conditions, having a higher dynamic range is crucial for maintaining accurate wavefront correction while still operating within the photon noise limit.

2.1.3.2 Dynamic of the PS-ZWFS

The main focus of my PhD research is to investigate the dynamic range of highly sensitive wavefront sensors. In this section, I study the dynamical range of the PS-ZWFS and evaluate its accuracy in handling large phase amplitudes, comparing its performance with that of the classical ZWFS.

The analysis begins with a comparison of the dynamic range of the ZWFS and PS-ZWFS across different spatial frequencies. The sensitivity curves in Fig.2.3 suggest that the dynamic range should remain consistent across all spatial frequencies, as Zernike-type WFS exhibit constant sensitivity for spatial frequencies greater than 1 cycle per pupil.

To test this assumption, Fig.2.4 shows the linearity curves for low, mid, and high spatial frequency modes from the Karhunen–Loève (KL) basis, specifically KL_4, KL_{36}, and KL_{136}. For the ZWFS, we plotted the reconstruction curves for each mode using different reconstruction techniques : the interaction matrix (iMat), the analytical linear reconstructor (Linear), and the $arcsine$ reconstructor. For the PS-ZWFS, we used the $atan2$ function.

The dynamic range of a phase mask is defined here as the range where the relative error between the estimated and input coefficients is less than 10%, as explained in chapter 1. Table 2.1 summaries the dynamic range for both WFS types and each mode, based on the respective reconstruction methods.

KL modes	iMat	Linear	$arcsine$	$atan2$
KL_4	RMS : 0.33 PV : 1.17	RMS : 0.33 PV : 1.17	RMS : 0.33 PV : 1.17	RMS : 0.56 PV : 1.95
KL_{36}	RMS : 0.30 PV : 1.89	RMS : 0.30 PV : 1.89	RMS : 0.30 PV : 1.89	RMS : 0.56 PV : 3.49
KL_{136}	RMS : 0.30 PV : 1.64	RMS : 0.30 PV :1.64	RMS : 0.30 PV : 1.64	RMS : 0.59 PV : 3.19

TABLEAU 2.1 – Dynamic range in rad RMS (maximum absolute value) and in rad PV (maximum absolute value) of the ZWFS and the PS-ZWFS for different spatial frequency KL modes.

From the results in Table 2.1, we observe that the different reconstruction methods for the ZWFS exhibit the same dynamic range across low, mid, and high spatial frequencies. Specifically, each KL mode can be estimated with a relative error of less than 10% when its amplitude is within the range of $[-0.30; 0.30]$ rad RMS. In contrast, the dynamic range of the PS-ZWFS shows significant improvement, with an increase of 70% for low spatial frequencies and over 85% for mid and high spatial frequencies, from $[-0.30; 0.30]$ to $[-0.56; 0.56]$.

The theoretical analysis in the previous section predicted a dynamic range of π (PV) for the ZWFS when using the $arcsine$ reconstructor. However, this is not reflected

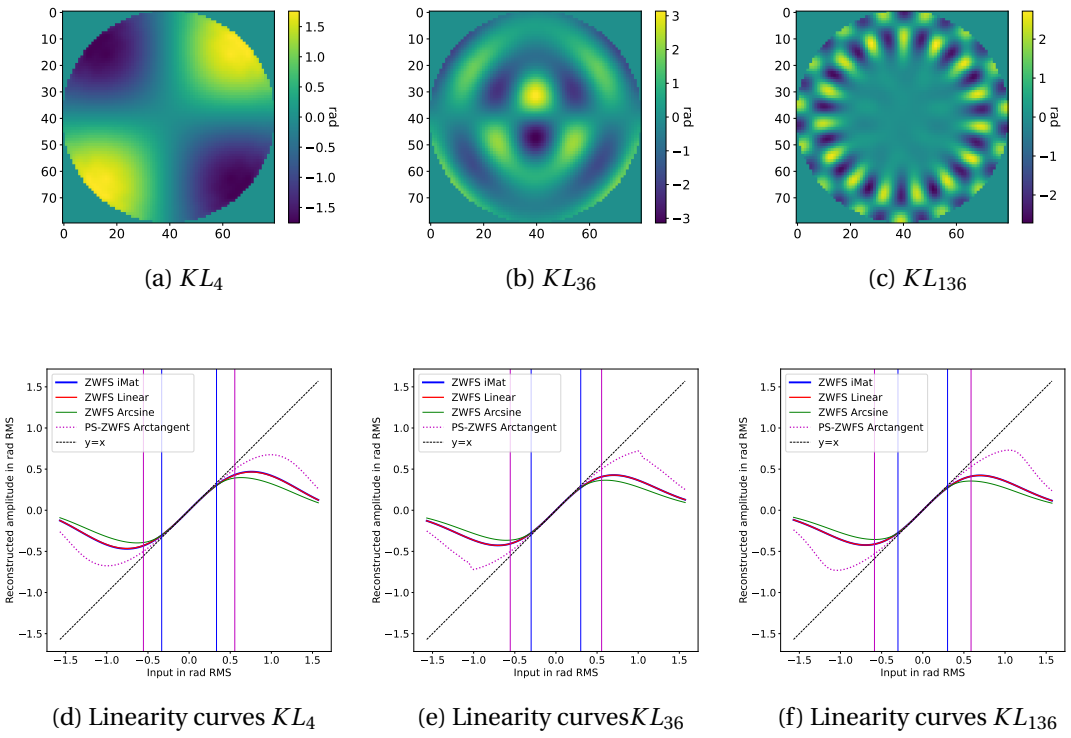

(a) KL_4 (b) KL_{36} (c) KL_{136}

(d) Linearity curves KL_4 (e) Linearity curvesKL_{36} (f) Linearity curves KL_{136}

FIGURE 2.4 – Dynamic study for the different KL modes from left to right KL_4, KL_{36} and KL_{136}. Top : KL mode of amplitude 1 rad RMS. Bottom : Linearity curves for the different modes of varying amplitude. The blue curve is the linearity curve obtained with iMat, the red one with the analytical linear model, the green one with the $arcsine$ reconstructor and the dotted-magenta curve with the $atan2$ reconstructor. The blue and magenta vertical lines represent the dynamic range of the ZWFS using the interaction matrix and the PS-ZWFS.

in our simulations for individual KL modes at various spatial frequencies. These discrepancies arise from the assumptions made during the mathematical derivation. The response of the ZWFS approximates a sine wave only under high Strehl ratio conditions. Figure 2.2 shows the intensity response of a single pixel when the input phase is a flat wavefront. In this ideal case, the signal can be inverted using the $arcsine$ function, provided the intensity and the wavefront of the reference are known. The key limitation of this approach is the assumption of a flat reference wavefront. When a phase mode is applied across the entrance pupil plane rather than a single pixel, the shape of the PSF is altered, invalidating the assumption of a flat reference wavefront (see Fig.2.5). Consequently, the model used to describe the relationship between phase and intensity (see equation 1.72) becomes inaccurate, as the actual reference wavefront is unknown, leading to inaccurate wavefront estimation. This explains why the $arcsine$ reconstructor yields results similar to those obtained using the interaction matrix or the analytical linear reconstructor.

The theoretical prediction of a doubled dynamic range for the PS-ZWFS was also based on the assumption of "small" phase amplitude. The same explanation applies here. For Zernike-type WFS, the phase mask filtering is most effective when the on-axis Strehl ratio is high. Once the PSF core begins to deviate from a diffraction-limited pattern, the filtering becomes less effective, and non-iterative reconstruction algorithms lose accuracy. However, with the additional diversity introduced by the PS-ZWFS, we successfully increase the dynamic range by 70%.

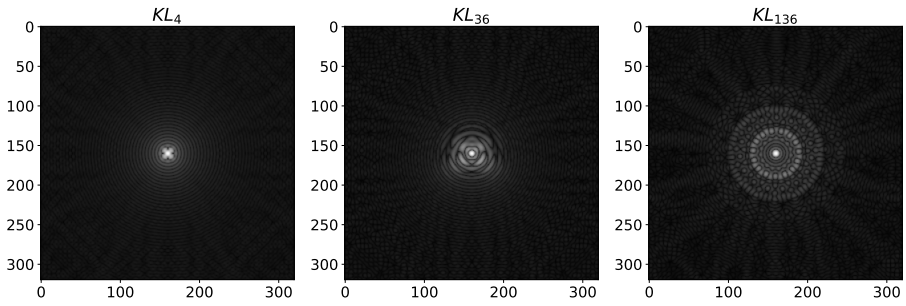

FIGURE 2.5 – PSF in logarithm scale of the KL modes : KL_4, KL_{36}, and KL_{136}, obtained for in input wavefront of amplitude 0.7 rad RMS.

To provide another perspective, we plotted in Fig.2.6 the wavefront error (WFE) of the KL modes KL_4, KL_{36}, and KL_{136} as a function of their amplitudes for the various reconstruction methods. For the classical ZWFS, the $arcsine$ reconstructor delivers the best performance for phase amplitudes below 0.4 rad RMS across different spatial frequencies. The accuracy of this reconstructor stems from its model-based approach. Since small phase aberrations minimally affect the PSF, assuming a flat reference wavefront in the reconstruction algorithm is valid under these conditions. However, as the phase amplitude increases, this assumption breaks down, and the $arcsine$ reconstructor becomes error-prone due to the incorrect reference wavefront. In another hand, the plot clearly shows that the PS-ZWFS significantly improves phase estimation, reducing the WFE by a factor of 2 for phase amplitudes below 1 rad RMS.

To further investigate the estimated phase, Fig.2.7 and Fig.2.8 show the residual coefficients and phase screens for an input phase amplitude of 0.7 rad RMS, which is outside the linear regime of both the ZWFS and PS-ZWFS. In this regime, the primary limitations are the underestimation of the wavefront (optical gain) and modal cross-talk, which reduce measurement accuracy. It is obvious that the classical ZWFS is more

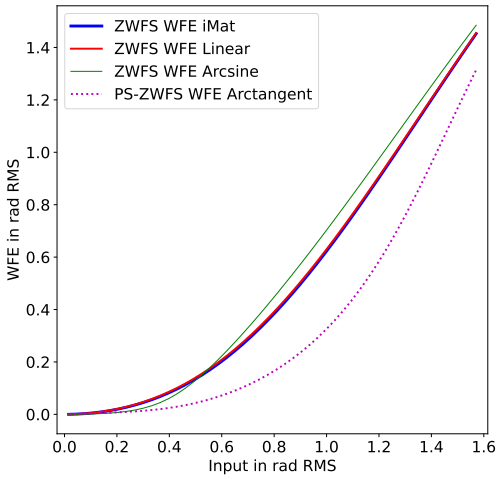

(a) KL_4

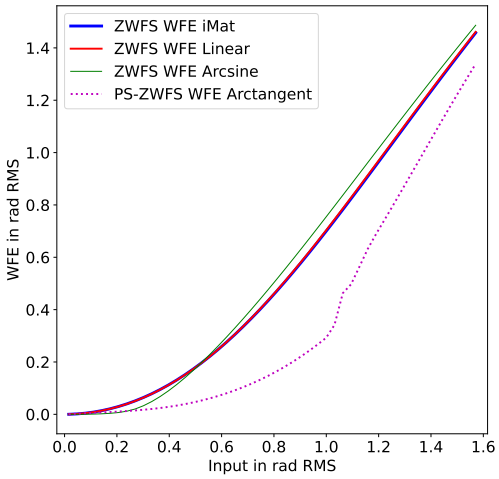

(b) KL_{36}

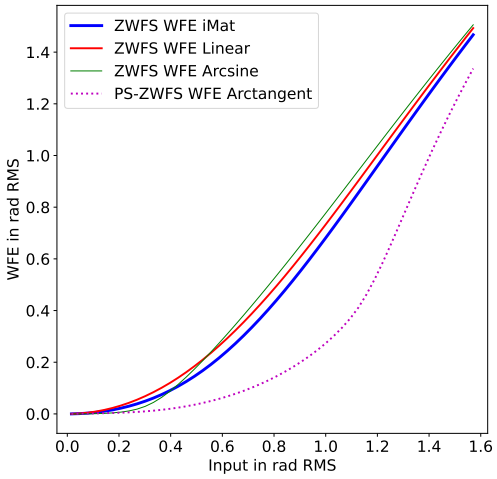

(c) KL_{136}

FIGURE 2.6 – WFE obtained for the different KL modes listed in Fig.2.4 with the different reconstructors : iMat, Linear and $arcsine$ for the ZWFS and $atan2$ for the PS-ZWFS.

affected by both optical gain and modal cross-talk compared to the PS-ZWFS, regardless of the reconstructor used. Specifically, the optical gain values for mode KL_4 are 66% and 84%, for KL_{36} are 61% and 85%, and for KL_{136} are 60% and 86%, when using the ZWFS (iMat) and the PS-ZWFS ($atan2$), respectively. Regarding modal cross-talk, it contributes between 15% and 5% depending on the mode and reconstruction method for the ZWFS, but it is absent in the estimations provided by the PS-ZWFS. These

phenomena reduce the accuracy of wavefront measurements, thereby increasing the WFE in the ZWFS. In contrast, for the PS-ZWFS, the non-linear effects primarily manifest as a gain issue, resulting in less impact on the overall accuracy.

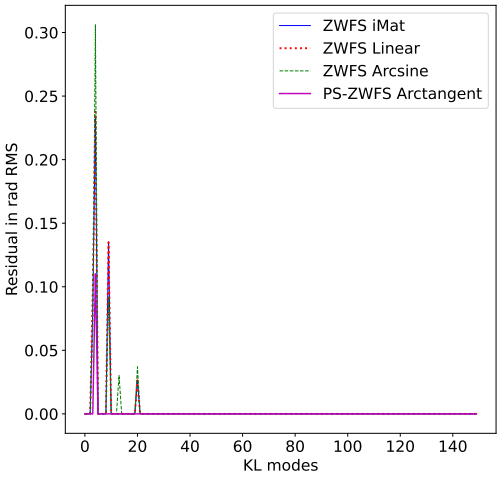

(a) KL_4

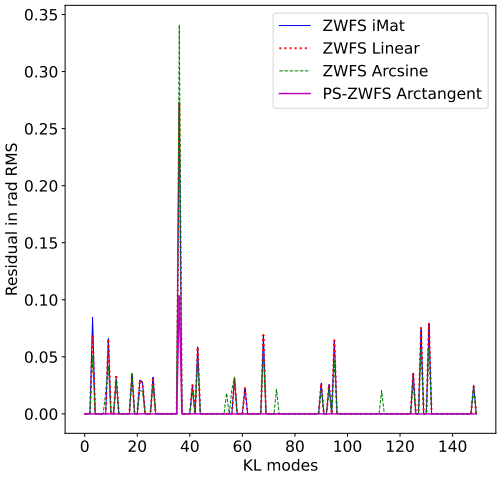

(b) KL_{36}

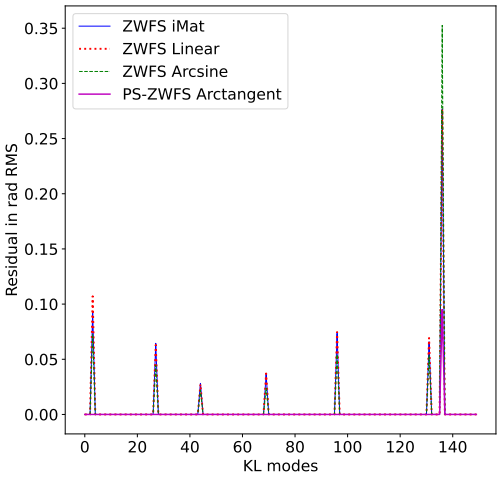

(c) KL_{136}

FIGURE 2.7 – Input modes of amplitude 0.7 rad RMS. Projection of the estimated phase with the different reconstructors : iMat, Linear and *arcsine* for the ZWFS and *atan2* for the PS-ZWFS.

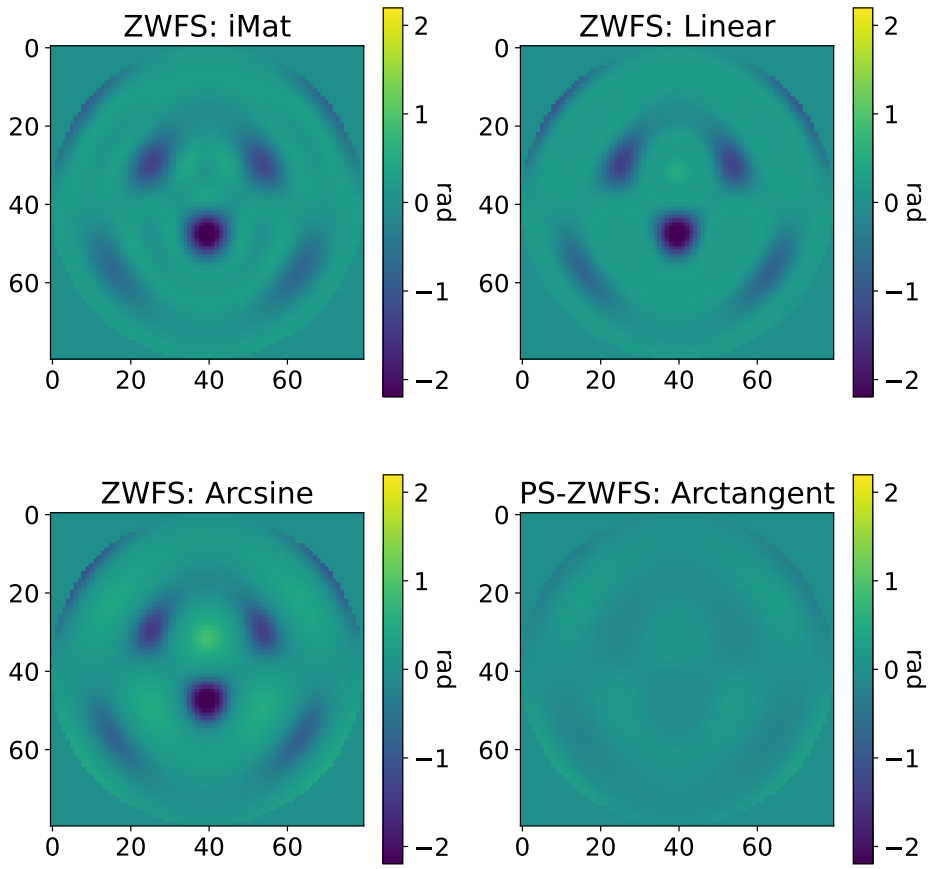

FIGURE 2.8 – Input mode KL_{36} of amplitude 0.7 rad RMS residual wavefront with the different reconstructors : iMat, Linear and $arcsine$ for the ZWFS and $atan2$ for the PS-ZWFS. The respective WFE are 0.35rad RMS (iMat), 0.35 rad RMS (Linear), 0.39 rad RMS ($arcsine$) and 0.11 rad ($atan2$)

Closed-loop dynamic range of Zernike-type WFS

The previous paragraphs introduced the dynamic range of Zernike-type WFS in an open-loop scenario. Yet, in wavefront sensing and control, the measurement is usually done in closed-loop. In that scenario, the dynamic range of the sensor will change. A simple explanation in the case of the ZWFS can be based on the sine response of the phase mask. Indeed as shown in Fig.2.2 and in Fig.2.9. The bijective regime of the ZWFS is $[-\lambda/8;3\lambda/8]$, the period of the sine wave is from $[-\lambda/4;3\lambda/4]$. If the incoming wavefront amplitude is within the range $[-\lambda/4;3\lambda/4]$ as pointed by the black crosses

in Fig.2.9, the phase will be underestimated at each iteration but the loop will converge because the sign of the estimated wavefront will be well estimated. In this scenario, at each iteration, the wavefront will converge till reaching the bijective regime of the WFS as depicted by the vertical red line. Once in this regime the WFE will reach zero. If the incoming wavefront amplitude is outside the range $[-\lambda/4;3\lambda/4]$ as pointed by the green crosses the sign of the estimated wavefront will be wrong making the loop diverge toward λ instead of zero. Therefore, in a close loop scenario, we can attest that the dynamic range of the ZWFS is $[-\lambda/4;3\lambda/4]$ so it is double compare to the open-loop dynamic range. However, as described in the previous paragraph, this description of the ZWFS response is representative under specific conditions (high SR regime, and PSF core not impacted by the aberrations) where the filtering of the phase mask is effective to encode the wavefront. In real condition, large amplitude wavefront affect the shape of the PSF making the filtering less efficient, thus modifying the response of the ZWFS so affecting the dynamic range in closed-loop scenario.

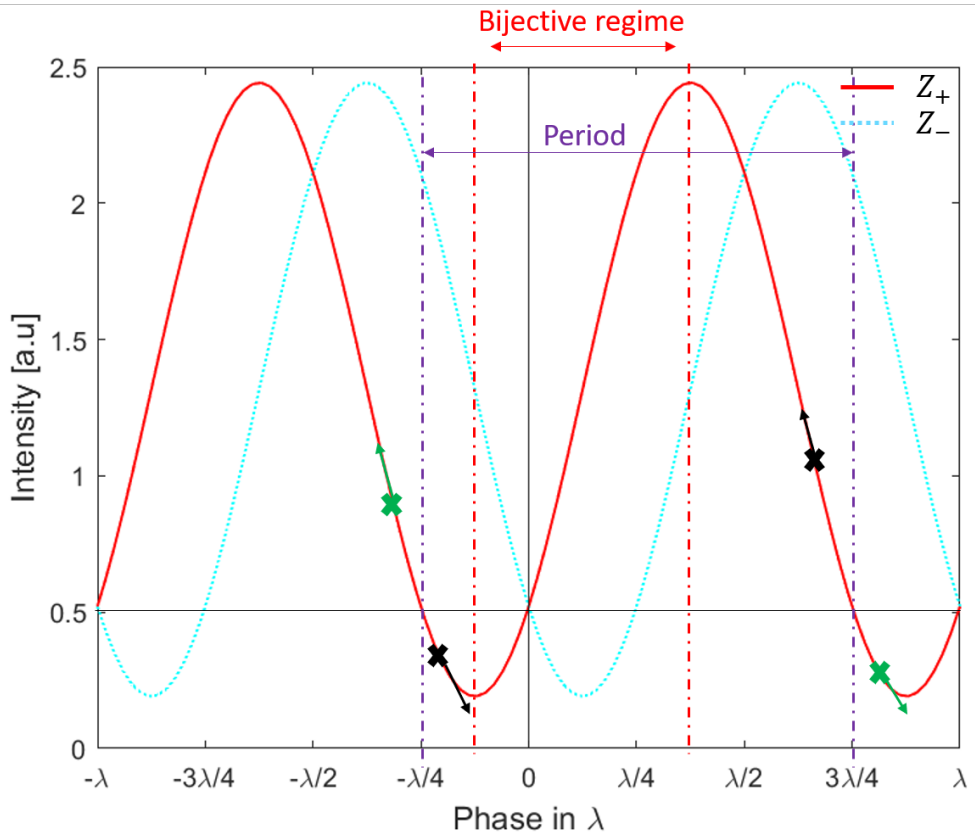

FIGURE 2.9 – Caption

To conclude this dynamic range study, we plotted the WFE as a function of phase amplitude for turbulent atmospheric phase screens in Fig.2.10. For this analysis, we conducted a statistical evaluation using $N = 20$ phase screens per amplitude. The phase screens follow the Kolmogorov spectrum and are projected onto 150 KL modes to minimise aliasing effects from higher spatial frequencies, which could distort

wavefront estimation. The atmospheric phase screens are normalised and then scaled from 0 to 1 rad RMS.

The simulation results align with the previous analysis of individual KL modes at different spatial frequencies. We observe the same trend with the $arcsine$ reconstructor, which performs best in the very small phase regime (< 0.5 rad RMS) when using a single Zernike mask. Beyond this threshold, the interaction matrix, the linear model, and the $arcsine$ reconstructor yield comparable results. However, the PS-ZWFS consistently outperforms the ZWFS across the entire phase amplitude range of [0;1] rad RMS. For larger amplitudes, the PS-ZWFS reduces the WFE by a factor of two compared to the ZWFS.

As an example, Fig.2.11 shows the residual phase screen for an atmospheric phase. With the ZWFS, all reconstructors struggle to reduce the WFE due to modal cross-talk and OG effects. The impact of OG is particularly evident in the top-left region of the input phase screen, where high phase amplitudes ($\phi > 1$ rad) are significantly underestimated and persist in the residual. In contrast, the PS-ZWFS is less affected by OG in these high-amplitude regions, allowing for better WFE reduction. For an input phase screen of 0.7 rad RMS, the PS-ZWFS reduces the WFE by a factor of two compared to the ZWFS.

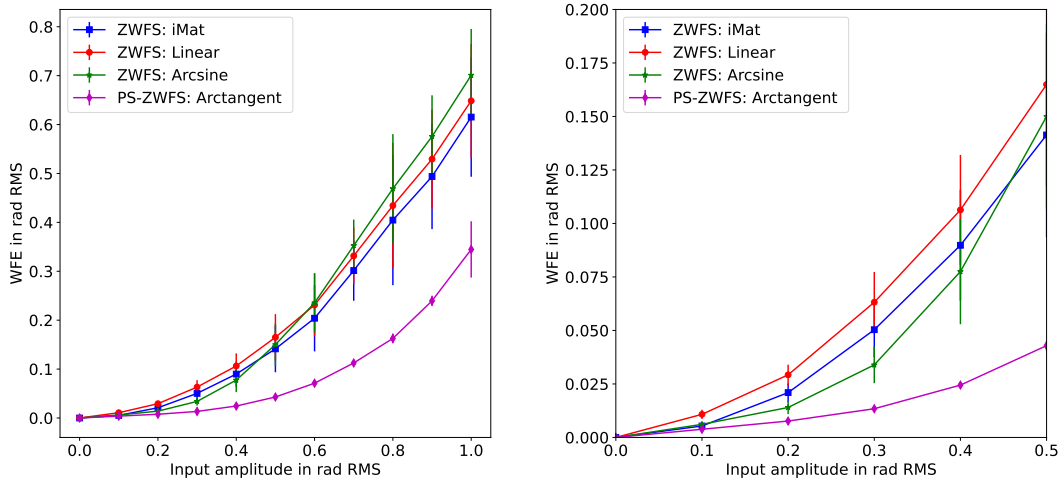

(a) (b)

FIGURE 2.10 – Average WFE as a function of the turbulent screen amplitude. The different reconstructors are : iMat, Linear and $arcsine$ for the ZWFS and $atan2$ for the PS-ZWFS. (b) Zoom on the range [0;0.5] rad RMS.

To further extend the dynamic range of both the ZWFS and PS-ZWFS, iterative algorithms present the most effective solution. The primary advantage of iterative methods, when using analytical formulas to estimate the wavefront, lies in the continuous updating of the reference wavefront. At each iteration, the reference wave is

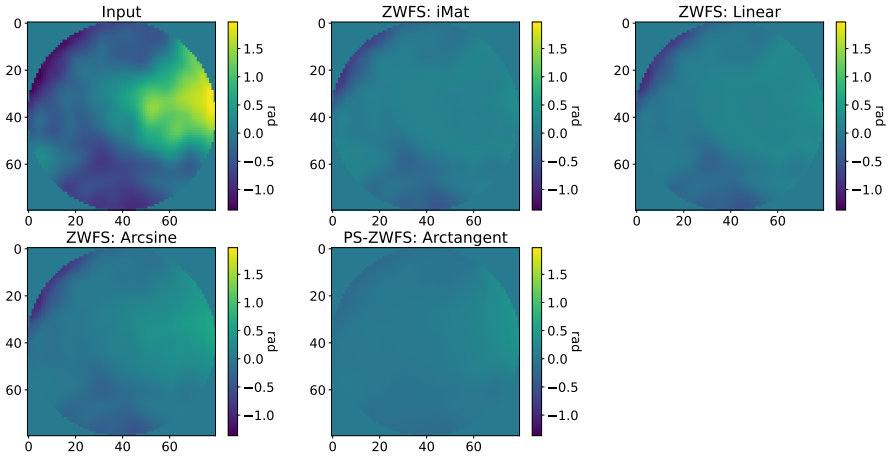

FIGURE 2.11 – Input phase of amplitude 0.7 rad RMS and residual wavefront with the different reconstructors : iMat, Linear and $arcsine$ for the ZWFS and $atan2$ for the PS-ZWFS. The respective WFE are 0.17rad RMS (iMat), 0.20 rad RMS (Linear), 0.24 rad RMS ($arcsine$) and 0.11 rad ($atan2$)

refined to more closely match the actual wavefront, resulting in increasingly accurate phase measurements. This approach has been demonstrated in a study I did during a visit at UCSC in the scope of the OWL program, along with Vincent Chambouleyron (Chambouleyron et al. 2024), and a figure from that study is shown in Fig.2.12.

The iterative process unfolds as follows : at iteration 0, it is assumed that the phase and intensity of the reference wavefront (β and I_b) are known (flat reference). At iteration 1, an initial phase estimate ϕ is computed using equation 1.72. In iteration 2, an updated reference phase and intensity (β' and I'_b) are derived from the prior phase estimate. The process is then repeated, with each new iteration producing an increasingly accurate phase estimate ϕ'.

The benefit of iterative correction is especially pronounced when using the PS-ZWFS. For instance, at a phase amplitude of 1 rad RMS, the iterative approach reduces the WFE by a factor of 7 compared to the iterative method applied to the ZWFS. Furthermore, for phase amplitudes below 0.6 rad RMS, the WFE is effectively reduced to 0 rad RMS. Achieving similar results with the ZWFS would require the use of phase probes, as discussed in (Haffert 2024).

2.1.3.3 Summary and application of the PS-ZWFS

In this section, we have demonstrated the significant gain in dynamic range achieved by using the PS-ZWFS over the classical ZWFS. The additional diversity introduced by the two pupil images on the detector allows for more than a 70% increase in dynamic range for a given phase mode and reduces the WFE by a factor of two when the wavefront amplitude is below 1 rad RMS. This improvement underscores the

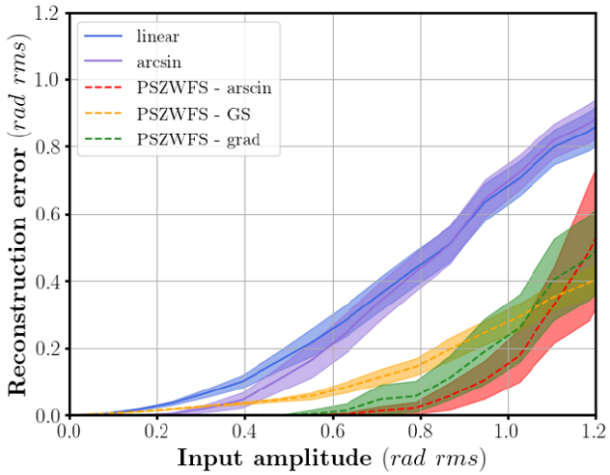

FIGURE 2.12 – Iterative approach *Credits : Chambouleyron et al. (2024)*

PS-ZWFS's ability to handle larger wavefront aberrations more effectively than the classical ZWFS.

Additionally, we discussed the use of iterative algorithms, as proposed in (Chambouleyron et al. 2024; Haffert 2024), to further expand the dynamic range of the PS-ZWFS. Iterative methods, by continuously updating the reference wavefront, can significantly enhance wavefront reconstruction accuracy, enabling better performance across a wider range of phase amplitudes. However, the iterative approach is not adapted for the real time constraints of wavefront sensing and control as the estimation process is longer than the standard linear approach. Nonetheless, with approaches such as Deep-Learning it is possible to develop non-linear phase reconstruction algorithm.

However, despite the increased dynamic range of the PS-ZWFS, there are still inherent limitations to its use due to the nature of Zernike-type wavefront sensors. Simulations on atmospheric phase screens illustrate these challenges clearly. While we focused on phase screens with amplitudes below 1 rad RMS, real atmospheric turbulence can have amplitudes up to ten times greater. In such cases, Zernike-type WFSs become ineffective, as they are unable to close the AO loop. This is due to the distortion of the PSF under large wavefront aberrations : instead of forming an Airy pattern, the PSF becomes dominated by speckles. As a result, the coherent core of the PSF, which provides the reference wavefront, is lost. Without this coherent core, interference patterns disappear, and the detector captures a nearly uniform intensity, preventing accurate wavefront measurement. In these conditions, it is impossible to "bootstrap" the AO loop using a Zernike-type WFS.

Thus, Zernike-type WFSs are mostly suitable in limited situations, such as in multi-stage AO systems where they operate after an initial correction, or for detecting specific types of phase aberrations such as phase discontinuities. These constraints highlight that Zernike-type sensors, while powerful in controlled regimes, are not viable for direct use in highly turbulent environments without supplementary corrections or enhancements.

In the following section, I will explore the application of Zernike-type WFSs in multi-stage AO systems. First, I will investigate their use for measuring differential piston on an ELT-like pupil. I will then examine the potential of Zernike-type sensors in high-contrast imaging, where they could play a role in cascaded AO systems to enhance performance close to the host star.

2.2 Applications to multi-stage AO systems

2.2.1 Measurement of differential piston using the PS-ZWFS

As introduced in chapter1, section1.3, Giant Segmented Telescopes (GST) may be prone to the building of a very specific aberrations called differential piston, or "petal modes". This aberration is a result of the large shadow introduced by the spiders of these telescopes, creating discontinuity in the pupil and in the AO WFS measurements. Standard WFSs, like the SH or the modulated PWFS are blind to such aberrations, while it can represent a large fraction of the final error budget for the AO systems.

First-light instruments of the ELT are addressing this differential piston effects from the control point of view by constraining DM actuators. For instance, Schwartz et al. (2018) introduced DM "minioning" to ensure wavefront continuity across the spider, reducing differential piston. Although the minioning of the DM enables to drastically reduce the differential piston, it does not solve entirely the problem and residual jumps of differential pistons, called "petal flares", appear in the AO simulations. These events degrade the quality of the AO corrections, which can have a detrimental impact especially for high-contrast instrument. To improve the performance, it would be necessary to implement a WFS dedicated to the petal estimation, so-called "petalometer". Examples of petalometers can be found in Bertrou-Cantou et al. (2020) or Levraud et al. (2024a). First introduced by Bertrou-Cantou et al. (2020) that expanded the work of Schwartz et al. (2018) by proposing a continuous basis that further reduces differential piston, along with a dedicated WFS to minimise residual petal errors. And continued by Levraud et al. (2024a) who proposed a two-path system with a modulated PWFS for atmospheric turbulence control and a petalometer made by a non-modulated PWFS with spatial filtering to limit the impact of the AO residuals on the petal estimation.

In this section we follow the work of Bertrou-Cantou et al. (2022) and Levraud et al. (2024a) to quantify Zernike-type WFS performance at measuring and controlling the petal modes as a petalometer. For that, we make use of AO corrected phase screens from an ELT simulation provided by Charlotte Bond (Research engineer at UKATC) (Bond et al. 2022) in the frame of the SCAO system of HARMONI. The parameters of the AO loop are listed in Table 2.2

Without any additional correction, this AO loop provides residual phase screens of average amplitude of 1.05 rad RMS ($@\lambda_{wfs}$) corresponding to a WFE of 145 nm RMS

Telescope	38.542m diameter
Resolution	400×400 pixels
WFS	PWFS $r_{mod} = 3\lambda/D$
WFS resolution	100×100 pixels
DM	4000 KL modes, from ELT M4 influence functions
Sensing wavelength	$\lambda_{wfs} = 800$ nm
Frequency	500 Hz
Noise	photon noise and $0.3e^{-1}/pix/frame$ RON
Seeing	$0.65''$ at 30° zenith
Atmospheric layers	3 layers
Average wind	$v = 8m.s^{-1}$
Telescope's wind shake	$8m.s^{-1}$
Star magnitude	8 (bright star)
SR	H-band @1.65μm or K-band @2.2μm

TABLEAU 2.2 – Simulation parameters of the ELT AO loop

(see Fig.2.13(a)). The phase screen where saved every 0.2 second corresponding to a total of 8 seconds simulation.

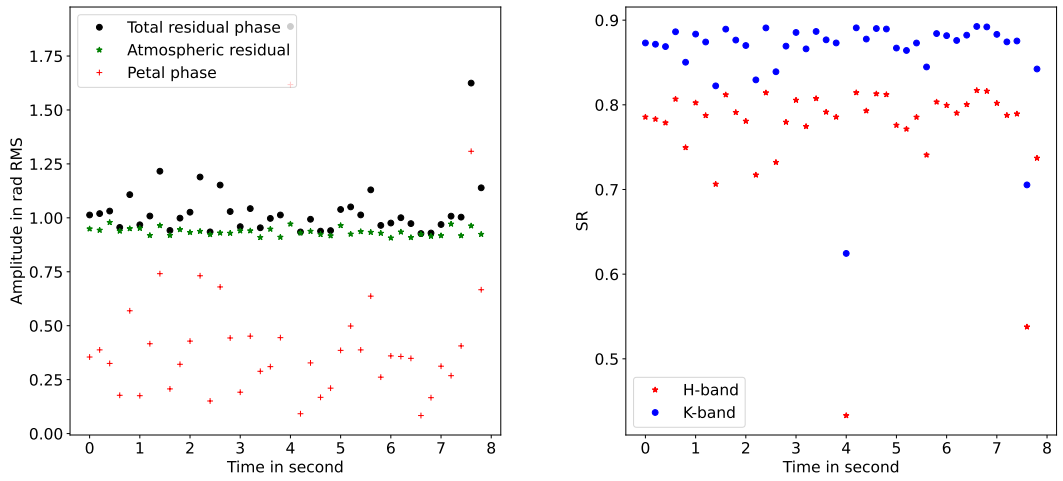

(a) (b)

FIGURE 2.13 – (a) Amplitude of the residual phase screens of the ELT AO-loop simulations. The black dot correspond to the total amplitude of the phase screen. The green stars correspond to the amplitude of the atmospheric residual (differential piston removed) and the red crosses to the amplitude of the differential piston for each screens. (b) SR in H-band and K-band for each phase screen of the ELT AO-loop simulations.

The SR in the H and K bands were computed for each phase screen using equation

1.40 and are presented in Fig. 2.13(b). The average SR achieved in the H-band is 77%, while the K-band reaches an average SR of 86%. Note that this SR accounts only for turbulence residuals, not for additional perturbations coming from the telescopes (windshake, etc ...). This plot reveals a noticeable drop in SR values at 4s and 7.6s, attributed to the build-up of a differential piston, the so-called "petal-flares" introduced above. Specifically, the differential pistons for these screens reach 1.62 rad RMS (equivalent to $\lambda_{wfs}/4$) and 1.31 rad RMS ($\lambda_{wfs}/5$) at the wavefront sensing wavelength, respectively, as shown in Fig. 2.14(top). This differential piston amplitude distorts the wavefront, reducing the achievable SR. The corresponding PSFs for these phase screens are displayed in Fig. 2.14(bottom), providing an illustration of the impact of these phase discontinuities on image quality. As an example, the SR is divided by two between the two instant 4s to 4.2s, describing a situation of high differential piston (at 4s), to a situation without piston (at 4.2s).

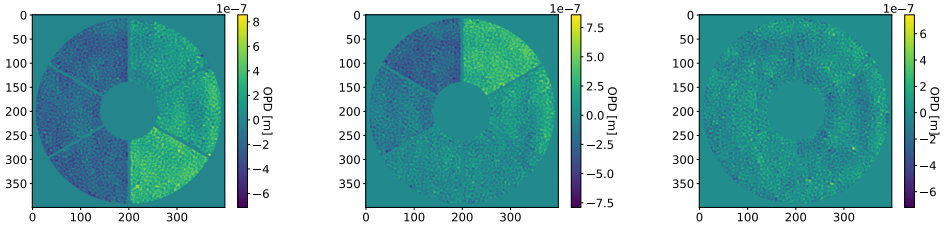

(a) Phase screen at 4s, SR_H = 43%, petal=$\lambda_H/8$ RMS

(b) Phase screen at 7.6s, SR_H = 54%, petal=$\lambda_H/10$ RMS

(c) Phase screen at 4.2s, SR_H = 81%, petal=$\lambda_H/142$ RMS

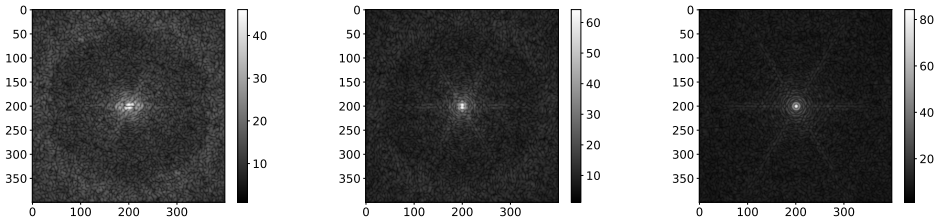

(d) PSF at 4s

(e) PSF at 7.6s

(f) PSF at 4.2s

FIGURE 2.14 – Turbulence phase screen with and without differential piston. Impact of the differential piston on the PSF at different time of the simulation. Top : Phase screen at 4, 7.6 and 4.2 seconds. Bottom : PSFs displayed in logarithm scale to highlight the differential piston effect. Their respective differential piston amplitude are [0.78;0.63;0.04] rad RMS @λ_H.

The next paragraph aims at quantifying the capability of the Zernike-type WFS in accurately measuring the differential piston in the presence of AO residuals.

The data, received from the ELT simulation in the frame of the SCAO system of HARMONI had an amplitude of around 1rad RMS @λ_{wfs} (cf Fig.2.13), so beyond the dynamic range of both the ZWFS and the PS-ZWFS (see section 2.1.3.2). We are then interested to test if a ZWFS or a PS-ZWFS could still be effective as a potential

petalometer. For this analysis, we focus on the phase screens presented in Fig.2.15. The procedure will be the following : (1) the initial differential piston component is subtracted from the AO residuals, (2) we inject back a single differential piston of varying amplitude, and compute the linearity response of the ZWFS and the PS-ZWFS.

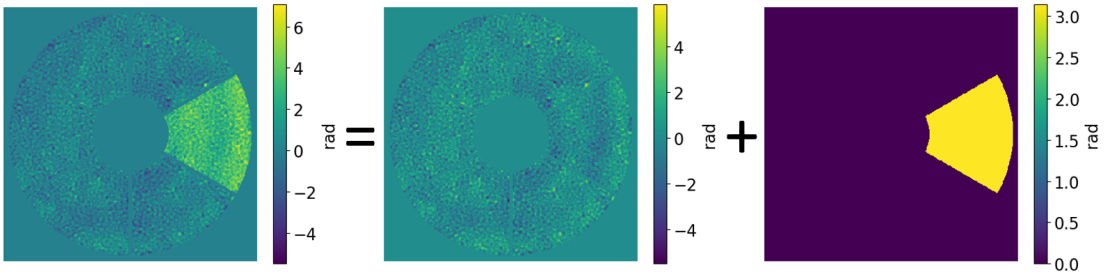

FIGURE 2.15 – ELT phase screen with varying differential piston. The amplitude of the residual is equal to 0.93 rad RMS @λ_{wfs} which corresponds to 118 nm RMS, so $SR_H = 81\%$.

Figure 2.16 shows the reconstruction curve of the petal mode both in the absence and presence of AO residuals. In this plot, we show the PV amplitude of the estimated petal as a function of the PV amplitude of the input petal. In the absence of AO residuals, we observe the expected periodic curve characteristic of petal mode reconstruction, as the estimation encounters the inherent λ-ambiguity. The signal will wrap so a petal of $\lambda/2$ PV amplitude provides the exact same signal as when no petal is present. These curves also demonstrate the limit of the analytical model. Indeed, as the petal amplitude increases, the shape of the PSF changes, while the analytical reconstructor assumes a flat reference wavefront, resulting in an underestimation of the petal mode.

In the presence of AO phase residuals with an amplitude of 118 nm RMS ($SR_H = 81\%$), we observe a reduction in the amplitude of the reconstruction curve (dashed-green plot and dotted-magenta plot), which limits the accuracy of petal mode measurement. Although the petal's amplitude may fall within the dynamic range of the phase mask, the overall amplitude of the phase screen exceeds the sensor's range (with an amplitude > 0.3 rad RMS for the ZWFS and > 0.6 rad RMS for the PS-ZWFS, as described in section 2.1.3.2). This high amplitude wavefront induces a significant alteration in the intensity pattern, which distort the estimation of the petal mode. This behaviour illustrates the OG issues, where the Zernike-type WFS underestimates the wavefront amplitude when operating conditions differ from those used in the reconstruction model. Again this is a direct consequence of the flat reference wavefront assumption, the model used to reconstruct the wavefront is wrong (cf equation 1.72). Yet, the PS-ZWFS is less affected by the OG as its dynamic range is larger than the one of the ZWFS.

The previous paragraph compared the PS-ZWFS and ZWFS abilities to retrieve petals in presence of AO residual. And as expected the PS-ZWFS presents a better dynamic behaviour as it is less affected by the OG and the cross-talk in presence of AO residuals

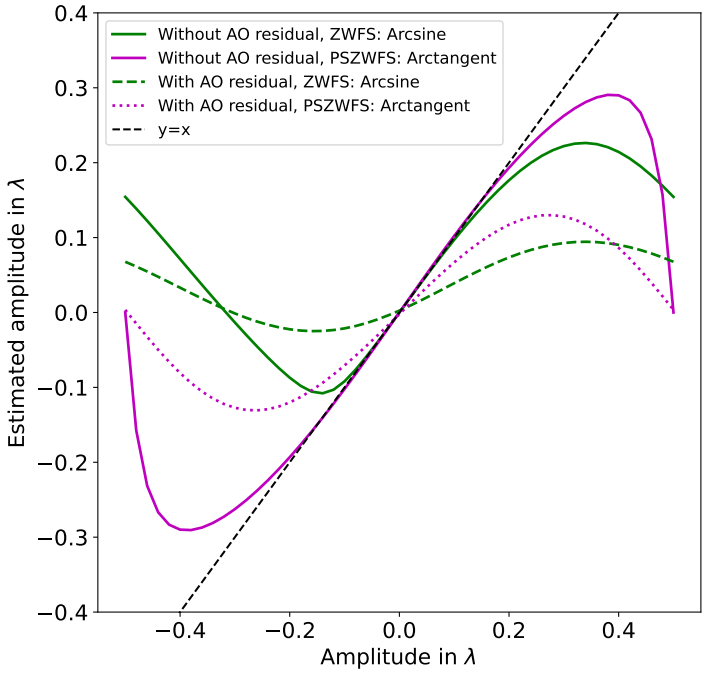

FIGURE 2.16 – Linearity curve of a petal mode with and without phase residual. The phase residual amplitude is 0.93 rad RMS $@\lambda_{wfs}$ (so $SR_H = 81\%$). We compare the $arcsine$ and the $atan2$ reconstructors respectively for the ZWFS and the PS-ZWFS.

corresponding to a SR of 81% in H-band. Now we test and compare these WFSs in the framework of a control loop. For that, we will assume a scheme similar to the one of Levraud et al. (2024a), where a dedicated WFS is devoted to the petal measurement. In our case this WFS will be either a ZWFS or a PS-ZWFS. The simulation conditions are the ones given in Table2.2. The principal AO loop is a modulated pyramid WFS, and our petalometers will work at the same visible wavelength.

Knowing that the input data is outside the dynamic regime of our sensors, we will make use of an iterative approach to reconstruct the petal modes from the ZWFS or the PS-ZWFS. The idea underneath is to mitigate the non-linear behaviour of these sensors in presence of large aberrations. As an illustration, Fig.2.17 shows the petal estimation for one data screen, after several iterations. We note that after only 2 iterations the PS-ZWFS reaches the minimum WFE for the differential piston when the ZWFS needs more iterations to reach its minimum value (0.05rad RMS). The ZWFS does not allow to null the differential piston because of mode confusion and cross-talk, as shown in Levraud et al. (2024a). In the following we therefore consider a petalometer working with 2 iterations, and we will compare the performance of the ZWFS and the PS-ZWFS.

Results are presented in Fig.2.18, where the green curve shows the residual when using a ZWFS and the magenta curve are the results for the PS-ZWFS. The average

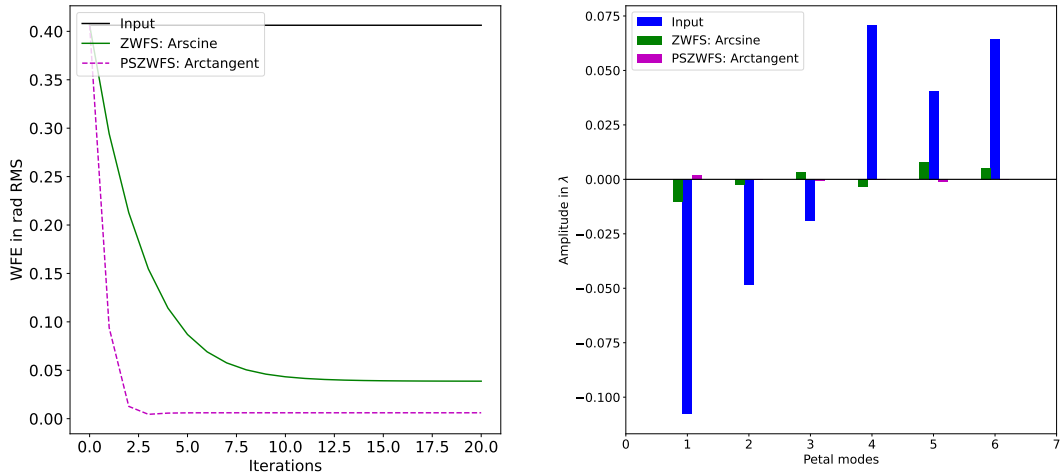

(a) Phase screen at 7.4s : AO Loop on the differential piston

(b) Phase screen at 7.4s : Residual differential piston coefficient after 20 iterations

FIGURE 2.17 – (a) AO loop of 20 iterations on the differential piston at 7.4s. (b) Coefficient of the residual piston at the end of the AO loop.

WFE in nm RMS of input differential piston is 53nm RMS. The remaining residual petal is 10 nm RMS with the PS-ZWFS and 28 nm RMS with the ZWFS. So a reduction of differential piston by a factor 5 in average when using the PS-ZWFS and a reduction by a factor 3 between the PS-ZWFS and the ZWFS. The average SR in H-band is respectively 80% or 79% if using a PS-ZWFS or a ZWFS. Hence an increased of 3 points compare to the scenario without the petalometer (cf Fig.2.13(b)), when using the PS-ZWFS. The gain in SR can appear to be small, however, the improvement in terms of contrast would be significant (Guyon 2005; van Kooten et al. 2022; Jensen-Clem et al. 2021; Ragland et al. 2022).

The remaining issue in this simulation is the estimation of large differential piston such as the one at 4s and 7.6s. The iterative process with only two iterations to measure these pistons is not effective. This is due to the high amplitude of the input piston, respectively of amplitude $\lambda_{wfs}/4$ RMS and $\lambda_{wfs}/5$ RMS. This is at the limit of the bijective regime of the ZWFS and the PS-ZWFS and the phase estimation may suffer from the λ wrapping.

One solution to avoid this situation is to have a petalometer working in the infrared. The amplitude of the differential piston will be smaller see Fig.2.19 - as an example, the differential piston of these screen in H-band is respectively 0.31λ PV and 0.32λ PV - so within the dynamic range of both sensor - making the H-band petalometer to converge.

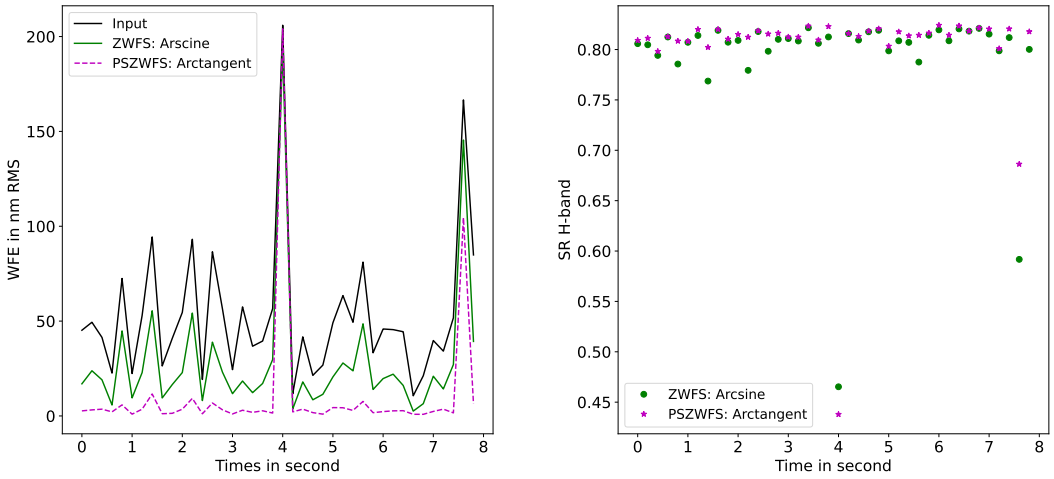

(a) Differential piston WFE (b) SR_H

FIGURE 2.18 – (a) Petalometer loop : Differential piston WFE versus the screen numbers. Each differential piston is estimated in two step measurement. (b) SR in H-band per phase screens.

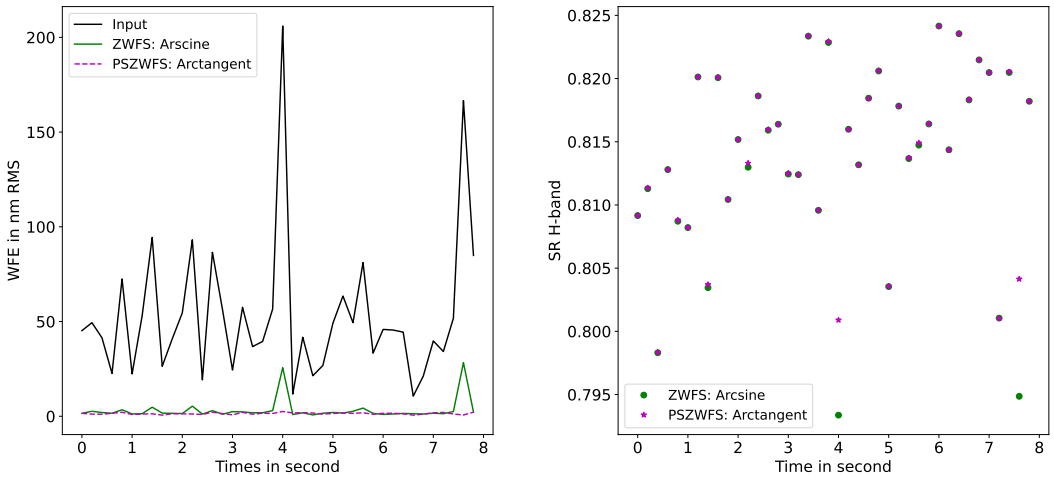

(a) Differential piston WFE : petalometer in H-band (b) SR_H

FIGURE 2.19 – (a) Petalometer in H-band. (b) SR in H-band

Summary

The combination of the minioning of the DM actuator on both side of the spider and a dedicated WFS to measure and control the residual petal allows to drastically

reduce the petal flares of the ELT AO loop. The use of the PS-ZWFS has to be preferred to the one of the classical ZWFS as it is more robust to the presence of phase residuals (SR_H = 76%) This scenario complicates the optical set up as a second WFS would have to be inserted in the AO WFS path, potentially sharing the photons with the main AO loop, or, if possible, making use of NIR photons. This could be done in the context of a multi-stage AO system which second loop aiming at controlling both the differential piston and reducing the temporal error of the main loop. The scenario of a loop dedicated to the fast control of AO residuals will be studied in the following section.

2.2.2 Cascaded-AO system for AO residuals control

The previous section ended with the use of Zernike-type WFS to measure specific aberrations, such as the phase discontinuities characteristic of the GST. We found that the PS-ZWFS is preferable because it offers better estimation of the differential piston between segments, especially in the presence of AO residuals (SR of 76% in J-band), due to its larger dynamic range. This gives us confidence in the feasibility of implementing Zernike-type sensors, particularly the PS-ZWFS, for controlling and measuring petal modes.

Another potential application of Zernike-type WFS would be in measuring phase residuals to enhance the AO correction, in a multi-stage configuration. For instance, a three-stage AO system is planned for the GMT with GMagAO-X (Haffert et al. 2022), featuring a Low-Order (LO) loop using a PWFS, a High-Order (HO) loop using a ZWFS and a dedicated piston sensor (HDFS), and a focal plane WFS for Non-Common Path Aberrations (NCPA) control. Additionally, the SPHERE AO system, SAXO, is set to undergo an upgrade - SAXO+ (Vidal et al. 2022; Mazoyer et al. 2024; Schreiber et al. 2023) - to increase contrast closer to the star and search for planets located between 3-10 AU. This upgrade implements a second stage AO loop, with a NIR PWFS and will serve as a technological demonstrator for a future XAO instrument for the ELT (Planetary Camera and Spectrograph (PCS) - Kasper et al. (2021).

Multi-stage AO systems can have different objectives depending on their architecture, but they all share a common goal of enhancing AO system performance. The specific architecture I am interested in is a cascaded AO system consisting of two WFS and two DMs. In this setup, the second stage is equipped with a LO DM that operates at a faster rate than the first DM, reducing the temporal error of the first stage for LO spatial frequencies. This design aims at improving AO correction at small inner-working angles, which is crucial for observing planetary systems located close to their host stars (as discussed in the Introduction of this manuscript).

The architecture of the considered AO system is illustrated in Fig. 2.20. In this setup, the residual errors from the first stage are sent to a faster second stage, and the residual phase after the second stage is then sent to the science instrument. The wavelengths used by the two WFS and the science instrument might be different. A key advantage of this configuration, in terms of implementation, is that the second stage operates independently of the first, allowing it to be integrated into the AO system

without modifying the first stage. Additionally, the stroke required on the second DM to correct LO modes is reduced, as it only needs to address AO residuals. Finally, this configuration allows the second stage to reduce the temporal error of the AO system by operating at a higher speed than the first stage (Cerpa-Urra et al. 2022). Other approaches for managing the 2 stages are possible, but my goal here being to study the impact of WFS choices, I will focus on this simple implementation.

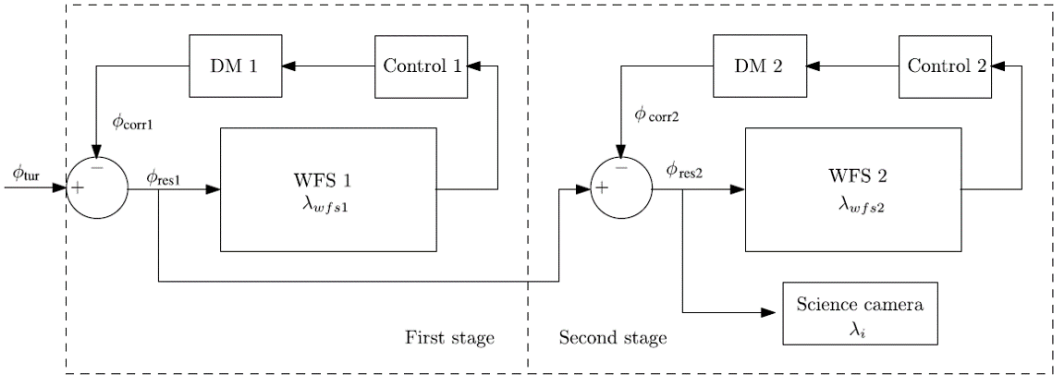

FIGURE 2.20 – Architecture of a cascade AO system. *Credits : Cerpa-Urra et al. (2022)*

2.2.2.1 Proposed AO system for evaluation

For the purpose of studying the impact of the WFS choices, we decided to use a 2 stage AO system defined with the parameters of Table 2.3.

First, we derive the error budget of the 1st stage, in order to get an idea of the level of correction provided, and define what the 2nd stage will see. To compute this AO error budget, we suppose that the two loops have a standard two-frames delay, with a standard integrator controller, and the 2nd stage will start after the bootstrap of the 1st stage. The AO error budget of the first stage is composed of the fitting error, the temporal error and the one induced by the WFS (noise). The errors terms are computed for the visible scientific wavelength $@\lambda_3 = 750nm$.

$$\sigma^2_{\phi} = \sigma^2_{fit} + \sigma^2_{tempo} + \sigma^2_{WFS}.$$

The fitting error is equal to

$$\begin{aligned} \sigma^2_{fit} &= 0.23\left(\frac{d_{act}}{r_0}\right)^{5/3} \\ &= 0.29 rad^2 \text{ best seeing case} \\ &= 0.58 rad^2 \text{ worst seeing case.} \end{aligned}$$

Telescope	8m
Resolution	160×160 pixels
DM_1	800 KL modes
WFS_1	PWFS $r_{mod} = 3\lambda/D$
WFS sampling	40×40 pixels
WFS wavelength	$\lambda_1 = 700$nm
RON	$0.2e^{-1}/pix/trame$
Frequency	1000 Hz
DM_2	200 KL modes
WFS_2	Zernike-type WFS ($1.06\lambda/D$ dimple)
WFS sampling	20×20 pixels
WFS wavelength	$\lambda_2 = 700$nm or $\lambda_2 = 1215$nm
RON	$0.2e^{-1}/pix/trame$
Frequency	3000 Hz
r_0	[10; 15] cm @500nm
Atmosphere	3 layers
Average wind	$13m.s^{-1}$
Star magnitude	7 in I band
Science wavelength	$\lambda_3 = 750$nm
Time of the loop	3s

TABLEAU 2.3 – Parameters of the two-stages AO system

The temporal error is equal to

$$\begin{aligned}\sigma^2_{tempo} &= 6.88\left(\frac{\bar{v}\tau}{r_0}\right)^{5/3} \\ &= 0.05 rad^2 \text{ best case} \\ &= 0.11 rad^2 \text{ worst case.}\end{aligned}$$

I will only consider the WFS error linked to the noise, the formula is from Chambouleyron et al. (2023), where N_{spp} stands for the number of pixels, σ^2 the RON of the camera, s^2_{ron} the RON sensitivity, s^2_{ph} the photon noise sensitivity and N the number of photons per frame

$$\begin{aligned}\sigma^2_{WFS} &= \frac{N_{spp} \times \sigma^2}{s^2_{ron} \times N^2} + \frac{1}{s^2_{ph} \times N} \\ &= 2 \times 10^{-3} rad^2.\end{aligned}$$

The total error budget of the first stage is

$$\begin{aligned}\sigma^2_\phi &= 0.35 rad^2 \text{ best case} \\ &= 0.69 rad^2 \text{ worst case.}\end{aligned}$$

Note that the error budget does not take into account the error induced by the reconstructor (non-linear error), thus this error budget is describing an ideal case where the PWFS of the first stage does not suffer from OG issues or cross-talk terms. The phase variance corresponds to a WFE of 66 nm RMS in the best case scenario - r_0 = 15cm @500nm - (respectively 92nm RMS in the worst case scenario - r_0 = 10cm @500nm). The expected SR according to Le Maréchal formula, given in equation 1.40, is $SR = 70\%\ @\lambda_3$ (respectively $SR = 50\%\ @\lambda_3$).

2.2.3 Choice of the second stage WFS

The choice of the second stage WFS is imposed by two different things : (i) the wavelength of the second stage λ_2 (ii) the level of aberrations after the first stage. The two aspects are linked and have to be driven by the scientific objectives. Especially when considering Zernike-type WFS, it is important to limit their non-linear behaviours in order to reach the expected level of correction close to the host star.

According to the dynamic study made in the previous section 2.1.3.2 and the AO error budget of the first stage, we are expecting around 90 nm RMS of WFE at the entrance of the second stage in the worst seeing case scenario. Therefore, in this scenario, the expected level of aberrations seen by the Zernike-type WFS will be :

1. If $\lambda_2 = \lambda_1 = 700$nm, $WFE = 0.83$rad RMS @700nm ($\approx \lambda_1/7$ RMS)
2. If $\lambda_2 = 1215$nm, $WFE = 0.48$rad RMS @1215nm ($\approx \lambda_2/13$ RMS)

In the case of the two WFS working at the same visible wavelength, the level of aberration is beyond the dynamic range of both the ZWFS and the PS-ZWFS. Yet, according to the study made in the previous section and especially Fig.2.10, the PS-ZWFS will be more effective as it will be able to reduced the WFE of the incoming wavefront by at least factor 2 in comparison to the use of the ZWFS. With the second WFS working in the NIR, the incoming wavefront at the entrance of the second stage is nearly diffraction limited ($\approx \lambda/13$) which will make the AO loop converge with any of the Zernike-type WFS, the ZWFS or the PS-ZWFS. In that scenario, I am expecting the same level of performance with both sensors.

The two configurations I will consider are : (i) a multi-stage system with a second WFS operating at the same wavelength as the first stage, and (ii) a SAXO+ type multi-stage AO system with a second WFS operating at a redder wavelength than the first stage. The first approach is designed for the detection of Earth-like planets in the visible spectrum, where having both stages operating at visible wavelengths minimises chromatic errors (Guyon 2005) when using a visible coronagraph (see previous

chapter, section1.2). The second configuration is focused on studying the regions where giant planets form, as this population is believed to reside within 10 AU of their host stars(Fernandes et al. 2019).

Metric to assess the performance : The metric I will consider to assess the performance of this two stage AO system will be the Power Spectral Density (PSD) of the residual wavefront. The PSD can be interpreted as the level of expected residual in the focal plane, in the case of a perfect coronagraph. Indeed, in the small phase regime, there is a direct relationship between the PSD and the PSF, and one can show that the PSD is equivalent to a perfect coronagraphic image. This is therefore an interesting metric for our application. These plots will enable us to quantify the benefit of using a second stage WFS in terms of reduction of low-order aberrations, hence close to the host star.

2.2.4 Second stage in the VIS

In this section, I analyse a two-stage AO system where both WFS operate at the same wavelength. As discussed in Chapter 1, the phase distortions are larger in the VIS than in the NIR, making it more challenging for the second-stage WFS to operate effectively.

The other simulation parameters can be found below :

Sensing wavelength	$\lambda_1 = 700 \pm 30$nm
Sensing wavelength	$\lambda_2 = 700 \pm 30$nm
Science	$\lambda_3 = 750 \pm 30$nm

TABLEAU 2.4 – Scenario 1 : Parameters of the two-stages AO system

Impact of the light splitting on the performance

When having two WFS working at the same wavelength, the first concern is to split properly the photons between the two branches to ensure an optimal correction. For that purpose we run AO loop for different splitting : 80/20, 70/30 and 50/50 for r_0 = 15cm @500nm, medium seeing. The gain of the first stage is fixed and is equal to 0.4, the gain of the second stage varies between 0.3 to 0.1 depending on the magnitude. [1]. The gain is adjusting by hand to ensure the loop stability.

This study is particularly important because the PS-ZWFS is more affected by RON than the ZWFS, as it requires twice as many pixels. In Fig.2.21, the WFE is plotted as a function of the star's magnitude in the I-band for the different stages. This metric was chosen to evaluate the correction provided by the second stage, as its goal is to improve the WFE. Therefore, the average WFE of the second stage should be equal to or lower than that of the first stage to increase contrast closer to the host star. From

1. The photon noise sensitivity of the Zernike type I am using is smaller than the one of the PWFS as the dimple size is $1.06\lambda/D$

figure Fig.2.21, we see that when using a PS-ZWFS, the optimal splitting is 70/30 up to a magnitude of 9. To extend the range to magnitude 10, a 50/50 split should be used, and for even fainter guide stars, one should either reduce the speed of the second stage or change the wavelength of the second WFS. The latter option will be explored in the following section.

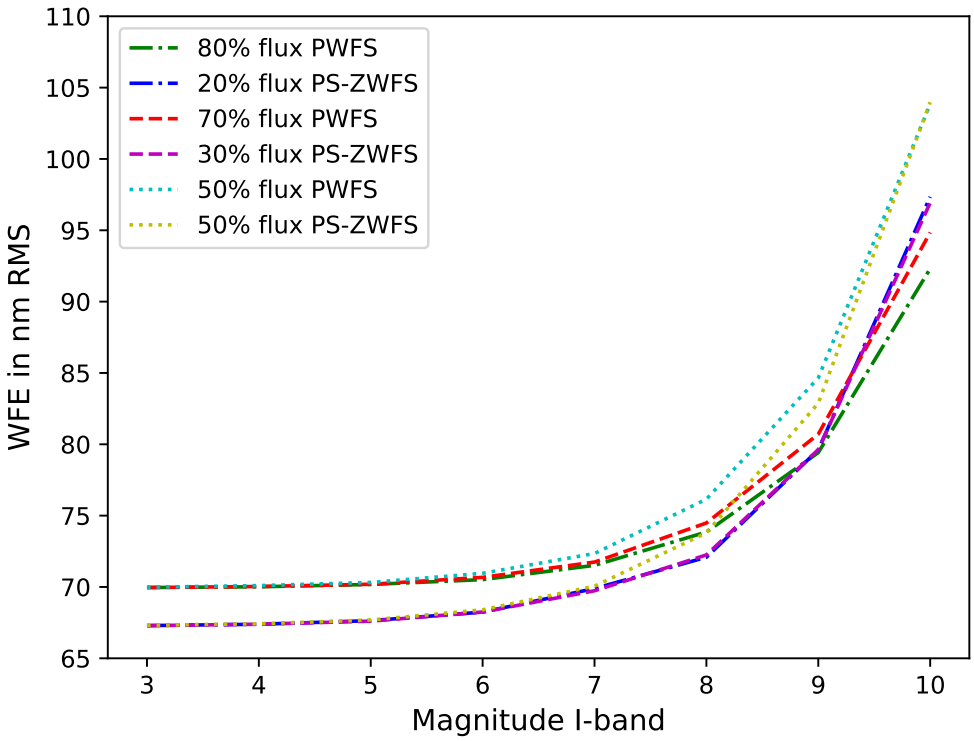

FIGURE 2.21 – WFE versus star magnitude in medium seeing condition for the different stages : 1st stage PWFS and 2nd stage PS-ZWFS.

Impact of the seeing conditions

The second step involves comparing the performance of the ZWFS and PS-ZWFS under different seeing conditions. This study is done in the high SNR regime, for a magnitude maximum of 7 in I-band. Taking into account the results of the SNR study above, all the flux splitting configuration are giving similar performance, and I choose a beamsplitter of 50/50 for simplification of the simulations. The loop gain of the first stage is maintained to 0.4 and the one of the second stage at 0.3, as these values provide the optimal performance.

Results are shown in Fig.2.22, where I plotted the PSD of the residual phase for the first stage only, and for the 2 stage system using either the ZWFS or PSWFS as second

stage. The 2 plots corresponds to the two different seeing conditions : r_0 = 15cm and r_0 = 10cm @500nm respectively.

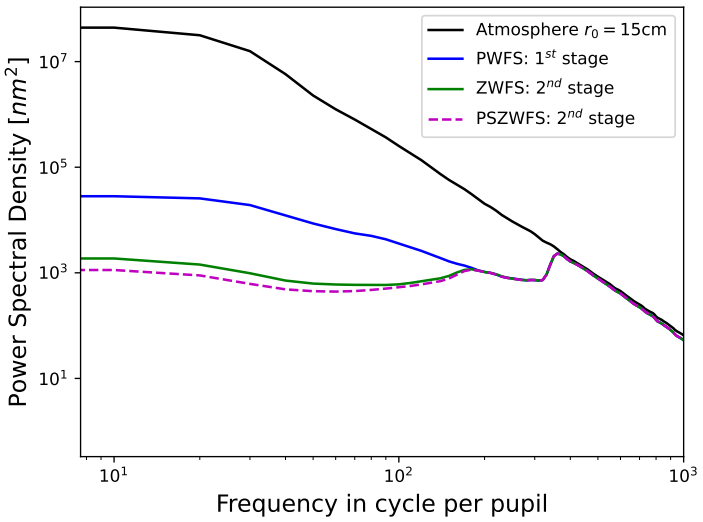

(a) r_0 = 15cm

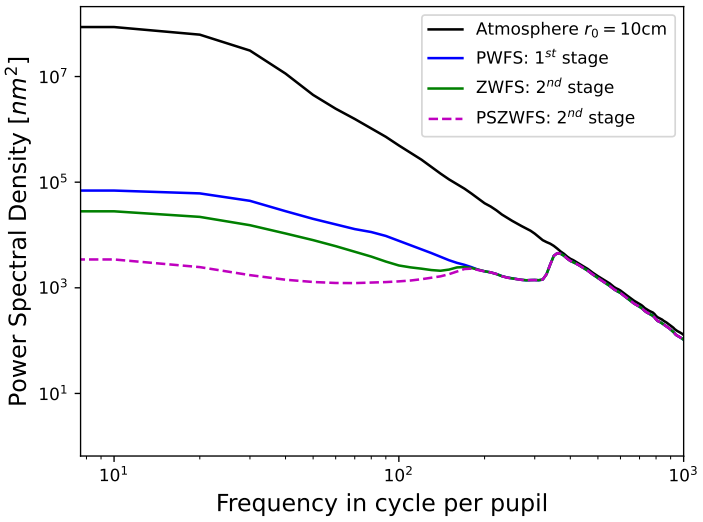

(b) r_0 = 10cm

FIGURE 2.22 – Power Spectrum Density (PSD) obtained for the different stages blue curve for the PWFS, green curve for the ZWFS and dashed-magenta curve for the PS-ZWFS. 1st and 2nd stage in I-band magnitude 7, split 50/50, science @750nm. Top : PSD obtained for a r_0 of 15cm@500nm. Bottom : PSD obtained for a r_0 of 10cm@500nm.

From Fig.2.22, we see that in medium seeing conditions (r_0 = 15cm), the average SR of the first stage is 70% as predicted by the AO error budget and the average SR after

the 2nd stage is 76% @λ_3 for both ZWFS and PS-ZWFS. Both sensors are providing similar results as the residual phase amplitude is small enough to remain in the linear regime of both WFSs. As r_0 decreases, the gap between the ZWFS and the PS-ZWFS widens. Both the performance of the ZWFS and the PS-ZWFS decrease compare to the previous case, the SR after the second stage of correction are respectively 54% and 57% @λ_3 when either using the ZWFS or the PS-ZWFS. In this scenario of strong turbulence (r_0 = 10cm which correspond to an average SR of 49% @λ_3 for the 1st stage), both the ZWFS and PS-ZWFS suffer from their non-linear responses as the sensors are working outside their dynamic regime, though the ZWFS is more significantly impacted than the PS-ZWFS (OG issues and cross-talk cf section 2.1.3.2). Thanks to its larger dynamic range, the PS-ZWFS allows to increase the SR by 3 points compare to the use of the ZWFS, and as shown by the PSD of the residual phase, the contrast could potentially be improved by a factor 2.

2.2.5 Second stage in the NIR

The other sub-system we will study implements a 2nd stage working at a redder wavelength than the first stage. The simulation parameters are the following :

Sensing wavelength	$\lambda_1 = 700 \pm 30$nm
Sensing wavelength	$\lambda_2 = 1215 \pm 260$nm
Science	$\lambda_3 = 750 \pm 30$nm

TABLEAU 2.5 – Scenario 2 : parameters of the two-stages AO system

To minimise chromatic error, it's crucial to have an AO correction at a wavelength close to that of the scientific instrument, as was the case with the sub-system described in the previous section. However, for a scientific instrument operating in the visible range, it can also be beneficial to have a second stage at a redder wavelength. In this spectral band, phase aberrations are smaller and will fall within the dynamic range of sensitive WFS like Zernike-type WFS as detailed in section 2.2.3. Therefore, even in this scenario, we expect improved performance in terms of contrast.

When each branch operates at a different wavelength, each branch receives 100% of the photons of its specific colour. A study was conducted on the maximum magnitude accessible in the J-band by the second stage WFS and the results are summarised in table 2.6. The optimisation of the loop gain was made by hand in order to minimise the WFE of the second loop and provide a stable control of the aberrations. Once the gain was optimised, we can reach a magnitude of 11 at 3 kHz. For fainter star the frequency of the loop needs to be reduced to maintain performance.

Impact of the seeing conditions

As for the previous analysis where the sensing was done in the visible, I compare the performance of the ZWFS and PS-ZWFS under two different seeing conditions, with r_0 = 10cm and r_0 = 15cm @500 nm. We also use the "bright" star condition, with a

Magnitude in J-band	7	8	9	10	11
Integrator gain	0.7	0.5	0.3	0.2	0.1

TABLEAU 2.6 – Second stage optimised integrator gain depending on the magnitude of the star in J-band. First stage I-band magnitude fixed at 7. The loop gain of the first stage was fixed to 0.4.

magnitude of 7 in both the I-band and J-band and the results are presented in Fig.2.23.

Figure 2.23(a) shows the PSD obtained for a r_0 of 15cm@500nm. This figure as to be compared with Fig.2.22(a) where the AO loop was running under the same seeing conditions but with a second stage working in the VIS. The results presented are consistent with the prediction as both sensors provide the same level of performance as in the previous case. Indeed, the average SR after the second stage are the same 76% @λ_3 for both the ZWFS and the PS-ZWFS. The amplitude of the incoming wavefront at the second stage fits within the dynamic range in closed-loop of both sensors.

Under stronger seeing conditions, when r_0 = 10cm, working in the NIR helps reducing the ZWFS non-linear response leading to the same level of performance as the one of the PS-ZWFS. In this configuration, both ZWFS and the PS-ZWFS provide an average SR of 58% @λ_3 when working in the NIR. It represents an increase of 1 point of SR compare the the previous situation where the PS-ZWFS was working in the VIS.

Conclusion

This study of the two-stage AO system highlights the PS-ZWFS's effectiveness as a second-stage wavefront sensor. Specifically, it shows that the PS-ZWFS can maintain a star magnitude limit of 8 in the I-band at a frequency of 3 kHz and reach up to magnitude 11 in the J-band. This feature is essential for achieving high-precision observations under challenging conditions, such as when the Fried parameter r_0 is as low as 10 cm at 500 nm. The PS-ZWFS performs reliably even in strong seeing conditions, unlike the classical ZWFS, which struggles in the VIS range due to its inherent non-linear behaviour. The PS-ZWFS overcomes this limitation by expanding its dynamic range, enabling more accurate wavefront estimation and enhanced contrast in demanding atmospheric conditions.

2.2.6 Summary

The initial section of this chapter was devoted to the characterisation of Zernike-type WFS, specifically the classical ZWFS and the PS-ZWFS, in terms of its sensitivity and dynamic range. I demonstrated a significant improvement in performance when employing the PS-ZWFS as a petalometer, and particularly within the context of multi-stage AO systems. In such systems, we presented simulation results for a cascaded AO configuration using two WFS and two DMs. The second loop was designed to operate at a higher frequency than the first, thus has to operate in low-flux regimes

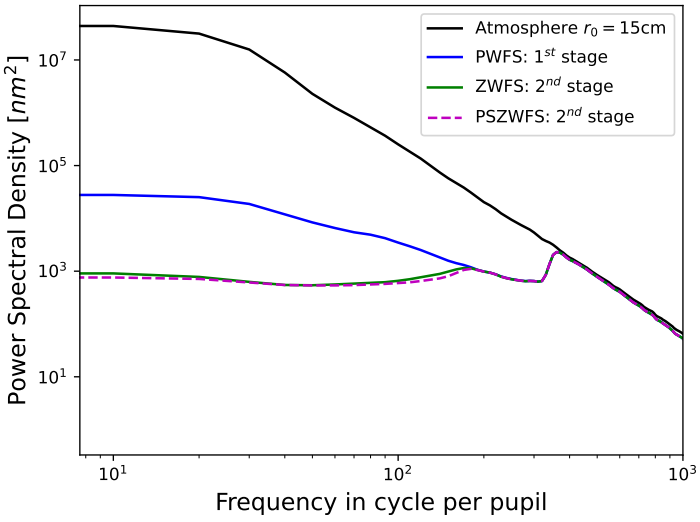

(a) $r_0 = 15$cm

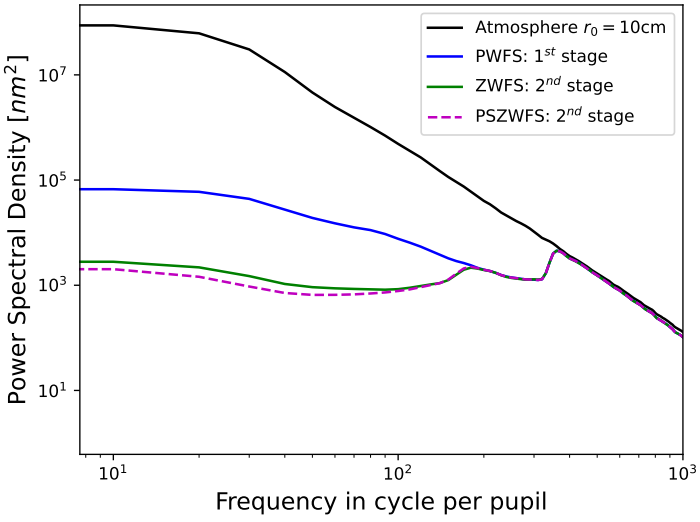

(b) $r_0 = 10$cm

FIGURE 2.23 – Power Spectrum Density (PSD) obtained for the different stages blue curve for the PWFS, green curve for the ZWFS and dashed-magenta curve for the PS-ZWFS. 1st stage in I-band magnitude 7, 2nd stage in J-band, magnitude 7, science @750nm, r_0 = 15cm @500nm. Top : PSD obtained for a r_0 of 15cm. Bottom : PSD obtained for a r_0 of 10cm.

and provide precise wavefront measurements, thereby enhancing contrast near the host star.

Due to time constraints, I was unable to simulate a more complex system incorpo-

rating NCPA or testing different multi-stage AO configurations. However, based on my findings, I am confident that the PS-ZWFS would be the preferred choice in such scenarios due to its extended dynamic range.

The next sections of this chapter are dedicated to the on-laboratory experiments I conducted in the framework of this PhD thesis using a PS-ZWFS. The objective of these experiments was to design a comprehensive multi-stage AO system on the PAPYRUS bench. First I present an overview of the PAPYRUS bench and then the ongoing experimental work about the implementation of the multi-stage AO using a PS-ZWFS.

2.3 Designing a second stage AO correction using the vector Zernike on the PAPYRUS testbed

2.3.1 Different technologies to manufacture the Phase-Shifted ZWFS

At the beginning of this chapter, we introduce the PS-ZWFS as a FF-WFS composed of two separated Zernike masks placed in the focal plane (cf Fig.2.1). This toy-model allowed us to differentiate the contributions of the two ZWFS and build the equations that lead to the reconstructor $atan2$. Although an optical set-up following this toy model could be used, there are "smarter" ways to manufacture such devices to avoid creating Non-Common Path Aberrations (NCPA) in the different branches of the masks.

In this section, we will explore two manufacturing processes, one using liquid crystals and the second using metasurfaces. This later is at the core of the experimental work that I initiated, and the development of the 2nd stage for PAPYRUS.

2.3.1.1 Liquid crystal phase mask

The substrate of the focal plane mask is composed of liquid crystals. This anisotropic material imposes an achromatic geometric phase on the incoming electromagnetic field. This phase shift, denoted as θ, is solely determined by the orientation of the fast axis of the mask and/or the alignment of the anisotropic molecules. Moreover, the geometric phase shift θ exhibits opposite signs for orthogonal circular polarisation states, resulting in distinct phase shifts of $\pm\theta$ Bloemhof (2014); Escuti et al. (2016). The use of liquid crystals requires a quarter-wave plate and a polarising beamsplitter within the optical setup. In the optical configuration employed by Doelman et al. (2019), the input polarisation states are right-handed and left-handed circular polarisation, which are transformed into linear polarisation by the quarter-wave plate and subsequently separated by the Wollaston prism (the polarising beamsplitter) to produce two distinct images on the detector (see Fig.2.24).

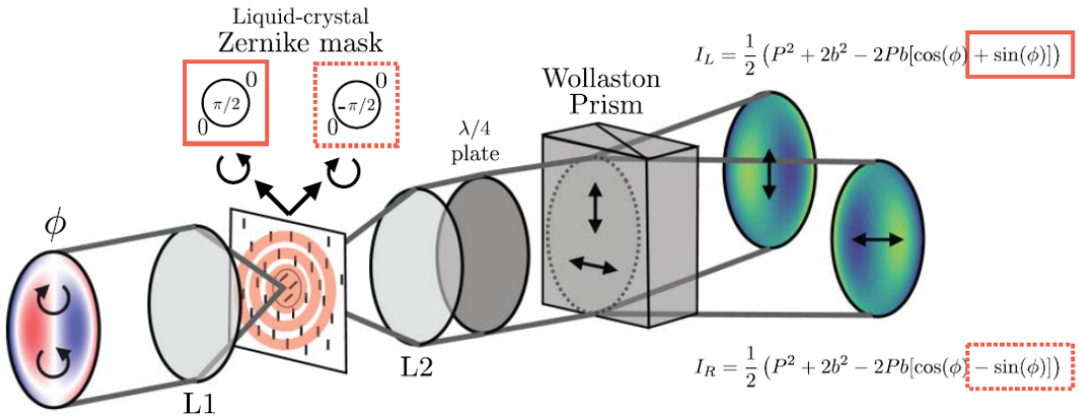

FIGURE 2.24 – Layout of the PS-ZWFS made of liquid crystals *Credits : Doelman et al. (2019)*.

2.3.1.2 Metasurface phase mask

An alternative method for fabricating this phase mask involves the use of metasurfaces. A metasurface substrate is an array of subwavelength structures that introduce a localised phase shift. While we are currently focusing on phase variations, metasurfaces can also manipulate the amplitude and polarisation state of light. The manufacturing of these structures relies on photolithographic techniques. Metasurfaces modify the phase of incoming light through light-matter interactions. Different mechanisms can be employed by metasurfaces to manipulate phase variation depending on the polarisation states : resonances with linearly polarised light and geometric phase for circularly polarised light (Hu et al. 2021). The latter mechanism is achromatic as it operates on the same principle described in the previous paragraph. The other mechanism imposes a phase-shift on linearly polarised light due to the optical path for each polarisation state. Since this phase-shift depends on the resonant features of the plasmonic structures, it is generally wavelength-dependent. In this case, the optical setup is simplified as it only requires a Wollaston to separate the two orthogonal linear polarisation states.

Figure 2.25 illustrates the surface of the metasurface PS-ZWFS. A straightforward explanation of how this substrate can apply two distinct phase shifts to two orthogonal polarisation states is that the nanostructures vary in size depending on the direction. As a result, one polarisation state interacts with a larger surface area, which imposes a greater optical path difference compared to the orthogonal polarisation.

A limitation of these technologies, however, lies in the OPD induced by the birefringent prism (in this case, the Wollaston prism as shown in the different figures). Since each polarisation state experiences a different refractive index when passing through the prism, a differential defocus - so an NCPA - occurs between the two images on the detector. This defocus may be compensated for by placing a glass plate in one of the optical branches after the prism. In the following section, this problematic induced

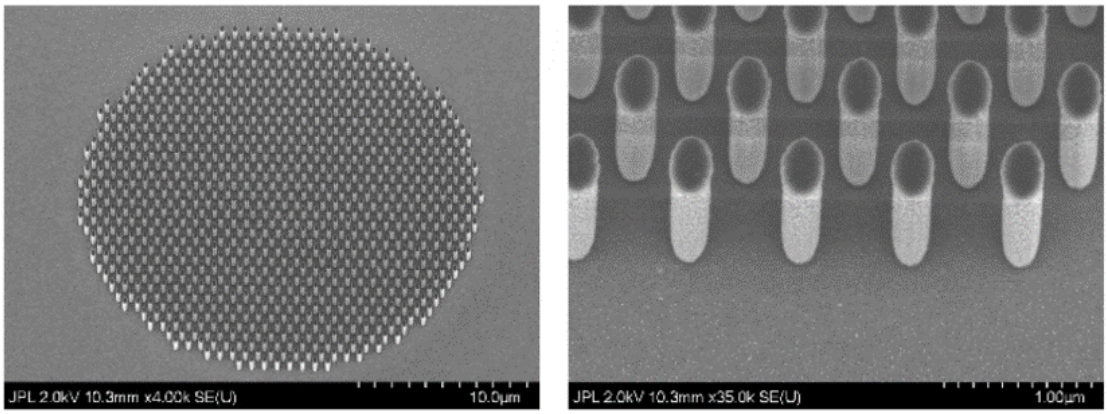

FIGURE 2.25 – Metasurface substrate of a PS-ZWFS *Credits : Wallace et al. (2023)*. Note that this mask is the one we received at LAM to be installed on PAPYRUS.

by the optical design will not be discussed as I did not have time to do a thorough study on its impact on the phase measurement. For instance, it would be interesting to understand the impact of differential aberrations between the 2 paths, and how this propagates to the phase reconstruction error. This could be a perspective of this work, setting back optical requirements on the optical quality required to perform efficient phase measurement with a PS-ZWFS.

This metasurface phase mask will be implemented in the PAPYRUS optical bench and the optical design is describe in section 2.3.3. This project is part of a collaboration between LAM, ONERA, JPL and UCSC to test and demonstrate the use of this technology and WFS as part of a multi-stage AO system. The theoretical work was developed during my participation at the Other World Laboratory (OWL) program organised in UCSC, during 1 week in 2023. Part of the results from this visit were published in a conference proceeding Chambouleyron et al. (2024) and was presented in section 2.1.3.2.

2.3.2 PAPYRUS, the Fourier filtering AO bench

The Provence Adaptive optics PYramid Run System (PAPYRUS) is a pyramid-based AO system installed at the Coudé focus of the 1.52m telescope (T152) at the Observatoire de Haute-Provence (OHP). This project is the result of a close collaboration between LAM and ONERA. PAPYRUS is a young researchers (PhD and postdoc) project that aims to strengthen our knowledge in AO. This bench is an education tool and a technological platform to test and better understand FF-WFS operating on sky. It started at the beginning of 2020 and the first light of the instrument was in June 2022. During my PhD, I participated to the development of PAPYRUS through several contributions, including the commissioning and first light operations. My main contribution was then to design the 2nd stage and start the implementation in a stand-alone bench that will be installed on PAPYRUS in 2025. In the following I provide some general information about PAPYRUS, and the first performance results we got on-sky, and



FIGURE 2.26 – PAPYRUS

then I describe in more details the develoment of the 2nd stage.

Description of the telescope, the site and the PAPYRUS bench

The T152 has a primary mirror of $1.52m$ diameter with a central obstruction of 33%. The telescope is made of four mirrors of reflectivity 88% each proving a total transmission of 52%. It is supported in a equatorial mount and the beam can be available at two Coudé focus with a F ratio of $F/D = 28$. A fifth mirror is used to switch the light toward the PAPYRUS AO bench. The main advantage of the T152 telescope is its availability, around 200 nights per year, allowing an easy access and operations for the PAPYRUS team. The main drawback of the telescope is its pointing accuracy of approximately ±2arcmin and a drift on the right ascension axis while tracking.

The atmospheric conditions at OHP show ≈ 60 nights of good seeing with $s < 2"$. The median seeing at OHP is between $s \in [2";4"]$, representing approximately 200 nights per year. These values give a typical Fried parameter that varies between $4 < r_0 < 6$cm at $\lambda = 600nm$. The median wind speed is $\approx 7m.s^{-1}$.

The PAPYRUS bench is composed of the following elements :

1. **a glass PWFS** working in the visible. Face angle equals to 8.9° and the deflection angle is ±5.44°
2. **an OCAM2K, EMCCD** wavefront sensing camera. A detector of $5.76 \times 5.76mm^2$ with 240 × 240pixels. The RON of the camera is $0.1e^-/pix/trame$
3. **a** 17 × 17 **ALPAO DM** of 37.5mm diameter with a stroke of $\pm 6\mu m$
4. **an ORCA** visible camera for PSF imaging. A detector size of $13.312 \times 13.312mm^2$ with 2048 × 2048pixels. The Field of View (FoV) is ±1"
5. **a CRED3** SWIR camera for PSF imaging. A detector size of $9.6 \times 7.68mm$ with a 640 × 512 pixels. The RON $< 40e^-/pix/trame$

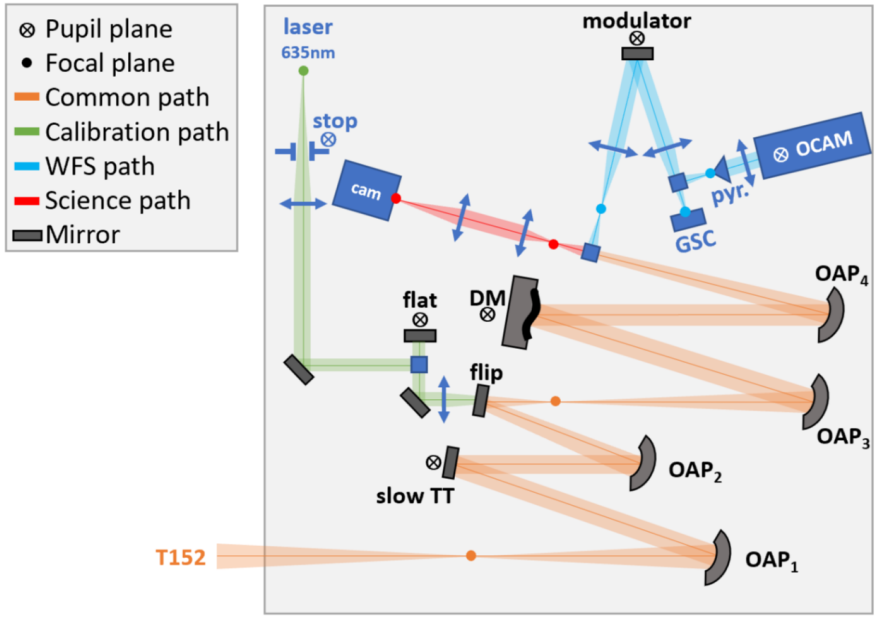

FIGURE 2.27 – PAPYRUS bench, *Credits : Fetick et al. (2023)*

A schematic of the bench is shown in Fig.2.27

The first on-sky results are shown in Figure 2.28 and reported in Fetick et al. (2023). Typically, PAPYRUS provides AO corrected images in the visible reaching up to 30% of SR.

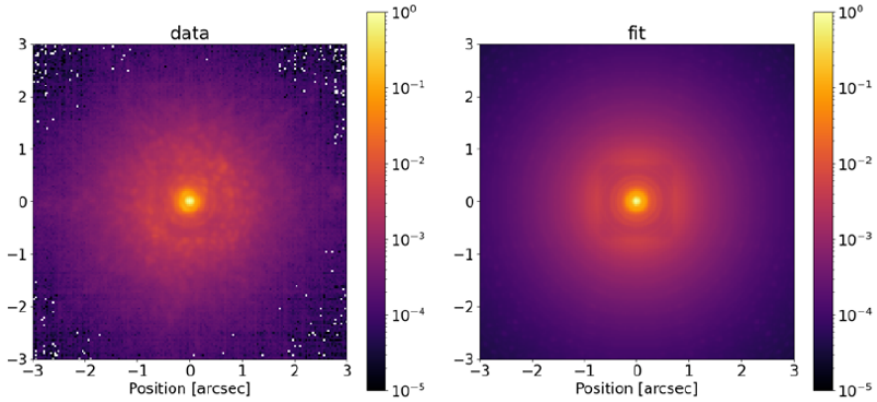

FIGURE 2.28 – PAPYRUS PSF, *Credits : Fetick et al. (2023)*

2.3.3 Second stage wavefront sensing in the Near Infrared

In the coming months, we will improve the PAPYRUS AO bench by implementing a second stage correction with a PS-ZWFS. This 2nd stage aims at significantly improve

the AO correction of the 1st stage by reducing the temporal error, which is the main limitation of the PAPYRUS bench. To do so, the 2nd stage will work in the NIR, with a low-order DM with running faster than the first DM.
The upgrade of the current AO system is composed of :

1. 9×9 ALPAO DM
2. PS-ZWFS made of metasurface as the one detailed in section 2.3.1 with a dot of $23\mu m$ diameter optimised for K-band. This
3. **a CRED2** SWIR camera for sensing. A detector size of $9.6 \times 7.68mm$ with a 640×512 pixels. The RON $< 30e^{-}/pix/trame$
4. RTC running up to 1.5kHz
5. Central wavelength $\lambda = 1.65\mu m$

The originality of the 2nd stage is in the use of a vector Zernike (vZWFS) or PS-ZWFS. The phase mask was developed by Wallace et al. (2023). With this vZWFS and its extended dynamic range, we will be able to sense bigger phase aberrations which is why we could use it as a 2nd stage WFS to correct phase residuals after the correction provided by the PWFS. Indeed, the PWFS is providing a SR between 10 to 30% in the visible corresponding to a SR up to 70% in K-band where the ZWFS is limited by its non-linear behaviour (see section 2.1).

Optical design of the second stage WFS

The design of the IR path is as follows : the focusing beam after the OAP4 will be split in two by a dichroïc beamsplitter, the visible light will go to the PWFS and the IR to the IR branch. The IR branch is split in three : for the imaging, the sensing, and the fibre injection module (VIPA). The design of the WFS path is given in Fig.2.29. After the dichroïc, a lens (L0) will be placed to form an optical relay with the OAP4. The magnification of this relay is around 0.3 to re-image the pupil of DM1 whose size is 37.5mm on DM2 whose size is 10.5mm. After the DM2, a dichroic beamsplitter is placed to split the light between the sensing and an IR imaging part. In this manner, the imaging will see the double correction. A second lens (L1) is used, with an f-number of 5.7. Therefore, the PSF size on top of the vZWFS is approximately

$$f\frac{\lambda}{D} \approx 9.4\mu m. \tag{2.6}$$

The size of the PSF arriving on top of the vZWFS is two times smaller than the dimple of the phase mask. This was done intentionally to increase the sensitivity of the phase mask. The larger the dimple compared to the PSF size, the more sensitive the ZWFS is (Chambouleyron et al. 2021a). After the vZWFS, a third lens (L2) is added. The configuration of L1-L2 differs from that of an optical relay. The magnification of this subsystem is 0.6. An intermediate pupil plane is located in the image plane of L2, and an intermediate focal point is formed after L2. Finally, a last lens (L3) is placed to re-image the pupil plane on the detector. The pupil image on the detector

was chosen to fit within the detector area of 256x320 pixels, because by cropping the region of interest, the detector can be used up to 1.5 kHz. Between L3 and the detector, a Wollaston prism is placed to split the pupil images on the detector. In the end, each sub-pupil is sampled with approximately 100 pixels in diameter

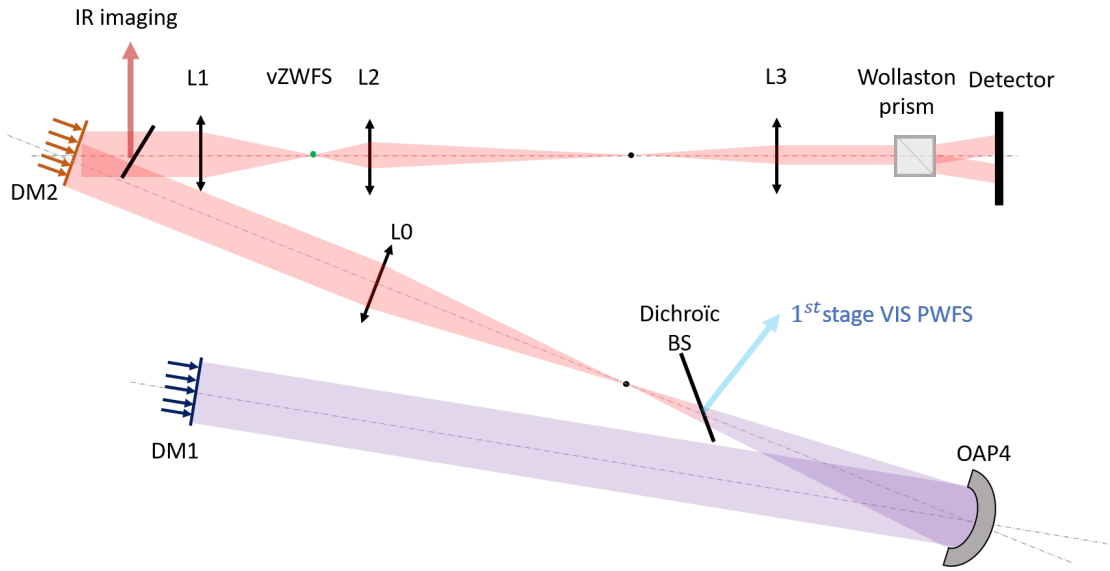

FIGURE 2.29 – Optical design of the second stage WFS

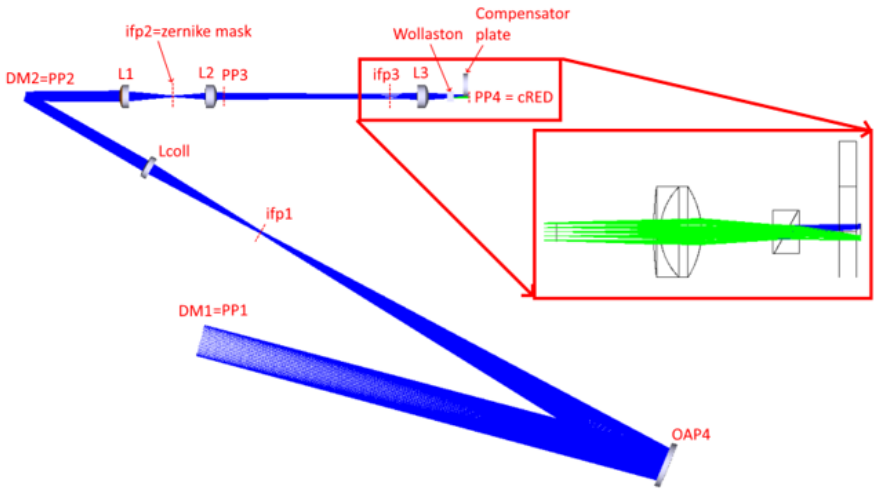

FIGURE 2.30 – Zemax : Optical design of the second stage WFS. *Credits : Eduard Muslimov optical designer at the University of Oxford*

The primary limitation of this optical design is the use of a birefringent prism, the Wollaston, which introduces an optical path difference between the two polarisation states. This results in a focus that can only be achieved for one sub-pupil, while the other will necessarily be out of focus. Alternatively, we could choose to defocus both

sub-apertures. To address this issue, our initial approach was to compensate for the blurring using a compensator plate for one of the beams. However, we encountered several challenges regarding the separation angle between the beams, the size of the pupils on the detector, and the mounting of the optics and detector. Ultimately, we determined that this solution was not practical for our application, but it is definitely a factor that needs to be investigated when using a vZWFS.

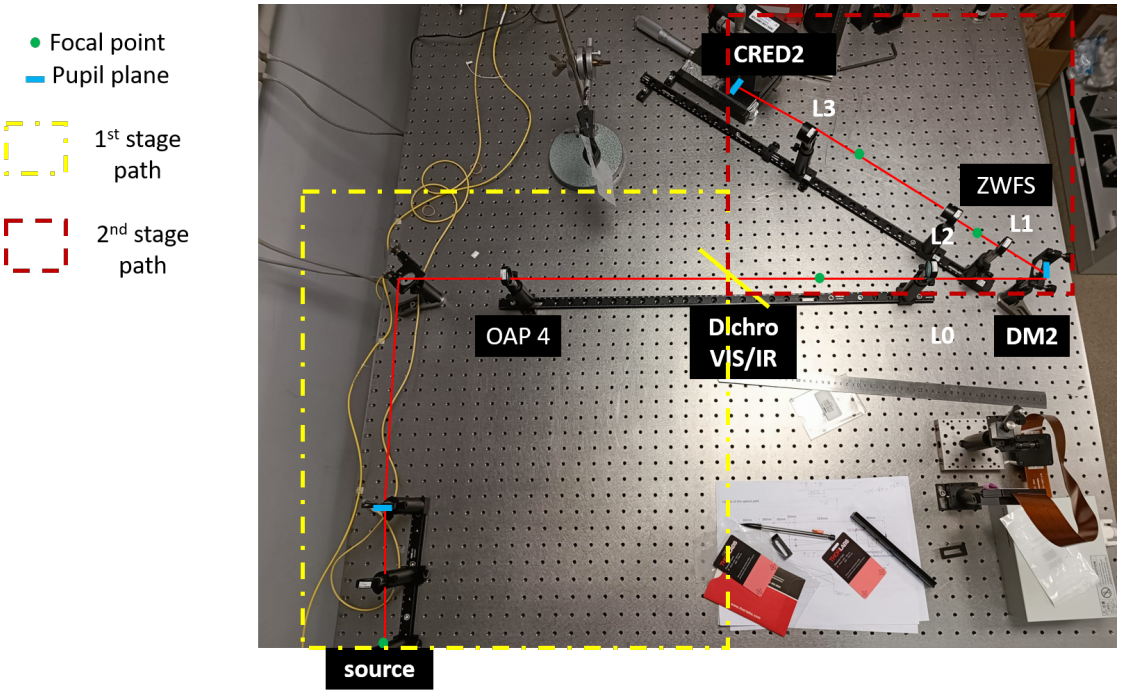

FIGURE 2.31 – Alignment of the second stage WFS

Figure 2.31 illustrates the optical setup used to characterise the vZWFS. The final second stage will be mounted on a separate optical plate and added to the PAPYRUS bench after the VIS/IR dichroïc beamsplitter (see Fig.2.27). In Fig.2.31, the section of the bench highlighted in the yellow box is used to create a collimated beam from a point source. The available source is a Thorlabs LASER operating @1.3μm. After the laser, a lens is used to collimate the beam and illuminate the diaphragm (the pupil). The beam is reflected by a flat mirror and directed to a lens with a focal length matching that of OAP4 on the PAPYRUS bench. The IR path, which will be mounted on the optical plate, begins from the lens after OAP4 (red box). This lens is used to re-image the pupil onto DM2. Currently, DM2 is replaced by a flat mirror to properly align the optics. The final pupil plane is located on the CRED2 camera.

Currently, I am still working on characterising the static aberrations of the bench using an IR PHASICS sensor. The next step will involve placing the vZWFS between L1 and L2 and positioning the Wollaston prism before the camera. After aligning these two elements, DM2 will be added to characterise the vZWFS. This characterisation is essential to determine the exact phase shift experienced by each circular polarisation state.

2.4 Conclusion

In this chapter, I conducted an in-depth study of Zernike-type WFS by examining the classical ZWFS and its enhanced counterpart, the PS-ZWFS. Through the analysis, I found that the PS-ZWFS offers a significant improvement over the traditional ZWFS, as it increases the dynamic range by a factor of two. This enhancement not only improves the robustness of the sensor but also allows for a more accurate estimation of higher phase amplitudes. Furthermore, this study demonstrated that the PS-ZWFS provides better measurements of differential piston on an ELT-like pupil. This capability positions the PS-ZWFS as a promising candidate for petalometer applications, following the work of Levraud et al. (2024a).

I pursued the research by incorporating Zernike-type WFS into a multi-stage AO system, particularly in the context of high-contrast imaging. The high sensitivity of the PS-ZWFS, coupled with its expanded dynamic range, enables its effective use even under more challenging seeing conditions. This improvement is crucial as it allows for better contrast enhancement in regions closer to the host star, thus significantly contributing to the overall performance of high-contrast imaging systems.

These studies have led to the development of a two-stage AO system on the PAPYRUS bench. This ambitious project, aimed at enhancing our practical understanding of Zernike-type WFS in on-sky operations. In the coming weeks, the characterisation of the vZWFS will be completed, after which the optical setup will be dismantled and re-aligned on the optical plate designated for the PAPYRUS bench. I did not had the time to finalise this work in the frame of my PhD, but a new PhD student and postdoc are taking over. By implementing this system, we aim to explore the potential of Zernike-type WFS in multi-stage AO configurations, paving the way for the next generation of AO systems and laying the groundwork for future innovations in the field.

3 MODELISATION OF THE NON-LINEARITIES OF FOURIER FILTERING WAVEFRONT SENSORS : EXAMPLE WITH THE PYRAMID

In this chapter we use a Linear Parameter Varying (LPV) for describing the FF-WFS non-linearity while remaining within the widely used matrix formalism. The non-linearity of Fourier-type WFS can be understood as an over-modulation that depends on the phase to be measured rather than a change of the operation condition. This approach enables to understand the non-linear responses of this class of WFS from an other perspective and completes the work done for the modulated PWFS to extend it to FF-WFS and in particular to the non-modulated PWFS.

Contents

3.1 Non-linear behaviour of Fourier-type sensors 146
3.1.1 1-Dimension analogy 146
3.2 Towards the specific matrix 148
3.2.1 Modelling/reconstruction error outside the linear regime 149
3.2.2 1-dimension analysis 150
3.2.3 Equation of propagation towards the specific matrix 151
3.2.4 First results with the specific matrix 156
3.3 Toward a practical implementation of the specific matrix 164
3.3.1 Adaptation of the optical gains formalism 164
3.3.2 Implementation in closed-loop for the non-modulated pyramid 171
3.4 Summary 174

The development of eXtrem Adaptive Optics (XAO) systems has sparked significant interest in extremely sensitive WFS, such as FF-WFS, as discussed in previous chapters. Among the most sensitive WFS are the Pyramid and Zernike WFS. The PWFS has been selected as the WFS for the next generation of SCAO instruments due to its ability to operate in low flux conditions and its extended dynamic range, thanks to the modulation stage allowing to cope with atmospheric turbulence (cf chapter 1). The ZWFS is currently used at several telescopes (Keck-KPIC, Subaru-SCExAO, MagAOx, etc...) to measure small phase aberrations like piston errors or LWE. However, many aspects of these WFS (Pyramid and Zernike mask) remain unresolved. The community is still working to understand and manage the non-linear behaviour of these WFS, which limits their use, especially when performing ultra-fine wavefront control. While the capabilities of these sensors to achieve high correction is well recognised, their non-linear response remains a key challenge, hindering their optimal use and the achievement of the expected performance of XAO systems.

There are two main strategies to consider when working with FF-WFS. The first strategy involves modifying the phase mask characteristics or employing light manipulation techniques to increase the dynamic range of these sensors, thereby enhancing the measurable wavefront amplitude. A prime example of light manipulation is the modulated PWFS. The pyramid was initially introduced with a modulation stage by Ragazzoni (1996) to address its limited dynamic range. Another example of phase mask modification is the PS-ZWFS, covered in chapter 2.

The second strategy targets the software, specifically the wavefront reconstruction process. The limitation of FF-WFS arises from their non-linear response, meaning the sensor's signal does not change linearly with the incoming wavefront, rendering traditional linear control laws ineffective. Consequently, a logical approach is to employ non-linear algorithms to estimate the wavefront from the FF-WFS signal.

The strategy at the core of this chapter represents a compromise between linear and non-linear approaches. It involves using a Linear Parameter Varying (LPV) approach while retaining the traditional matrix formalism. The aim of this chapter is to develop a phase reconstructor capable of eliminating modelling and reconstruction errors for a given WFS, regardless of the phase regime. The LPV approach is employed to account for the non-linear behaviour of an FF-WFS, and the method presented here is applicable to all FF-WFS.

This chapter is the detailed version of an article under review for jatis focusing on implementing this new reconstructor for the non-modulated PWFS.

The following notation will be used in this chapter :

Explanation of the notation : the interaction matrix around the reference wavefront is referred as $\boldsymbol{M}$*. When the matrix exhibits several variables* $\boldsymbol{M}(A,B)$*, the first variable A stands for the phase to be measured, and the second variable B describes the operating point.*

ϕ_r	reference wavefront
ϕ	incoming wavefront
$\delta\phi = \phi - \phi_r$	phase to be measured
$\mathbf{M}(0,\phi_r) = \mathbf{M}$	interaction matrix around the reference wavefront ϕ_r
$\mathbf{M}(0,\phi_r + \delta\phi)$	push-pull matrix around the phase to be measured

TABLEAU 3.1 – Mathematical notation

3.1 Non-linear behaviour of Fourier-type sensors

The PWFS was introduced in chapter 1 with its modulation stage. Yet, even with modulation, the PWFS suffers from inherent non-linear behaviour that occurs when the amplitude of the phase to be measured is too important or when the operating conditions are different from the one at calibration. This loss of sensitivity induced by the change of regime lead to multiple studies to compensate for it, (Korkiakoski et al. 2008; Deo et al. 2019; Chambouleyron et al. 2021b), through the Optical gains (OG) formalism.

However, in chapter 1, section 1.4.3, we discussed the limitations of the OG formalism, noting that it fails to account for all the non-linear responses of FF-WFS. In essence, this method effectively shifts the operating point of the system. By updating the reconstructor frame-by-frame with the OG, the system no longer operates around the reference wavefront but instead adapts to a new wavefront that reflects the AO loop's performance. Moreover, this gain compensation does not address the modal confusion that arises when the WFS operates outside its linear regime. Additionally, without any approximation, using the matrix $\mathbf{M}(0,\phi_r + \delta\phi)$ (cf equation 1.89), computed directly around the phase, tends to increase the WFE. This presents a fundamental contradiction : while the OG approximation offers a partial solution to the non-linear behaviour of FF-WFS, extending the formalism further by using the matrix approach proves ineffective.

3.1.1 1-Dimension analogy

The mathematical formalism was developed in collaboration with Olivier Fauvarque, who is a co-author of the publication currently under review.

To have a better understanding of this behaviour let's consider a 1-dimension analogy of the input/output relation of the WFS. In this 1D model, the incident phase ϕ, the phase to be measured $\delta\phi$ and the reference phase ϕ_r are assimilated to real scalars respectively denoted x, δx and x_r. The intensity I is likewise simplified with a scalar function f. The function f exhibits a linear behaviour around the reference

value x_r and non-linear behaviour for larger value of x.

$$\begin{aligned} \phi &\Longleftrightarrow x \\ I(\phi) &\Longleftrightarrow f(x) \\ \Delta I(\phi) &\Longleftrightarrow f(x_r+\delta x)-f(x_r) \end{aligned}$$

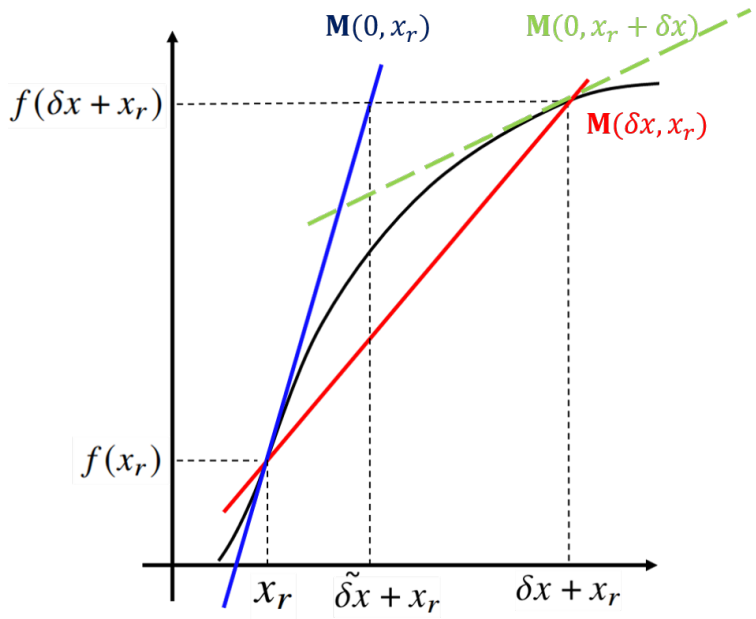

FIGURE 3.1 – 1D analogy with f(x)

Using this 1D analogy and the first order Taylor expansion of the function f around the reference wavefront

$$f(a+h)=f(a)+f'(a)h+\mathcal{O}(a).$$

It leads to

$$\widehat{\delta x}=\frac{f(x_r+\delta x)-f(x_r)}{f'(x_r)}, \tag{3.1}$$

this expression is valid for small value of $\delta x \ll 1$.

If we go back to the matrix formalism, in the linear regime, the reconstructor is the interaction matrix **M** as express in equation 1.83, each column of this matrix correspond to the push-pull of a mode. Hence when the amplitude of the push-pull is small, each column of the interaction matrix is the derivative of the intensity around the reference wavefront

$$\delta I(B_i) = \frac{\Delta I(+\epsilon B_i) - \Delta I(-\epsilon B_i)}{2\epsilon}.$$

From this we can directly make the connection with the 1D analogy,

$$\mathbf{M} \Longleftrightarrow f'(x).$$

In Fig 3.1, the blue curve is the equivalent of the push-pull interaction matrix **M**. By carry on this analogy and using equation 3.1, the pseudo-inverse of the interaction matrix is the equivalent to the inverse of the derivative :

$$\mathbf{M}^{\dagger} \Longleftrightarrow \frac{1}{f'(x)}$$

Yet outside the linear regime, the command matrix does not provide an accurate estimation of the wavefront. Indeed, with this 1D model and equation 3.1, one understands that when δx is big compared to the reference point x_r, the estimated value $\widehat{\delta x}$ differs from the true one, $\widehat{\delta x} \neq \delta x$, as it will be underestimated.

It is widely accepted that one way to account for non-linearities is to construct the interaction matrix around the operational point, which is analogous to the dashed-green curve in this 1D model, (Korkiakoski et al. 2008; Deo et al. 2019; Agapito et al. 2023). However, as demonstrated in Fig.1.35, this matrix does not serve as the correct reconstructor. The matrix formalism links the reference wavefront to the wavefront that needs to be measured, describing a linear evolution of the signal from the reference $(\phi_r, \Delta I(\phi_r))$, to the turbulent wavefront $(\delta\phi, \Delta I(\delta\phi))$. To effectively use the matrix computed around the operating point, a crucial piece of information is missing : the signal of the reference phase $\Delta I(\phi_r)$.

The current issue is : to identify a reconstructor that allows us to work around the reference wavefront. As discussed in this section, using either the OG or the full matrix alters the system's operating point. The desired reconstructor **R** should offer the most accurate wavefront estimation regardless of the operating regime, while still maintaining operation around the reference wavefront.

3.2 Towards the specific matrix

Our goal is now to find a reconstructor in the matrix formalism capable of estimating the wavefront regardless of its amplitude. In other words and by using the 1D analogy, we would like to have access to the red curve of Fig.3.1 as it is the linear link between the wavefront and the reference.

3.2.1 Modelling/reconstruction error outside the linear regime

The reconstructor $\mathbf{M}^{\dagger}$ allows an accurate phase estimation when the amplitude is small compared to the reference wavefront. When the phase to be measured has a larger amplitude, the linearisation of the reduced intensity, given by equation 1.82, is no longer valid and the use of the $\mathbf{M}^{\dagger}$ reconstructor no longer provides an accurate estimation of $\delta\phi$. This limitation is due to the intrinsic non-linearity of FF-WFS which is caused in equation 1.55 by the term

$$\left(e^{\imath(\delta\phi|_{\vec{\mathbf{r}}}-\delta\phi|_{\vec{\mathbf{r}}})}-1\right). \tag{3.2}$$

This non-linearity introduces modelling/reconstruction errors which reveal themselves in two ways as the amplitude of the phase to be measured increases :

1. The first effect of non-linearity is an underestimation of the phase to be measured. Such an error is due to the fact that the sensitivity of the FF-WFS depends on the energy distribution of the electromagnetic field that comes onto the filtering mask. The tip/tilt modulation used with the PWFS is a perfect example of this behaviour : as the modulation radius increases, the energy spreads on the focal plane, and the sensitivity to low spatial frequencies decreases. The same phenomenon occurs when a phase to be measured has a large amplitude : its extended PSF can be compared to a self-modulation which reduces the sensitivity of the WFS. The modal coefficients, which reflect the loss of modal sensitivity, constitute a diagonal matrix known as the OG matrix. There are many methods to correct this first consequence of the non-linearities, (Korkiakoski et al. 2008; Deo et al. 2019; Chambouleyron et al. 2020), but they remain inaccurate as the amplitude of the phase to be measured increases, as there are the first order approximation of the non-linear behaviour of the FF-WFS.
2. The second non-linear effect which occurs when the phase to be measured have a larger amplitude (but still lower than the reference wavefront), is to cause cross-talk between the modes (seen in Fig.1.32 with the example of the ZWFS). In other words, in addition to being underestimated, each mode Φ_i will have its estimation distorted by the presence of other modes the incoming phase.

It is important to emphasise that we cannot disentangle the loss of sensitivity per mode with the apparition of cross-terms in the estimated phase. A good analogy would be communicating vessels, when a mode is underestimated in the reconstruction process, another more is overestimated and vice-versa. That is why handling the non-linear responses of the FF-WFS with only the OG is not perfect. It does not take into account this phenomena.

We aim to prove that it is possible to remove the modelling/reconstruction error due to non-linearity while remaining within the matrix formalism. The challenge is to determine the matrix that accurately describes the behaviour of the WFS when measuring $\delta\phi$, independently of its amplitude. It can already be mentioned that this matrix will depend on the phase to be measured since non-linearity may be

manage as a self-modulation of the wavefront which changes the WFS sensitivity. As a consequence, this matrix, which perfectly describes the behaviour of the sensor, is called the specific matrix

$$\mathbf{M}(\delta\phi, \phi_r), \tag{3.3}$$

which depends on the reference phase and on the phase to be measured. The specific matrix has to satisfy the following strict equality

$$\Delta I(\delta\phi, \phi_r) = \mathbf{M}(\delta\phi, \phi_r)\mathbf{a}(\delta\phi). \tag{3.4}$$

The pseudo-inverse of this specific matrix corresponds to the perfect reconstructor since it allows an exact estimation of the phase to be measured from the reduced intensity :

$$\mathbf{a}(\delta\phi) = \mathbf{M}(\delta\phi, \phi_r)^{\dagger}\Delta I(\delta\phi, \phi_r). \tag{3.5}$$

As a consequence, the modelling/reconstruction error due to non-linearity is purely cancelled in the continuous space of $\mathbb{R}^2$.

3.2.2 1-dimension analysis

We begin from the simplified 1D case introduced in the previous section to gain insight into the nature of this specific reconstructor. Our objective is to establish a linear relationship between the reference point and the point of interest, specifically the phase we aim to measure. This relationship is illustrated in Fig3.1 by the red curve, as it is the only straight line that connects the reference phase with the current phase to be estimated. One immediate observation is that this relationship is not fixed; it varies with the wavefront. Consequently, a different linear relationship must be identified for each new wavefront, indicating that the relationship is phase-dependent. To determine the phase, one must already have some knowledge of it. This particular challenge will be addressed in the following sections.

To obtain a perfect estimation of $\delta x \iff \delta\phi$ (cf Fig.3.1), one needs the slope of the red curve which is equal to

$$\frac{f(x_r + \delta x) - f(x_r)}{\delta x}, \tag{3.6}$$

when $\delta x \to 0$, $\lim_{\delta x \to 0} \frac{f(x_r+\delta x)-f(x_r)}{\delta x} = f'(x_r)$, so the slope is equal to the derivative of the function around x_r as in equation 3.1.

This 1D analogy together with equation 3.6 confirms that the rate of change or the slope that will provide the exact estimation of the quantity δx depends on δx. Taking a close look at this expression, one realises it can also be written as the integral of the derivative of the function f between x_r and $x_r + \delta x$

$$\frac{f(x_r+\delta x)-f(x_r)}{\delta x}=\int_0^1 f'(x_r+t\delta x)\mathrm{d}t. \tag{3.7}$$

Outside the linear domain of the function f, the perfect slope is expressed by the rate of change given in equation 3.7. Following exactly the same equivalence between the interaction matrices and the derivatives, ($\mathbf{M} \iff f'(x)$), the matrix that will provide the perfect phase estimation could be written as

$$\mathbf{M}(\delta\phi,\phi_r)=\int_0^1 \mathbf{M}(0,\phi_r+t\delta\phi)\mathrm{d}t, \tag{3.8}$$

where $\mathbf{M}(\delta\phi,\phi_r)$ is the **only** matrix that link these two points : $\big(\phi_r,\Delta I(\phi_r)\big)$ and $\big(\delta\phi,\Delta I(\delta\phi)\big)$. It creates a linear relation between the reference point and the one of interest. The matrix $\mathbf{M}(0,\phi_r+t\delta\phi)$ is a push-pull matrix computed around the phase $\phi_r+t\delta\phi$.

The specific matrix is not a classic push-pull interaction matrix but the average of several push-pull matrices. The characteristics of this matrix will be studied in the following sections.

Physical interpretation

The physical interpretation of the specific matrix can be linked to modulation. Since, the signal from a modulated WFS is the sum of incoherent propagation of the wavefront and the tip/tilt phases, the resulting modulated interaction matrix is the average of push-pull matrices around variable operational points. In the same way, the specific matrix is the average of interaction matrices built around moving operational points from ϕ_r to the incoming wavefront $\phi=\phi_r+\delta\phi$. These moving operational points can be interpreted as modulation.

3.2.3 Equation of propagation towards the specific matrix

The previous section enabled us to understand and express the ideal reconstructor in a non-rigorous way as a function of push-pull interaction matrices around variable operational points. We will prove it with the equations of propagation.

The expression of the intensity given in equation 1.55 can be written using the kernel formalism, (Fauvarque et al. 2019)

$$\Delta I(\delta\phi,\phi_r)|_{\vec{\mathbf{R}}}=\int_{\mathbb{R}^2}(\mathbb{I}_P|_{\vec{\mathbf{r}}}\delta\phi|_{\vec{\mathbf{r}}})\ \mathbf{K}(\delta\phi;\phi_r)|_{\vec{\mathbf{R}},\vec{\mathbf{r}}}\mathrm{d}\vec{\mathbf{r}},$$

with the non-linear kernel $\mathbf{K}(\delta\phi,\phi_r)$ equals to

$$\mathbf{K}(\delta\phi;\phi_r)|_{\vec{\mathbf{R}};\vec{\mathbf{r}}} = 2\mathbf{Im}\left[\bar{\mathscr{F}}(t)|_{\vec{\mathbf{R}}-\vec{\mathbf{r}}}\int_{\mathbb{R}^2}\mathbb{I}_P|_{\vec{\mathbf{r}}'}\mathscr{F}(t)|_{\vec{\mathbf{R}}-\vec{\mathbf{r}}'}\right.$$
$$\left.\mathscr{F}(w)|_{\vec{\mathbf{r}}'-\vec{\mathbf{r}}}e^{\imath(\phi_r|_{\vec{\mathbf{r}}'}-\phi_r|_{\vec{\mathbf{r}}})}\frac{e^{\imath(\delta\phi|_{\vec{\mathbf{r}}'}-\delta\phi|_{\vec{\mathbf{r}}})}-1}{\imath(\delta\phi|_{\vec{\mathbf{r}}'}-\delta\phi|_{\vec{\mathbf{r}}})}\right]\mathrm{d}^2\vec{\mathbf{r}}'.$$

where it should be noted that

$$\frac{e^{\imath(\delta\phi|_{\vec{\mathbf{r}}'}-\delta\phi|_{\vec{\mathbf{r}}})}-1}{\imath(\delta\phi|_{\vec{\mathbf{r}}'}-\delta\phi|_{\vec{\mathbf{r}}})} = \int_0^1 e^{\imath t(\delta\phi|_{\vec{\mathbf{r}}'}-\delta\phi|_{\vec{\mathbf{r}}})}\mathrm{d}t. \tag{3.9}$$

Consequently, the non-linear Kernel may be written as an integral of linear kernel (given by equation 1.81) with a moving reference phase

$$\mathbf{K}(\delta\phi,\phi_r) = \int_0^1 \mathbf{K}(0,\phi_r+t\delta\phi)\mathrm{d}t, \tag{3.10}$$

and therefore, the intensity can be expressed as

$$\Delta I(\delta\phi,\phi_r)|_{\vec{\mathbf{R}}} = \int \mathbb{I}_p\delta\phi|_{\vec{\mathbf{r}}}\mathbf{K}(\delta\phi,\phi_r)\mathrm{d}^2\vec{\mathbf{r}} \tag{3.11}$$
$$= \int_0^1\left(\int \mathbb{I}_p\delta\phi|_{\vec{\mathbf{r}}}\mathbf{K}(0,\phi_r+a\delta\phi)\mathrm{d}^2\vec{\mathbf{r}}\right)\mathrm{d}\vec{\mathbf{a}}. \tag{3.12}$$

Following the same logic, as the one for the interaction matrix and the linear kernel (see chapter 1) and using equation 3.10, the specific matrix is expressed as

$$\mathbf{M}(\delta\phi;\phi_r)_i|_{\vec{\mathbf{R}}} = \int_0^1 \mathrm{d}t\int_{\mathbb{R}^2}\mathbb{I}_P|_{\vec{\mathbf{r}}}B_i|_{\vec{\mathbf{r}}}\mathbf{K}(0;\phi_r+t\delta\phi)|_{\vec{\mathbf{R}},\vec{\mathbf{r}}}\mathrm{d}\vec{\mathbf{r}}$$
$$= \int_0^1 \mathbf{M}(0,\phi_r+t\delta\phi)_i|_{\vec{\mathbf{R}}}\mathrm{d}t \tag{3.13}$$

where $\mathbf{M}(0,\phi_r+t\delta\phi)$ is the interaction matrix computed around the wavefront $\phi_r+t\delta\phi$. When the phase to be measured tends towards zero, the specific matrix becomes the simple interaction matrix $\mathbf{M}$ around the reference phase.

In practice, the integral of equation 3.13 is approximated by a discretised sum such as the one given in 3.14. One can keep in mind that the sampling of the integral does not have to be necessary uniform.

$$\mathbf{M}_m(\delta\phi,\phi_r) = \frac{1}{m}\sum_{i=1}^{m}\mathbf{M}\left(0,\phi_r+\frac{i}{m+1}\delta\phi\right) \tag{3.14}$$

where $\mathbf{M}\left(0,\phi_r+\frac{i}{m+1}\delta\phi\right)$ is the push-pull matrix computed around the phase ϕ_r+

$\frac{i}{m+1}\delta\phi$, with $i \in [1;m]$ and m is an integer corresponding to the number of push-pull interaction matrices used to approximate the specific matrix. We define m as the degree of the discrete specific matrix $\mathbf{M}_m$. As m increases, $\mathbf{M}_m$ is expected to gradually tend towards the real specific matrix $\mathbf{M}(\delta\phi, \phi_r)$.

$$\lim_{m\to\infty} \frac{1}{m} \sum_{i=1}^{m} \mathbf{M}\left(0, \phi_r + \frac{i}{m+1}\delta\phi\right) = \mathbf{M}(\delta\phi, \phi_r).$$

From the discretised formula of the specific matrix given by equation 3.14, it is interesting to note that depending on the required precision, one can limit the number of push-pull matrices to be computed. Furthermore, if we consider a WFS working at λ_0 and by using the scaling of the phase with the wavelength (cf equation 3.15), computing a specific matrix means doing push-pull matrix at redder wavelength because $\varphi' = \frac{i}{m+1}\delta\phi < \delta\phi$. For instance, if $\lambda_0 = 600nm$ and one decides to approximate the specific matrix with 3 matrices, the different wavelengths will be $\lambda_1 = 2400nm$, $\lambda_2 = 1200nm$ and $\lambda_3 = 800nm$.

The initial part of this section demonstrated, using a 1D toy model and the propagation equations, how to derive the expression for the ideal matrix to estimate the wavefront. I will now analyse this formula and assess the performance of the specific matrix in simulation using Object-Oriented Matlab Adaptive Optics toolbox (OOMAO) (Conan & Correia 2014)

Analysis of the specific matrix formula

The mathematical derivation done in the previous section has two notable advantages :

1. It does not rely on any assumptions about the phase regime. Even outside the linear regime of a FF-WFS, this specific matrix serves as the perfect reconstructor within the matrix formalism.
2. It makes no assumptions about the phase mask. Consequently, this formalism is applicable to all FF-WFS configurations.

However, this final point requires further clarification. No specific assumptions were made about the nature of the WFS, which allows for the computation of the specific matrix using wavelength-dependent phase scaling. The phase variation with respect to the wavelength, given the same optical path difference, can be described as follows :

$$\begin{aligned} \phi_1 &= \frac{2\pi\delta}{\lambda_1}, \\ \phi_2 &= \frac{2\pi\delta}{\lambda_2} = \frac{\lambda_1}{\lambda_2}\phi_1 \neq \phi_1. \end{aligned} \tag{3.15}$$

In this scenario, the WFS must be **achromatic in phase**, meaning that the WFS signal remains independent of the "colour" for a given phase amplitude. This concept could involve introducing a dispersive element into the optical path to split the wavelengths, with a detector in the next pupil plane capturing images across the different colours. The specific matrix could then be directly computed from the different intensities, functioning similarly to a rainbow WFS (as illustrated in Fig 3.2).

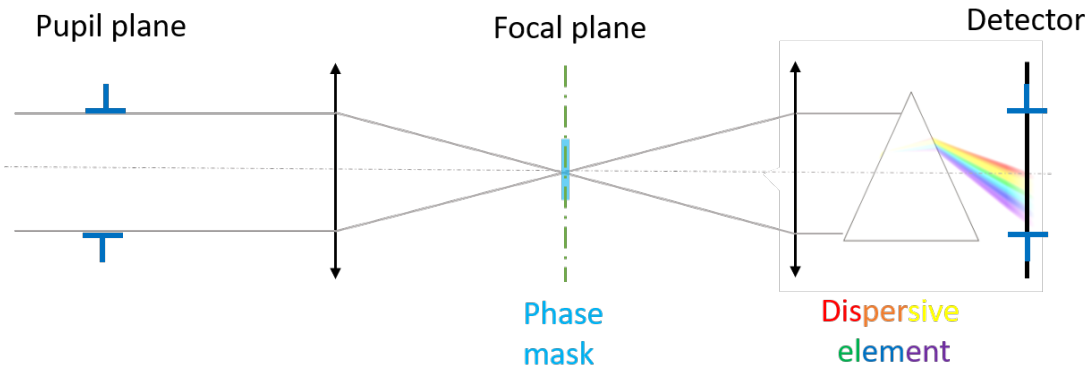

FIGURE 3.2 – Rainbow WFS

Ideally, the response of the sensor has to be the same independently from the wavelength of the beam. It is the case of the non-modulated PWFS working around a flat wavefront ($\phi_r = 0$) that acts the same on all the wavelengths. However, it is not the case of the PWFS working off-zero, i.e, when $\phi_r \neq 0$ and the case of Zernike-type WFS.

Chromatic WFSs : an example of a chromatic WFS is the ZWFS. It was introduced in the previous chapter 2 and a schematic of the mask is provided in Fig 1.22. The Zernike mask is two times chromatic because of its phase shift and the size of the dimple. The manufacture of a ZWFS is optimised for a given wavelength λ_1 as the size of the dimple has to be equal to few times the diffraction at the chosen wavelength $\approx \lambda_1/D$ and its depth to $\lambda_1/4$ in order to provide a phase shift of $\pi/2$ at this wavelength. For the phase shift, technologies mentioned in the previous chapter such as liquid crystals or metasurfaces allow to impose a $\pi/2$ phase shift to a larger spectral band. The problem of the size of the dimple has not been solved yet.

With this multi-wavelength approach and using equation 3.14 to compute the specific matrix we illustrate the chromatic issues using an optical set-up with 3 different wavelengths and a ZWFS manufactured for λ_1. We also consider that the system is working around the flat wavefront for seek of simplicity; $\phi_r = 0$. The discreet specific matrix is equal to :

$$\mathbf{M}_m(\delta\phi, 0) = \frac{1}{3}\Big(\mathbf{M}(0, \frac{1}{4}\delta\phi) + \mathbf{M}(0, \frac{1}{2}\delta\phi) + \mathbf{M}(0, \frac{3}{4}\delta\phi)\Big), \tag{3.16}$$

where the matrices $\mathbf{M}(0, \frac{i}{4}\delta\phi)$ with $i \in \{1,2,3\}$ correspond to the push-pull matrices at respectively $\lambda_2 = 4\lambda_1$, $\lambda_3 = 2\lambda_1$ and $\lambda_4 = 4\lambda_1/3$. For each wavelength, the phase-shift introduced by the Zernike mask (not made of liquid crystal or metasurfaces) would be respectively : $\pi/4$, $\pi/8$ and $3\pi/8$. When applying the propagation equation 1.63 one realises that the intensities retain their linear dependency (after the Taylor expansion) with the phase, which means that the matrix formalism remains valid. Yet the noise propagation would be different for the different wavelengths, as it depends on the phase shift induced by the Zernike mask, (Chambouleyron et al. 2021a). Furthermore, the dynamic range will also be different (see Janin-Potiron (2017) and Fig.3.3).

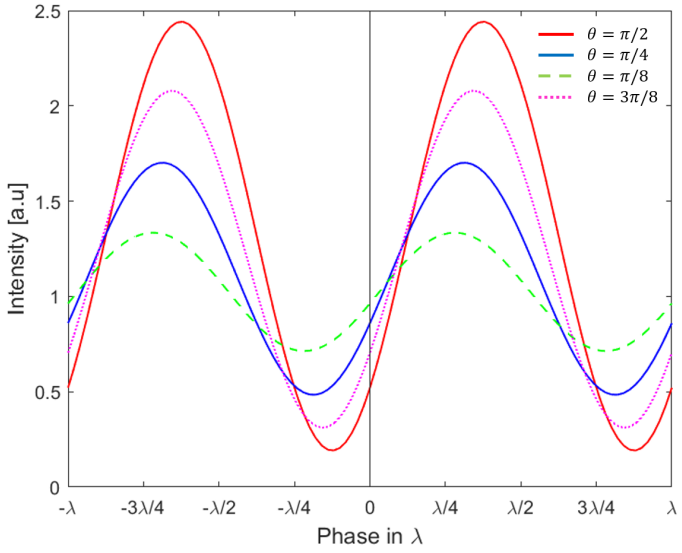

FIGURE 3.3 – Intensity as a function of the phase for the different configurations : classical ZWFS with $\theta = \pi/2$ in red, $\theta = \pi/4$ in blue, $\theta = \pi/8$ in dashed-green and $\theta = 3\pi/8$ in dotted-magenta.

Another problem comes from the size of the dimple "seen" by the different PSFs. In our case, the PSF cores will be respectively; $\lambda_2/D = 4\lambda_1/D$, $\lambda_3/D = 2\lambda_1/D$ and $\lambda_3/D = \frac{4}{3}\lambda_1/D$. So the size of the dimple seen by the different wavelength will be respectively : $p = 0.27\lambda_2/D$, $p = 0.53\lambda_3/D$ and $p = 0.80\lambda_4/D$. We directly notice that none of the wavelength sees an optimal Zernike mask. Hence, the portion of the EM field affected by the filtering will be reduced as the core of the PSFs are getting larger. By taking the changes of phase-shift and the sizes of the dimple seen by the different wavelengths, the variations of the intensities given in Fig.3.3 become those of Fig.3.4 where we can see that the sensing capabilities of the ZWFS are drastically reduced for λ_2 and λ_3.

Therefore, to make the rainbow optical set-up useful, one needs to use an achromatic sensor. The non-modulated pyramid is an achromatic sensor for instance. With this sensor, the rainbow optical set-up is feasible using broad band detector such as MKIDS for example (O'Connor et al. 2019). A practical implementation of the specific

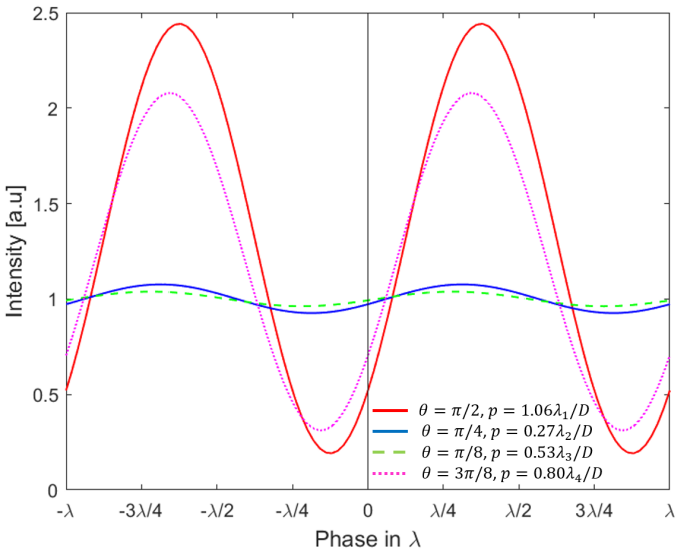

FIGURE 3.4 – Intensity as a function of the phase for the different configuration : classical ZWFS with $\theta = \pi/2$ and $p = 1.06\lambda_1/D$ in red, $\theta = \pi/4$ and $p = 0.27\lambda_2/D$ in blue, $\theta = \pi/8$ and $p = 0.53\lambda_3/D$ in dashed-green and $\theta = 3\pi/8$ and $p = 0.80\lambda_4/D$ in dotted-magenta.

matrix is given in section 3.3.1.

3.2.4 First results with the specific matrix

For the following sections, the reference wavefront is assumed to be null, $\phi_r = 0$, it will be removed from the variable of the matrices. Furthermore, if $\phi_r = 0 \longrightarrow \delta\phi = \phi$.

First order approximation of the discrete specific matrix

It is interesting to look into the construction of the specific matrix. At first order, the matrix can be approximated by

$$\mathbf{M}_1(\delta\phi, \phi_r = 0) \quad = \quad \mathbf{M}(0, \delta\phi/2), \tag{3.17}$$

where $\mathbf{M}_1$ is the push-pull matrix around the phase to be measured divided by two $\delta\phi/2$, which will be called the median matrix thereafter. The median matrix $\mathbf{M}(0, \delta\phi/2)$ is the first order approximation of the specific matrix and not the matrix build around the operational point. The median matrix will provide a more accurate estimation of the wavefront than the matrix computed around the operating point, $\mathbf{M}(0, \delta\phi)$. In other words, if the full specific matrix cannot be built, a good alternative would be to use a push-pull matrix built around half the phase.

Another interesting reconstructor is the average between the interaction matrix and the push-pull matrix around the operational point given by

$$\mathbf{M}_{av} = \frac{1}{2}\left(\mathbf{M}(0,\delta\phi) + \mathbf{M}\right), \tag{3.18}$$

where depending on how the integral of equation 3.13 is discretised, this average matrix would also be a first order approximation.

To assess the capacities of this new tool at describing the behaviour of the WFS we compare in Fig.3.5 the end-to-end (E2E) reduced intensity of an unmodulated PWFS for a high amplitude phase $\delta\phi$, to several linear models based on different matrices :

1. the classic approach with the interaction matrix around the reference phase $\mathbf{M}$,
2. a linear model using the push-pull matrix around the phase to be measured $\mathbf{M}(0,\delta\phi)$
3. another linear model using the average of the two previous matrices given by equation 3.18.
4. and linear models using the estimations of the specific matrix $\mathbf{M}_n(\delta\phi;0)$ with n is equal to 1, 5, 10 and 20.

The different reconstructors are computed using the Moore-Penrose algorithm to obtained the pseudo-inverse of the matrices. The WFE is computed on the controlled part of the turbulence : $\epsilon = \phi_{//} - \widehat{\phi_{//}}$.

The simulation parameter can be found in Table 3.2.

TABLEAU 3.2 – Simulation parameters

Telescope	8m
Pupil resolution	160 across the pupil diameter
Phase basis	1000 Karhunen-Loève (KL) modes
Sensing path	$\lambda = 850nm$ - 40 x 40 subpupils in D

The first observation is that the classic linear description is not representative of the behaviour of the WFS (see Fig.3.5 dashed-red curve). The interaction matrix around the reference wavefront is not able to reproduce the response of the WFS because the WFS is working outside its linear regime.

The description provided by the matrix calculated around the phase to be measured $\mathbf{M}(0,\delta\phi)$ is also not accurate (see Fig.3.5 dashed-blue curve). However, the reconstructor obtained from the average between the matrix around the operating point and the interaction matrix $\mathbf{M}_{av}$ (yellow-dashed curve) allows a better description of the WFS response reducing the WFE when estimating the phase (see Table3.3). It provides similar results than the reconstructor $\mathbf{M}_1$, i.e. the push-pull matrix calculated around the median operating point $\mathbf{M}_1 = \mathbf{M}(0,1/2\delta\phi)$ (green curve).

As n increases, the linear models based on $\mathbf{M}_n$ tends gradually towards the real reduced intensity (the End-to-End (E2E) model), proving that it is possible to obtain a perfectly satisfactory numerical approximation of the specific matrix. With only 5 steps, when computing the discretised specific matrix, the reconstructor derived from the specific matrix gives very satisfactory results and is even able to provide an unwrapped phase.

As the amplitude of the input wavefront increases, the main limitation of the numerical specific matrix $\mathbf{M}_n$ is the fitting and the aliasing. Indeed, the formalism behind the specific matrix states that this matrix is the perfect reconstructor when considering the phase in the continuous space of $\mathbb{R}^2$. However, when using an AO system, the phase is decomposed on a basis because of the limited spatial frequencies the DM can control (cf equation 1.13). On top of that there is also the sampling of the WFS intensity on the detector creating aliasing leading to

$$I_{det}(\phi) = (I(\phi)) * \Pi_d).\mathrm{III}_d \text{ and} \tag{3.19}$$

$$\Delta I_{det}(\delta\phi, \phi_r = 0) = (\Delta I(\delta\phi; 0)) * \Pi_d).\mathrm{III}_d, \tag{3.20}$$

where Π_d is the top hat function of size d, d the sampling of the detector. The convolution by Π_d acts like a low-pass filter. The III_d is the Dirac comb indicating the positions of the centres of the pixels of the detector. This multiplication by III_d creates aliasing. Yet, it has been shown that the aliasing of the PWFS is negligible, especially compared to that of the Shack-Hartmann WFS (Vérinaud 2004; Correia et al. 2020). Hence to obtain the optimal estimation of the wavefront and cancel the WFE in our formalism, the simulation needs to be over sampled. Yet for a given AO system, the specific matrix will provide the most accurate estimation in comparison with the other reconstruction matrices.

Reconstructor	$\mathbf{M}^{\dagger}$	$\mathbf{M}(0;\delta\phi)^{\dagger}$	$\mathbf{M}^{\dagger}_{av}$	$\mathbf{M}^{\dagger}_{1}$	$\mathbf{M}^{\dagger}_{5}$	$\mathbf{M}^{\dagger}_{10}$	$\mathbf{M}^{\dagger}_{20}$
WFE (rad RMS)	0.98	0.84	0.54	0.42	0.13	0.07	0.04

TABLEAU 3.3 – WFE in radian RMS using different reconstructors. The reference phase equals zero. The incident phase is shown in Fig. 3.5, its RMS norm is 1.51 rad RMS.

It has been shown that it is possible to describe the non-linearity of Fourier filtering WFS in the matrix formalism. To do this, the matrix describing the WFS outside the low phase regime has to depend on the phase to be measured. That is the reason why this matrix is called the specific matrix. We also demonstrated that the specific matrix is different from the push-pull matrix around the operating point, and the first approximation of the specific matrix are either the median or the average matrix not the one around the operational point. Its analytical expression has been given and shows that the specific matrix can be obtained as an average of push-pull matrices computed around different operating points. Such a fact confirms that non-linearity may be understood as self-modulation.

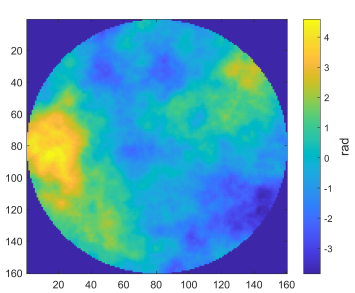

(a) Input phase $\delta\phi$: amplitude 1.51 rad RMS

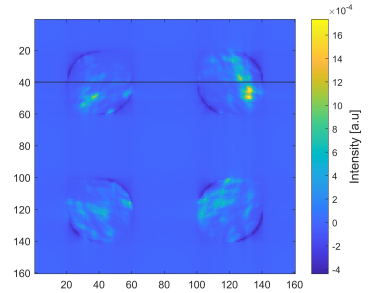

(b) E2E intensity

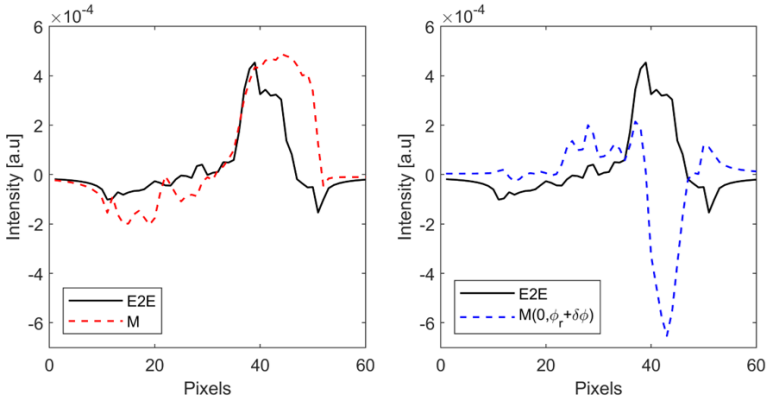

(c) Intensity cut obtained with **M**and $\mathbf{M}(0;\delta\phi)$

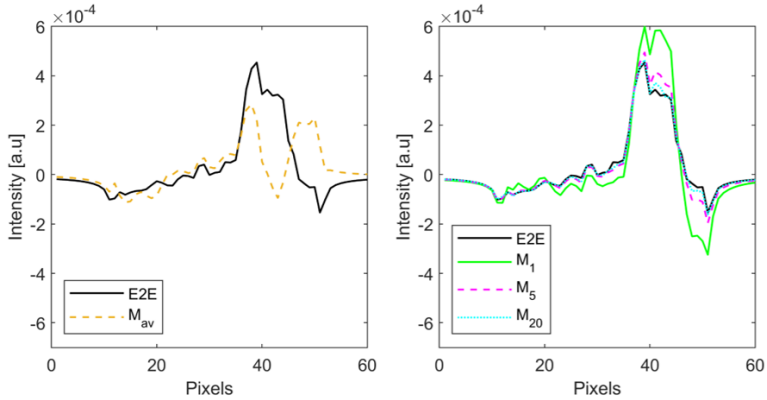

(d) Intensity cut obtained with and $\mathbf{M}_{av}$,$\mathbf{M}_1$, $\mathbf{M}_5$and $\mathbf{M}_{20}$

FIGURE 3.5 – Top : input phase and corresponding E2E intensity. Middle : intensity cuts obtained with the interaction matrix **M** in dashed red and with the push-pull matrix around the phase $\mathbf{M}(0,\delta\phi)$ in dashed blue. Bottom : intensity cuts obtained with the average matrix $\mathbf{M}_{av}$ in dashed yellow and with the different approximation of the specific matrix $\mathbf{M}_n$ with $n \in \{1;5;20\}$.

Specificity of the reconstructor

An important aspect of this reconstructor is its specificity, indeed, the specific matrix is built to provide a proper estimation of one given phase $\delta\phi$ of a given amplitude. When estimating another phase screen, the reconstructor has to be changed. One way to understand this is to consider a situation where the phase is wrapped. The wrapping being unique to each phase screen, a given specific matrix built for this phase will no longer provide a proper estimation of another phase screen because the specific matrix unwraps the phase. This situation is illustrated in Fig.3.6 and in Fig.3.7 where one can see the intensity cut from the E2E simulation (incoming phase $\delta\phi$) and the one provided by our linear model $\mathbf{M}(\delta\phi",0)$ is far from reproducing the E2E simulation intensity. So in the non-linear regime of the WFS, the specific matrix are not interchangeable.

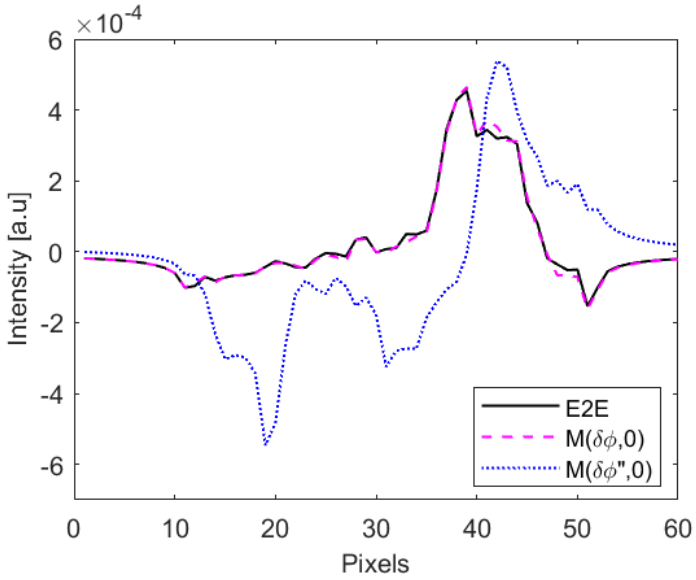

FIGURE 3.6 – Intensity cut obtained with E2E simulation and two different specific matrices $\mathbf{M}(\delta\phi,0)$ and $\mathbf{M}(\delta\phi",0)$ to demonstrate the specificity of the reconstructor.

In search of the true OG

The specific matrix is a great tool that demonstrates the possibility of using matrix formalism in any phase regime to accurately estimate the wavefront. However, its dependency on the phase to be measured makes it impossible to use in practice. Therefore, it is necessary to explore ways to approximate this perfect reconstructor. This approximation is made through the gain matrix formalism. We aim at building a dense gain matrix containing both the OG and the coupling terms, representative of the phase we intend to measure. The reconstructor has to be as close as possible from the specific matrix, as the later is the best reconstructor in the matrix formalism.

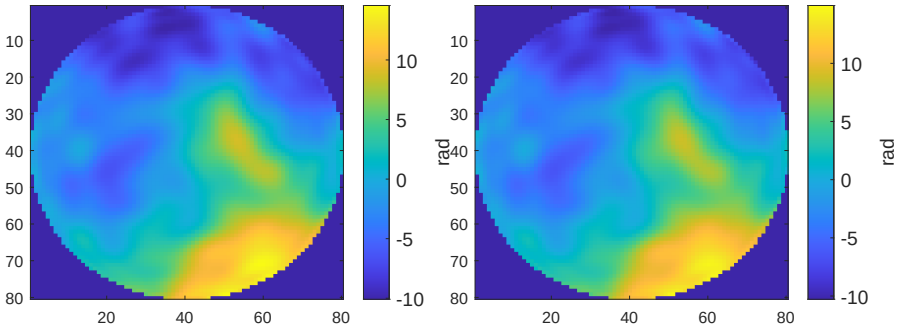

(a) Input phase $\delta\phi$: amplitude 5.7 rad RMS

(b) Estimated phase obtained $\mathbf{M}(\delta\phi;0)$: WFE 0.16 rad RMS

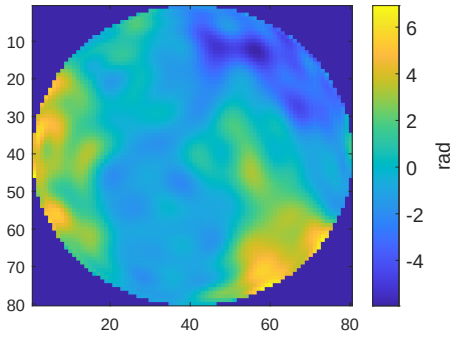

(c) Estimated phase obtained with $\mathbf{M}(\delta\phi,0)$: WFE 4.9 rad RMS

FIGURE 3.7 – Specificity of the specific matrix in a strong turbulence regime, example of phase unwrapping

When it comes to optical gain formalism, one thinks about the modulated PWFS as explained in section 1.4.3, as it allows to compensate for the loss of sensitivity when the operating conditions change from the one of the calibration. Yet, this way of explaining the non-linearities of the sensor is incomplete. In this section we look for the true OG. Our concern is to find the real modal gains and the coupling terms that translate optimally the non-linear response of the WFS. In this framework, the non-linear behaviour of the WFS can be understood as caused by the amplitude of the phase to be measured and not by the change of the operating condition, as we wish the system to work around the reference wavefront. To do so we will use the following strategy. We will consider the estimation of one KL mode KL_i in two different phase regimes : linear phase regime and the strong phase regime. In the strong phase regime, we will consider first the modal gain compensation and then the full gain compensation (OG + coupling). For that purpose, we will consider a modulated PWFS, $r_{mod} = 3\lambda/D$. The different reconstructors we are considering are the interaction matrix around the flat wavefront $\mathbf{M}$, the specific matrix $\mathbf{M}(\delta\phi,0)$ and the push-pull matrix around the considered wavefront $\mathbf{M}(0,\delta\phi)$.

In the linear regime, as expected, the three matrices give similar results, they all

provide an accurate estimation of the amplitude of KL_i, see Fig.3.8.

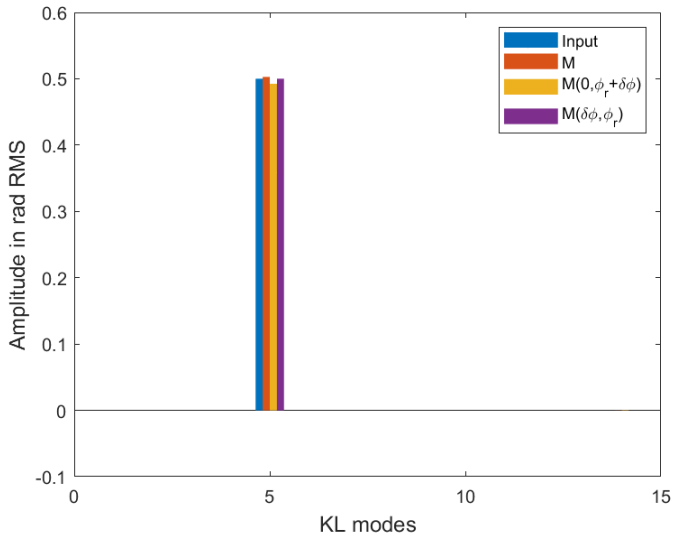

FIGURE 3.8 – Phase coefficients using different reconstructors in the linear regime

In the strong regime the input amplitude of the KL mode KL_i is 2π rad RMS. We can directly see in Fig.3.9(b) that the estimation provided by the interaction matrix **M** is an underestimation of the input mode at first order. When considering only a modal gain compensation, the ideal gain would be the ratio of the amplitude of the input wavefront and the one provided by the interaction matrix **M**. In our case this gain is equal to 0.66. We use the approach described in Chambouleyron et al. (2020); Chambouleyron et al. (2021b) and in section 1.4.3 summarised in equation 1.90 to compute the OG. With this approach, the OG comes from the diagonal of the matrix that results from the projection of the push-pull matrix around the wavefront and the interaction matrix. The resulting matrix should provide information about how far from the linear regime the system is.

We use the same formalism for the specific matrix and build another gain matrix $\mathbf{T}(\delta\phi, 0)$. By comparing the diagonal of the two matrices, we can conclude that the OG from the specific matrix are the "true" ones. The gain of the considered mode is 0.68 when the one from the push-pull around the phase is 0.1 (cf Fig.3.9). Therefore, with this example, we demonstrated that to compensate for the loss of sensitivity caused by the amplitude of the phase, one should used the OG resulting from the specific matrix. Another alternative would consist in using the gain from the average between the push-pull around the wavefront and the interaction matrix $\mathbf{OG}_{av}$ (see Fig.3.9) as there are closer from the real ones.

If considering the coupling between the modes induced by the interaction matrix estimation, we need to compare the performance of the matrices $\mathbf{T}(0, \delta\phi)$ and $\mathbf{T}(\delta\phi, 0)$. In this scenario, the new phase reconstructor is $\left(\mathbf{MT}(0, \delta\phi)\right)^{\dagger}$ or $\left(\mathbf{MT}(\delta\phi, 0)\right)^{\dagger}$. One can see that using the matrix $\mathbf{T}(\delta\phi, 0)$ helps to compensate for the OG by increasing the

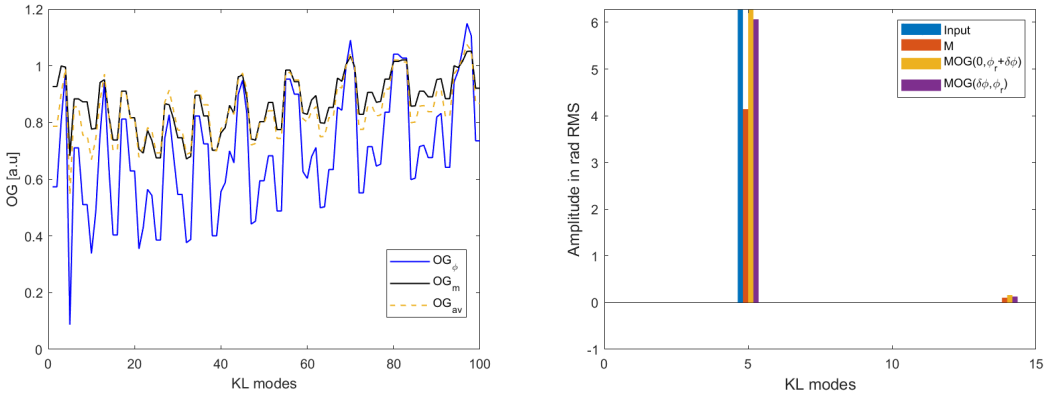

(a) Estimation with full matrices (b) Estimation after OG compensation

FIGURE 3.9 – Left : Optical gains. Right : Projected coefficients after gain compensation

amplitude of the mode of interest KL_i and cancel out the coupling induced by the matrix $\mathbf{M}$ (see Fig.3.10).

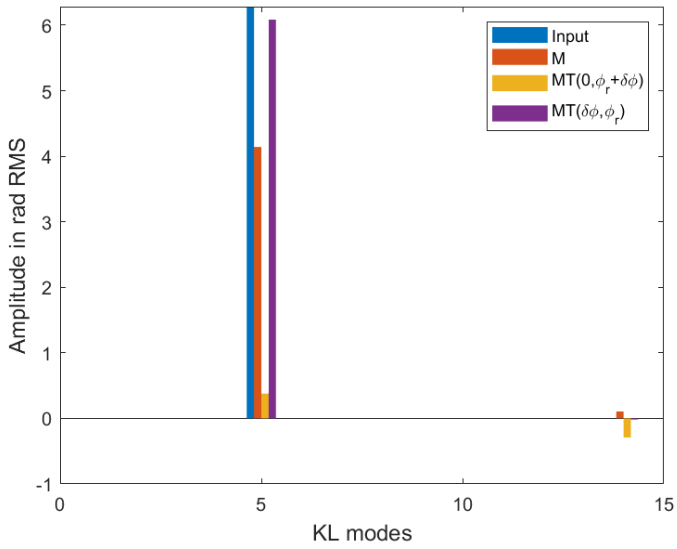

FIGURE 3.10 – Projected coefficients after full compensation, reconstructors $\left(\mathbf{MT}(0,\delta\phi)\right)^{\dagger}$ and $\left(\mathbf{MT}(\delta\phi,0)\right)^{\dagger}$.

With the example of the reconstruction of one phase mode KL_i using a PWFS with a modulation radius of $3\lambda/D$, we prove the usefulness of the specific matrix and its approximation to measure the absolute phase, in particular in strong phase regime. This example tackles the loss of sensitivity of the sensor due to the amplitude of the phase itself. The specific matrix should be seen as the **targeted reconstructor** and all the attempts to build the best phase estimator in the matrix formalism should go

toward that matrix. However it is not an easy task, as shown in the previous section, this formalism only applies to achromatic WFS and it is phase dependent. Now the next question is : how can we approximate this reconstructor?

3.3 Toward a practical implementation of the specific matrix

The dependency on the phase to be measured and the complex optical set-up needed to perform multi-wavelength calibration could make the practical use of the specific matrix difficult. Therefore, our approach consists of considering the specific matrix as the target reconstructor and explore potential approximations that allow its practical implementation. In particular, through the OG formalism as described above in the previous section.

The following formalism will be consistent with the classical approach for obtaining OG (Chambouleyron et al. 2020). However, rather than using the matrix computed around the operating point, we will use the specific matrix.

The other difference compared to the classical approach, which generally only considers the diagonal of the gain matrix, is to now use the full gain matrix. This allows to compensate for the coupling terms, hence improving the phase estimation. But the challenge consists in finding practical ways to obtain this dense gain matrix, on a frame-by-frame basis, as the turbulence evolves dynamically.

Research on the frame-by-frame OG compensation led to the use of a focal plane camera (so-called Gain Scheduling Camera - GSC) located after the modulation mirror and from which the modal gains can be estimated (Chambouleyron et al. 2021b). Following this idea, we propose the use of an hybrid method which consists of using this same focal plane camera GSC for a frame-by-frame estimation of the modal gains, complemented by a statistical approach to estimate the coupling terms using the specific matrix formalism.

3.3.1 Adaptation of the optical gains formalism

The first step of the construction of our hybrid reconstructor is the determination of the modal gain. To compute the OG from the PSF image, called later in the text $\mathbf{OG}_{PSF}$, we use the convolutional model developed by Fauvarque et al. (2015) and Chambouleyron et al. (2021b) and especially equation 14 from Chambouleyron et al. (2021b). Indeed, in Chambouleyron et al. (2021b) it has been shown that the gains obtained from the GSC are a very good estimation of the gains resulting from a push-pull done around the phase itself. However, we have shown in the previous section that a better estimation of the gains is obtained from the specific matrix. We also demonstrate that a good approximation for these specific gains or true gains is obtained by averaging the interaction matrix and the push-pull matrix around the operating point in the

modulated case.

The first step to build our approximated specific matrix, also called hybrid reconstructor is then to adjust the gains obtained with the GSC so their value correspond to the real gains as follows

$$\begin{aligned} \mathbf{OG}_{av} &= \frac{1}{2}\left(\mathbf{diag}(\mathbf{M}^{\dagger}\mathbf{M}) + \mathbf{diag}(\mathbf{M}^{\dagger}\mathbf{M}(0,\delta\phi))\right) \\ &= \frac{1}{2}\left(\mathbf{diag}(\mathbf{I}_d) + \mathbf{OG}(0,\delta\phi)\right), \end{aligned} \tag{3.21}$$

where $\mathbf{I}_d$ is the identity matrix.

This is major difference compared to previous work, and we claim here that previous OG estimations were not the optimal ones. When working around small phase $\delta\phi \ll 1$, the impact is small as the gain are closer to unity, but for systems working around large static phase this can have a significant performance impact.

As an illustration, we use aberrations constructed from a PSD with a power-law exponent of -2.5 to mimic AO residuals. In Fig.3.11, in the modulated case, we show that the OG estimated from the specific matrix (black curve) are higher than the one obtained with the matrix $\mathbf{M}(0,\delta\phi)$ around the residuals (blue curve). We also show that the OG estimated from the GSC (green curve) are consistent with those estimated around the current operating point, which is consistent with previous results in Chambouleyron et al. (2021b) . Finally, we show that the correct OG can be approximated from the GSC, following equation 3.21 (magenta curve) as there are similar to the average gains in yellow.

A more nuanced conclusion can be made in the unmodulated case plotted in Fig.3.11. Indeed, there is a match between the average gains obtained from equation 3.21 and the exact ones extracted from the specific matrix. But there is mismatch between the $\mathbf{OG}_{PSF}$ and the one extracted from the push-pull matrix around the residuals. This is due to a limitation of the convolutional model, which is based on a linear assumption, thus not perfectly accounting for the specificity of the non-modulated pyramid. We note a correct match for the very low order modes between the $\mathbf{OG}_{PSF}$ and $\mathbf{OG}(0,\delta\phi)$ and for the high-order modes between $\mathbf{OG}_{PSF}$ and the specific ones $\mathbf{OG}(\delta\phi,0)$. Therefore, when adjusting $\mathbf{OG}_{PSF}$ using equation 3.21, we will have a correct estimation of the low-order OG but a less accurate estimation of the high-order OG.

The second step toward the construction of the hybrid reconstructor is obtaining the statistical coupling terms. For that purpose, we consider a set $\mathbb{E}$ of residual phase screens describing different seeing conditions. Each set contains $N = 20$ phase screens and for each one of them, a specific matrix is computed. The resulting gain matrices are obtained using equation 1.90 on the average specific matrices over the different

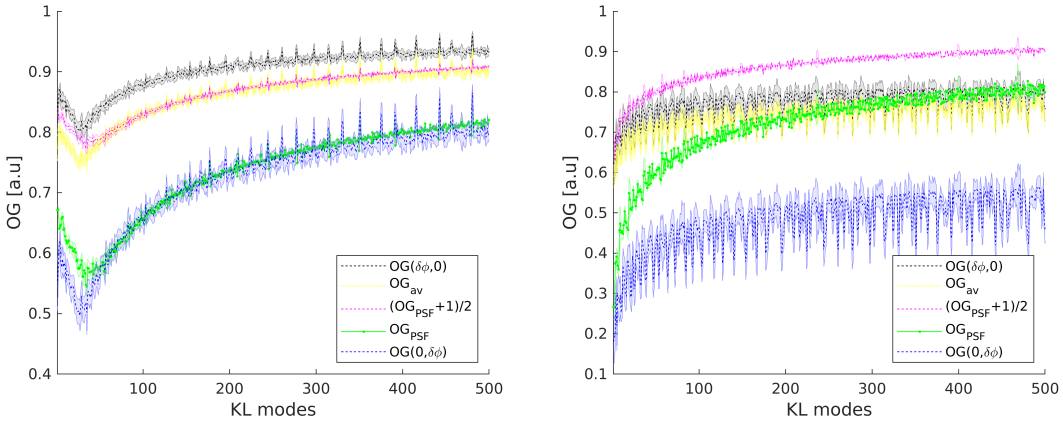

(a) Modulated pyramid OG $r_{mod} = 3\lambda/D$ (b) Non-modulated pyramid OG

FIGURE 3.11 – Average OG obtained for 20 residual phase screens. The equivalent Strehl ratio is 55% in the H band. The OG are obtained from the different matrices $\mathbf{OG}(0,\delta\phi)$, $\mathbf{OG}(\delta\phi,0)$ and $\mathbf{OG}_{av}$ and the focal plane camera $\mathbf{OG}_{PSF}$. The first 500 modes are shown for clarity. The shaded area represents the standard deviation.

phase realisations (see Fig.3.12). In this manner, we have in our disposal several gain matrices $\mathbf{T}_i$ describing different seeing conditions. An example of the full dense gain matrix obtained for a Strehl ratio of 42% in shown in Fig.3.13.

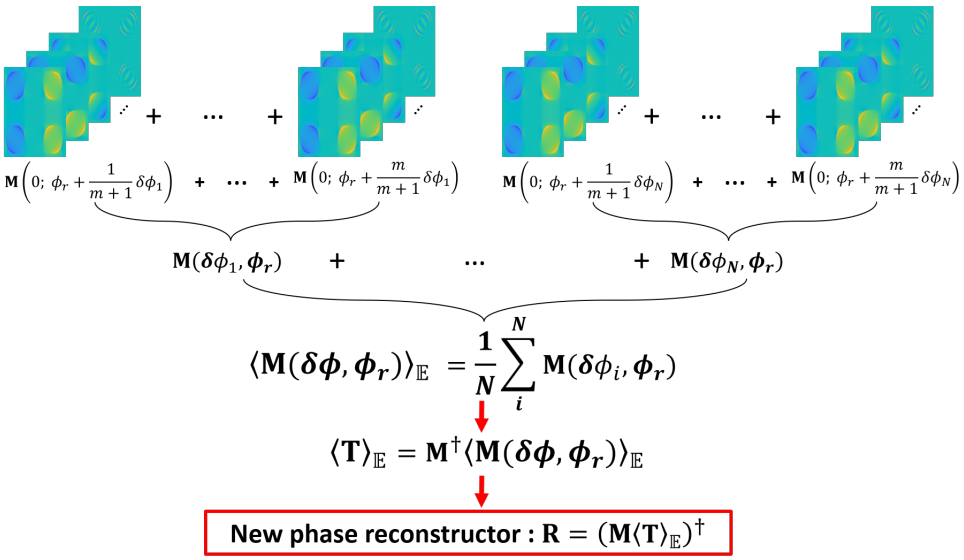

FIGURE 3.12 – Schematic of the statistical approach to obtain the coupling terms

These mean gain matrices give a representative idea of the strength of the coupling with the observation conditions. For example, Fig.3.13 shows a row of this matrix after normalising it with its diagonal term, the OG. The strength of the coupling varies from a few percent (1 – 2%) to a few ten percent (about 10% of the OG). The coupling will

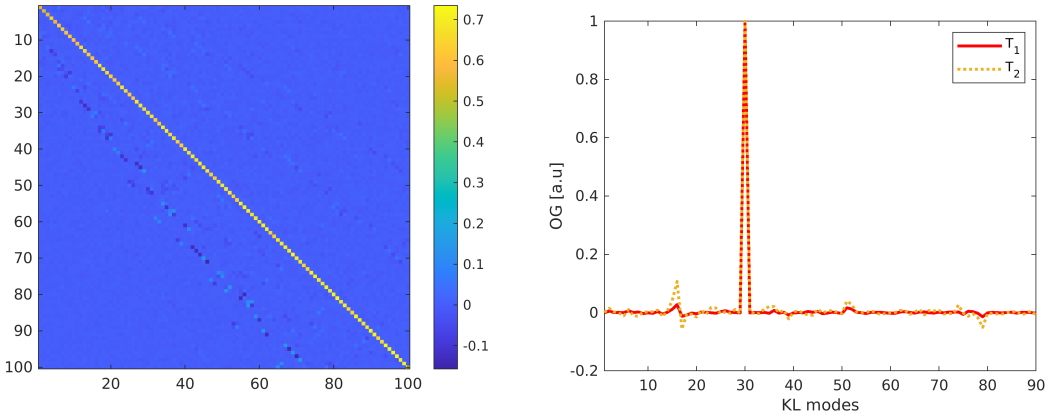

(a) Full gain matrix $\mathbf{T}_1$

(b) Coupling of KL_{30}

FIGURE 3.13 – Left : full average gain matrix obtained for a phase set whose Strehl ratio is equal to 42% in H band. Right : line 30 of gain matrices describing the coupling between the modes. The lines are normalised by the OG value. T_1 and T_2 are the average gain matrices obtained for a set of phases whose equivalent Strehl ratio is respectively 85% and 42% in H band.

be higher for higher residual phases, but still as a proportional fraction of the OG.

The hybrid reconstructor is obtained by following the procedure described in equation 3.22. The first step of the procedure is to normalise the average gain matrix by its diagonal. This step allows to obtain an intermediate matrix $\mathbf{T}_{int}$ with the ones on its diagonal and the weight of each coupling term, with respect to their respective OG, outside the diagonal. This matrix is then multiplied by the new OG extracted from the GSC image. Finally, the interaction matrix, $\mathbf{M}$, is updated with this updated dense gain matrix and the product will be used as reconstructor. In this way, the reconstructor used at each iteration is closer to the specific matrix of the phase screen considered. The mathematical process is the following

$$\begin{aligned} \mathbf{T}_{int} &= \frac{\langle \mathbf{T} \rangle_{\mathbb{E}}}{\langle \mathbf{OG} \rangle_{\mathbb{E}}}, \\ \mathbf{T}_{updated} &= \langle \mathbf{T} \rangle_{int} \times \mathbf{OG}_{PSF}, \\ \mathbf{R}_{updated} &= \left(\mathbf{M}\mathbf{T}_{updated} \right)^{\dagger}, \end{aligned} \tag{3.22}$$

where × stand for the terms by terms multiplication.

Frame-by-frame estimation using the hybrid reconstructor

This section focuses on the frame-by-frame estimation of residual phase screens of increasing amplitude using a non-modulated PWFS. For that purpose, we compare

the reconstruction using the full matrices : $\mathbf{M}$, $\mathbf{M}(\delta\phi,0)$, $\mathbf{M}(0,\delta\phi)$, $\mathbf{M}_{av}$ and the reconstruction using the hybrid matrices. Results are shown in Fig. 3.14, in that case, the WFE is computed on the full phase $WFE = \delta\phi - \widehat{\delta\phi}$.

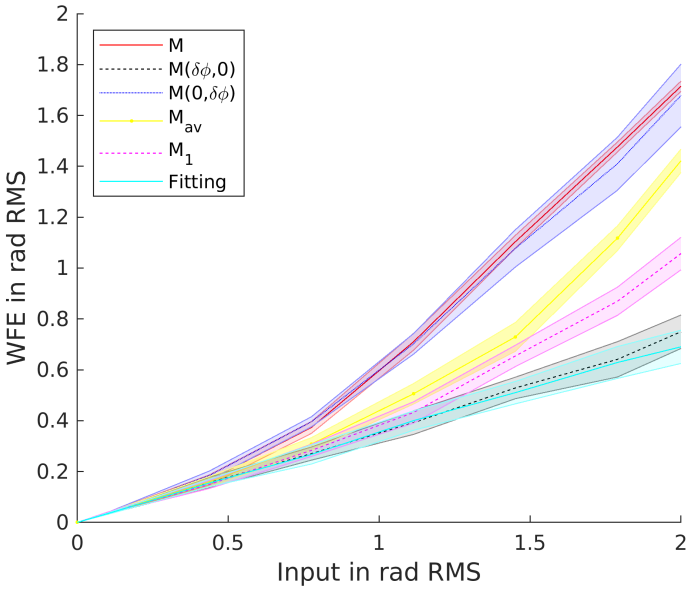

(a) WFE obtained with the full matrices.

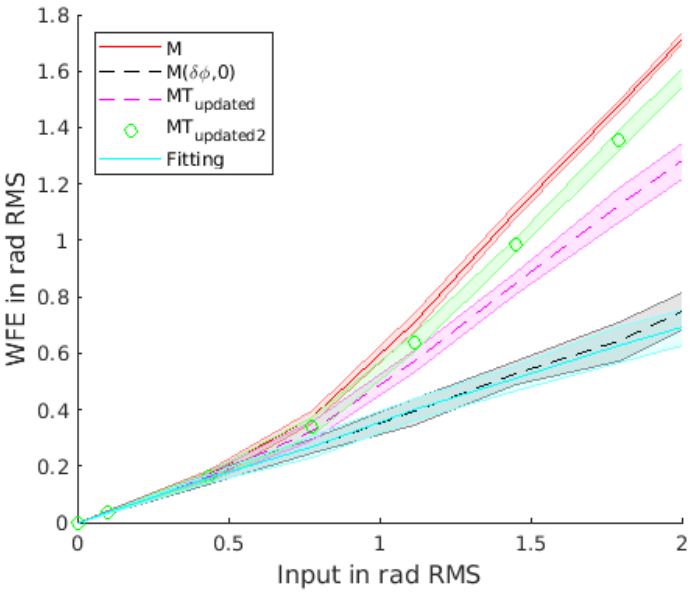

(b) WFE obtained with the hybrid matrices.

FIGURE 3.14 – WFE for residual phase screens, the equivalent Strehl ratio in the H band is within the range SR $\in$ [30;99]%. The shaded area represents the standard deviation.

From Fig.3.14 we see that the specific matrix (dotted-black curve) provides the best results as the WFE reaches the fitting error (cyan curve). As predicted with the 1D approach (see Fig.3.6), we confirm that the matrix computed around the residual, $\mathbf{M}(0,\delta\phi)$, provides an inaccurate phase reconstruction (blue curve). One solution to improve the estimation is to use the average matrix $\mathbf{M}_{av}$ (yellow curve) to ensure a systematic reduction of the WFE in comparison with the matrices $\mathbf{M}$ and $\mathbf{M}(0,\delta\phi)$. $\mathbf{M}_{av}$, is a good alternative to the specific matrix as it requires less computational time, and its dependency on the matrix computed around the phase itself makes it easier to approximate through the gain formalism. Indeed, as shown in Fig.3.11 the average gain $\mathbf{OG}_{av}$ is correctly estimated by adjusting the ones obtained with the focal plane camera (cf equation 3.21), especially in the modulated case.

Another interesting reconstructor is the median matrix $\mathbf{M}_1$, i.e, the matrix computed around half the wavefront. This matrix $\mathbf{M}_1$ is the specific matrix of degree $n = 1$ and its WFE is plotted in magenta in Fig.3.14. For small residual, the performance of this matrix is the same as the average matrix. However, when the amplitude increases one should prefer the use of the median matrix over the average matrix as it reduces the WFE more effectively. These differences between $\mathbf{M}_1$ and $\mathbf{M}_{av}$ come from the dependency of $\mathbf{M}_{av}$ with the push-pull matrix around the phase, $\mathbf{M}(0,\delta\phi)$. The larger the amplitude of the phase, the less representative of the linear relation between the intensity and the wavefront the matrix $\mathbf{M}(0,\delta\phi)$ is, which will taint with error the estimation of the average matrix, $\mathbf{M}_{av}$. Thus, using the matrix $\mathbf{M}_1$ corresponding to the push-pull matrix computed around half the wavefront should be prefer to the use of the average matrix in strong phase regime.

Reconstructors	$\mathbf{M}$	$\mathbf{M}(\phi,0)$	$\mathbf{M}(0,\phi)$	$\mathbf{M}_{av}$	$\mathbf{M}_1$
Hypothesis	$\|\|\phi\|\|_2 \ll 1$	$\|\|\phi\|\|_2 \in \mathbb{R}$	$\|\|\phi\|\|_2 \ll 1$	$\|\|\phi\|\|_2 \leq 1.2$	$\|\|\phi\|\|_2 \leq 1.5$

TABLEAU 3.4 – Phase regime summary for different reconstructors considering a 10% deviation from the fitting error.

The results obtained with the hybrid approach are plotted in Fig.3.14 bottom. The magenta curve now represents the WFE after estimating the phase screen using the hybrid reconstructor where the dense gain matrix is updated with the raw OG extracted from the GSC. Contrary to the green dots that represents the WFE of the hybrid approach using the OG adjusted of equation 3.21. We notice similar performance of the two approaches in the small phase regime (amplitude below 1.3rad RMS), yet, when the amplitude increase, the using the raw $\mathbf{OG}_{PSF}$ is more effective. Indeed, in strong turbulence regime or when using an unmodulated PWFS, the gain extracted from the GSC or their adjusted values either match with the specific gains respectively on the high-order modes or on the low-order modes, thus they are not representative of the true OG from the specific matrix because of the limitation of the convolutional approach (see Fig.3.11). However, these results are less promising as those from the specific matrix, but their allow for a 30% reduction in WFE compared to the classical approach. Furthermore, this performance is comparable to those achieved using the

average matrix $\mathbf{M}_{av}$.

We also performed the same simulation using one dense gain matrix for the whole range of phase residual, and by updating the diagonal of this matrix, we obtained the same result as using an average dense gain matrix corresponding at each amplitude (see Fig.3.15 blue squares). The gain matrix use for that demonstration is the one obtained for the worst seeing condition $\mathbf{T}_{SR=30\%}$. Therefore, this method is robust enough to describe the current seeing condition using one dense gain matrix and computing the current OG with the GSC.

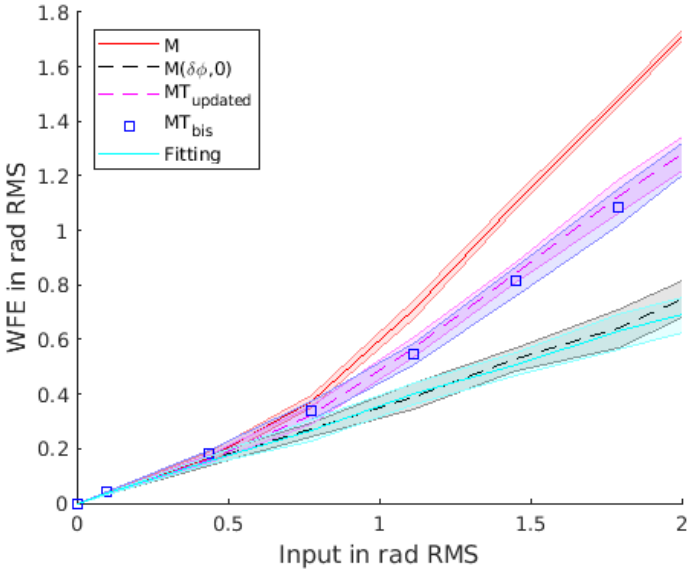

FIGURE 3.15 – WFE for residual phase screens, the reconstructor $\mathbf{MT}_{bis}$ corresponds to the updated reconstructor using equation 3.22 but with a unique dense gain matrix for the whole range. The equivalent Strehl ratio in the H band is within the range SR $\in$ [30;99]%. The shaded area represents the standard deviation.

Practical implementation of the hybrid reconstructor

How can we build such reconstructor in practice?
Following the "recipe" outlined in the previous section, we require : (i) a focal plane camera for gains tracking, and (ii) a coupling matrix. The primary challenge lies in acquiring these coupling terms since they depend on the specific matrix formalism. Therefore, the real question is : how can we obtain the specific matrix for a given phase?

For on lab experiment :

— **monochromatic source** : proceed the same way as in simulation. One can send phase residual on the DM or Spatial Light Modulator (SLM) of the bench and calibrate around different amplitude of this phase. By doing this for a set of phase

screen, one can obtain a gain matrix representative of this seeing condition and use it in close-loop by updating this matrix with the OG from the GSC.

— **polychromatic source** : one needs to have a broad band detector such as MKIDS for example (O'Connor et al. 2019) and a prism before the detector to split the different wavelengths. By sending one phase residual on the DM and by calibrating around this phase, the MKIDS detector allows to have the push-pull matrices at different wavelengths.

For on sky experiment : A parallel can be made with the construction of a pseudo-synthetic interaction matrix (Heritier 2019). In that scenario, an accurate "clone" of the AO system is needed to perform the simulations to obtained the dense gain matrix. This matrix will be updated on sky with the focal plane camera.

Conclusion

The analysis of the frame-by-frame estimation of phase residuals using the hybrid methods gives us confidence in using this method in close-loop system with a non-linear WFS such as the unmodulated PWFS.

3.3.2 Implementation in closed-loop for the non-modulated pyramid

In this section, we assess the performance of the hybrid method in a closed-loop with a unmodulated PWFS. Two scenario will be compared : (i) OG compensation only and (ii) full gain compensation. The idea is to understand the limits of the gain compensation and its ability to close the loop without modulation. This simulation will also help in understanding the importance of the non-diagonal terms appearing in the gain matrix to help the loop converge, especially in strong turbulence regime. The performance of the unmodulated PWFS will be compared with the classical modulated PWFS using the standard interaction matrix. The AO loop parameters can be found in Table 3.5. The gain matrix used for the simulations with the unmodulated PWFS is built around residuals corresponding to a Strehl ratio of 30% in the H band. The update of this matrix is done using the focal plane camera image (see equation 3.22). The closed-loop simulations are done for three different r_0 values in the V-band (500 nm), specifically $r_0 \in \{6.9, 7.9, 10\}$ cm, corresponding to seeing conditions of $\{1.5; 1.3; 1\}$ arcsec at 500 nm, respectively. The chosen seeing conditions are quite harsh but were chosen to assess the robustness of this approach.

The simulations are done without noise so the star magnitude is not a concern here. The idea is to prove the feasibility of closing the loop without modulation using our hybrid method. A thorough analysis regarding the noise was made in Agapito et al. (2023) comparing the performance of the unmodulated PWFS and its modulated version. It is clear that the use of the unmodulated PWFS is preferred in the low flux regime due to its high sensitivity.

TABLEAU 3.5 – Closed-loop parameters

Frequency	1kHz
Time of the loop	1s
Frames delay	2
Integrator gain	0.4
Leak factor	0.99
Sensing wavelength	850nm, I-band
Atmosphere	3 layers
Wind	$v = 5m.s^{-1}$ ground layer
Noise	0

All the closed-loop were made with the same loop gain of g=0.4. We chose to fix the value of the gain to compare the different reconstructor in the same loop configuration. The results are presented in Table 3.6.

r_0 (cm)	PWFS $r_{mod} = 0\lambda/D$			PWFS $r_{mod} = 3\lambda/D$	Fitting
	M	**MOG**	**MT**$_{updated}$	**M**	
10	144 ± 39	138 ± 38	94 ± 10	103 ± 11	86
7.9	390 ± 75	254 ± 66	145 ± 25	143 ± 21	110
6.9	602 ± 82	276 ± 50	210 ± 44	181 ± 36	124

TABLEAU 3.6 – Statistical study of close-loop for three different r_0 made for 20 different atmosphere screens for each r_0. The average wind speed is $6.7m.s^{-1}$ considering the 3 atmospheric layers. The close-loop WFE and the standard deviation are specified in nm RMS. The average WFE is computed for the last 800 iterations.

From Table 3.6, we see that, for median seeing condition (1" $\iff$ r_0 = 10cm) the unmodulated PWFS performs better than the modulated PWFS reducing the WFE of 10nm RMS on average (increase of 3 points of SR in H band from 85% with the modulation to 88% without modulation). For seeing condition of 1.3" $\iff$ r_0 = 7.9cm, we obtained the same performances as the modulated pyramid using the hybrid method on the unmodulated version.

Yet, when the seeing increases and reaches 1.5" $\iff$ r_0 = 6.9cm, the modulated PWFS performs better on average. One reason could be the accuracy of the OG obtained from the GSC, as they prove to be an approximation of the real specific gains, matching either the low-orders or the high-orders or not matching at all for strong turbulence (see Fig.3.11). This mismatch may dominate here; however, it is important to highlight that with the proposed method it is possible to close the loop without modulation even under such harsh seeing conditions (seeing below 1.5").

The results obtained with the gain compensation only reduce the WFE compared to using the interaction matrix alone but do not reach the performance of the hybrid approach. The benefit of the OG compensation is clear, especially in strong seeing

condition (1.5" $\Longleftrightarrow$ r_0 = 6.9cm), when it allows for a reduction of the WFE by half. Yet, with our study using a fix loop gain it is not enough to converge close to the fitting error (even in medium seeing condition). Increasing the loop gain might be helpful but one should prefer the use of the full gain compensation as it is more robust in any conditions.

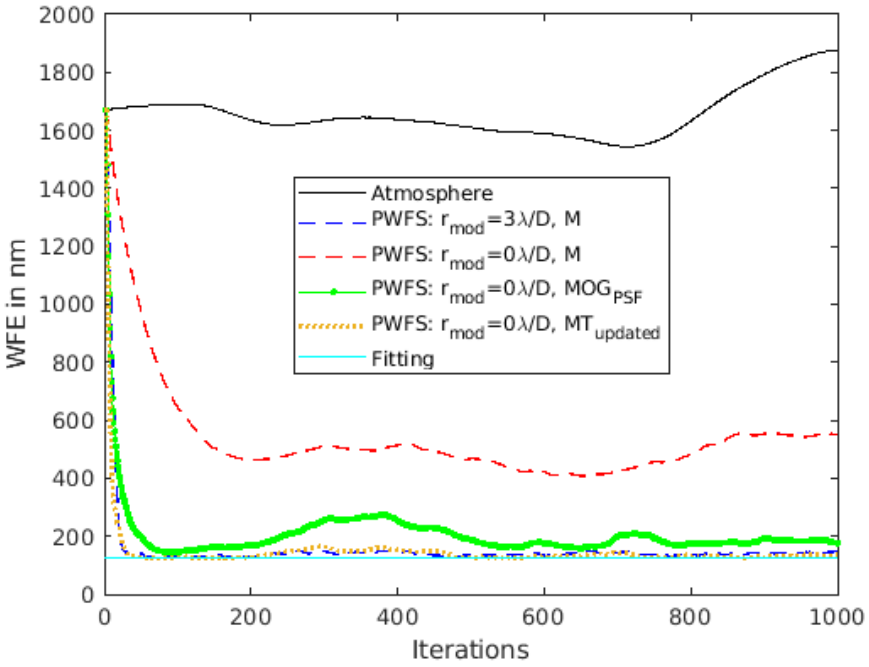

(a) Closed-loop

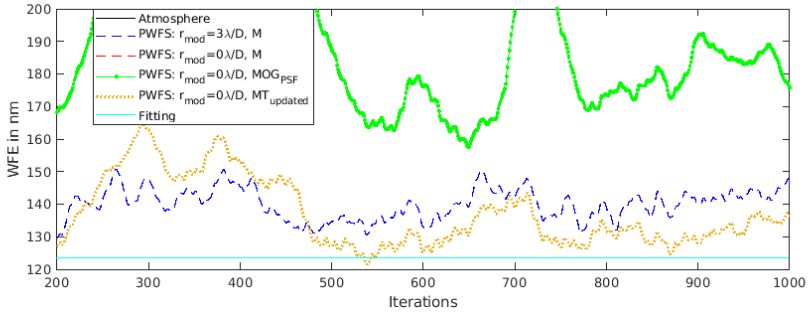

(b) Closed-loop zoom

FIGURE 3.16 – Closed-loop r_0 = 6.9cm and average wind speed of $v = 6.7 m.s^{-1}$, loop gain=0.4. Comparison between the classical modulated PWFS $r_{mod} = 3\lambda/D$ blue dashed curve and the different reconstructor using the non-modulated PWFS. The classical interaction matrix in red dashed curve, modal gain compensation in green curve and the full gain compensation in yellow dotted curve. The fitting error is plotted in cyan.

3.4 Summary

In this chapter, I have demonstrated that it is possible to accurately describe the non-linearity of Fourier filtering WFS using the matrix formalism, hence a linear formalism. This matrix can be determined as the average of push-pull matrices around moving operational points. It has the property of being dependent on the phase to be measured, hence its named specific matrix. It perfectly describes the loss of sensitivity associated with the expansion of the PSF in the focal plane; non-linearity can therefore be interpreted as an over-modulation. An algorithm was presented to obtain the specific matrix in numerical simulations; its pseudo-inverse was then used to estimate the phase regardless of its amplitude. This result proves that it is possible to find an optimal matrix reconstructor outside the FF-WFS dynamic range.

When considering an achromatic sensor such as the non-modulated PWFS working around the flat wavefront, it is possible to get this specific matrix in practice. To do so, the moving operational points around which the push-pull interaction matrices are done are obtained through a polychromatic approach. This allows to take advantage of the phase scaling with the wavelength and explains why the specific matrix is able to estimate highly wrapped phases.

The framework proposed in this chapter serves as a versatile model for FF-WFS. No hypothesis except for the achromaticity of the phase mask was made. With technology such as liquid crystal, achromatic ZWFS could be manufactured, which will allow to adapt the specific matrix formalism to the Zernike-type WFS.

The dependency of the specific matrix with the phase to be measured suggests an update of the reconstructor at each frame. Such a constraint may be not realistic for standard AO systems. I therefore exposed two approaches to approximate the specific matrix : the average matrix $\mathbf{M}_{av}$ and the median matrix $\mathbf{M}(0, \phi_r + \delta\phi/2)$. I proved that the gain of the average matrix, which is the closest to the true gain from the specific matrix can be approximated through the gain formalism using accessible tools such as a focal plane camera, in particular when considering the modulated PWFS. The coupling terms (off diagonal terms in the dense gain matrix) which will help maintaining correct performance especially in strong turbulence regime are obtained statistically depending on the expected seeing condition. These coupling terms are derived by averaging several specific matrices to accurately represent the dominant coupling interactions depending on the observation conditions. This matrix is then fed with the frame-by-frame OG estimation provided by the GSC, creating an hybrid reconstructor mixing a statistical and a frame-by-frame method. It is important to emphasise that by updating the average gain matrix, we adjust the value of the coupling terms making possible the use of an average gain matrix built for a given seeing condition on different seeing conditions. The proposed hybrid method enables to close the loop with an unmodulated pyramid, even under challenging seeing conditions as severe as 1.3", which was previously not possible.

CONCLUSION

Adaptive optics (AO) systems are essential for high-resolution imaging in ground-based astronomy, enabling telescopes to approach their theoretical diffraction limits. With the advent of giant segmented telescopes (GSTs), such as the Extremely Large Telescope (ELT) and other next-generation observatories, the demand for more advanced AO systems has grown. These systems must not only correct for atmospheric turbulence, which degrades the resolution of ground-based facilities, but also deal with new types of aberrations caused by their immense structures, such as pupil fragmentation and the Low Wind Effect. These aberrations have specific amplitudes, spatial frequencies and temporal behaviours that differ from those of atmospheric disturbances, posing problems for traditional WFS and AO systems in terms of measurement, control and correction. WFS must gain in both sensitivity and dynamic ranges whereas AO systems must therefore push back the limits of correction capabilities, taking into account atmospheric turbulence and telescope-produced aberrations, to enable the detection of exoplanets located in the close environment of their host star.

To achieve this goal, the AO system's wavefront sensor (WFS) must provide accurate measurements of optical aberrations, particularly under difficult conditions of low flux and high-speed operation. These two conditions are crucial for reducing the AO system's temporal error and extending their associated sky coverage. By effectively targeting less luminous guide stars, astronomers can explore more of the sky and observe objects that were previously out of reach of conventional systems. To achieve this, the WFS needs to be exceptionally sensitive, so that it can provide accurate phase estimates even when the signal-to-noise ratio (SNR) is low. The high sensitivity of the WFS will enable more accurate wavefront correction, which is essential for maintaining high resolution. This advance is necessary not only for the discovery of new exoplanets, but also for a wide range of astronomical observations requiring the highest possible resolution. The continued development of AO systems and WFS technology is therefore fundamental to the future of observational astronomy.

In this context, this PhD thesis focuses on the study of the next generation of wavefront sensors, in particular the class of Fourier-filtered wavefront sensors (FF-WFS). Within this class, we have focused on two particularly emerging sensors : the Zernike wavefront sensor (ZWFS) and the pyramidal wavefront sensor (PWFS). These advanced sensors will play a central role in GST AO systems, thanks to their exquisite sensitivity. The PWFS, for example, is expected to be the WFS for single conjugate adaptive optics (SCAO) modules in most first-light instruments for the ELT and the Giant Magellan Telescope (GMT), while the ZWFS is planned as a second-stage WFS

for high-contrast imaging modes. These sensors are essential for achieving the high levels of correction needed to observe distant, faint astronomical objects. However, PWFS and ZWFS are known to suffer from inherent non-linear behaviours, which pose significant challenges to their optimal performance, particularly when using traditional linear reconstruction approaches. Solving these problems has been one of the main objectives of this work. We have sought to deepen our understanding of the non-linear responses exhibited by these sensors, and to develop solutions that could either extend their linear operational regime, or adapt reconstruction algorithms to take account of their non-linear characteristics. In addressing these issues, we have sought to improve the performance of AO systems in the GST, ensuring that these powerful telescopes can realise their full potential in providing unprecedented observational capabilities.

This doctoral thesis focused mainly on extending the dynamic range of these WFSs, due to the nature of the wavefront (turbulence and local telescope effects) and the final performance required for high-contrast imaging. Achieving this level of wavefront accuracy has led the AO community to seek multi-level correction systems. Upgrades to current AO systems are focused on this type of development, as illustrated by projects such as RISTRETTO, SAXO+ and future ELT instruments such as PCS.

From the WFS concept perspective, the study of the nonlinear behaviour of the ZWFS has led to the study and characterisation of a new variant of the Zernike mask : the phase-shifted Zernike wavefront sensor (PS-ZWFS) developed by Doelman et al. (2019) and characterised in terms of sensitivity and dynamic range in the framework of this thesis. This innovative phase mask consists of two ZWFS, each imposing an opposite phase shift of $\pm\pi/2$. In this way, the PS-ZWFS increases the signal diversity, thus broadening the bijective regime of the sensor. As a result, the dynamic range of the sensor is significantly improved, allowing more accurate wavefront measurements even in scenarios involving high amplitude phase. We have demonstrated the significant improvement offered by the PS-ZWFS over the traditional ZWFS in the measurement of differential piston in the presence of AO residuals. Our results showed that PS-ZWFS reduces differential piston by a factor of three on an ELT-type pupil. The ability of PS-ZWFS to provide more accurate differential piston measurements is particularly valuable in the context of GST, where minimising differential piston is crucial to achieve optimal performance. This improvement makes PS-ZWFS an ideal WFS for accurate petal measurements, following the work done by Bertrou-Cantou (2021) and Levraud (2023).

We also compared the performance of PS-ZWFS and classical ZWFS in a multi-stage correction context to improve the near-core correction of the point spread function (PSF). This improvement is essential for detecting exoplanets in regions close to their host stars. The extended dynamic range of PS-ZWFS makes it more robust under strong observing conditions, paving the way for wider use and more robust systems. These studies led to the development of a two-stage AO system on the PAPYRUS bench.

This project aims not only to demonstrate the feasibility of integrating PS-ZWFS into on-sky operations, but also to showcase the performance improvements that this WFS can bring. In many ways, this system serves as a crucial test platform for future ELT instruments, providing valuable information and hands-on experience of using Zernike-type WFS as part of a multi-stage system. By rigorously testing and refining this approach, the project paves the way for advanced AO systems that will be crucial to ELT.

The final and most fundamental approach of this work focused on modifying the phase reconstructor to ensure accurate phase estimation beyond the linear regime of a FF-WFS (note that this approach can be adapted and extended to any type of WFS). This strategy sought a balance between linear and nonlinear methods, using a Linear Parameter Varying (LPV) approach to preserve the traditional matrix formalism. It led to the development of a reconstructor that efficiently handles nonlinear responses of the FF-WFS class. More precisely, for unmodulated PWFS, we extended the previous optical gain (OG) formalism established by Korkiakoski et al. (2008), Fauvarque (2017), Deo (2019) and Chambouleyron (2021). This new methodology allows the construction of a dense gain matrix that not only integrates the modal gain but also includes the coupling terms responsible for modal confusion. By accounting for these coupling effects, the reconstructor allows for a more accurate measurement of the wavefront. The reconstructor integrates frame-by-frame tracking of the OG using a gain-scheduling camera (GSC), as introduced by Chambouleyron et al. (2021b), with a statistical approach to account for off-diagonal terms. This combination allows for dynamic adjustment of the reconstruction process within the loop, ensuring that the system can adapt to changes in the wavefront and improve the overall measurement accuracy. Using the example of unmodulated PWFS, we have demonstrated the feasibility of this method, showing that it is possible to effectively close the loop without modulation under strong-seeing conditions. This significant advance could enable the use of unmodulated pyramid sensors to control both atmospheric turbulence and specific aberrations associated with the GST, such as differential piston. The ability to handle these aberrations without modulation represents a major advance, potentially improving the performance of AO systems in next-generation telescopes. The LPV-based reconstructor thus represents a significant advance in the ability to correct non-linearities in AO systems, leading to more reliable and accurate wavefront measurements, which are crucial for high-resolution astronomical observations.

PERSPECTIVES

The studies performed on FF-WFS, in particular with PS-ZWFS and unmodulated PWFS, open new possibilities for future AO systems. These advances not only allow to extend the dynamic range and accuracy of wavefront measurements, but also address the crucial challenge of building a phase estimator that accounts for the non-linearities inherent in FF-WFS. The LPV approach, which allows for precise wavefront correction without requiring modulation, paves the way for more versatile and robust AO systems, able to handle both atmospheric turbulence and specific GST aberrations.

Naturally, to continue this work, an experimental validation would be essential to confirm the simulation predictions. The existing experimental platforms at LAM and ONERA offer ideal environments for such investigations. The first step is to complete the characterisation of the PS-ZWFS and the DM before implementing it on the PAPYRUS bench. A thorough study of the control laws of multi-stage systems should be performed in order to optimise the performance of the future two-stage AO system in PAPYRUS. By integrating the second-stage correction with the PS-ZWFS operating at a higher frame rate than the first stage, we can experimentally validate a two-stage correction system and compare the different control strategies. Moreover, the introduction of a segmented DM in a pupil plane could be interesting to evaluate the performance of petal measurement in the presence of AO residuals. The LOOPS bench, equipped with a spatial light modulator (SLM), both in the pupil and in the focal plane, can simulate an ELT-type pupil and various FF-WFS configurations, including ZWFS, PS-ZWFS and unmodulated PWFS. These configurations provide comprehensive platforms to compare these sensors in the context of petal measurements and quantify the impact of noise on their performance.

The research conducted in this PhD could be used for the development of future ground-based systems, such as SAXO+, RISTRETTO, PCS and ANDES, which are all dedicated to the study of circumstellar disks, giant planet formation and the detection of Earth-like exoplanets and will use multi-stage AO correction to achieve the required contrast. And to achieve these goals, extreme wavefront correction and control are required.

However, the implications of this work go far beyond ground-based observations. The synergy between ground-based and space-based observatories plays a vital role in advancing our knowledge of the universe, as each platform offers unique advantages. Together, they create a comprehensive observational strategy that can answer some of the most challenging questions in astronomy. In the near future, the launch of the Nancy Grace Roman Space Telescope (RST) will be a major milestone in the use of

active optics in space. The RST will not only serve as a powerful tool for astronomical discovery, but also as a technology demonstrator for the upcoming Habitable World Observatory (HWO) project.

Although space observatories do not experience atmospheric turbulence, they still need to correct quasi-static aberrations at a sub-nanometer level. These aberrations can be caused by thermal expansion, vibrations, or misalignments in the optics, which require precise correction to ensure the resolution of the observations. Achieving this level of precision is made possible by the use of extremely sensitive WFSs such as the FF-WFS. Therefore, research on Zernike-type WFSs and phase reconstructors is particularly relevant for space applications, as it contributes to the development of systems that can meet the stringent requirements of future space observatories.

Finally, a particularly promising area of research for the future is the application of deep learning techniques to address the nonlinear response of FF-WFS. Nonlinear approaches such as deep learning can effectively handle the nonlinear responses of FF-WFS, but they are limited to the bijective regime of WFS. Traditional AO systems rely on indirect measurement of the wavefront from intensities on the detector, and solving this inverse problem at high speeds typically requires linear assumptions. However, FF-WFSs are inherently nonlinear with respect to the wavefront, making them a challenging target for conventional AO control algorithms. Deep learning offers a powerful alternative by learning complex nonlinear relationships directly from the data. Recent studies have demonstrated promising results in using deep learning to overcome the nonlinearity of FF-WFS and improve the accuracy of wavefront reconstruction. By exploiting the capabilities of deep learning, we can potentially develop more accurate and robust AO systems that can efficiently handle the nonlinear characteristics of FF-WFS. This opens new possibilities for high-performance AO applications in astronomy.

Bibliographie

Agapito, G., Pinna, E., Esposito, S., Heritier, C. T., & Oberti, S. 2023, Astronomy and Astrophysics, 677, A168

Babcock, H. W. 1953, Publications of the Astronomical Society of the Pacific, 65, 229

Basden, A., Myers, R., & Gendron, E. 2012, Monthly Notices of the Royal Astronomical Society, 419, 1628

Bennett, D. P. 2008, Exoplanets : Detection, Formation, Properties, Habitability, 47

Bertram, T., Absil, O., Bizenberger, P., et al. 2018, in Adaptive optics systems vi, Vol. 10703, SPIE, 357–367

Bertram, T., Bizenberger, P., van Boekel, R., et al. 2023, in Adaptive Optics for Extremely Large Telescopes 7th Edition

Bertrou-Cantou, A. 2021, PhD thesis, Université Paris Cité

Bertrou-Cantou, A., Gendron, E., Rousset, G., et al. 2022, Astronomy and Astrophysics, 658, A49

Bertrou-Cantou, A., Gendron, E., Rousset, G., et al. 2020, in Society of Photo-Optical Instrumentation Engineers (SPIE) Conference Series, Vol. 11448, Adaptive Optics Systems VII, ed. L. Schreiber, D. Schmidt, & E. Vernet, 1144812

Beuzit, J.-L., Feldt, M., Dohlen, K., et al. 2008, in Society of Photo-Optical Instrumentation Engineers (SPIE) Conference Series, Vol. 7014, Ground-based and Airborne Instrumentation for Astronomy II, ed. I. S. McLean & M. M. Casali, 701418

Beuzit, J. L., Vigan, A., Mouillet, D., et al. 2019, Astronomy and Astrophysics, 631, A155

Blanc, A., Fusco, T., Hartung, M., Mugnier, L., & Rousset, G. 2003, Astronomy Astrophysics, 399, 373

Blind, N., Chazelas, B., Kühn, J., et al. 2022, in Adaptive Optics Systems VIII, Vol. 12185, SPIE, 2213–2221

Bloemhof, E. 2014, in Complex Light and Optical Forces VIII, Vol. 8999, SPIE, 221–228

Bond, C. Z., Sauvage, J.-F., Schwartz, N., et al. 2022, in Adaptive Optics Systems VIII, Vol. 12185, SPIE, 389–400

Bond, C. Z., Wizinowich, P., Chun, M., et al. 2018, in Adaptive Optics Systems VI, Vol. 10703, SPIE, 642–652

Brandl, B. R., Feldt, M., Glasse, A., et al. 2014, in Society of Photo-Optical Instrumentation Engineers (SPIE) Conference Series, Vol. 9147, Ground-based and Airborne Instrumentation for Astronomy V, ed. S. K. Ramsay, I. S. McLean, & H. Takami, 914721

Cantalloube, F., Farley, O. J., Milli, J., et al. 2020, Astronomy & Astrophysics, 638, A98

Cantalloube, F., Mouillet, D., Mugnier, L., et al. 2015, Astronomy & Astrophysics, 582, A89

Cavarroc, C., Boccaletti, A., Baudoz, P., Fusco, T., & Rouan, D. 2006, Astronomy & Astrophysics, 447, 397

Cerpa-Urra, N., Kasper, M., Kulcsár, C., Raynaud, H.-F., & Taïssir Heritier, C. 2022, Journal of Astronomical Telescopes, Instruments, and Systems, 8, 019001

Chambouleyron, V. 2021, PhD thesis, Aix-Marseille Université

Chambouleyron, V., Cissé, M., Salama, M., et al. 2024, in Adaptive Optics Systems IX, Vol. 13097, SPIE, 349–361

Chambouleyron, V., Fauvarque, O., Janin-Potiron, P., et al. 2020, Astronomy and Astrophysics, 644, A6

Chambouleyron, V., Fauvarque, O., Plantet, C., et al. 2023, Astronomy & Astrophysics, 670, A153

Chambouleyron, V., Fauvarque, O., Sauvage, J.-F., et al. 2021a, Astronomy & Astrophysics, 650, L8

Chambouleyron, V., Fauvarque, O., Sauvage, J.-F., Neichel, B., & Fusco, T. 2021b, arXiv preprint arXiv :2103.02297

Chassat, F. 1992, PhD thesis, Paris 11

Chauvin, G., Desidera, S., Lagrange, A.-M., et al. 2017, Astronomy & Astrophysics, 605, L9

Chauvin, G., Lagrange, A.-M., Dumas, C., et al. 2004, Astronomy & Astrophysics, 425, L29

Cisse, M., Fauvarque, O., Chambouleyron, V., et al. 2024, in Adaptive Optics Systems IX, Vol. 13097, SPIE, 218–228

Clénet, Y., Buey, T., Gendron, E., et al. 2019, in Adaptive Optics for Extremely Large Telescopes conference, 6th edition

Cochran, W. & Hatzes, A. 1996, Astrophysics and Space Science, 241, 43

Conan, R. & Correia, C. 2014, in Adaptive optics systems IV, Vol. 9148, SPIE, 2066–2082, https://github.com/rconan/OOMAO

Consortini, A., Ronchi, L., & Moroder, E. 1973, JOSA, 63, 1246

Correia, C. M., Fauvarque, O., Bond, C. Z., et al. 2020, Monthly Notices of the Royal Astronomical Society, 495, 4380

Crass, J. 2014, PhD thesis

Currie, T., Fukagawa, M., Thalmann, C., Matsumura, S., & Plavchan, P. 2012, The Astrophysical Journal Letters, 755, L34

Dai, G.-m. 1995, JOSA A, 12, 2182

Davies, R. & Kasper, M. 2012, Annual Review of Astronomy and Astrophysics, 50, 305

Davies, R., Schubert, J., Hartl, M., et al. 2016, in Ground-based and Airborne Instrumentation for Astronomy VI, Vol. 9908, SPIE, 621–632

Deo, V. 2019, PhD thesis, Université Paris Cité

Deo, V., Gendron, E., Rousset, G., et al. 2018, Astronomy & Astrophysics, 619, A56

Deo, V., Gendron, É., Rousset, G., et al. 2019, Astronomy and Astrophysics, 629, A107

Doelman, D. S., Auer, F. F., Escuti, M. J., & Snik, F. 2019, Optics letters, 44, 17

Dohlen, K., Langlois, M., Lanzoni, P., et al. 2006, in Ground-based and Airborne Telescopes, Vol. 6267, SPIE, 1093–1103

Dohlen, K., Morris, T., Lopez, J. P., et al. 2018, in Adaptive Optics Systems VI, Vol. 10703, SPIE, 1107–1117

Engler, B., Le Louarn, M., Vérinaud, C., Weddell, S., & Clare, R. 2022, Journal of Astronomical Telescopes, Instruments, and Systems, 8, 021502

Escuti, M. J., Kim, J., & Kudenov, M. W. 2016, Optics and Photonics News, 27, 22

Esposito, S. & Riccardi, A. 2001, Astronomy & Astrophysics, 369, L9

Fanson, J., McCarthy, P. J., Bernstein, R., et al. 2018, in Ground-based and Airborne Telescopes VII, Vol. 10700, SPIE, 319–332

Fauvarque, O. 2017, PhD thesis, Aix-Marseille Universite ; Laboratoire d'Astrophysique de Marseille

Fauvarque, O., Janin-Potiron, P., Correia, C., et al. 2019, JOSA A, 36, 1241

Fauvarque, O., Neichel, B., Fusco, T., & Sauvage, J.-F. 2015, Optics Letters, 40, 3528

Fauvarque, O., Neichel, B., Fusco, T., Sauvage, J.-F., & Girault, O. 2016, Optica, 3, 1440

Fauvarque, O., Neichel, B., Fusco, T., Sauvage, J.-F., & Girault, O. 2017, Journal of Astronomical Telescopes, Instruments, and Systems, 3, 019001

Fernandes, R. B., Mulders, G. D., Pascucci, I., Mordasini, C., & Emsenhuber, A. 2019, The Astrophysical Journal, 874, 81

Fetick, R., Chambouleyron, V., Muslimov, E., et al. 2023, in Adaptive Optics for Extremely Large Telescopes 7th Edition

Fried, D. L. 1966, JOSA, 56, 1372

Fried, D. L. 1982, JOSA, 72, 52

Fried, D. L. 1990, JOSA A, 7, 1224

Fusco, T., Rousset, G., Sauvage, J.-F., et al. 2006, Optics Express, 14, 7515

Fusco, T., Sauvage, J.-F., Dohlen, K., et al. 2015in

Fusco, T., Thatte, N., Meimon, S., et al. 2010, in Adaptive Optics Systems II, Vol. 7736, SPIE, 1101–1112

Ghedina, A., Cecconi, M., Ragazzoni, R., et al. 2003, in Adaptive Optical System Technologies II, Vol. 4839, SPIE, 869–877

Gilles, L. & Ellerbroek, B. L. 2006, Applied Optics, 45, 6568

Gilmozzi, R. & Spyromilio, J. 2007, The Messenger, 127, 3

Goodman, J. W. 2005, Introduction to Fourier optics (Roberts and Company publishers)

Graham, J. R., Macintosh, B., Doyon, R., et al. 2007, arXiv preprint arXiv :0704.1454

Gunnels, S., Davison, W. B., Cuerden, B., & Hertz, E. 2004, in Astronomical Structures and Mechanisms Technology, Vol. 5495, SPIE, 168–179

Guyon, O. 2005, The Astrophysical Journal, 629, 592

Guyon, O., Martinache, F., Clergeon, C., et al. 2011, in Astronomical Adaptive Optics Systems and Applications IV, Vol. 8149, SPIE, 79–84

Haffert, S. Y. 2024, Astronomy & Astrophysics, 683, A113

Haffert, S. Y., Close, L. M., Hedglen, A. D., et al. 2022, Journal of Astronomical Telescopes, Instruments, and Systems, 8, 021513

Haffert, S. Y., Males, J. R., Close, L. M., et al. 2022, in Society of Photo-Optical Instrumentation Engineers (SPIE) Conference Series, Vol. 12185, Adaptive Optics Systems VIII, ed. L. Schreiber, D. Schmidt, & E. Vernet, 121853D

Heritier, C. T. 2019, PhD thesis, Aix Marseille Université

Hodapp, K. W., Jensen, J. B., Irwin, E. M., et al. 2003, Publications of the Astronomical Society of the Pacific, 115, 1388

Hours, A., Carlotti, A., Mouillet, D., et al. 2022, in Adaptive Optics Systems VIII, Vol. 12185, SPIE, 736–749

Hu, J., Bandyopadhyay, S., Liu, Y.-h., & Shao, L.-y. 2021, Frontiers in Physics, 8, 586087

Janin-Potiron, P. 2017, PhD thesis, Université Côte d'Azur

Jensen-Clem, R., Hinz, P., von Kooten, M., et al. 2021, in Society of Photo-Optical Instrumentation Engineers (SPIE) Conference Series, Vol. 11823, Techniques and Instrumentation for Detection of Exoplanets X, ed. S. B. Shaklan & G. J. Ruane, 1182309

Jovanovic, N., Absil, O., Baudoz, P., et al. 2018, in Adaptive Optics Systems VI, Vol. 10703, SPIE, 573–590

Kasper, M., Urra, N. C., Pathak, P., et al. 2021, arXiv preprint arXiv :2103.11196

Khan, M. S., Jenkins, J., & Yoma, N. B. 2017, IEEE Signal Processing Magazine, 34, 104

Kolmogorov, A. N. 1941, Numbers. In Dokl. Akad. Nauk SSSR, 30, 301

Korkiakoski, V., Vérinaud, C., & Le Louarn, M. 2008, Applied optics, 47, 79

Leboulleux, L. 2023, arXiv preprint arXiv :2311.14000

Levraud, N. 2023, PhD thesis, thèse de doctorat dirigée par Fusco, Thierry et Esposito, Simone PHYSIQUE SCIENCES DE LA MATIERE - Spécialité : INSTRUMENTATION Aix-Marseille 2023

Levraud, N., Chambouleyron, V., Sauvage, J. F., et al. 2024a, Astronomy & Astrophysics, 682, A84

Levraud, N., Cisse, M., Chambouleyron, V., et al. 2024b, in Adaptive Optics Systems IX, Vol. 13097, SPIE, 130972E

Lyot, B. 1932, Zeitschrift für Astrophysik, Vol. 5, p. 73, 5, 73

Macintosh, B., Graham, J. R., Ingraham, P., et al. 2014, Proceedings of the National Academy of Science, 111, 12661

Macintosh, B. A., Graham, J. R., Palmer, D. W., et al. 2008, in Society of Photo-Optical Instrumentation Engineers (SPIE) Conference Series, Vol. 7015, Adaptive Optics Systems, ed. N. Hubin, C. E. Max, & P. L. Wizinowich, 701518

Madec, P.-Y. 2012, in Adaptive optics systems III, Vol. 8447, SPIE, 22–39

Mahajan, V. N. 1983, JOSA, 73, 860

Malacara, D. 2007, Wiely Interscience

Malbet, F. 1996, Astronomy and Astrophysics, Supplement, 115, 161

Marconi, A., Abreu, M., Adibekyan, V., et al. 2022, in Ground-based and Airborne Instrumentation for Astronomy IX, Vol. 12184, SPIE, 720–735

Marois, C., Lafreniere, D., Doyon, R., Macintosh, B., & Nadeau, D. 2006, The Astrophysical Journal, 641, 556

Marois, C., Macintosh, B., Barman, T., et al. 2008, science, 322, 1348

Martins, D., Holzlöhner, R., Verinaud, C., & Kleinclaus, C. 2022, in Modeling, Systems Engineering, and Project Management for Astronomy X, Vol. 12187, SPIE, 492–505

Matthews, K., Ghez, A., Weinberger, A., & Neugebauer, G. 1996, Publications of the Astronomical Society of the Pacific, 108, 615

Mawet, D., Riaud, P., Absil, O., & Surdej, J. 2005, Astrophysical Journal, 633, 1191

Mayor, M. & Queloz, D. 1995, Nature, 378, 355

Mazoyer, J., Goulas, C., Vidal, F., et al. 2024, arXiv e-prints, arXiv :2406.18424

Medwadowski, S. J. 1989, Astrophysics and Space Science, 160, 33

Mennesson, B., Juanola-Parramon, R., Nemati, B., et al. 2020, arXiv preprint arXiv :2008.05624

Milli, J., Kasper, M., Bourget, P., et al. 2018, in Adaptive Optics Systems VI, Vol. 10703, SPIE, 752–771

Moore, E. H. 1920, Bulletin of the American Mathematical Society, 26, 394

Mugnier, L. M., Cornia, A., Sauvage, J.-F., et al. 2009, JOSA A, 26, 1326

Neichel, B., Rigaut, F., Vidal, F., et al. 2010, Monthly Notices of the Royal Astronomical Society, 406, 2267

Nelson, J. & Sanders, G. H. 2008, in Ground-based and Airborne Telescopes II, Vol. 7012, SPIE, 504–521

Nicolle, M. 2006, PhD thesis, Paris 11

Nicolle, M., Fusco, T., Rousset, G., & Michau, V. 2004, Optics letters, 29, 2743

N'Diaye, M., Dohlen, K., Fusco, T., & Paul, B. 2013, Astronomy & Astrophysics, 555, A94

O'Connor, E., Shearer, A., & O'Brien, K. 2019, New Astronomy Reviews, 87, 101526

Penrose, R. 1955, Proceedings of the Cambridge Philosophical Society, 51, 406

Quattri, M., Zago, L., & Plötz, F. 1988, in Very Large Telescopes and their Instrumentation, Vol. 2, Vol. 30, 127

Quirós-Pacheco, F., van Dam, M., Bouchez, A. H., et al. 2022, in Adaptive Optics Systems VIII, Vol. 12185, SPIE, 348–360

Ragazzoni, R. 1996, Journal of modern optics, 43, 289

Ragazzoni, R. 2000, in ESO Conference on Adaptive Optics for Very Large Telescopes, 307–313

Ragland, S., Wizinowich, P., van Kooten, M., et al. 2022, in Society of Photo-Optical Instrumentation Engineers (SPIE) Conference Series, Vol. 12185, Adaptive Optics Systems VIII, ed. L. Schreiber, D. Schmidt, & E. Vernet, 121850Y

Rayleigh, L. 1880, Monthly Notices of the Royal Astronomical Society, Vol. 40, p. 254, 40, 254

Rigaut, F., Ellerbroek, B. L., & Flicker, R. 2000, in Proceedings of the SPIE, Vol. 4007, 1022–1031

Rigaut, F. & Gendron, E. 1992, Astronomy and Astrophysics (ISSN 0004-6361), vol. 261, no. 2, p. 677-684., 261, 677

Riggs, A. J. E., Bailey, V., Moody, D. C., et al. 2021, in Society of Photo-Optical Instrumentation Engineers (SPIE) Conference Series, Vol. 11823, Techniques and Instrumentation for Detection of Exoplanets X, ed. S. B. Shaklan & G. J. Ruane, 118231Y

Roddier, F. 1999

Roddier, F. & Roddier, C. 1997, Publications of the Astronomical Society of the Pacific, 109, 815

Rousset, G., Fontanella, J.-C., Kern, P., Gigan, P., & Rigaut, F. 1990, Astronomy and Astrophysics (ISSN 0004-6361), vol. 230, no. 2, April 1990, p. L29-L32. Research supported by the European Southern Observatory, Ministere de la Recherche et de la Technologie, Ministere de l'Education Nationale, INSU, DRET, and Ministere de la Defense., 230, L29

Ruane, G., Riggs, A., Mazoyer, J., et al. 2018, in Space Telescopes and Instrumentation 2018 : Optical, Infrared, and Millimeter Wave, Vol. 10698, SPIE, 851–869

Ruane, G., Wallace, J. K., Steeves, J., et al. 2020, Journal of Astronomical Telescopes, Instruments, and Systems, 6, 045005

Sabelhaus, P. A. & Decker, J. E. 2004, Optical, Infrared, and Millimeter Space Telescopes, 5487, 550

Salama, M., Guthery, C., Chambouleyron, V., et al. 2024a, The Astrophysical Journal, 967, 171

Salama, M., Guthery, C., Chambouleyron, V., et al. 2024b, arXiv preprint arXiv :2407.16791

Sanders, G. H. 2013, Journal of Astrophysics and Astronomy, 34, 81

Sauvage, J.-F., Fusco, T., Guesalaga, A., et al. 2015in

Sauvage, J.-F., Fusco, T., Rousset, G., & Petit, C. 2007, JOSAA, 24, 2334

Schnetler, H., Bond, C., Chulani, H., et al. 2022, in Modeling, Systems Engineering, and Project Management for Astronomy X, Vol. 12187, SPIE, 85–104

Schreiber, L., Langlois, M., Jolissaint, L., et al. 2023, in Adaptive Optics for Extremely Large Telescopes 7th Edition

Schwartz, N., Sauvage, J.-F., Correia, C., et al. 2018, arXiv preprint arXiv :1809.08839

Schwider, J. 1990, in progress in optics, Vol. 28 (Elsevier), 271–359

Shack, R. V. 1971, in Spring Meeting of Optical Society of America, 1971, Vol. 656

Shi, F., Balasubramanian, K., Hein, R., et al. 2016, Journal of Astronomical Telescopes, Instruments, and Systems, 2, 011021

Sivo, G. 2013, PhD thesis, Université Paris 13

Smith, B. A. & Terrile, R. J. 1984, Science, 226, 1421

Sparrow, C. M. 1916, Astrophysical Journal, vol. 44, p. 76, 44, 76

Steeves, J., Wallace, J. K., Kettenbeil, C., & Jewell, J. 2020, Optica, 7, 1267

Strehl, K. 1895, Zeitschrift für Instrumentenkunde, 15, 362

Taylor, G. I. 1933, Proceedings of the Royal Society of London. Series A, Mathematical and Physical Sciences, 164, 476

Thomas, S., Fusco, T., Tokovinin, A., et al. 2006, Monthly Notices of the Royal Astronomical Society, 371, 323

Tokovinin, A., Els, S., Hinnen, P., et al. 2005, Publications of the Astronomical Society of the Pacific, 117, 395

Tozzi, A., Stefanini, P., Pinna, E., & Esposito, S. 2008, in Adaptive Optics Systems, Vol. 7015, SPIE, 1454–1462

van Kooten, M. A. M., Ragland, S., Jensen-Clem, R., et al. 2022, Astrophysical Journal, 932, 109

Vérinaud, C. 2004, Optics Communications, 233, 27

Vidal, F., Goulas, C., Galicher, R., et al. 2022, in Adaptive Optics Systems VIII, Vol. 12185, SPIE, 1305–1317

Vigan, A., Bonnefoy, M., Ginski, C., et al. 2016, Astronomy & Astrophysics, 587, A55

Von Karman, T. 1948, Proceedings of the National Academy of Sciences, 34, 530

Wallace, J., Wenger, T., Jewell, J., et al. 2023, in Adaptive Optics for Extremely Large Telescopes 7th Edition

Wang, Y. & Vaughan, A. H. 1988, Applied Optics, 27, 27

Wirenstrand, K. 1995, Telescope Control Systems, 2479, 129

Wright, J. T. & Gaudi, B. S. 2012, arXiv preprint arXiv :1210.2471

Zernike, F. 1934, Monthly Notices of the Royal Astronomical Society, Vol. 94, p. 377-384, 94, 377